Spin Relaxation of Hydrogen and Deuterium in Storage Cells

Bernd Braun
Ludwig-Maximilians-University
Munich, Germany

MPI H – V 25 – 1995

Translated by M.Kaiser, M.A., and R.Kaiser, PhD, Berlin 1998.

Summary

The following thesis summarizes the results of developmental work at a Breit-Rabi polarimeter which will be used in the measurement of polarization in the target of the HERMES experiment. In this experiment at the HERA storage ring in Hamburg an internal polarized target is used in a deep inelastic scattering experiment aimed at discerning the spin structure of the nucleon. The required target density is achieved through the use of an open target cell.

At a test set-up at the Max Planck Institute (MPI) for Nuclear Physics in Heidelberg measurements on the spin relaxation of hydrogen and deuterium atoms in storage cells were carried out using an improved Breit-Rabi polarimeter. The experimental results were in agreement with a model which traces spin relaxation to collisions with the storage cell walls and spin exchange collisions.

It is the goal of the developmental work at the Breit-Rabi polarimeter and the relaxation measurements, to produce polarization of hydrogen or deuterium atoms in a storage cell with an uncertainty of $\Delta P < 0.03$. The major steps on the way to this goal are:

- Development of a highly sensitive and highly precise detector for the Breit-Rabi polarimeter and the improvement of the vacuum conditions in the region of particle beam detection in order to reduce the statistical errors.
- Work out a calibration procedure to determine the analyzing power of the Breit-Rabi polarimeterṪhe errors on this analyzing power determine the systematic errors of the polarization measurement. This method, once developed, can be conducted during the HERMES experiment without requiring extensive reconstruction.
- The measurement and explanation of spin relaxation in a storage cell within the framework of a theoretical model. On hand of this model all corrections can be calculated and added to the measured polarization for an account of the target polarization, so that the relaxation in the storage cell is understood within the required error bars.

The particular sensitivity of the atomic beam detector allows, under the conditions of the HERMES experiment, measurements of the nuclear polarization of hydrogen atoms in the storage cell within 10 s with a statistical error of $\Delta P < 0.03$. In the case of the vector polarization of the deuterium atoms about 30 s are required while 60 s are needed to achieve this accuracy for the tensor polarization.

The uncertainty of the calibration procedure is strongly dependant on the analyzing power of the Breit-Rabi polarimeter. It has been shown that the polarimeter can be calibrated with high precision if all components relevant for the polarization analysis achieve a working efficiency of close to 100 %. At this stage in the HERMES experiment the following systematic errors are to be expected: $\Delta P_z = 0.03$ on the vector polarization of hydrogen and deuterium and $\Delta P_{zz} = 0.05$ on the tensor polarization of deuterium. Methods for a further reduction of these errors will be shown.

The results of the relaxation measurements show that although wall collisions cause a pronounced loss of electron polarization, the nuclear polarization in strong external magnetic fields is only negligibly affected by wall collisions. This is a result of the decoupling of the nucleon spin from the electron spins. In a specially constructed storage cell with drifilm coating designed for highly accurate relaxation measurements, in which atoms during their stay complete 3500 wall collisions, the loss of nucleon polarization through wall collisions with a holding field of 350 mT - the planned longitudinal holding field for the HERMES target - are only 10^{-3} for hydrogen and even only 10^{-4} for deuterium during the entire time in the storage cell. Even if the storage cell is cooled to a temperature of 100 K no increase in these low polarization losses can be detected.

More important for the relaxation of the nucleon spin are spin exchange collisions through which vector polarization of the nucleon is transferred to the electron or vice versa. Although the hydrogen atoms only complete between 1.5 and 15 spin exchange collisions during their stay in the storage cell, their effects on the hyperfine occupancy can be clearly shown. The detection is made through the so-called *fast* spin exchange reactions which have been detected for the first time in this work. In the test storage cells, as a product of spin exchange collisions within a holding field of 350 mT, about 1 % of the injected nuclear polarization is transferred to the unpolarized electrons. In the case of hydrogen the average length of stay is increased and thus the average number of spin exchanges is also increased by a factor of $\sqrt{2}$. The smaller critical field of the deuterium atoms and the related improved decoupling of nucleon and electron spins results in a markedly smaller polarization loss through spin exchange collisions than in the case of hydrogen (with the same holding field), with values of 0.3 % for the vector polarization and 0.7 % for the tensor polarization.

In the HERMES experiment the atoms experience an average of 310 wall collisions during their stay in the target storage cell. The average length of stay is also a factor of 10 shorter, with an average density which is a factor of 10 greater than in the test storage cells. Due to the small number of wall collisions their effect on the target polarization may be disregarded. The polarization losses resulting from wall collisions are about two orders of magnitude smaller than polarization losses caused by spin exchange collisions. Since the higher density is roughly compensated for by the shorter duration of stay, the effects of the spin exchange collisions can be transferred directly from the test storage cell to the target storage cell. With hydrogen in a transverse guiding field of 154 mT a polarization of $P_z = \pm 0.89(2)$ and in a longitudinal guiding field of 350 mT a polarization of $P_z = \pm 0.96(1)$ can be expected. The expected polarization losses during the relaxation inside the storage cell are 1.5 % at 350 mT and 7 % at 154 mT, which are caused by an average value of 1.5 spin exchange collisions. In the case of deuterium the polarization losses are on the order of fractions of a percent, therefore the polarization is largely independant of whether the target is running at 154 mT or at 350 mT. The expected vector polarization has values of $P_z = +0.88(1)$ and $P_z = -0.90(1)$, respectively, the expected tensor polarization is $P_{zz} = +0.98(2)$ and $P_{zz} = -1.78(2)$, respectively. These values consider the polarization injected by the atomic beam source as well as the relaxation caused by wall and spin exchange collisions.

Contents

1 Introduction

1.1 The Spin Structure of the Nucleon

The spin structure of nucleons may be described by several independant *spin structure functions.* These state how the polarization of target nucleons manifests itself in an asymmetry in deep inelastic scattering of polarized leptons on the charged constituents of the nucleons. One of the most important and experimentally explored is $g_1(x, Q^2)$. Using the parton model it can be interpreted as the superposition of the quark distributions $q_f^+(x, Q^2)$ and $q_f^-(x, Q^2)$ summed over all flavours f:

$$g_1(x, Q^2) = \frac{1}{2}\sum_f e_f^2 \left[q_f^+(x, Q^2) - q_f^-(x, Q^2)\right] = \frac{1}{2}\sum_f e_f^2 \left[\Delta q_f(x, Q^2)\right]. \tag{1.1}$$

$q_f^+(x, Q^2)$ is the probability to scatter on a quark with spin parallel and $q_f^-(x, Q^2)$ with spin anti-parallel to the nucleon spin. e_f is the charge of the quark with flavour f. Q^2 is the negative square of the invariant mass of the virtual photon exchanged in the scattering process. $x = Q^2/2M\nu$ is described as the Bjorken scaling variable. In the Breit system, in which the energy transfer through the virtual photon vanishes, x describes the portion of the total momentum carried by the hit parton [1, 2]. M describes the mass of the nucleon and $\nu = E - E'$ the energy transfer in the scattering process.

For the spin structure functions $g_1(x, Q^2)$ J.D. Bjorken derived a sum rule from fundamental principles of QCD. In this rule the integral over the difference of this structure function for proton and neutron is related to the ratio g_A/g_V of axial and vector coupling constant that is known from neutron beta decay [3, 4]:

$$\int_0^1 \left[g_1^p(x) - g_1^n(x)\right] \mathrm{d}x = \frac{1}{6}\frac{g_A}{g_V}\left(1 - \frac{\alpha_S}{\pi}\right). \tag{1.2}$$

Through the comparison of the beta decay of the Ξ^- with neutron beta decay J. Ellis and R. Jaffe derived separate sum rules for proton and neutron under the assumption that the SU(3) flavour symmetry is fulfilled and that the strange sea of the nucleon is not polarized ($\Delta s = 0$) [5]:

$$\Gamma_1^p(Q^2) = \int_0^1 g_1^p(x, Q^2)\ \mathrm{d}x = 0.160 \pm 0.006 \tag{1.3}$$

$$\Gamma_1^n(Q^2) = \int_0^1 g_1^n(x, Q^2)\ \mathrm{d}x = -0.021 \pm 0.018. \tag{1.4}$$

The numerical value for Γ_1^p is given in [6], it was calculated with a QCD radiative correction according to [7] for $Q^2 = 3\,\mathrm{GeV}^2$. The value for the neutron stems from [8] and was calculated with a radiative correction after [9] for $Q^2 = 2\,\mathrm{GeV}^2$.

First measurements of the spin structure function $g_1^p(x, Q^2)$ through deep inelastic scattering of polarized electrons on a solid target were undertaken at SLAC by the collaborations E80 and E130 [10, 11, 12]. The spin structure function is measured through the scattering of longitudinally polarized leptons on a longitudinally polarized proton target. The experimental results were in agreement with the theoretical predictions of the Ellis-Jaffe sum rule (1.3). These experiments reached a minimal value of $x = 0.1$. It was only when the EMC collaboration at CERN, through the use of polarized muons, with energies of up to 200 GeV, extended the measured region up to $x = 0.01$ that a deviation from the Ellis-Jaffe sum rule for the proton was indicated with a significance of two standard deviations [13, 14].

This result caused further experiments for the investigation of the spin structure. Among them are: another CERN experiment, the so-called SMC experiment [15], which uses polarized muons as projectiles, an experiment at SLAC by the E143 collaboration [6], which uses polarized electrons and has shown the smallest errors for Γ_1^p so far and the HERMES experiment, from which results on Γ_1^p are expected for 1996. The two former experiments show the following results:

$$\begin{array}{llll} \text{SMC}: & \Gamma_1^p & = & 0.136 \pm 0.011(\text{stat.}) \pm 0.011(\text{syst.}) \quad \text{for } Q^2 = 10\,\text{GeV}^2 \\ \text{E143}: & \Gamma_1^p & = & 0.127 \pm 0.004(\text{stat.}) \pm 0.010(\text{syst.}) \quad \text{for } Q^2 = 3\,\text{GeV}^2. \end{array} \tag{1.5}$$

Both experiments confirm a deviation from the theoretical prediction of the Ellis-Jaffe sum rule in agreement with the result of the EMC collaboration. The E143 experiment with a significance of even more than two standard deviations.

In order to test the fundamental Bjorken sum rule(1.2), scattering experiments have to be carried out with nuclei that contain neutrons. The E143 and SMC collaborations used a polarized deuterium target to this end, at SLAC, the E142 collaboration conducted an experiment with polarized ^{3}He [8].

After a combined analysis of all published data regarding spin structure functions, the violation of the Ellis-Jaffe sum rule is confirmed and traced to a negative polarization of the strange quarks in the sea of $\Delta s = -0.11 \pm 0.08$. A further important conclusion which may be drawn from these experiments is that the quarks in the nucleon only contribute $\Delta\Sigma = 0.24 \pm 0.23$ to it's spin. This stands against the prediction derived from the Ellis-Jaffe sum rule of $\Delta\Sigma = 0.60 \pm 0.12$ [9]. The Bjorken sum rule (1.2) is confirmed by the experiments within the errors.

A further important structure function is $g_2\left(x, Q^2\right)$ which can be measured through deep inelastic scattering of longitudinally polarized leptons on a transversally polarized target. The sum rule for this structure function was derived by H. Burkhardt and W.N. Cottingham [18]:

$$\Gamma_2 = \int_0^1 g_2\left(x, Q^2\right)\, \mathrm{d}x = 0. \tag{1.6}$$

Experimental results which confirm this sum rule have been published by the SMC collaboration. The E143 collaboration has also conducted measurements on this structure function, with publication still pending.

All experiments conducted to date with the purpose of measuring spin structure functions used an external target. In order to achieve sufficient counting rates from the resulting low average beam currents, high density targets must be used.

The E142 collaboration used a ^{3}He target in a thin-walled sealed glass cell under a high pressure of 8 bar. The polarization was created through spin exchange collisions with optically pumped rubidium vapor [20, 21]. The target polarization varied between 0.3 and 0.4. Since a portion of the electron from the beam were scattered on the glass walls, the effective target polarization is highly diluted.

In the case of hydrogen and deuterium generally ammonia or butane targets are used, in which free protons are dynamically polarized [14]. First paramagnetic centers, i.e. uncoupled electrons, are created in the target by irradiation with electrons. These electrons are then polarized through a strong magnetic field of 2.5 T at a temperature of 0.5 K. The thus created electron polarization is transferred onto the nucleon through microwave radiation. Although in this way a proton polarization of about 0.8 may be reached, the average polarization of the protons in the target is significantly smaller because of the unpolarized nitrogen, carbon and oxygen nuclei in the target material. This is taken into account through a so-called dilution factor, which in e.g. in the case of an ammonia target is 3/17.

1.2 The HERMES Experiment

The HERMES experiment [22, 23] began construction in the winter of 1994/95 in one of the four experimental halls of the HERA ring, which is a positron-proton collider at DESY in Hamburg and has just begun operation. In contrast to the previously discussed experiments, this is a storage ring experiment with an internal thin gas target. Achievable luminosities in such an experiment are comparable with those of external target experiments [24], since much higher beam currents are used with concomitantly lower target densities. It is a significant advantage that the target polarization is not diluted through other nuclei.

The HERMES experiment uses the positron beam of the HERA ring. The energy of the positrons is between 30 and 35 GeV with a current of up to 60 mA. Depending on the target luminosities between 1.8 and $50 \cdot 10^{31}\,\mathrm{cm}^{-2}\,\mathrm{s}^{-1}$ are expected.

The positrons are transversally polarized as a result of the Sokolov-Ternov effect[25]. With the help of a pair of spin rotators [26], the spin is rotated by 90° into the longitudinal direction in front of the experiment and rotated back behind the experiment. The beam polarization is measured with the help of a Compton polarimeter [27]; during operation of the spin rotators a beam polarization of $P_B = 0.65$ was achieved [28].

Hydrogen, deuterium and ^{3}He are used for targets. The polarization of the ^{3}He targets is built up through the optical pumping of helium atoms that previously were excited into the metastable $^3\mathrm{S}_1$-state. The polarization is transferred to helium atoms in the ground state through exchange collisions [29]. The polarized hydrogen and deuterium target will be described in more detail in chapter 1.3.

The measurment program of the HERMES experiment will allow a much more profound view into the spin structure of nucleons than was possible in previously conducted experiments. The measurement program contains:

- The measurement of the spin structure functions $g_1(x, Q^2)$, $g_2(x, Q^2)$ and an examination of the associated sum rules for proton and neutron (1.2), (1.3), (1.4) und (1.6).
- The measurement of structure functions belonging to the tensor spin observable of the deuterium atom $b_1(x, Q^2)$ [30, 31] and $\Delta(x, Q^2)$ [32].
- Semi-inclusive measurements, where additional to the scattered lepton the leading hadron is detected in coincidence. [33]:
  - Direct detection of the strangeness polarization Δs through the measurement of K^- asymmetries [34].
  - Measurement of the valence quark polarizations Δu^v and Δd^v through the measurement of asymmetries in scattering processes with charged pions in the final state [35].
  - Measurement of the transverse spin structure function h_1 with odd chirality[36].

The first point provides for a complete examination of all previously conducted measurements of spin structure functions. The violation of the Ellis-Jaffe sum rule can thus be examined once more in an independant experiment.

The measurement of the deuterium structure functions $b_1(x, Q^2)$ and $\Delta(x, Q^2)$ requires a target with high tensor polarization and negligible vector polarization. The internal gas target of the HERMES experiment can fill this requirement, in contrast to previously used solid state targets (chapters 1.3 and 14.3).

A semi-inclusive measurement with acceptable error bars and the detection of hadrons in the final state in coincidence with the scattered lepton is made possible only by the use of a thin target which pions and kaons, that are created through fragmentation, can leave largely undisturbed [37]. A direct measurement of the strangeness polarization is necessary for the definitive interpretation of the violation of the Ellis-Jaffe sum rule since gluons can also contribute to the spin of the nucleon.

1.3 The Hydrogen and Deuterium Target of the HERMES Experiment

A necessary requirement for a sufficient luminosity in the HERMES experiment is the achievement of a target area density in the range of $10^{14}\,\mathrm{cm}^{-2}$. With a gas jet target, in which a polarized particle beam is brought into contact with the storage ring beam, the surface densities achieved were only $2 \cdot 10^{11}\,\mathrm{cm}^{-2}$ [38]. As often suggested [39, 40, 41], it is possible to increase the target density by more than two orders of magnitude by injecting the particle beam into a T-shaped storage cell. Through this, the polarized gas is held for a period of about 3 ms in the interaction region and the target area density is increased. This principle is illustrated in figure 1.1. The current state of development suggests that a target area density of $8 \cdot 10^{13}\,\mathrm{cm}^{-2}$ can be expected for the hydrogen or deuterium target (Tables14.3 and 14.4).

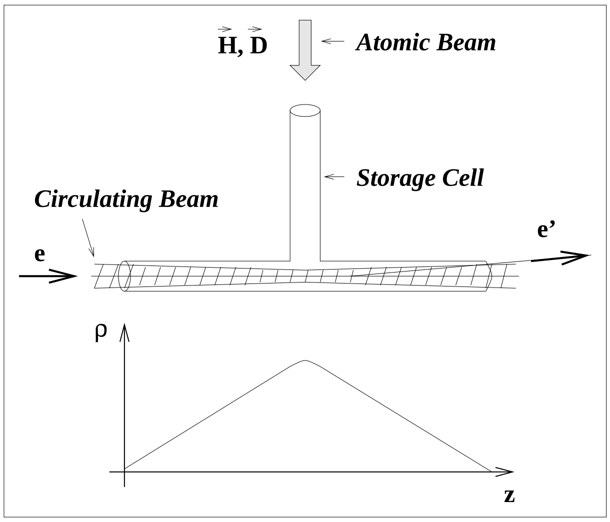

Fig. 1.1:
Principle of a storage cell target and density profile along the beam pipe. The polarized gas is injected from a source through a pipe on the side of the storage cell and is held there for some time because of the low conductance.

The positrons of the HERA ring pass the target section along the 40 cm long beampipe of the storage cell with its elliptical cross section, without touching the walls. Some positrons are scattered on the polarized nucleons of the gas inside the storage cell. The storage cell of the HERMES experiment consists of thin aluminum walls whose surface is covered with drifilm[1] so as to reduce relaxation caused by wall collisions.

The polarized atomic beam is produced in an atomic beam source[45, 46, 47] through Stern-Gerlach spin separation in the inhomogeneous field of a sextupole magnet. Here, the dependence of hyperfine splitting on an external magnetic field is exploited. Figure 1.2 depicts the four hyperfine states of a hydrogen atom in its basic state. The states are numbered in accordance with their energy. The increase in energy of the two top states $|\,1\,\rangle$ and $|\,2\,\rangle$ causes an acceleration towards the direction of weaker fields in the inhomogeneous field of a sextupole magnet. These two states are focused on the axis of the magnet. The two other states $|\,3\,\rangle$ and $|\,4\,\rangle$ accelerate towards the direction of stronger fields, are directed away from the axis of the magnet and are

[1] After [42]: 50 % of as solution of dimethyldimethoxysilane $(CH_3)_2Si(OCH_3)_2$, trimethylmethoxysilane $(CH_3)_3SiOCH_3$ and four drops of acetic acid per 100 ml solution. The coating procedure is described in[43]

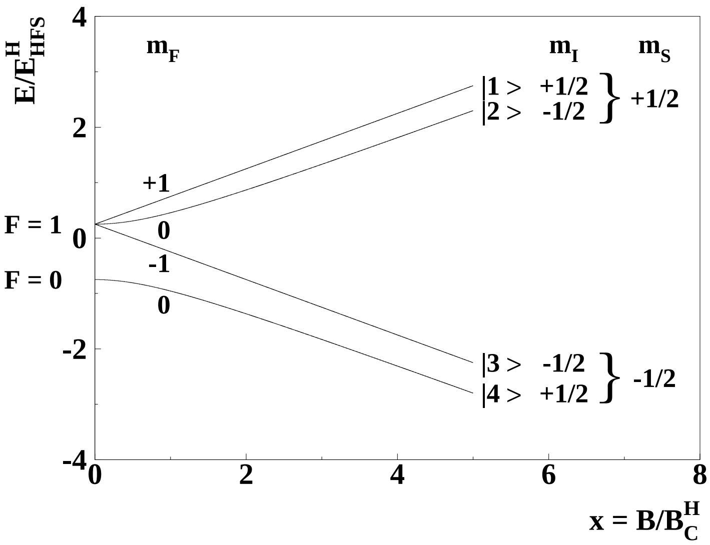

Fig. 1.2:
Breit-Rabi diagram after [44]. Energy Eigenvalues for the hyperfine structure of a hydrogen atom in an external magnetic field. The calculation of these energy Eigenvalues is treated in chapter 2. $E^{\rm H}_{\rm HFS}$ is the hyperfine structure splitting energy, $x = B/B^{\rm H}_C$ is the ratio between the external and the critical magnetic field. m_I und m_S are the magnetic quantum numbers of nuclear spin and electron spin, m_F is the magnetic quantum number of the total angular momentum F.

removed from the atomic beam. The figure $m_S = +1/2$ applies to both focused states which means that after the sextupole magnet the atomic beam has a high positive degree of electron polarization.

With the aid of adiabatic high energy transitions which cause the almost complete conversion within the hyperfine structure, the polarization of the electron may be transferred to the nucleus. If one were to induce an exchange of populations $|\,2\,\rangle$ and $|\,4\,\rangle$ after the sextupole magnet, the resulting particle beam would contain mostly the states $|\,1\,\rangle$ and $|\,4\,\rangle$, which in a strong magnetic field corresponds to a high positive nuclear polarization. A beam with negative nuclear polarization can be created through an exchange of $|\,1\,\rangle$ and $|\,3\,\rangle$. It is possible to select the sign of the polarization through the application of the appropriate high frequency transitions which can be changed within seconds to minimize systematic errors.

The target atoms in the storage cell are exposed to a multitude of interactions which reduce the nuclear polarization. These include:

- Spin exchange collisions of target atoms with one another,
- Collisions of the target atoms with the walls of the storage cell,
- Interactions of the target atoms with the electromagnetic fields which are created by the positrons of the beam in the HERA ring, the so-called bunch-field depolarization [48] and
- the recombination of the atoms at the walls of the storage cell.

The polarization of the target must be monitored during the experiment. To this end the Breit-Rabi polarimeter is used [49, 50] which will be described further in chapter 1.5. A portion of the gas of the storage cell will be fed to the polarimeter which will analyze this sample. The axes of the beam source and the polarimeter are set at an angle of 30^0 relative to the horizontal plane. In doing this, the target atoms cannot leave the storage cell without first being exposed to the interactions of the central target section.

Internal targets have already been used successfully several times. These instances include: The electron storage rings VEPP-3 in Novosibirsk [51, 52], the electron stretcher ring AmPS in Amsterdam [53] for the measurement of the tensor analyzing power T_{20} in the scattering of electrons on deuterium, and IUCF in Bloomington for the examination of the scattering of polarized protons on a polarized proton target [54], where an atomic beam source similar to the

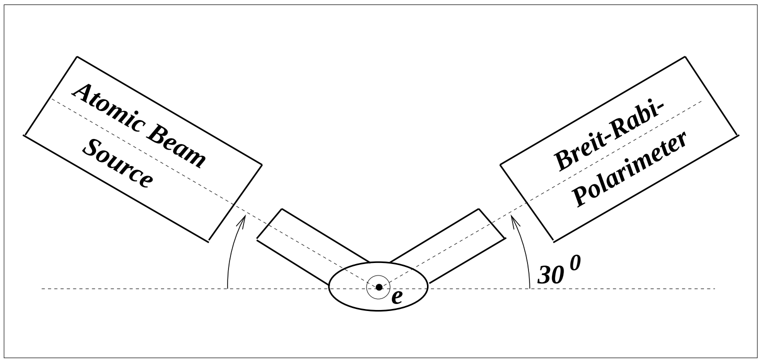

Fig. 1.3:
Schematic drawing of the spin polarized gas target for hydrogen and deuterium in the HERMES experiment. The storage cell with elliptical beam pipe is in the middle, along with the injection pipe and and the exit pipe. The axes of source and polarimeter are tilted by 30^0 relative to the horizontal plane.

HERMES source was used. A further experiment with a storage cell target was conducted at the test storage ring (TSR) in Heidelberg, where the HERMES atomic beam source was used albeit with a modified sextupole magnet. The properties of the target, particularly density and polarization were measured [56, 57] and a stored proton beam was polarised by exploiting the spin dependant cross section of the pp-scattering [58, 59]. The target polarization achieved in this experiment will be discussed in chapter 14.1 in relationship with the relaxation process in the storage cell.

1.4 The Test Stand for the Breit-Rabi Polarimeter

The following description of the construction of the apparatus to measure the polarization of atomic beams stemming from a storage cell (figure 1.4) reflects the model for the planned internal gas targets for hydrogen and deuterium of the HERMES experiment (figure 1.3). An atomic beam source injects a polarized particle beam into a storage cell, wherein the atoms remain for some time and experience interactions with one another and the wall. By use of an exit tube a sample beam is formed that can be analyzed by the Breit-Rabi polarimeter. Three significant goals will be pursued:

- to gain operational experience with the Breit-Rabi detector under conditions similar to those which will be experienced during the HERMES experiment,
- to examine relaxation mechanisms which induce conversions in the hyperfine structure and then affect the polarization of the gas (chapter12), and
- to measure the efficiency of high energy transitions for the calibration of the polarimeter using a modified construction without storage cell between atomic beam source and polarimeter (chapter 8).

In contrast to the setup of the HERMES target the atomic beam source and the polarimeter are arranged in a collinear fashion. Thus a beam block was installed in the storage cell to prevent the atoms from flying directly through the storage cell. The electron beam of the HERA ring is missing from this setup and therefore beam target interactions, like bunch field depolarization [48] cannot be examined. The atomic beam source is operated with only one sextupole magnet and so not all polarization states of a deuterium beam required by the HERMES experiment could be prepared. In the case of relaxation measurements a WFT 1-3 for hydrogen and the three high frequency transitions SFT 1-6, SFT 2-6 and SFT 3-5 for deuterium provide a sufficient number of preparation possibilities. The storage cells were especially prepared for the highly sensitive relaxation measurements, in which the atoms on average experience 3500 wall collisions before they leave the cell again (table A.3) . In the storage cell of the HERMES target it is

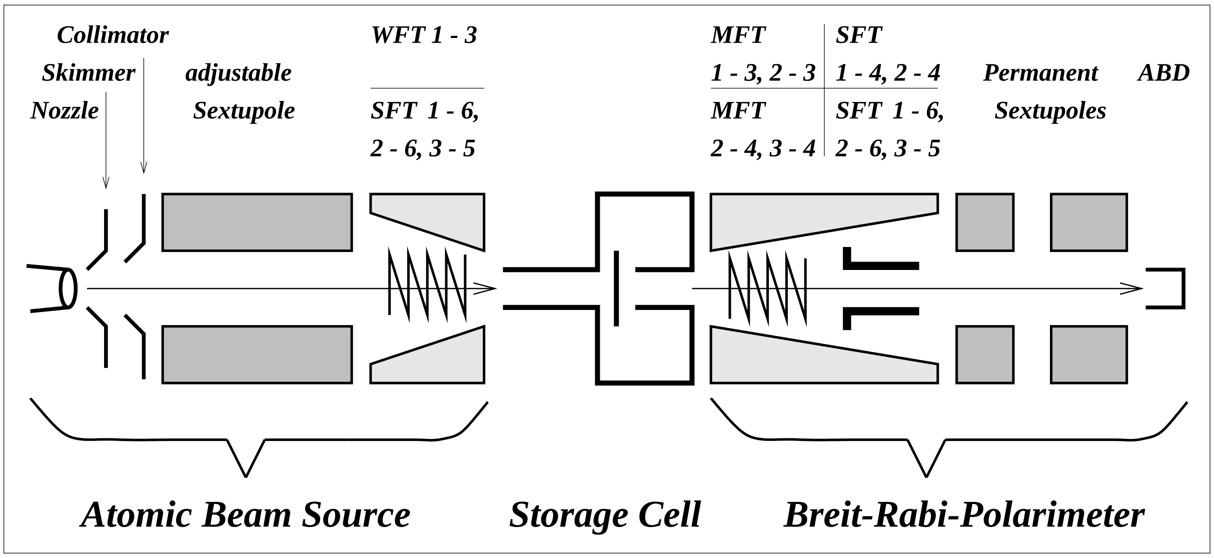

Fig. 1.4:
Setup for polarization measurements with storage cells. The polarized atom beam is produced by an atomic beam source using a sextupole magnet and a high frequency transition and injected into a storage cell. A sample beam is formed through an exit tube. Its polarization is in turn analyzed in the Breit-Rabi polarimeter using high frequency transitions and sextupole magnets. The atomic beam is detected by an atomic beam detector (**ABD**), consisting of a chopper and a quadrupole mass spectrometer. The higher listed high frequency transitions refer to measurements with hydrogen, the lower listed ones refer to measurements with deuterium. WFT stands for **W**eak **F**ield **T**ransition, SFT for **S**trong **F**ield **T**ransition and MFT for **M**edium **F**ield **T**ransition. The nomenclature for the high frequency transitions and their properties are treated in chapter 5. The high frequency field for the strong field transitions for deuterium in the source is not created by a coil as shown in the drawing, but with a band conductance resonator. In the case of the WFT 1-3 for hydrogen the drawing is correct.

an average of 310 wall collisions (table A.5). The setup of the Breit-Rabi polarimeter shown in figure 1.4 will be used tin the HERMES experiment, except for the modifications made to allow the calibration measurements described in chapter 8.8.

1.5 The Breit-Rabi Polarimeter

The principle of the Breit-Rabi polarimeter is based on exchange and selection of individual hyperfine states in an atomic beam which is to be examined. The atomic beam of unknown polarization coming in from the left, flies through a section with different, individually switchable adiabatic high frequency transitions with whose help the occupation of two hyperfine states can be practically entirely exchanged within the beam. In the immediately following sextupole magnet system those states with a negative electron spin projection are defocussed and removed from the atomic beam. In the case of hydrogen the states $|\,3\,\rangle$ and $|\,4\,\rangle$ are meant. The higher states $|\,1\,\rangle$ and $|\,2\,\rangle$ (figure 1.2) stay in the beam and are detected by the atom beam detector.

If one switches the high frequency transitions which occur before the sextupole magnet on or off, then the hyperfine structure states, which are produced by the high frequency transitions, will be differently occupied and the intensity measured by the atom beam detector will vary. This change in intensity is used to measure relative occupation numbers n_i, which lead to the probability of finding a state $|\,i\,\rangle$ in the atomic beam. The occupation numbers define the nuclear and electron polarization of the atomic beam unambiguously, as will be shown in chapter 2.

The functionality of the components that analyze the polarization can be illustrated with an occupation tuple, which contain the occupation probabilities n_i as components. In the case of hydrogen only four component tuples are needed. The extension of the formalism to deuterium consists only in the use of a six component tuple instead.

In this first example all of the high frequency transitions are turned off. The atomic beam passes through the high frequency transition points unchanged and ideally $n_3 = n_4 = 0$ after the sextupole magnets have been passed.

$$\begin{pmatrix} n_1 \\ n_2 \\ n_3 \\ n_4 \end{pmatrix} \xrightarrow{\text{sextupole}} \begin{pmatrix} n_1 \\ n_2 \\ 0 \\ 0 \end{pmatrix}. \tag{1.7}$$

In turning SFT 2-4 on, which switches the states $|\,2\,\rangle$ and $|\,4\,\rangle$ in the beam, then the sextupole magnets focus the initially injected states $|\,1\,\rangle$ and $|\,4\,\rangle$:

$$\begin{pmatrix} n_1 \\ n_2 \\ n_3 \\ n_4 \end{pmatrix} \xrightarrow{2\leftrightarrow 4} \begin{pmatrix} n_1 \\ n_4 \\ n_3 \\ n_2 \end{pmatrix} \xrightarrow{\text{sextupole}} \begin{pmatrix} n_1 \\ n_4 \\ 0 \\ 0 \end{pmatrix}. \tag{1.8}$$

The ratio R_{24} of these two beam intensities may be described as:

$$R_{24} = \frac{n_1 + n_4}{n_1 + n_2} = 1 - \frac{n_2 - n_4}{n_1 + n_2} \tag{1.9}$$

and is independant of the beam intensity at the entrance of the polarimeter.

The sextupole magnets are sensitive to the electron spin of the atoms in the beam. In order so that the intensity of the beam is able to change behind the sextupole system a transition before the sextupole magnet must be induced in such a way that an exchange between hyperfine structure components of different electron spin projections is induced; this means between one of the two (three) upper and one of the two (three) lower states as seen in the Breit-Rabi diagram 1.2 and 2.2.

In the case of hydrogen there are four useful and technically realized high frequency transitions which are termed MFT 1-3, MFT 2-3, SFT 1-4 and SFT 2-4. An exchange between the states $|\,3\,\rangle$ and $|\,4\,\rangle$ would not change the beam intensity behind the sextupole magnets. In the case of deuterium there are the seven useful and practicable high frequency transitions MFT 1-4, MFT 2-4, MFT 3-4, SFT 1-6, SFT 2-6, SFT 3-5 and SFT 2-5/3-6. The high frequency transitions MFT 1-4 and SFT 2-5/3-6 were not used for the purposes of this thesis.

Generally, a hydrogen transition $i \leftrightarrow j$ has the intensity ratio

$$R_{ij} = 1 - \frac{n_i - n_j}{n_1 + n_2}. \tag{1.10}$$

In using the normalizing condition $\sum_i n_i = 1$, three of these equations are sufficient for the creation of a linear equation system for the four missing occupation numbers. For example, using the transitions SFT 1-4, SFT 2-4 and MFT 2-3 the following equations result:

$$\begin{pmatrix} 1 & 1 & 1 & 1 \\ -R_{14} & 1 - R_{14} & 0 & 1 \\ 1 - R_{24} & -R_{24} & 0 & 1 \\ 1 - R_{23} & -R_{23} & 1 & 0 \end{pmatrix} \begin{pmatrix} n_1 \\ n_2 \\ n_3 \\ n_4 \end{pmatrix} = \begin{pmatrix} 1 \\ 0 \\ 0 \\ 0 \end{pmatrix}, \tag{1.11}$$

where the first line expresses the normalization condition, and the other lines result from solving the equations of the type (1.10).

In solving these equation systems by applying the Cramer rule, the result is a simple and complete representation for the occupation numbers as a function of the measured signal ratios. For the calculation of n_i, the i-th column of the matrix of the equation system is replaced with the column vector on the right side of the equation. This leads to matrices of the following structure:

$$\tilde{M}_1 = \begin{pmatrix} 1 & 1 & 1 & 1 \\ 0 & & & \\ 0 & & M_1 & \\ 0 & & & \end{pmatrix}, \tag{1.12}$$

whose determinants must be calculated.

The zeros in the column vector serve to ensure that the determinants of matrices $\tilde{M}_i$ are equal to the determinants of the submatrices M_i. Therefore there are only 3×3 determinants to calculate. The only 4×4 determinant which remains to be calculated stems from the original matrix in the linear equation system (1.11). However, this may be represented as the sum of 3×3 determinants $|M_i|$. The sought after occupancy numbers thus receive their closed form:

$$n_i = \frac{(-1)^{i+1} \cdot |M_i|}{\sum_i (-1)^{i+1} \cdot |M_i|}. \tag{1.13}$$

This representation has the same structure as the expression of relative occupancy numbers through absolute ones:

$$n_i = \frac{N_i}{\sum_i N_i}. \tag{1.14}$$

The determinants of the submatrices (1.12) are thus proportional to the occupancy figures $(-1)^{i+1} \cdot |M_i| = c \cdot N_i$ and the sum of all determinants corresponds to the normalizing factor $\sum_i N_i$, given that the determinants use the correct spin.

The calculation for deuterium atom beams leads to a system of six equations for the occupancy numbers of the six hyperfine structure states of the deuterium atom. For the determination of the matrix elements five signal ratios must be measured from which five linear equations may be derived. The sixth equation is derived in the same way as is done for hydrogen, namely from the normalization.

1.6 Alternative Methods of Polarization Measurment

Since beam an target polarization pass quadratically into the quality of any scattering experiment using polarized particles, not only is a high polarization critical but also exact understanding of the polarization itself. The selection of a suitable exact target polarimeter is of central importance for the HERMES experiment. The following are several methods of polarization measurement. These will be discussed in regards to their suitability.

- Optical Methods:
  - Opacity measurement using circularly polarized laser light,
  - laser induced fluorescence, and
  - the Balmer-Polarimeter.
- Asymmetry measurement in nuclear scattering:
  - Vector polarization of hydrogen: ^{4}He(p, p)^{4}He at 27 MeV and ^{6}Li(p, ^{3}He)^{4}He at 290 keV.

  - Vector polarization of deuterium: ^{2}H(d, p)^{3}H between 150 keV and 1 MeV.
  - Tensor polarization of Deuterium: ^{3}H(d, n)^{4}He at 50 keV:
    * The electron-pick-up polarimeter and
    * the ion-extraction polarimeter.
- High frequency methods:
  - The maser polarimeter,
  - the Lamb-shift polarimeter and
  - the Breit-Rabi polarimeter.

Optical Methods: The measurement of polarization using circularly polarized laser light is used in combination with optically pumped alkali gases in storage cells. It was A. Kastler[61] who first suggested that alkali atoms become polarized through irradiation form circularly polarized laser light. The transition from $^2\mathrm{S}_{1/2}$ to $^2\mathrm{P}_{1/2}$ is excited and as determined by the choice of circular polarization either only with $\Delta m_F = +1$ or only with $\Delta m_F = -1$. However, the decay of this excited state occurs with $\Delta m_F = 0,\ \pm 1$. In this way over time all atoms are pumped into a state of maximum or minimum m_F value, from which they cannot be excited further. It is evident that the optically pumped medium becomes increasingly transparent with increasing polarization. This means that the opacity of the medium in relationship to the circular polarized light becomes a measure of its polarization. In this way it is possible to measure the electron polarization $\langle \mathcal{S}_z \rangle$ and the occupation difference of both hyperfine structure levels with different total angular momentum F, the expectation value $\langle \mathcal{S} \cdot \mathcal{I} \rangle$.

The first relaxation measurements using this method were undertaken in 1956 by H.G. Dehmelt on sodium [62] and shortly afterward on rubidium by W. Franzen [63], who coined the term *"relaxation in the dark"*. In this case the pump beam is turned off for a short time and opacity is measured after it is turned on again. In more contemporary experiments a test beam of low power is used. It was M.A. Bouchiat who explained and theoretically described relaxation through the interactions of the atoms with the walls of the storage cell [64, 65]. Exactly this model is used for the purpose of this thesis in order to explain wall collision relaxation of hydrogen and deuterium (chapter 3.1). Since then the relaxation of alkali atoms on different surface materials was examined by several groups. Noteworthy are the works of M.A. Bouchiat and J. Brossel [66], who had recognized the effects of spin exchange collisions of the alkali atoms with one another, as well as the works of D.R. Swenson und L.W. Anderson [43, 67], J.C. Camparo [68] and C.D.P. Levy, W. Schmor und W.M. Law [69].

Laser induced fluorescence allows the selective excitation of certain transitions and detects the excitation through the fluorescence light. This method has also been successfully used in experiments with polarized alkali atoms on surfaces [70].

In the application of these methods on hydrogen and deuterium, lasers would be required which are active in the ultraviolet region. Unfortunately their current performance is too weak to be useful. They are therefore not considered further for the purposes of the HERMES experiment.

In using Balmer polarimeters [71, 72, 73] hydrogen is excited, through electron collisions into a state with the main quantum number $n = 3$. In this way part of the polarization of the electrons is transferred onto the orbital angular momentum. The Balmer light that is emitted during decay is thus circularly polarized and this circular polarization is then a measure for the original electron polarization. In a weak magnetic field the nuclear polarization equals the electron polarization in very good approximation, $P_e = P_z$. The Balmer polarimeter can thus be used to measure the nuclear polarization, although its use is limited to weak magnetic fields. The target of the HERMES experiment is operated in a strong magnetic field and therefore it is unsuitable in this case. The temperature dependence of the relaxation of polarized hydrogen was experimentally examined using a Balmer polarimeter by W. Luck [71].

The asymmetry measurement in nuclear scattering is with certainty the most direct method of measuring nuclear polarization. In contrast to all the other available methods it's great advantage lies in the fact that also nuclear polarization inside of molecules can be measured [74]. The elastic scattering reaction ^{4}He(p, p)^{4}He at 27 MeV was used to measure the polarization of an internal polarized hydrogen target in an above mentioned experiment [56, 57]. However, the beam energy required to achieve a sufficient analyzing power requires an accelerator system whose expense is not to be justified for the HERMES experiment. Possible nuclear reaction which achieve a sufficient analyzing power even with moderate energies include ^{6}Li(p, ^{3}He)^{4}He at 290 keV and ^{2}H(d, p)^{3}H at energies between 150 keV and 1 MeV for the determination of the vector polarization of deuterium [76, 77, 78].

The tensor polarization of deuterium can already be measured at 50 keV in the reaction ^{3}H(d, n)^{4}He. Since the first measurements on the relaxation of hydrogen and deuterium in target storage cells used this method [79], two experiments of this kind [80] will quickly be described.

The electron-pick-up polarimeter [81] is limited, like the Balmer polarimeter, to using weak magnetic fields, since it is only sensitive to electron polarization in the storage cell. A beam of deuterons passes the beam pipe and is partially neutralized through electron pick up. In this way the polarization of the electrons is transferred, through hyperfine interactions onto the deuterium nucleons. The neutralized deuterium atoms are separated from the ions, are again ionized, accelerated to 50 keV and scattered on a tritium target, where the tensor polarization manifests itself in a detectable asymmetry.

Conversely, the ion-extraction polarimeter [74] is largely limited to strong magnetic fields. These are required to force the deuterium ions, excited through electron collisions, into tight spiral trajectories inside the storage cell, so that they do not collide with the walls. Along these trajectories they diffuse toward the ends of the beam pipe, where they are electrostatically extracted, accelerated and again scattered on a tritium target.

The large technical effort involved with realizing such a polarimeter on an internal target and the radioactivity of the tritium have been factors leading to the decision to not use these methods in the HERMES experiment.

High frequency methods: A passively operated hydrogen maser offers a further possibility to measure the polarization of hydrogen atoms. A signal, which can be taken from such a system, is proportional to the difference of population in the hyperfine states $|\,2\,\rangle$ und $|\,4\,\rangle$. Through the induction of hyperfine transitions in the Zeeman triplet in front of the maser cavity additional differences in the hyperfine occupations can be detected, although a complete resolution of the hyperfine occupation has not yet been achieved. A test model of such a polarimeter was successfully realized at MIT [82].

The Lamb-shift polarimeter was suggested in 1970 by J.E. Brolley, G.P. Lawrence and G.G. Ohlsen [83], and it was T.B. Clegg and S.K. Lemieux who successfully realized the idea in 1990[84]. Another polarimeter of this type is at present being constructed for the EDDA experiment at the COSY proton accelerator in Jülich [85]. A spin filter, which is also used in a Lamb-shift source [86] to create polarization, is used for the analysis of the polarization. First of all a portion of the atoms must be excited into a metastable state $2^2S_{1/2}$. To this end the atoms are first ionized, accelerated to an energy of 550 eV in the case of hydrogen and 1, 1 keV in the case of deuterium and then neutralized again in a caesium cell. Certain ions recombine in this process into the desired metastable state and pass through the spin filter. Here the static magnetic field leads to an energy level overlap in the region of 50 mT. This is arrived at as a product of the increasing energy differences in the hyperfine splitting of metastable $2^2S_{1/2}$ and short lived $2^2P_{1/2}$ states. Through the superposition of an electric quench field the two states, with their differing parities, mix and the metastable states decay. With the additional superposition of a high frequency field and thus a hyperfine transition of the $2^2S_{1/2}$ state, a three state interaction leads to a stabilization of all states with the same z-component of the nucleon spin m_I. The desired component m_I can be selected for by choosing one of static magnetic fields predefined by the level overlap; it passes through the spin filter without decaying. In the electric field behind the spin filter the passing state is quenched into a basic state and detected through Lyman-alpha detection. The stabilization of states in the spin filter may be easily understood with the help of a simple mechanical analogy. Three pendula, coupled together through springs, can be swung in such a way that the two outer pendula swing in opposite directions while the middle pendulum rests[87].

The Lamb-shift polarimeter is a thoroughly viable alternative for measuring the target polarization at HERMES. The occupation of each level with the same magnetic quantum number m_I is the information required to describe the nuclear polarization in the target storage cell. Of course information regarding the electron polarization is lost through the ionization process. Although this initially may be of no importance, in the end effect all interactions which lead to spin relaxation in the storage cell affect the electron spin. The nucleon spin is only affected by the hyperfine interactions. The behaviour of the electron polarization is defining for the relaxation processes in the storage cell.

The Breit-Rabi polarimeter is the only known process with which it is possible to completely resolve the hyperfine occupation in an atomic beam and thereby measure the nucleon as well as the electron polarization. It is exactly this quality which allowed the relaxation measurements to be almost completely understood and traced back to two interactions, wall and spin exchange collisions, both of which are theoretically well understood (chapter 3).

1.7 Structure of the Thesis

In the following two chapters the theoretical foundations will be discussed. In chapter 2 hyperfine splitting of hydrogen and deuterium in a magnetic field will be discussed which will form the basis for the entire thesis, and in chapter 3 spin relaxation will be discussed.

Chapters 4 through 6 describe in detail the chosen test construction and those components which are critical for the Breit-Rabi polarimeter, the high frequency transitions and the sextupole magnets.

The calibration of the Breit-Rabi polarimeter is comprehensively and extensively discussed in chapters 7 through 10. In chapter 7 efficiencies and transmissions are introduced and used in the description of the analyzing power of the Breit-Rabi detector. The purely experimental determination of efficiencies occurs in chapter 8, the determination of transmissions, which are based in part on simulations occurs in chapter 9. The results of the calibration, the uncertainties of a polarization measurement are summarized in chapter 10. Readers largely interested in the relaxation processes in the storage cells can skip this portion of the thesis.

Chapters 11 through 13 are concerned with the analysis, results and interpretation of relaxation measurements conducted on the experimental test setup. Those perspectives garnered are then applied, in chapter 14, to an experiment with a storage cell target conducted at the test storage ring (TSR) in Heidelberg an also at the HERMES experiment. The thesis ends with a short discussion in chapter 15.

The appendices contain important data of all storage cells used, an assessment of gas flow in the vacuum system of the Breit-Rabi polarimeter, the results of alternate analyses of the relaxation measurements and the determination of the initial polarization injected into the storage cells at TSR and the HERMES experiment. The remaining appendices are the formulas used in analyzing the polarization measurements, the explicit rate equations for the spin relaxation and a Runge-Kutta method used in its solution. An overview, to scale, of the test setup may be found in appendix H.

2 Hyperfine Structure Splitting in a Magnetic Field

All line splittings within atomic spectra caused by the interactions of the atomic nucleus with the electron shells are called hyperfine. In particular those which arise from the magnetic momenta of the nucleus and the electron shell are of interest. Several portions of this thesis are based on the dependancy of this type of hyperfine splitting on an external magnetic field:

- The generation of a polarized atomic beam through the use of an atomic beam source.
- The calculation of nucleus and electron polarization from the hyperfine occupancies measured by the Breit-Rabi polarimeter (2.22) and (2.30).
- The theoretical description of field dependancy of relaxation mechanisms in storage cells (chapter 3).
- The precise calculation of trajectories of single atoms in sextupole magnets (chapter 6). These being required for the transmission corrections of polarization and efficiency measurements (chapters 8 and 9).

Due to its fundamental importance for this thesis the hyperfine splitting of hydrogen will be covered in some detail in the first portion of this chapter, the terminology follows [88]. The hyperfine splitting of deuterium will be discussed in the second half of the chapter.

2.1 The Hyperfine Structure of Hydrogen

If a hydrogen atom is in its basic state of $1S_{1/2}$, then, as a result of the absent orbital angular momentum, the spin orbit coupling and the nuclear spin couple directly to the magnetic moment of the electron. Since both proton as well as electron are spin-1/2 particles, they can either couple to a total angular momentum $F = 0$ or $F = 1$. Without an external magnetic field the state with $F = 1$ is triply degenerate in respect to the magnetic quantum number m_F which can have values of -1, 0 and $+1$. The difference in energy between the energy levels belonging to $F = 0$ and $F = 1$ is described as the hyperfine splitting energy $E^{\mathrm{H}}_{\mathrm{HFS}}$.

In addition to the interactions between the magnetic moments of proton and electron there are the interactions of the individual moments with the external field through which the degeneration of the energy levels with $F = 1$ is broken. This field dependant splitting may be described through the following Hamilton operator:

$$\mathcal{H} = a\mathcal{I} \cdot \mathcal{S} + \frac{g_S \mu_B}{\hbar} \mathcal{S}_Z B_Z - \frac{g_P \mu_K}{\hbar} \mathcal{I}_Z B_Z \tag{2.1}$$

The first term with the proportionality constant a takes the coupling between the proton spin $\mathcal{I}$ and the electron spin $\mathcal{S}$ into consideration, while the second term describes the interactions of the electron spin with the external magnetic field. g_S is the g-factor of the electron and μ_B is the Bohr magneton. The third term with the g-factor of the proton g_P and the nuclear magneton μ_K describes the interaction of the proton spin with the external field. It is permissible to neglect this term due to the small size of the nuclear magneton for magnetic fields up to about 30 T. In neglecting this term, and after introducing the Larmor frequency of the electron

$$\omega_S = \frac{g_S \mu_B}{\hbar} B_Z \tag{2.2}$$

the Hamilton operator

$$\mathcal{H} = a\mathcal{I} \cdot \mathcal{S} + \omega_S \mathcal{S}_Z, \tag{2.3}$$

is arrived at which in the following is diagonalized. With the aid of the identity

$$\mathcal{I} \cdot \mathcal{S} = \mathcal{I}_Z \mathcal{S}_Z + \frac{1}{2} \left(\mathcal{I}_+ \mathcal{S}_- + \mathcal{I}_- \mathcal{S}_+ \right) \tag{2.4}$$

the matrix elements of the Hamilton operator (2.3) may be calculated in the base of the spin angular momentum eigenfunctions

$$|\, m_S, m_I \,\rangle = |\, \pm\tfrac{1}{2}, \pm\tfrac{1}{2} \,\rangle \tag{2.5}$$

where m_S and m_I represent the magnetic quantum numbers of electron and nucleon spin, respectively. For greater clarity, the spin of the electron will be represented as an arrow while the nucleon spin will be represented by its sign.

The states $|\uparrow +\rangle$ and $|\downarrow -\rangle$ are independant from the external magnetic field eigenfunctions of the Hamilton operator (2.3). The calculation of eigenvalues in the subspace spanned by the remaining states $|\uparrow -\rangle$ and $|\downarrow +\rangle$ leads to a characteristic polynomial of the second degree and therefore poses no problems. The following energy eigenvalues may be derived for the for possible states

$$\begin{aligned}
E_1^{\mathrm{H}} &= \frac{a_{\mathrm{H}}\hbar^2}{4} + \frac{\hbar\omega_S}{2} &&= E_{\mathrm{HFS}}^{\mathrm{H}} \cdot \left(\frac{1}{4} + \frac{1}{2}x \right) \\
E_2^{\mathrm{H}} &= -\frac{a_{\mathrm{H}}\hbar^2}{4} + \frac{a_H\hbar^2}{2}\sqrt{1 + \frac{\omega_S^2}{a_{\mathrm{H}}^2\hbar^2}} &&= E_{\mathrm{HFS}}^{\mathrm{H}} \cdot \left(-\frac{1}{4} + \frac{1}{2}\sqrt{1+x^2} \right) \\
E_3^{\mathrm{H}} &= \frac{a_{\mathrm{H}}\hbar^2}{4} - \frac{\hbar\omega_S}{2} &&= E_{\mathrm{HFS}}^{\mathrm{H}} \cdot \left(\frac{1}{4} - \frac{1}{2}x \right) \\
E_4^{\mathrm{H}} &= -\frac{a_{\mathrm{H}}\hbar^2}{4} - \frac{a_{\mathrm{H}}\hbar^2}{2}\sqrt{1 + \frac{\omega_S^2}{a_{\mathrm{H}}^2\hbar^2}} &&= E_{\mathrm{HFS}}^{\mathrm{H}} \cdot \left(-\frac{1}{4} - \frac{1}{2}\sqrt{1+x^2} \right).
\end{aligned} \tag{2.6}$$

The progression of these energy eigenvalues in dependancy on an external magnetic field was shown in figure 1.2. The hyperfine splitting energy is chosen as the energy unit.

$$E_{\mathrm{HFS}}^{\mathrm{H}} = a_{\mathrm{H}}\hbar^2. \tag{2.7}$$

The frequency that belongs to this transition energy can be precisely measured using a hydrogen maser [89, 90]:

$$\nu_{HFS}^{\mathrm{H}} = \frac{a_{\mathrm{H}}\hbar}{2\pi} = 1\,420\,405\,751.768(1)\ \mathrm{Hz}. \tag{2.8}$$

This is among the most exactly measured values in physics.

As the magnetic field unit, the critical field for the hydrogen atom B_C^{H} was chosen which is defined by the following condition:

$$\hbar\omega_S = a_{\mathrm{H}}\hbar^2 \tag{2.9}$$

It has the following value:

$$B_C^{\mathrm{H}} = \frac{a_{\mathrm{H}}\hbar^2}{g_S\mu_B} = 50.7\ \mathrm{mT}. \tag{2.10}$$

The ratio of the external field and the critical field is generally labelled as x:

$$x = \frac{B}{B_C^{\mathrm{H}}}. \tag{2.11}$$

Thus the energy difference between the states $|\,1\,\rangle$ and $|\,3\,\rangle$ in the critical field is equal to that of the hyperfine splitting energy. Further, this defines the magnetic field in which the second term of the Hamilton operator (2.3) begins to dominate the first. In other words, the external magnetic field becomes stronger than the field of the proton spin, which is experienced on average by the electron.

The critical field further places a barrier between two regions in the Breit-Rabi diagram (figure 1.2). In the *Zeeman region* the following applies; $B \ll B_C$ or $x \ll 1$, respectively. The interaction of the electron with the field can be treated as a perturbation. In this case the eigenfunctions to the total angular momentum $|\,F, m_F\,\rangle$ form a suitable basis for describing the four hyperfine states:

$$\begin{aligned}
|\,1\,\rangle &= |\,F=1, m_F=+1\,\rangle &&= |\!\uparrow +\rangle \\
|\,2\,\rangle &= |\,F=1, m_F=0\,\rangle &&= \frac{1}{\sqrt{2}}\cdot(|\!\uparrow -\rangle + |\!\downarrow +\rangle) \\
|\,3\,\rangle &= |\,F=1, m_F=-1\,\rangle &&= |\!\downarrow -\rangle \\
|\,4\,\rangle &= |\,F=0, m_F=0\,\rangle &&= \frac{1}{\sqrt{2}}\cdot(|\!\uparrow -\rangle - |\!\downarrow +\rangle)\,.
\end{aligned} \tag{2.12}$$

The states of $F = 1$ form a symmetric triplet while the singulett state at $F = 0$ is antisymmetric.

In the so-called *Paschen-Back region*, $B \gg B_C$ and the coupling between nucleon and electron spin can be treated as a perturbation. In this case the four already introduced angular momentum eigenfunctions (2.5) provide a suitable basis for the four states:

$$\begin{aligned}
|\,1\,\rangle &= |\!\uparrow +\rangle & \qquad |\,3\,\rangle &= |\!\downarrow -\rangle \\
|\,2\,\rangle &= |\!\uparrow -\rangle & \qquad |\,4\,\rangle &= |\!\downarrow +\rangle\,.
\end{aligned} \tag{2.13}$$

In the Paschen-Back region, all four states have practically complete electron, as well as nucleon polarization. This may be defined for spin-1/2 particles, such as the proton or the electron, as

$$P = \frac{N_+ - N_-}{N_+ + N_-} = n_+ - n_- \tag{2.14}$$

where N_+ and N_- represent the numbers of particles which may be found in the spin states of $+1/2$ or $-1/2$. n_+ and n_- describe the *relative occupation numbers*.

In defining the polarization of protons and electrons that are bound in hydrogen atoms, consideration must be given to the coupling of the two spins. Since as a consequence of this the mixed states $|\,2\,\rangle$ and $|\,4\,\rangle$ with $m_F = 0$ in weak magnetic fields do not contribute to either electron or nucleon polarization. In the transition region around the critical field the amount of nuclear and electron polarization of these states grows with the growing field and in strong fields approaches the value of 1 asymptotically.

Once the expectation values of the polarization for the individual hyperfine states are known, the polarization of a sample of hydrogen atoms may be described with the help of the density matrix $\rho = \sum_i |\,\Phi_i\,\rangle\, p_i\,\langle\,\Phi_i\,|$. Generally the expectation value of a quantum mechanical operator is calculated through the following [91]:

$$\langle\,\mathcal{O}\,\rangle = \mathrm{Tr}\,(\rho\mathcal{O}) = \sum_i p_i \cdot \langle\,\Phi_i\,|\,\mathcal{O}\,|\,\Phi_i\,\rangle \tag{2.15}$$

Whereby p_i represents the probability of finding the state $|\,\Phi_i\,\rangle$ in a sample. After adjustment to the nomenclature used here, the nuclear and electron polarization of a sample of hydrogen atoms is given as

$$P_{e,z} = \sum_{i=1}^{4} n_i \cdot \langle\,i\,|\,\mathcal{P}_{e,z}\,|\,i\,\rangle. \tag{2.16}$$

The *relative occupancy numbers* n_i are the measurands of the Breit-Rabi polarimeter. For these the following normalization condition applies:

$$\sum_i n_i = 1. \tag{2.17}$$

For the calculation of the expectation values of nuclear and electron polarization of the four hyperfine states in a finite magnetic field, a basis of eigenstates to the Hamilton operator (2.3) must be established that is suitable for any magnetic field. Since the states $|\,1\,\rangle$ and $|\,3\,\rangle$ are already eigenstates over the entire field range it suffices to diagonalize the Hamilton operator in the two dimensional subspace, which is spanned by the states $|\uparrow\,-\,\rangle$ and $|\downarrow\,+\,\rangle$ [92]. The mixing of these two states can be described though an external field dependant mixing angle θ, as defined by the following equation:

$$\tan 2\theta = \frac{a\hbar}{\omega_S} = \frac{1}{x} \tag{2.18}$$

By applying trigonometric relations the calculation of eigenstates is significantly simplified. The four eigenstates are obtained in a form which is valid in all magnetic fields and to which the approximation (2.3) may be applied.

$$\begin{aligned}
|\,1\,\rangle &= |\uparrow\,+\,\rangle \\
|\,2\,\rangle &= \cos\theta\cdot|\uparrow\,-\,\rangle + \sin\theta\cdot|\downarrow\,+\,\rangle \\
|\,3\,\rangle &= |\downarrow\,-\,\rangle \\
|\,4\,\rangle &= \sin\theta\cdot|\uparrow\,-\,\rangle - \cos\theta\cdot|\downarrow\,+\,\rangle\,.
\end{aligned} \tag{2.19}$$

For each of the respective borderline cases the eigenstates devolve into the figures (2.12) and (2.13).

The expectation values for nuclear and electron polarization P_z and P_e agree with the expectation values of the operators $\mathcal{I}_Z$ and $\mathcal{S}_Z$ to within a factor of $\hbar/2$. In using figure (2.19) the following polarization expectation values are arrived at for the individual hyperfine states:

$$\begin{aligned}
\langle\,1\,|\,\mathcal{P}_e\,|\,1\,\rangle &= +1 & \langle\,1\,|\,\mathcal{P}_z\,|\,1\,\rangle &= +1 \\
\langle\,2\,|\,\mathcal{P}_e\,|\,2\,\rangle &= +\cos 2\theta & \langle\,2\,|\,\mathcal{P}_z\,|\,2\,\rangle &= -\cos 2\theta \\
\langle\,3\,|\,\mathcal{P}_e\,|\,3\,\rangle &= -1 & \langle\,3\,|\,\mathcal{P}_z\,|\,3\,\rangle &= -1 \\
\langle\,4\,|\,\mathcal{P}_e\,|\,4\,\rangle &= -\cos 2\theta & \langle\,4\,|\,\mathcal{P}_z\,|\,4\,\rangle &= +\cos 2\theta.
\end{aligned} \tag{2.20}$$

Through trigonometric transformations of (2.18) the following relationship may be derived:

$$\cos 2\theta = \frac{x}{\sqrt{1+x^2}}. \tag{2.21}$$

The expectation values for the polarization are represented in figure (2.1) as a function of an external magnetic field. Following figures (2.16) and (2.20), electron and nuclear polarization are obtained as a function of the relative occupation numbers in dependancy of an external magnetic field:

$$\begin{aligned}
P_e &= n_1 - n_3 + (n_2 - n_4)\cos 2\theta \\
P_z &= n_1 - n_3 - (n_2 - n_4)\cos 2\theta.
\end{aligned} \tag{2.22}$$

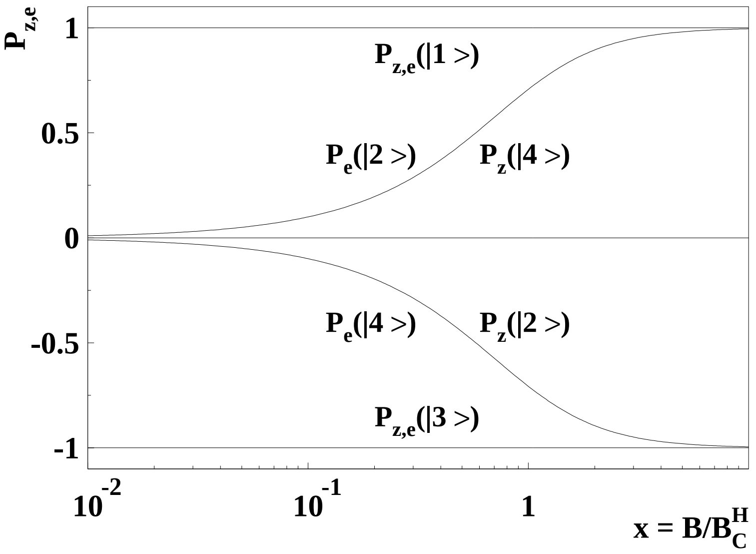

Fig. 2.1:
Expectation values for nuclear and electron polarization of the four hyperfine states of a hydrogen atom in its basic state, as a function of external magnetic field.

2.2 The Hyperfine Structure of Deuterium

The hyperfine splitting in the deuterium atom is different from that of the hydrogen atom largely due to the nuclear spin of the deuteron $I = 1$. It can either couple with the spin of the electron shell to a total angular momentum of $F = 3/2$ or $F = 1/2$. Without an external magnetic field the state $F = 3/2$ is four times degenerated while the state $F = 1/2$ is twice degenerated. Thus there are in total six hyperfine states possible for the deuterium atom. Though the use of an external magnetic field the energy degeneration is broken.

In numbering the states according, to their energy, as was done with the hydrogen atom, the energy eigenvalues of the individual states may be given as [93]:

$$
\begin{aligned}
E_1^{\mathrm{D}} &= E_{\mathrm{HFS}}^{\mathrm{D}} \cdot \left(\frac{1}{2} + \frac{3}{4}x \right) \\
E_2^{\mathrm{D}} &= E_{\mathrm{HFS}}^{\mathrm{D}} \cdot \left(-\frac{1}{4} + \frac{3}{4}\sqrt{1 + \frac{2}{3}x + x^2} \right) \\
E_3^{\mathrm{D}} &= E_{\mathrm{HFS}}^{\mathrm{D}} \cdot \left(-\frac{1}{4} + \frac{3}{4}\sqrt{1 - \frac{2}{3}x + x^2} \right) \\
E_4^{\mathrm{D}} &= E_{\mathrm{HFS}}^{\mathrm{D}} \cdot \left(\frac{1}{2} - \frac{3}{4}x \right) \\
E_5^{\mathrm{D}} &= E_{\mathrm{HFS}}^{\mathrm{D}} \cdot \left(-\frac{1}{4} - \frac{3}{4}\sqrt{1 - \frac{2}{3}x + x^2} \right) \\
E_6^{\mathrm{D}} &= E_{\mathrm{HFS}}^{\mathrm{D}} \cdot \left(-\frac{1}{4} - \frac{3}{4}\sqrt{1 + \frac{2}{3}x + x^2} \right) .
\end{aligned}
\tag{2.23}
$$

The dependancy of the energy eigenvalues on an external magnetic field is shown in figure 2.2. As an energy unit the hyperfine splitting energy in the deuterium atom $E_{\mathrm{HFS}}^{\mathrm{D}}$ was chosen. The transition frequency to this energy is $\nu_{HFS}^{\mathrm{D}} = 327.384\,352\,51(5)\,\mathrm{MHz}$ [94, 90].

For the construction of a basis that is suitable for any magnetic field and comprised from eigenstates of the Hamilton operator (2.3) two mixing angles are required for deuterium. These are defined by the equation

$$\tan 2\theta_{\pm} = \frac{\sqrt{8}}{3x \pm 1} \tag{2.24}$$

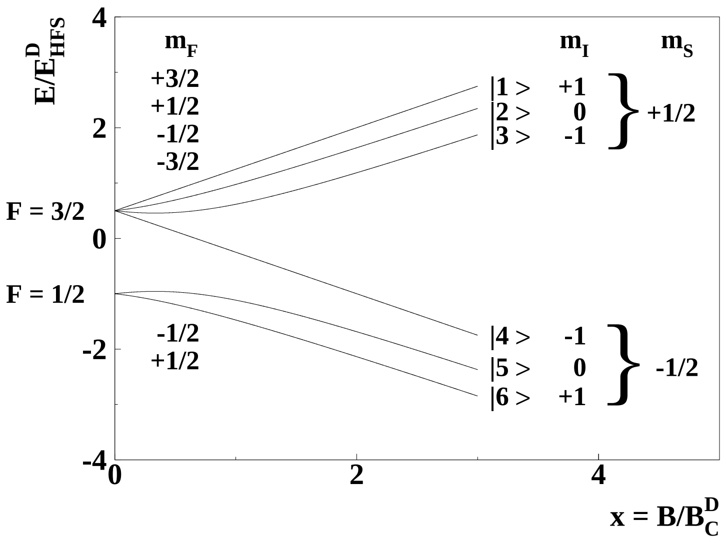

Fig. 2.2:
Breit-Rabi diagram after [44]. Energy eigenvalues for the hyperfine splitting of a deuterium atom in an external magnetic field. $E^{\mathrm{D}}_{\mathrm{HFS}}$ is the hyperfine splitting energy. $x = B/B^{\mathrm{D}}_C$ is the ratio between the external and the critical magnetic field. The critical field for deuterium is $B^{\mathrm{D}}_C = 11.7\,\mathrm{mT}$.

In using this definition the following six basic states are obtained:

$$\begin{aligned}
|\,1\,\rangle &= |\uparrow +\rangle \\
|\,2\,\rangle &= \cos\theta_+\,|\uparrow 0\,\rangle + \sin\theta_+\,|\downarrow +\rangle \\
|\,3\,\rangle &= \cos\theta_-\,|\uparrow -\rangle + \sin\theta_-\,|\downarrow 0\,\rangle \\
|\,4\,\rangle &= |\downarrow -\rangle \\
|\,5\,\rangle &= \sin\theta_-\,|\uparrow -\rangle - \cos\theta_-\,|\downarrow 0\,\rangle \\
|\,6\,\rangle &= \sin\theta_+\,|\uparrow 0\,\rangle - \cos\theta_+\,|\downarrow +\rangle ,
\end{aligned} \tag{2.25}$$

As in the case of hydrogen atoms, the basic states allow the calculation of expectation values for the nuclear and electron polarization in a sample of deuterium atoms as follows:

$$\begin{aligned}
\langle\,1\,|\,\mathcal{P}_e\,|\,1\,\rangle &= +1 & \langle\,1\,|\,\mathcal{P}_z\,|\,1\,\rangle &= +1 \\
\langle\,2\,|\,\mathcal{P}_e\,|\,2\,\rangle &= +\cos 2\theta_+ & \langle\,2\,|\,\mathcal{P}_z\,|\,2\,\rangle &= +\tfrac{1}{2}\,(1-\cos 2\theta_+) \\
\langle\,3\,|\,\mathcal{P}_e\,|\,3\,\rangle &= +\cos 2\theta_- & \langle\,3\,|\,\mathcal{P}_z\,|\,3\,\rangle &= -\tfrac{1}{2}\,(1+\cos 2\theta_-) \\
\langle\,4\,|\,\mathcal{P}_e\,|\,4\,\rangle &= -1 & \langle\,4\,|\,\mathcal{P}_z\,|\,4\,\rangle &= -1 \\
\langle\,5\,|\,\mathcal{P}_e\,|\,5\,\rangle &= -\cos 2\theta_- & \langle\,5\,|\,\mathcal{P}_z\,|\,5\,\rangle &= -\tfrac{1}{2}\,(1-\cos 2\theta_-) \\
\langle\,6\,|\,\mathcal{P}_e\,|\,6\,\rangle &= -\cos 2\theta_+ & \langle\,6\,|\,\mathcal{P}_z\,|\,6\,\rangle &= +\tfrac{1}{2}\,(1+\cos 2\theta_+)\,.
\end{aligned} \tag{2.26}$$

The dependancy of these expectation values on the magnetic field is represented in figure 2.3. After trigonometric transformations the following is obtained from (2.24):

$$\cos 2\theta_\pm = \frac{3x \pm 1}{\sqrt{9x^2 \pm 6x + 9}}. \tag{2.27}$$

By virtue of its spin $I = 1$, three settings are possible in the magnetic field for the deuterium nucleus. These are characterized by their magnetic quantum numbers $m_i = +1$, 0 and -1. The determination of *one* polarization can therefore not be sufficient for an unequivocal determination of occupation probabilities for the three quantum states. Additional to the *vector polarization* (2.14) a polarization of higher order is needed [95], the so-called *tensor polarization*:

$$P_{zz} = n_+ + n_- - 2n_0 = 1 - 3n_0. \tag{2.28}$$

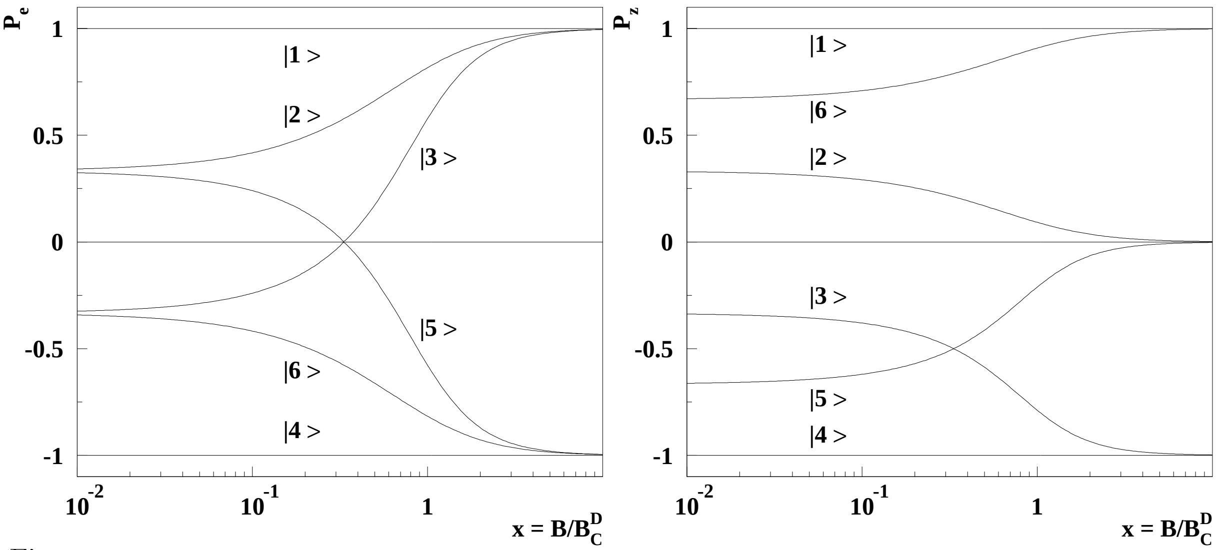

Fig. 2.3:
Expectation values for the polarization of the hyperfine states of deuterium as a function of an external magnetic field. To the left are the expected values for electron polarization, while to the right the vector polarization of deuterium nuclei is plotted.

The tensor polarization describes the degree of alignment of the spins along the quantization axis. The values of both polarizations P_z and P_{zz} unequivocally determine the distribution of the three spin states in a sample of deuterium nuclei. The expectation values for the polarization tensor can be calculated, like those of the vector polarization, from the basis states (2.25). It must be noted, that in the case of the expectation value of an uncoupled nuclear spin $\langle\, m_I = 0\,|\,\mathcal{P}_{zz}\,|\, m_I = 0\,\rangle\; = \; -2$ and $\langle\, m_I = \pm 1\,|\,\mathcal{P}_{zz}\,|\, m_I = \pm 1\,\rangle\; = \; +1$ are valid. The following relations result for the expectation values of the tensor polarization:

$$\begin{aligned}
\langle\, 1\,|\,\mathcal{P}_{zz}\,|\, 1\,\rangle &= +1 & \langle\, 4\,|\,\mathcal{P}_{zz}\,|\, 4\,\rangle &= +1 \\
\langle\, 2\,|\,\mathcal{P}_{zz}\,|\, 2\,\rangle &= -\tfrac{1}{2}\,(1+3\cos 2\theta_+) & \langle\, 5\,|\,\mathcal{P}_{zz}\,|\, 5\,\rangle &= -\tfrac{1}{2}\,(1+3\cos 2\theta_-) \\
\langle\, 3\,|\,\mathcal{P}_{zz}\,|\, 3\,\rangle &= -\tfrac{1}{2}\,(1-3\cos 2\theta_-) & \langle\, 6\,|\,\mathcal{P}_{zz}\,|\, 6\,\rangle &= -\tfrac{1}{2}\,(1-3\cos 2\theta_+)\,. \qquad (2.29)
\end{aligned}$$

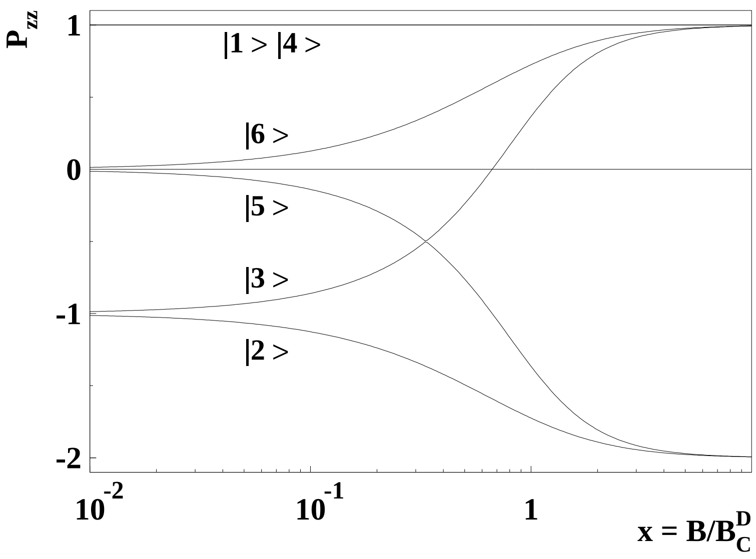

Fig. 2.4:
Expectation values for the tensor polarization of the hyperfine states of the deuterium atom in dependancy of an external magnetic field.

Electron, vector and tensor polarization are derived following (2.16), (2.26) and (2.29) as a function of relative occupation numbers in dependancy of an external magnetic field:

$$
\begin{aligned}
P_e &= n_1 - n_4 \\
&\quad + (n_2 - n_6)\cos 2\theta_+ + (n_3 - n_5)\cos 2\theta_- \\
P_z &= n_1 - n_4 + \tfrac{1}{2}(n_2 + n_6 - n_3 - n_5) \\
&\quad - \tfrac{1}{2}(n_2 - n_6)\cos 2\theta_+ - \tfrac{1}{2}(n_3 - n_5)\cos 2\theta_- \\
P_{zz} &= n_1 + n_4 - \tfrac{1}{2}(n_2 + n_3 + n_5 + n_6) \\
&\quad - \tfrac{3}{2}(n_2 - n_6)\cos 2\theta_+ + \tfrac{3}{2}(n_3 - n_5)\cos 2\theta_- .
\end{aligned}
\tag{2.30}
$$

3 Theoretical Foundations of Spin Relaxation

The relaxation processes which change the hyperfine occupancy of gas within a storage cell may be described through a master equation. The results of the relaxation measurements, which will be described in chapter 12, may be well understood through two mechanisms, wall collisions and spin exchange collisions. The following master equation additionally takes the flow through the gas cell into account and describes the hyperfine occupancy of the gas in the storage cell:

$$\frac{\mathrm{d}n_c}{\mathrm{d}t} = \sum_a R_{ac} n_a + T_{AA}^{-1} \sum_{a,b} M_{ab}^c n_a n_b + T_{\mathrm{res}}^{-1} \left(n_{c0} - n_c \right). \tag{3.1}$$

Not taken into account is the recombination of atoms at the walls of the storage cell and the bunch field depolarization occurring from the positron beam of the HERA ring[48]. A compilation of master equations that were explicitly calculated according to the following described methods may be found in appendix F.

The first term describes the relaxation which occurs through the collision of atoms with the walls of the storage cell. The relaxation rate T_{wall}^{-1} is contained within the transition coefficients R_{ac}. The calculation of these coefficients is discussed in chapter 3.1. The second term represents the spin exchange collisions of the atoms amongst one another. For any change in the occupation probability to occur two atoms have to collide. Therefore this term is dependant on two occupation probabilities, while the transition coefficients have three indices. The index AA is either meant for two hydrogen or two deuterium atoms. The calculation of transition probabilities during a spin exchange collision can be found in chapter 3.2. The third term contains the initial occupancy, n_{c0}, at the time of atom injection, and the occupation probability n_c at the time of exit from the storage cell. T_{res} is the average amount of time the atoms stay in the storage cell.

The number of wall collisions, given the densities within the storage cell target, is generally high in comparison with the number of spin exchange collisions. The interactions at the wall are far weaker. The total effect of a storage cell on the hyperfine occupancy of stored gases is therefore comparable in order of magnitude for both processes.

3.1 Wall Collisions

The storage cell walls represent an unpolarized reservoir for stored polarized gas. Thus angular momentum, and with it polarization, escape the system of stored atoms and pass into the wall. The stored gas becomes depolarized.

On polymer surfaces the atoms are adsorbed, so-called physisorption, as a result of the Van der Waals interaction. After a stay on the surface which is given by the Arrhenius law

$$\tau_S = \tau_0 \exp\left(\frac{E_S}{kT}\right) \tag{3.2}$$

the atoms deabsorb again from the surface and are in a different hyperfine state than before the wall collision. This state is dependant on the type of surface, its temperature, and a static external field. τ_0 is the limit for high temperatures of τ_S, where E_S is the adsorption energy and kT the thermal energy.

During the time in which the atoms are on the surface, the magnetic momenta of the adsorbed electrons interact with the nuclear spins of hydrogen atoms within the chemical compound of which the surface consists. The electrons of the hydrogen atoms are bound to the surface through a covalent bound and therefore do not give any contribution to the magnetic fields on the surface. The theoretical description of this interaction and the calculation of rates of transition goes back to M.A. Bouchiat [64, 65]. The nomenclature used in this chapter follows that of D.R. Swenson and L.W. Anderson [43].

As a result of their diffusion, the adsorbed atoms on the surface are exposed to a fluctuating field $\mathbf{b}(t)$. The interaction of the adsorbed electron spin with this field may be described through the Hamilton operator:

$$\mathcal{H} = \gamma_S \mathbf{b}(t) \cdot \mathcal{S} \tag{3.3}$$

γ_S is the gyromagnetic ratio and $\mathcal{S}$ is the spin vector of the adsorbate's valence electron. The following transition rates are obtained:

$$R_{ab} = C \left| \langle a \,|\, \mathcal{S} \,|\, b \rangle \right|^2 \cdot j(\omega_{ab}), \tag{3.4}$$

These may be found in detail in appendix F. $j(\omega_{ab})$ represents the spectrum of the correlation function. Using a previously described ansatz[96] a simple exponential law can be derived. It describes the fluctuation of the fields due to the diffusion of the adsorbate on the surface:

$$j(\omega_{ab}) = \frac{1}{1 + (\omega_a - \omega_b)^2 \tau_C^2}. \tag{3.5}$$

The factor $2\tau_C$, which usually occurs in the spectral function was considered in reference to [43] with the amplitude C (3.6). The correlation time τ_C may be interpreted as the average time which an adsorbed atom requires to diffuse from a spot on the surface to which it is more strongly bound to another spot in which the binding circumstances are the same. This may in part be interpreted as staying time and equated with τ_S [66].

The Larmor frequencies ω_a and ω_b are dependant on the static magnetic field and may be calculated from the energy eigenvalues of the hyperfine states (2.6 and 2.23). The amplitude

$$C = \frac{2}{3} \frac{\tau_S}{\tau_S + \tau_F} \gamma_S^2 b^2 \tau_C \tag{3.6}$$

consists of the average length of stay on the surface τ_S, average flight time between two wall collisions τ_F and the correlation time τ_C. b represents the strength of the magnetic field which causes the relaxation. The factor 1/3 takes into account that only those components of b which are vertical or parallel to the static field can induce a transition. The relaxation rate through wall collisions is expressed as:

$$T_{HW}^{-1} = C j(\omega_{ab}) \tag{3.7}$$

It depends on the hyperfine states which pass over into one another. The dependancy of the static field passes over $j(\omega_{ab})$ into the relaxation rate.

The significant effects of wall collisions on the hyperfine occupancy and the polarization of gas in a storage cell are well shown by using the example of hydrogen. Deuterium will not be further considered at this point.

In a strong magnetic field the nuclear spins are uncoupled from the electron spins. Since the interaction on the surface attacks the electron spin of the adsorbate, one might expect that the nucleons relax far more slowly than the electrons. Figure 3.1 illustrates the relaxation behaviour over time of an initially polarized gas which is then left alone.

The upper figures show the relaxation in the hyperfine occupancy. As a product of the strong static field there are only minimal differences between the pure and the mixed states. They show practically identical relaxation behaviour. The lower diagram shows the associated behaviour of nucleon and electron polarization plotted over time.

Initially, as seen from the left, the states $|\,1\,\rangle$ and $|\,2\,\rangle$ are occupied, the electrons are polarized $P_{e0} \approx 1$ and the nuclei are unpolarized. Already after about 10 ms a noticeable depolarization

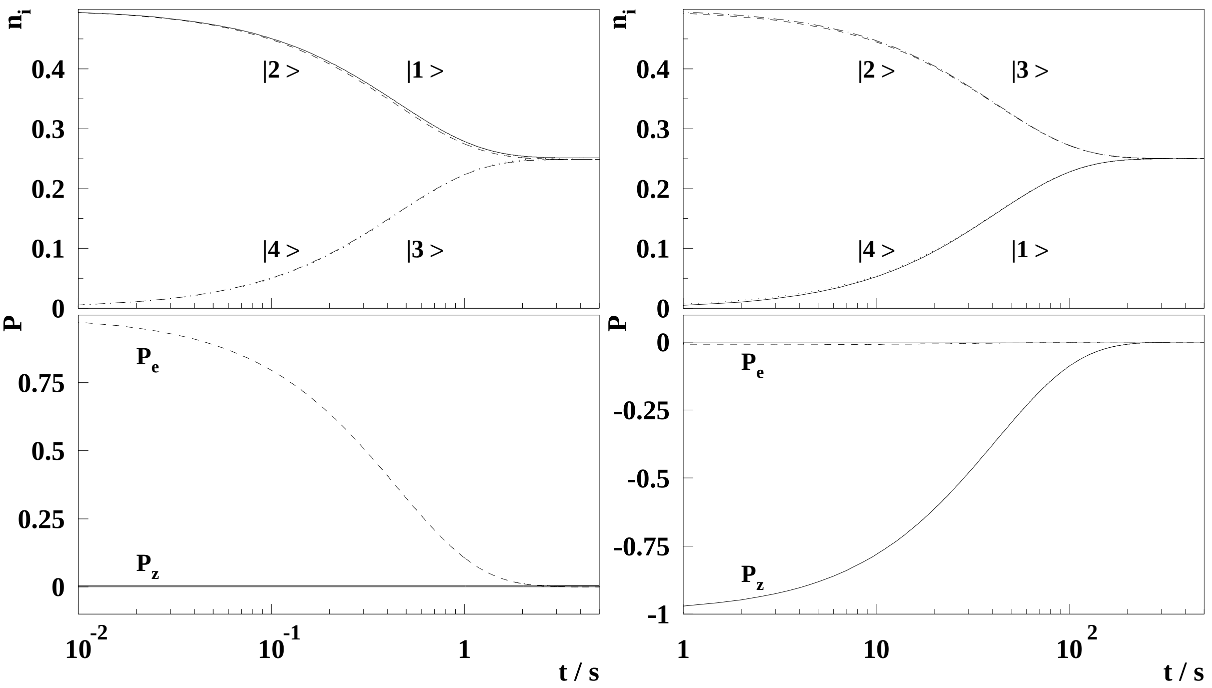

Fig. 3.1:
Spin relaxation of hydrogen through wall collisions in a strong magnetic field of $B = 350\,\mathrm{mT}$. Above: Relaxation of occupancy numbers. Below: Polarization Behaviour. To the left ate the initial states of $|\,2\,\rangle$ and $|\,3\,\rangle$, each occupied to 0.5. To the right are the states $|\,2\,\rangle$ and $|\,3\,\rangle$. The time scale is stretched from left to right so that the right is a factor of 100 larger. The measured results were made with a Drifilm cell (Table 11.1), for the correlation time and the amplitude: $\tau_c = 5.41 \cdot 10^{-12}\,\mathrm{s}$ and $C = 2.70\,\mathrm{s}^{-1}$.

of the electrons sets in. In comparing this time with the average length of stay in the storage cell of about 70 ms, a significant effect must be expected for the relaxation measurements.

In the diagrams to the right the states $|\,2\,\rangle$ and $|\,3\,\rangle$ are initially occupied. In this case the electrons are unpolarized and the nucleons have a negative polarization of $P_{z0} \approx -1$. The relaxation behaviour in this case is very similar to that of the initially polarized electrons, although in this diagram the time scale is stretched by a factor of 100. Noticeable effects on the nucleon polarization set in after about 1 s. Therefore it is not to be expected that with the storage cells used for this thesis a nucleon depolarization can be directly measured. Although during the atoms collide more than 3500 times with a wall during their length of stay (appendix A.3).

In a weak magnetic field the nucleon spin is coupled to the electron spin. This coupling only has a marginal effect on the interaction of the electrons with the surface fields, it does however lead to the fact that the nucleons relax as quickly as the electrons. Beyond the sign of the polarization there are no essential differences in initial occupancy to those in strong magnetic fields. Therefore figure 3.2 only shows the relaxation behaviour in the situation that the states $|\,2\,\rangle$ and $|\,3\,\rangle$ are occupied.

Since the two states $|\,2\,\rangle$ and $|\,4\,\rangle$ are mixed they show a markedly faster relaxation in a weak field than the two pure states $|\,1\,\rangle$ and $|\,3\,\rangle$. Since the state $|\,2\,\rangle$ in a weak field carries no polarization, the initial polarization of nucleons and electrons is $P_{e0} \approx P_{z0} \approx -0.5$ Similarly, the rates of relaxation for nucleons and electrons are about equal and correspond to relaxation rates of electrons in strong fields.

Therefore, the relaxation behaviour of electrons is largely independant from a static magnetic field and is mainly determined by the conditions on the surface. Through the hyperfine

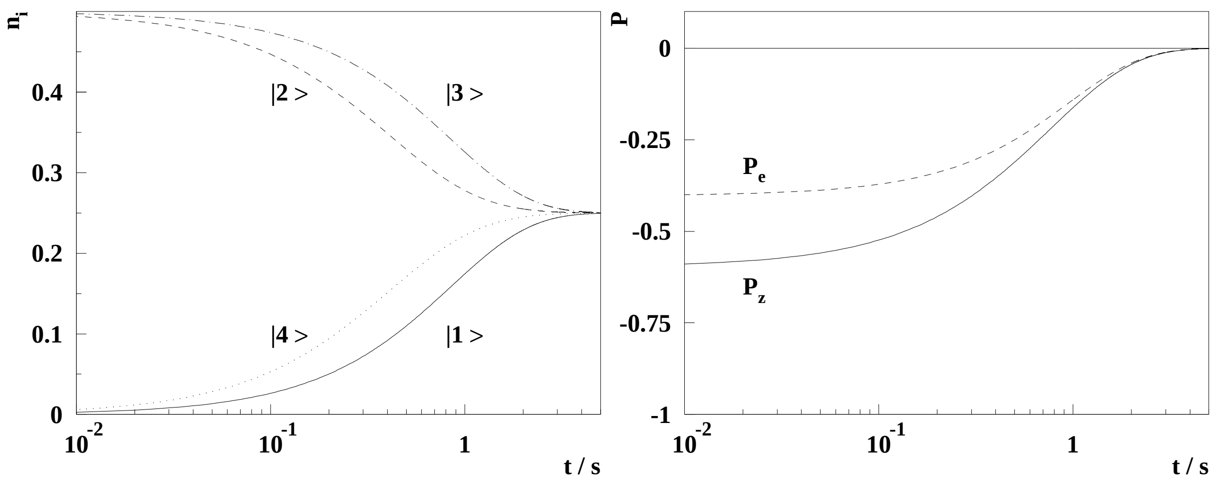

Fig. 3.2:
Spin relaxation of hydrogen through wall collisions in a weak magnetic field of $B = 10\,\mathrm{mT}$. To the beginning the states $|\,2\,\rangle$ and $|\,3\,\rangle$ are occupied each to 0.5. Left: Relaxation of the occupation numbers. Right: Behaviour of the polarization. For the correlation time and the amplitude measured values from a Drifilm cell were used (Table 11.1): $\tau_c = 5.41 \cdot 10^{-12}\,\mathrm{s}$ and $C = 2.70\,\mathrm{s}^{-1}$.

interaction the static field has an effect on how strongly the nucleons take part in the relaxation of the electrons.

3.2 Spin Exchange Collisions

A spin exchange collision describes an interaction of atoms with one another. This spin exchange collision takes place in the gas phase while the atoms fly from wall to wall. For example, two hydrogen atoms or deuterium atoms collide, whereby their electrons interact through their respective spins. As a result of this interaction the hyperfine states of the participating atoms can be different both before and after the collision. The effects of the nuclear spin can be disregarded. Already in 1956 E.M. Purcell and G.B. Field [97] discovered a method of calculating the transition amplitude during a spin exchange collision. The effect of spin exchange collisions is described by a time development operator

$$\mathcal{U} = \mathcal{P}_s + \mathrm{e}^{-i\Phi}\mathcal{P}_t \tag{3.8}$$

which conveys the two atoms in state $|\,ab\,\rangle$ into the state $\mathcal{U}\,|\,ab\,\rangle$. The probability of finding both atoms after the collision in the state $|\,cd\,\rangle$ is expressed as $|\langle\, cd\,|\mathcal{U}\,|\,ab\,\rangle|^2$. $\mathcal{P}_s$ and $\mathcal{P}_t$ are the projection operators on the singlet or triplet state of the coupled electron spin system. a, b, c and d each refer to a hyperfine state (2.19) and (2.25). The phase Φ is derived through the difference in potential between triplet and singlet, divided by $\hbar$, over the interaction time:

$$\Phi = \int \frac{V_t - V_s}{\hbar}\,\mathrm{d}t \gg 2\pi. \tag{3.9}$$

A spin exchange collision has a long interaction time in comparison to the period of an oscillation between a singlet and a triplet state, and thus $\Phi \gg 2\pi$ applies. This is often deemed a so-called hard collision. The phases are approximately evenly distributed, so that averages of them can be made. It follows, that electron spins of participating atoms after a spin exchange collision have been exchanged with a probability of 1/2. The spin exchange rate is given as

$$T_{AA}^{-1} = n\,\langle\,\sigma_{SE} v\,\rangle \tag{3.10}$$

where n represents the particle density, σ_{SE} the cross section for a spin exchange interaction and v represents the relative speed of both atoms. σ_{SE} is for a given energy after [98] defined as the sum of all partial waves with angular momentum l

$$\sigma_{SE} = \frac{\pi}{k^2} \sum_{l=0}^{\infty} (2l+1) \sin^2 \left(\eta_l^{(0)} - \eta_l^{(1)} \right) \tag{3.11}$$

with $k = \mu v/h$, where μ represents the reduced mass, and the scattering phases $\eta_l^{(0)}$, $\eta_l^{(1)}$ represent the singlet or triplet states. In disregarding the deflection of atoms during the scattering process, also known as straight line scattering, going back to H.S.W. Massey and C.B.O. Mohr [99], the following approximation [98, 100] is derived from (3.11) with b as the impact parameter.

$$\sigma_{SE} = 2\pi \int_0^{\infty} \sin^2 \left(\tfrac{1}{2} \Phi\,(b) \right) b \,\mathrm{d}b. \tag{3.12}$$

In the definition of the spin exchange cross section following (3.11) and (3.12) the 50 % probability for an exchange of electrons is not included. That is to say, consideration is also given to collisions in which the hyperfine states of participating atoms are maintained. The cross section for spin exchange collisions between hydrogen atoms was measured in the storage cell of a hydrogen maser as a function of temperature [101]. In good agreement with theoretical calculations for thermal velocities [102, 103, 104] an almost constant value of $\sigma_{SE} = 2.31(28) \cdot 10^{-15}\,\mathrm{cm}^2$ was measured in a temperature range between 77 and 363 K .

Since the average velocity increases proportionally to $\sqrt{T}$, and the density in the storage cell through the increase of the conductance [105] decreases proportionally to $1/\sqrt{T}$, the spin exchange collision rate is independant of temperature. This given; in a storage cell in which the temperature is constant, and between the range examined in this thesis of 90 to 300 K, the spin exchange collision rate is independant of the temperature if the averaging in (3.10) is disregarded. Ultimately, the total effect of a storage cell through spin exchange collisions is temperature dependant since the length of stay in the cell is proportional to $1/\sqrt{T}$.

T. Walker and L.W. Anderson [106] examined the consequences, which arise from spin exchange collisions for hydrogen and deuterium gas targets. Especially for so-called spin exchange sources [107], in which hydrogen or deuterium atoms are polarized through spin exchange collisions with optically pumped potassium atoms, spin exchange collisions are very important as a result of the high densities used in these sources. On the one hand they are used to polarize the hydrogen or deuterium atoms, on the other hand spin exchange collisions of the hydrogen and deuterium atoms with one another lead to a change in the occupation of the hyperfine levels. Thus polarization is transferred from the electrons to the nuclei in these sources. The spin exchange collisions influence the occupancy of the hyperfine states of the injected polarized gases also within the storage cell.

3.2.1 Spin Exchange Collisions between Hydrogen Atoms

In a very strong magnetic field the nuclear spins and the electron spins are practically completely decoupled and they ideally can be regarded as spectators in a spin exchange collision. In the case of hydrogen therefore there is only one spin exchange reaction in strong magnetic fields that can change the states of the involved atoms:

$$|\uparrow,+\rangle + |\downarrow,-\rangle \longleftrightarrow |\downarrow,+\rangle + |\uparrow,-\rangle \quad \text{corresponds to} \quad |1\rangle + |3\rangle \longleftrightarrow |4\rangle + |2\rangle . \tag{3.13}$$

However, this reaction does not influence the nuclear and electron polarization, as these vanish both before and after the collision.

In a finite magnetic field other spin exchange reactions may take place due to the mixing of the states $|\uparrow,-\rangle$ and $|\downarrow,+\rangle$ which may change the polarization of the involved atoms. Due to angular momentum conservation the sum of the magnetic quantum numbers of the total angular momentum has to be the same before and after the collision:

$$m_F^{(1)} + m_F^{(2)} = \text{constant.} \tag{3.14}$$

With respect to the spin exchange collisions the polarized atoms in the storage cell may be regarded as a closed system, no polarization can be lost. Polarization can only be transferred from electrons to nuclei or vice versa.

The possible spin exchange reaction can be easily found using the conservation of angular momentum, by ordering pairs of hyperfine states into groups for which the sum of the magnetic quantum numbers $\sum m_F$ is identical, as can be seen in table 3.1. Spin exchange collisions can only transform a given initial state $|ab\rangle$ into a final state $|cd\rangle$ if it belongs to the same group in the table. Therefore only those transition coefficients need to be calculated that refer to transitions within one row. From the table, one important property of spin exchange collisions can be seen immediately. Hydrogen atoms, which are completely in a pure state $|1\rangle$ or $|3\rangle$ cannot relax through spin exchange collisions alone. In these case the hyperfine occupancy stays constant.

The transition coefficients depend on the external magnetic field through the mixing angle θ and can be calculated according to [106] as follows. To this end for a general state $|q\rangle$ the notation

$$|q\rangle = q_\uparrow\,|\uparrow, m_q - 1/2\rangle + q_\downarrow\,|\downarrow, m_q + 1/2\rangle \tag{3.15}$$

is introduced, where $m_q = \langle q\,|\,F_z\,|\,q\rangle$ applies. The transition coefficients M_{ab}^c for the master equation (3.1 are obtained from

$$\begin{aligned} M_{ab}^c \;=\; \sum_d \;& -2\,\langle c\,|\,a\rangle\langle d\,|\,b\rangle\,(a_\uparrow b_\downarrow c_\uparrow d_\downarrow + a_\downarrow b_\uparrow c_\downarrow d_\uparrow) \\ & + \langle m_c\,|\,m_a\rangle\langle m_d\,|\,m_b\rangle\,(a_\uparrow b_\downarrow c_\uparrow d_\downarrow + a_\downarrow b_\uparrow c_\downarrow d_\uparrow)^2 \\ & + \langle m_c\,|\,m_a - 1\rangle\langle m_d\,|\,m_b + 1\rangle\,(a_\uparrow b_\downarrow c_\uparrow d_\downarrow)^2 \\ & + \langle m_c\,|\,m_a + 1\rangle\langle m_d\,|\,m_b - 1\rangle\,(a_\downarrow b_\uparrow c_\downarrow d_\uparrow)^2 . \end{aligned} \tag{3.16}$$

The here explicitly calculated rate equations may be found in the appendix F. These equations can be simplified considerably using the normalizing condition $\sum_i n_i = 1$ and the fact that due to conservation of angular momentum $\langle F_z\rangle = n_1 - n_3$ is a conserved parameter:

$$T_{HH}\frac{\mathrm{d}(n_2 - n_4)}{\mathrm{d}t} = -sin^2 2\theta\,(n_2 - n_4) \tag{3.17}$$

$$T_{HH}\frac{\mathrm{d}(n_2 + n_4)}{\mathrm{d}t} = -(n_2 + n_4) + \frac{1 - (n_1 - n_3)^2}{2} + \frac{\cos^2 2\theta}{2}(n_2 - n_4)^2 . \tag{3.18}$$

$\sum_i m_F^{(i)}$	$\|ab\rangle$			
2	$\|11\rangle$			
1	$\|12\rangle$	$\|14\rangle$		
0	$\|13\rangle$	$\|22\rangle$	$\|24\rangle$	$\|44\rangle$
-1	$\|23\rangle$	$\|34\rangle$		
-2	$\|33\rangle$			

Tab. 3.1:
Pairs of hyperfine states in the hydrogen atom ordered according to the sum of the magnetic quantum numbers of the total angular momentum. Spin exchange collisions can transform a given initial state $|ab\rangle$ only into a final state $|cd\rangle$ within the same group. Transitions from one group to another are excluded due to angular momentum conservation.

As shown by the integration of (3.17), an exponential decay of the occupation difference between the mixed states $|\,2\,\rangle$ and $|\,4\,\rangle$ is a significant effect of spin exchange collisions on the hyperfine occupancy of hydrogen atoms:

$$n_2 - n_4 = (n_2 - n_4)_0 \exp\left(-t \cdot \frac{\sin^2 2\theta}{T_{HH}}\right). \tag{3.19}$$

The second equation describes the relaxation between the mixed states $|\,2\,\rangle$ and $|\,4\,\rangle$ and the pure states $|\,1\,\rangle$ and $|\,3\,\rangle$. The behaviour of the occupation numbers under the influence of spin exchange collisions is shown in the left plot of figure 3.3. The chosen initial condition of $n_2 = n_3 = 0.5$ also was examined within the framework of the relaxation measurements in chapter 12.

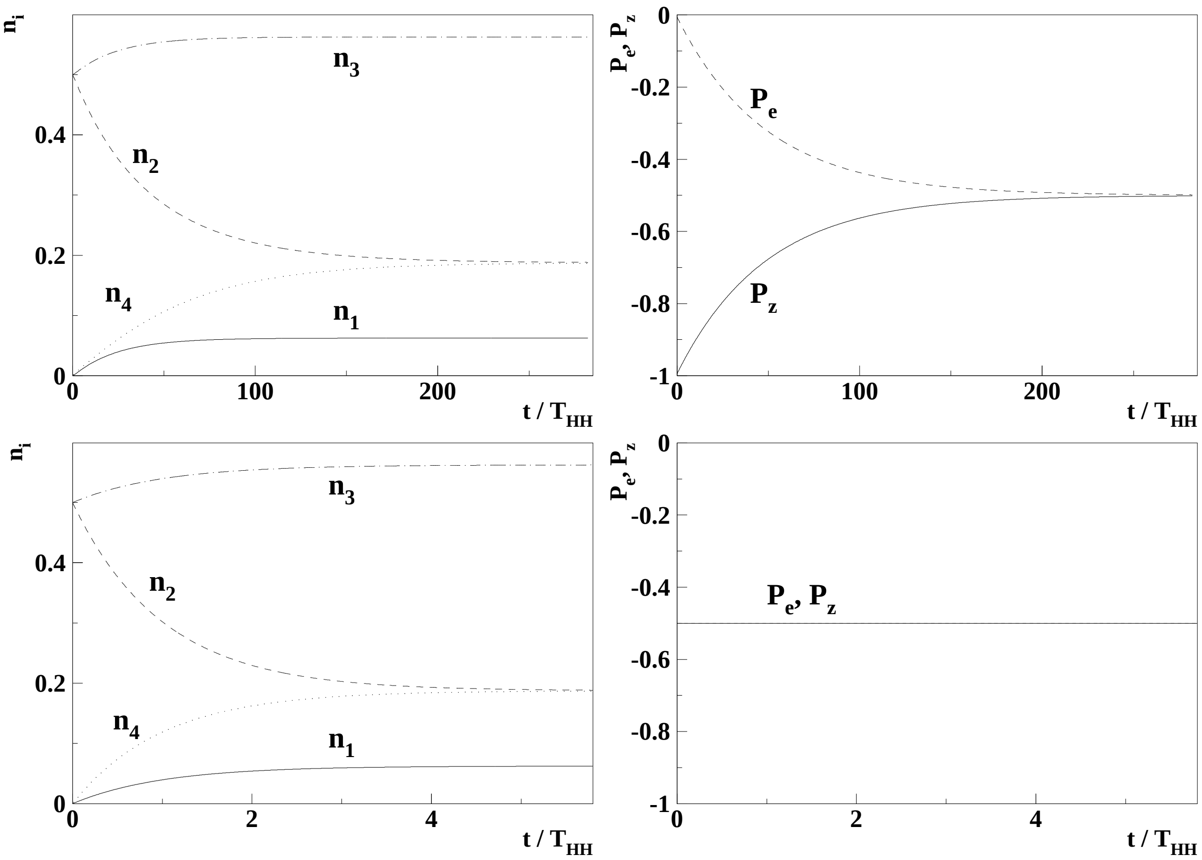

Fig. 3.3:
Time dependence of hyperfine occupation, electron and nuclear polarization of hydrogen atoms under the influence of spin exchange collisions. Above at a holding field of $350\,\mathrm{mT}$ and below without field. The average time between two spin exchange collisions T_{HH} was chosen as time unit. The initial hyperfine occupancies were assumed as $n_1 = n_4 = 0$ and $n_2 = n_3 = 0.5$, as they also could be created almost like this with the test source (chapter 4.1)

From equation (3.19) the time constant may be derived with which the system approaches its equilibrium:

$$T_{EQ} = \frac{T_{HH}}{\sin^2 2\theta} = (1 + x^2)\, T_{HH}. \tag{3.20}$$

Thus the external field mostly leads to a stretching of the time scale by a factor of $1 + x^2$ and therefore slows the relaxation process down. In a strong field about 250 spin exchange collisions are taken to arrive at the equilibrium, without field only 5 spin exchane collisions are sufficient. Besides this stretching of the time scale the behaviour of the hyperfine occupancy is almost identical, the differences can hardly be seen in figure 3.3 top and bottom on the left side.

Nevertheless there are significant differences in the behaviour of nuclear and electron polarization. Since the states $|\,2\,\rangle$ and $|\,4\,\rangle$ in zero field carry no polarization, the polarizations are determined by $n_1 - n_3$ alone. This difference is conserved in spin exchange collisions, P_e as well as P_z are constant (figure 3.3 bottom right). The behaviour of the polarizations in strong fields is shown in figure 3.3 top right. Spin exchange collisions lead to an equalization of the spin temperatures of both subsystems, electrons and protons. The polarization that initially is carried only by the protons is divided up over time equally between electrons and protons.

3.2.2 Spin Exchange Collisions between Deuterium Atoms

Some important properties of spin exchange collisions can be transferred directly from hydrogen to deuterium. Naturally, also in collisions between deuterium atoms the angular momentum is conserved and as in (3.14) again a table can be constructed from which all possible spin exchange reactions can be seen in a simple way (table 3.2). The transition coefficients for the master equations M^c_{ab} can be calculated according to (3.16) as in the case of hydrogen. However, this calculation is far more involved (appendix F) and the rate equations can no longer be integrated analytically.

Resulting from the significantly higher number of possible spin exchange reactions, deuterium shows a much more complex behaviour, as can be seen from figure 3.4. Here the time dependence of the relaxation of the hyperfine occupancies (top) and the polarization (bottom) is shown for a strong magnetic field of $B = 5 \cdot B_C^{\mathrm{D}}$ for four different initial occupancies that can be approximately produced with the test source (table 4.1) and that have been examined in the relaxation measurements (chapter 12.3.3 and 12.3.4).

Despite the considerably more complex behaviour in comparison to hydrogen some simple properties can be seen from this figure. The occupation numbers and the polarization observables with the exception of case (2) approach the same equilibrium values. All initial occupations approach $n_2 = n_6$, $n_3 = n_5$, $P_z > P_e$ and $P_{zz} > 0$. after reaching the equilibrium. An initial electron polarization is transferred to the vector polarization of the nuclei similarly to the case of hydrogen, but only partly for deuterium. This can be seen from the figures (1) and (2) on the left, where for the initial conditions (2) only the initial electron polarization was reduced to 1/3 compared to the case (1). The initial polarization is not divided up equally between P_e and P_z. To the contrary, although for the initial conditions (3) and (4) $P_e = P_z$, the vector polarization increases slightly and P_e decreases. The tensor polarization P_{zz} is not conserved and a high tensor polarization decays about on the time scale of the exchange between electron and vector polarization.

$\sum_i m_F^{(i)}$	$\|\,ab\,\rangle$				
3	$\|\,11\,\rangle$				
2	$\|\,12\,\rangle$	$\|\,16\,\rangle$			
1	$\|\,13\,\rangle$	$\|\,15\,\rangle$	$\|\,22\,\rangle$	$\|\,26\,\rangle$	$\|\,66\,\rangle$
0	$\|\,14\,\rangle$	$\|\,23\,\rangle$	$\|\,25\,\rangle$	$\|\,36\,\rangle$	$\|\,56\,\rangle$
-1	$\|\,24\,\rangle$	$\|\,33\,\rangle$	$\|\,35\,\rangle$	$\|\,46\,\rangle$	$\|\,55\,\rangle$
-2	$\|\,34\,\rangle$	$\|\,45\,\rangle$			
-3	$\|\,44\,\rangle$				

Tab. 3.2:
Pairs of hyperfine states in deuterium atoms ordered according to the sum of their magnetic quantum numbers of the total angular momentum. Spin exchange collisions can only transform an initial state $|\,ab\,\rangle$ into a final state $|\,cd\,\rangle$ within the same group. Transitions from one group to another are excluded due to angular momentum conservation.

The extremely fast rise of the occupation of state $|1\rangle$ for the initial conditions (3) and of state $|2\rangle$ for the initial conditions (4) is remarkable. These occupation numbers reach their maximum already after 2 to 3 spin exchange collisions and decrease slowly thereafter. It is noteworthy that this obvious change in the hyperfine occupation does not influence any of the polarization observables. These stay, as can be seen from the lower figures, mostly constant over this time period.

There is a simple explanation for this behaviour. As in the case of hydrogen (3.13), there are also a small number of spin exchange reactions between deuterium atoms, in which the nuclei are spectators in the limit of a strong magnetic field. These reactions lead to a fast rearrangement of the hyperfine occupation, but they do not change the electron, vector or tensor polarization. These are the spin exchange reactions

$$|\uparrow,+\rangle+|\downarrow,0\rangle \longleftrightarrow |\downarrow,+\rangle+|\uparrow,0\rangle \quad \text{corresponds to} \quad |1\rangle+|5\rangle \longleftrightarrow |6\rangle+|2\rangle \tag{3.21}$$

$$|\uparrow,+\rangle+|\downarrow,-\rangle \longleftrightarrow |\downarrow,+\rangle+|\uparrow,-\rangle \quad \text{corresponds to} \quad |1\rangle+|4\rangle \longleftrightarrow |6\rangle+|3\rangle \tag{3.22}$$

$$|\uparrow,0\rangle+|\downarrow,-\rangle \longleftrightarrow |\downarrow,0\rangle+|\uparrow,-\rangle \quad \text{corresponds to} \quad |2\rangle+|4\rangle \longleftrightarrow |5\rangle+|3\rangle\,. \tag{3.23}$$

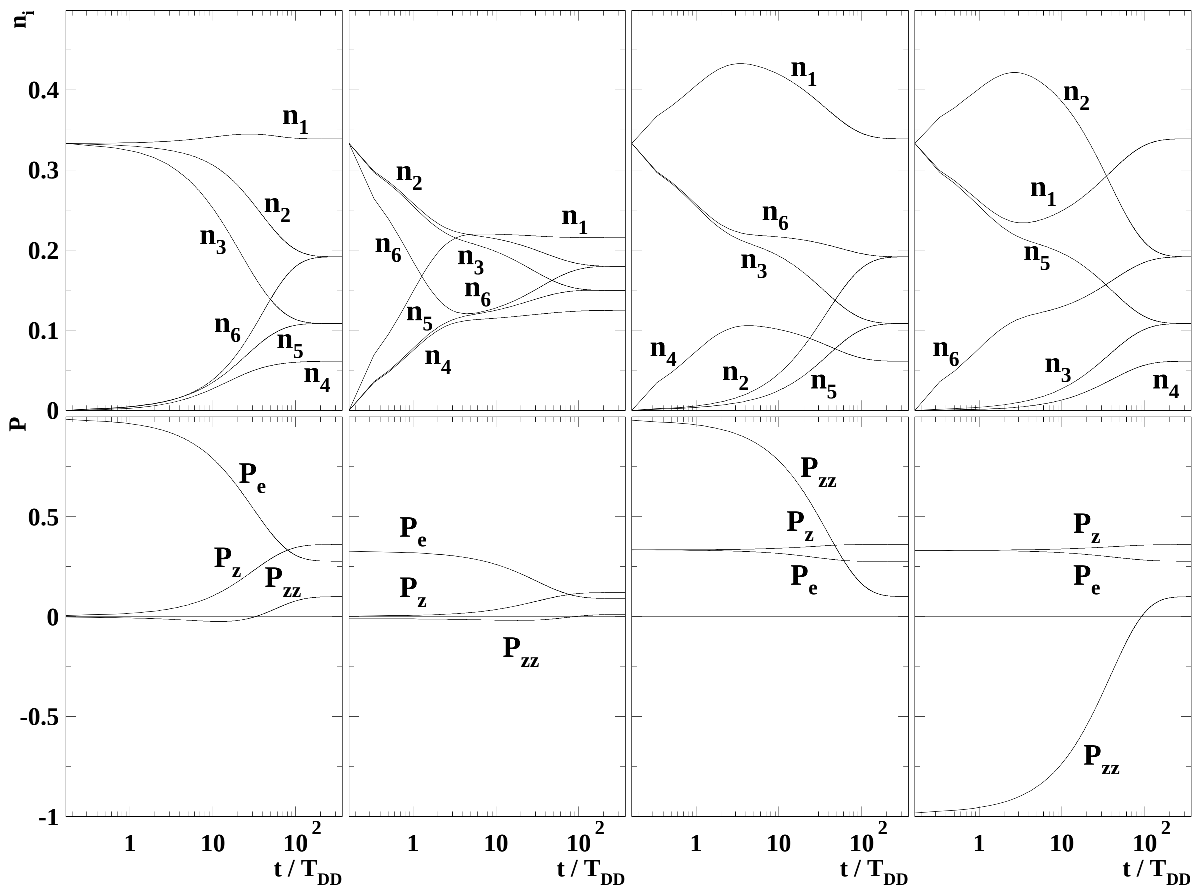

Fig. 3.4:
Time dependence of the hyperfine occupancy and polarization of deuterium atoms and the influence on spin exchange collisions in a magnetic field of $B = 5 \cdot B_C^{\mathrm{D}}$. The average time between two spin exchange collisions T_{DD} was chosen as time unit. The initial conditions are from left to right: 1.) $n_1 = n_2 = n_3 = 1/3$ and $n_4 = n_5 = n_6 = 0$. 2.) $n_2 = n_3 = n_6 = 1/3$ and $n_1 = n_4 = n_5 = 0$. 3.) $n_1 = n_3 = n_6 = 1/3$ and $n_2 = n_4 = n_5 = 0$. 4.) $n_1 = n_2 = n_5 = 1/3$ and $n_3 = n_4 = n_6 = 0$. The behaviour of the hyperfine occupancy is shown above, the after (2.30) resulting polarization observables are shown below.

In figure 3.4 (3) the states $|\,1\,\rangle$, $|\,3\,\rangle$ and $|\,6\,\rangle$ are occupied in the beginning, from which the states $|\,3\,\rangle$ and $|\,6\,\rangle$ transform into the states $|\,1\,\rangle$ and $|\,4\,\rangle$ through the fast spin exchange reaction (3.22):

$$\begin{array}{lcl} |\,1\,\rangle & \longrightarrow & |\,1\,\rangle \\ |\,3\,\rangle & \longrightarrow & |\,4\,\rangle \\ |\,6\,\rangle & \longrightarrow & |\,1\,\rangle\,. \end{array} \tag{3.24}$$

For the state $|\,1\,\rangle$ that is occupied to 1/3 in the beginning no practical collision partner for a fast spin exchange reaction exists, therefore n_1 increases in the beginning. Analogously, the reaction (3.21) leads to an increase of n_2 in figure 3.4 (4):

$$\begin{array}{lcl} |\,1\,\rangle & \longrightarrow & |\,6\,\rangle \\ |\,2\,\rangle & \longrightarrow & |\,2\,\rangle \\ |\,5\,\rangle & \longrightarrow & |\,2\,\rangle\,. \end{array} \tag{3.25}$$

This striking behaviour, that is marked by several occupation probabilities moving even further away from their equilibrium values, allows the conclusive detection of spin exchange collisions in strong fields even for the extremely low particle densities in the region of 10^{10} to $10^{13}\,\mathrm{cm}^{-3}$ that are typically used in storage cells (chapter 12.3.3). This effect only appears if at least three different states of deuterium are injected into the storage cell.

Finally it should be mentioned that in contrast to hydrogen (figure 3.3 left) spin exchange collisions in strong or weak fields for deuterium show a significantly different behaviour with respect to the relaxation of the hyperfine occupation. Especially the fast spin exchange reactions (3.21) and (3.22) are masked by competing reactions that appear stronger due to the mixing of states in weaker fields. As a result the fast increase of n_1 or n_2 is not observed. However, the presentation of the behaviour of deuterium in a weak field was waived here.

4 Setup of the Experiment

An overview of the test setup for the Breit-Rabi polarimeter was already given in chapter 1.4. In the following, the fundamental aspects as well as the technical functionality of the different components of the apparatus will be laid out in detail.

4.1 The Atomic Beam Source of the Test Setup

The atomic beam source depicted in figure 1.4 is operated with only one sextupole magnet and one high frequency transition for hydrogen or deuterium, respectively. Therefore it is not possible to produce all polarization states that are necessary for the HERMES experiment with a freely selectable sign, as it is possible with the source that was built for the HERMES experiment itself [45, 46, 47]. The flux of polarized atoms that is injected into the test storage cell is with about $1,0\,(5)\cdot 10^{15}\,\mathrm{s}^{-1}$ (table 11.1) significantly below the flux of $5-7\cdot 10^{16}\,\mathrm{s}^{-1}$ which after extensive measures is injected into the HERMES storage cell [108] (tables 14.2 and 14.4). The differences are in part due to the low acceptance of the used test storage cells. However, the test source has an electrically excited and therefore adjustable sextupole magnet. This variability of the sextupole field in this magnet is used in particular in the chapters 8 and 9.

The production of nuclear spin polarized hydrogen and deuterium atoms using the atomic beam method goes back to [109]. In a high frequency discharge in a dissociator molecules are separated into hydrogen or deuterium atoms. These flow through a nozzle into the high vacuum region of the source. A small part of these atoms is formed into an atomic beam with the help of a skimmer and a collimator. Skimmer and collimator at the same time also separate three vacuum chambers inside the source from one another and in this way form a *differential pumping system*, within which the rest gas pressure is reduced step by step from one chamber to the next.

In the gradient field of the sextupole magnet the atoms are separated according to the projection of their electron spin, which leads to the build-up of an electron polarization in the focused beam. The effect of the sextupole magnet is that out of the four hyperfine states of the hydrogen atom the states $|\,1\,\rangle$ and $|\,2\,\rangle$ are focused and the states $|\,3\,\rangle$ and $|\,4\,\rangle$ are removed from the beam. In the case of deuterium the upper three of the six hyperfine states are focused.

The following adiabatically operated high frequency transition (chapter 5.1) exchanges an occupied and an unoccupied state in the hyperfine occupation structure, e.g. the weak field transition WFT 1-3 in the case of hydrogen exchanges the occupation of the states $|\,1\,\rangle$ and $|\,3\,\rangle$. This transforms an atomic beam that consists of the states $|\,1\,\rangle$ and $|\,2\,\rangle$ into a beam that only contains the states $|\,2\,\rangle$ and $|\,3\,\rangle$. In a successive weak field this corresponds to a sign change for nuclear and electron polarization from $P=+0,5$ to $P=-0,5$, in a strong field this results in a transfer of the electron polarization produced in the sextupole magnet to the nuclei (table 4.1). A strong field transition is used for the production of nuclear spin polarization in deuterium atom beams. In the case of hydrogen the solenoid used for the production of the high frequency field in the WFT 1-3 is replaced by a band conductivity resonator. This strong field transition allows a total of four transformations in the hyperfine occupation of the deuterium beam, of which however only three are used. The possible hyperfine occupations and the resulting polarization states of electrons and nuclei are listed in table 4.1.

Tab. 4.1:
Hyperfine structure occupations in hydrogen and deuterium atom beams which are possible with the atomic beam source. The table lists the resulting electron polarization P_e as well as the vector and tensor polarization P_z and P_{zz} for the limits of weak and strong external field. For the polarization values an ideal sextupole magnet and perfectly working high frequency transitions are assumed.

			Weak Field			Strong Field		
		States	P_e	P_z	P_{zz}	P_e	P_z	P_{zz}
H	HFT off	$\vert 1\rangle\,\vert 2\rangle$	+1/2	+1/2	—	+1	0	—
	WFT 1-3	$\vert 2\rangle\,\vert 3\rangle$	−1/2	−1/2	—	0	−1	—
D	HFT off	$\vert 1\rangle\,\vert 2\rangle\,\vert 3\rangle$	+1/3	+1/3	−1/3	+1	0	0
	SFT 1-6	$\vert 2\rangle\,\vert 3\rangle\,\vert 6\rangle$	−1/9	+2/9	−2/3	+1/3	0	0
	SFT 2-6	$\vert 1\rangle\,\vert 3\rangle\,\vert 6\rangle$	+1/9	+4/9	0	+1/3	+1/3	+1
	SFT 3-5	$\vert 1\rangle\,\vert 2\rangle\,\vert 5\rangle$	+5/9	+2/9	0	+1/3	+1/3	−1

4.2 The Storage Cells of the Test Setup

The test storage cells (figure 4.1) are especially designed for the examination of relaxation mechanisms. To reach a sensitivity in this regard that is as high as possible, a long storage time and a correspondingly large number of wall collisions in the cell is required. Two cell geometries are used for the measurements, which differ from one another in their cell volume and in the length of the exit tube. The temperature of the storage cell can be adjusted to values between 90 and 300 K using the combination of liquid nitrogen cooling and a heating filament. A PID regulator (**P**roportional-, **I**ntegral- and **D**ifferential regulator) stabilizes the mean temperature with a precision of 0.5 K. The temperature differences between the three thermal sensors are between 5 and 10 K. A dipole magnet produces an adjustable holding field between 0.01 and 0.75 T over the storage cell. The position of the pole shoes is shown in figure 4.1.

Using differently constructed storage cells three types of surfaces are examined with regard to their effect on the relaxation of the hyperfine occupancies of the injected gases:

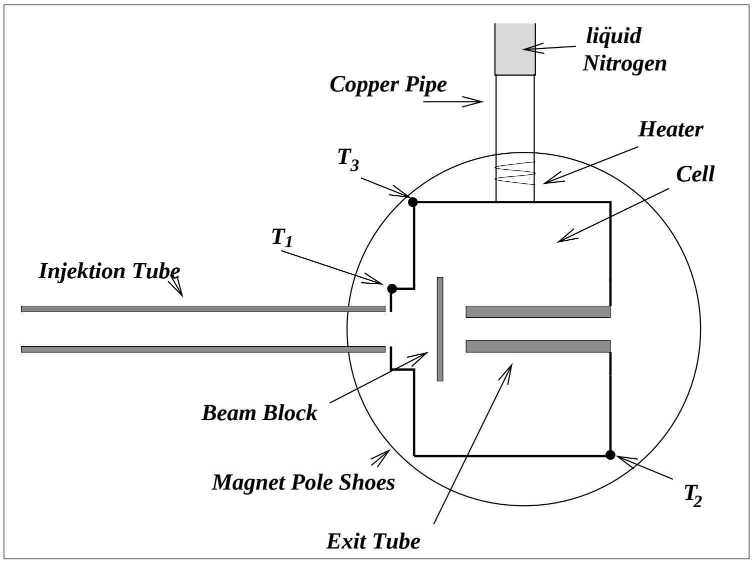

Fig. 4.1:
Storage cell for the examination of relaxation mechanisms. The cell is mounted on a copper pipe which is cooled with liquid nitrogen. Using a heating filament, the temperature and be freely adjusted between 90 K and 300 K. Three platinum thermoresistors (T1, T2 and T3) are used for monitoring and in conjunction with a PID regulator for the stabilization of the cell temperature. The beam block prevents the free flight of the atoms trough the cell.

- an uncoated aluminum cell which before installation was cleaned using ultrasound in acetone,
- an aluminum cell coated with drifilm[2] and
- two aluminum cells coated with teflon[3]

For each of the three surfaces one large cell with a 60 mm exit tube is available. The only small cell is coated with teflon.

An enlargement of the cell volume leads to a reduction of the probability of an atom hitting one of the openings of the two exit tubes during the diffusion through the cell. As a result the storage time in the cell as well as the mean number of wall collisions is increased. All other parameters stay unaffected. A longer exit tube reduces the transmission probability of an atom leaving the cell through the tube after entering the tube from one side. Also this results in an increase of the storage time and the mean number of wall collisions. Because a longer tube is also less conductive, the density in the cell is increased as well. The mean number of wall collisions of the atoms in the storage cell can be determined from a Monte Carlo simulation for molecular flow. The large cell with a volume of about 260 cm^3 and a 60 mm long exit tube has a mean number of wall collisions of 3505 (14) for state $|1\rangle$. The small cell with a volume of about 130 cm^3 and a 30 mm long exit tube counts 1456 (6) collisions. For the other hyperfine states marginally different collision counts are arrived at, due to the different phase space distributions in the atomic beam source behind the sextupole magnet (appendix A.3). The given collision count refers exclusively to those atoms which leave the cell through the exit tube and thus can be analyzed with the Breit-Rabi polarimeter. The atoms in the storage cell of the HERMES experiment see only an average of 308.8 (3) wall collisions (table A.5).

The fraction of the injected gas that leaves the cell through the exit tube in the direction of the polarimeter and is thus available for analysis is defined by the fraction of the total conductance represented by the conductance of the exit tube. A small conductance value of the injection tube reduces the backward flow towards the source and thus leads to a higher intensity of the test beam. The injection tube is relatively long with a length of 155 mm and is located outside the region of the pole shoes. Therefore the magnetic holding field is smaller inside the injection tube than inside the actual storage cell. The injection tube is also not mechanically connected to the cell and therefore also not cooled. For this reason the conditions inside the injection tube depend strongly on the conditions inside the storage cell. Monte Carlo simulations show that atoms that reach the polarimeter in the case of the large cell have 3.7 % and in the case of the small cell 6.4 % of their wall collisions inside the injection tube. These results are again valid for the state $|1\rangle$, the values for the other states are very similar. To minimize the impact of the wall collisions inside the injection pipe on the hyperfine occupancy of the atoms a Teflon coated injection tube was used for all measurements. A drifilm coated injection pipe was not available. Especially in the measurements with uncoated aluminum an uncoated injection pipe would cause strong recombination and depolarization due to the high temperature and the weak field (chapter 12.1). This would worsen the results of the measurements at low temperatures.

[2] According to [42]: 50 % each of a solution of dimethyledimethoxysilane $(CH_3)_2Si(OCH_3)_2$, trimethylemethoxysilane $(CH_3)_3SiOCH_3$ and four drops of acetic acid per 100 ml solution. The coating procedure is described in [43]. The cell was manufactured and coated in Novosibirsk. A deviation from the given recipe cannot be excluded completely.

[3] Du Pont: Teflon FPFE 3170. The suspension is diluted with distilled water in a ratio of 1:1. After application of this diluted suspension the parts of the cell are baked for 3 hours at 300° C.

4.3 The Breit-Rabi Polarimeter

4.3.1 The Vacuum system

Gas flows between $2 \cdot 10^{13}\,\mathrm{s}^{-1}$ and $2 \cdot 10^{14}\,\mathrm{s}^{-1}$ were injected into the entry valve of the Breit-Rabi polarimeter (figure 4.2). Of these only 4.4 (10) to $31.2\,(18) \cdot 10^{10}\,\mathrm{s}^{-1}$ reached the sensitive region of the atomic beam detector. According to table B.2 this relates to an equivalent partial pressure of 1.6 (4) to $17.9\,(13) \cdot 10^{-11}$ mbar.

One of the most important conditions for the intensity measurement of an atomic beam of such a low intensity is the vacuum system of the Breit-Rabi polarimeter. Especially inside the detector chamber the partial pressures of molecules that contain hydrogen, such as H_2 or water, must be as low as possible. These rest gas molecules are created in the formation chamber of the mass spectrometer by dissociative ionization of hydrogen ions. These hydrogen atoms contribute to the background of the measurements on the atomic beam (figure 4.8).

The vacuum system of the polarimeter is designed as a differential pumping system consisting of three pumping stages. Figure 4.2 shows an overview. The first two stages, the HFT chamber and the sextupole chamber are located in a common vacuum chamber. The first sextupole magnet limits the conductance between both chambers. Both stages are pumped by cryo pumps (with $2000\,\mathrm{l\,s}^{-1}$ each). The third stage contains the atomic beam detector. This chamber is connected to the sextupole chamber by a 210 mm long pipe with a diameter of 35 mm. To effectively suppress the rest gas background, the detector chamber was equipped with a titanium sublimator. A ball made from a titanium-tungsten alloy is electrically heated to more than 900^0 C evaporating titanium that re-condenses on the chamber walls. A titanium covered chamber wall has a suction power of $2\,\mathrm{l\,s}^{-1}\,\mathrm{cm}^{-2}$ for hydrogen and deuterium. Heavier gases are pumped out by an ion getter pump ($60\,\mathrm{l\,s}^{-1}$). The atomic beam detector is basically located in the center of a titanium sublimation pump with a total suction power of 10.000 to $20.000\,\mathrm{l\,s}^{-1}$, depending on the titanium coverage. This leads to an extremely low hydrogen partial pressure in the detection region. Without the gas ballast from an atomic beam pressures below 10^{-10} mbar hydrogen equivalent can be reached. Even with the gas ballast from the beam out of a storage cell the pressure does not exceed $5 \cdot 10^{-9}$ mbar (table B.1). Before the pumping procedure the detector

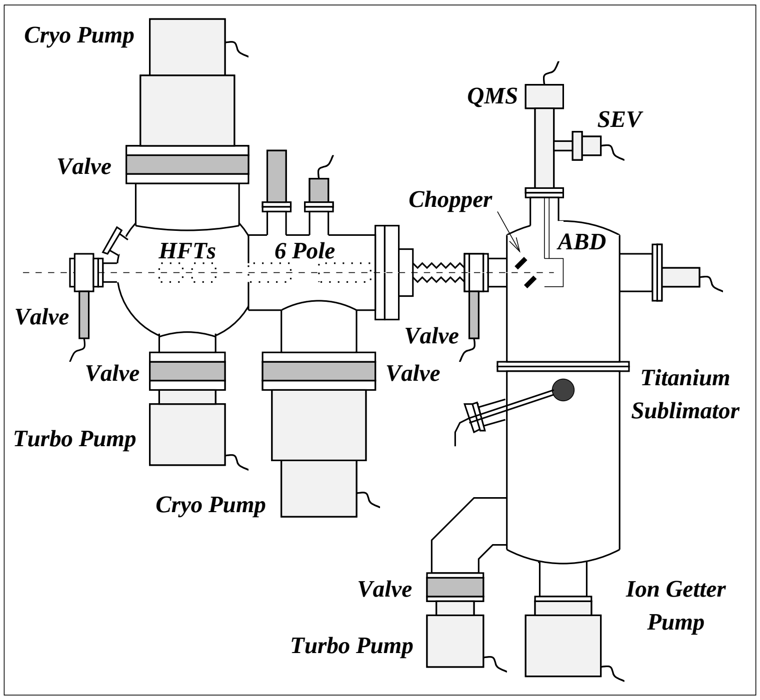

Fig. 4.2:
Vacuum system of the Breit-Rabi polarimeter. The front chamber (left) contains the high frequency transitions and the sextupole magnets, the detector chamber (right) contains the atomic beam detector consisting of a chopper, a quadrupole mass spectrometer (QMS) and a secondary electron multiplier (SEM). The axis of the atomic beam is indicated as a dashed line.

chamber is heated to 200° C for about 24 h to bake out the water which makes up the dominant contribution to the partial pressure in the detection of the atomic beam. Both chambers are equipped with a pre-vacuum system and turbo molecular pumps to start the pumping procedure. During the measurements these are separated from the chambers by valves.

4.3.2 The High Frequency Transitions

To completely determine the hyperfine occupancies in the case of hydrogen three and in the case of deuterium five high frequency transitions are necessary (figure 1.4 and chapter 1.5). For hydrogen even four transitions could be technically realized; the fourth transition can be used to check the polarimeter during the polarization measurement itself. For both elements exclusively strong and medium field transitions are used. Due to the fact that the transitions for hydrogen and deuterium are operated at different frequencies, a different flange exists for each atom type on which, in both cases, a coil for the medium field transitions and a band conductivity resonator for the strong field transitions are mounted. By exchanging these flanges the Breit-Rabi polarimeter can be quickly switched from hydrogen to deuterium. The frequency of each resonator is fixed and the resonances of the transitions are set by choosing the static magnetic field.

The high frequency field for the medium field transitions[4] is generated by a coil that is fed by a high frequency emitter and an amplifier. A static magnetic field with perpendicular orientation and a gradient that decrease along the direction of the atomic beam is superimposed, as is indicated in figure 4.3 by the pole shoes of the magnet. The field gradient enables the complete exchange of the involved hyperfine states following the method of adiabatic high frequency transitions (chapter 5.1). The operating frequencies of the high frequency transitions are 68.2 MHz for hydrogen and 17.0 MHz for deuterium.

The high frequency field for a strong field transition is generated by a so called band conductivity resonator (figure 4.4 right) [110]. The high frequency is coupled galvanically to one of the two resonator rods. The second rod is excited into oscillations by the HF field, so that it has to oscillate in anti-phase with the first one. This way the high frequency magnetic fields can constructively interfere in the middle between the two rods. The length of the resonator rods should in principle be equal to one quarter of a standing wave. This relates to about 5.25 cm for hydrogen and 22.8 cm for deuterium. In reality the share of the standing wave is shortened to a value of less than $\lambda/4$ due to the capacitive load at the right end of the rods [111]. As a result the high frequency transition can be constructed shorter, keeping the course of the atomic beam to the first sextupole magnet short. This optimizes the accepted spatial angle and therefore the intensity of the atomic beam in the detection region. Furthermore, the resonator can be tuned to a suitable frequency by varying the the distance between the two capacitor plates. The resonator for the hydrogen transitions was operated at 1425 MHz, the resonator for the deuterium transitions at 419 MHz. In the case of the band conductivity resonator for the hydrogen measurements the static magnetic field is perpendicular to the resonator rods and therefore parallel to the HF field (figure 4.4). This transition is thus designed as a pure σ-transition (chapter 5.2) for the operation of a SFT 2-4. However, inhomogeneities in the static field of the C-magnet cause a small component of the static field to be perpendicular to the HF-field, which also allows for the operation of the π-transition SFT 1-4. On the other hand this SFT 1-4 is not as stable

[4] A continuous monitoring of the amplitude of the high frequency field using a pick-up loop as in the strong field transitions (figure 4.4) was not implemented in the framework of this thesis. However, it is anticipated for the HERMES experiment.

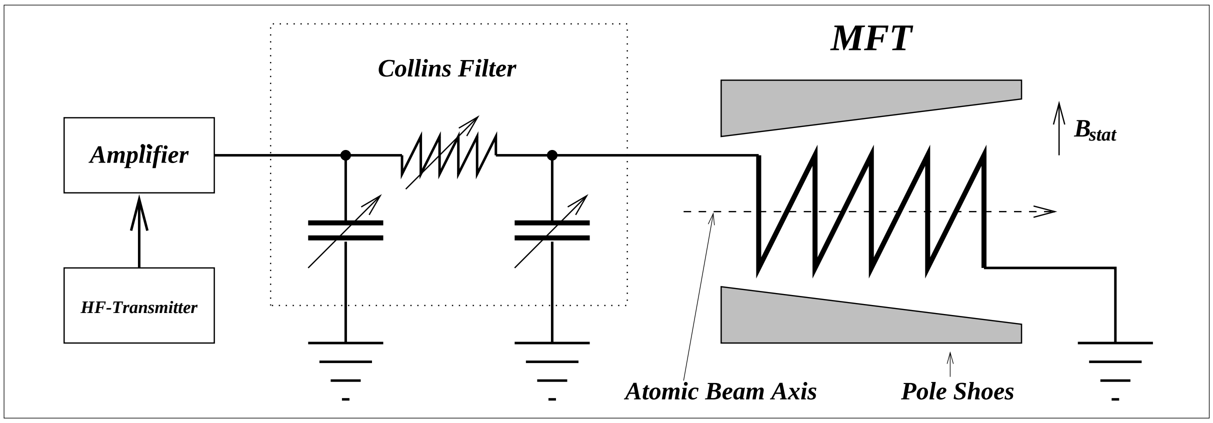

Fig. 4.3:
Structure of a medium field transition. The high frequency field is generated by a coil and oscillates perpendicularly to the static field. The shape of the pole shoes indicates a gradient field that decreases along the direction of the atomic beam. In reality the gradient field is generated by a coil as well and thus can be tuned. The Collins filter allows the adjustment of the impedance of the overall setup to $50\,\Omega$.

as the SFT 2-4 and it's efficiency is high aat 96 % (table 8.1), but still significantly smaller than the efficiency of the SFT 2-4.

The requirement to be able to use a single band conductivity resonator for π- as well as σ-transitions has led to the development of resonators with resonator rods that are tilted relative to the axis of the atomic beam, and thus relative to the static field (figure 4.5). These resonators have been successfully used for the deuterium measurements both inside the source and in the polarimeter (chapter 5.5)[112]. A resonator with tilted rods for the operation of the two strong field transitions for hydrogen was also constructed, but not used.

As a result of the input HF-power of several Watts the resonators heat up during the operation and the length of the resonator rods changes accordingly. This shortens the plate distance in the terminating capacitance and shifts the resonator frequency.

If the resonator is fed by a frequency stable HF-emitter it becomes difficult to find a stable setting for the resonator frequency.

The phase control shown in figure 4.4 automatically sets the correct frequency. Using a directional coupler (DC) part of the HF-power is coupled out of the supply line in front of the

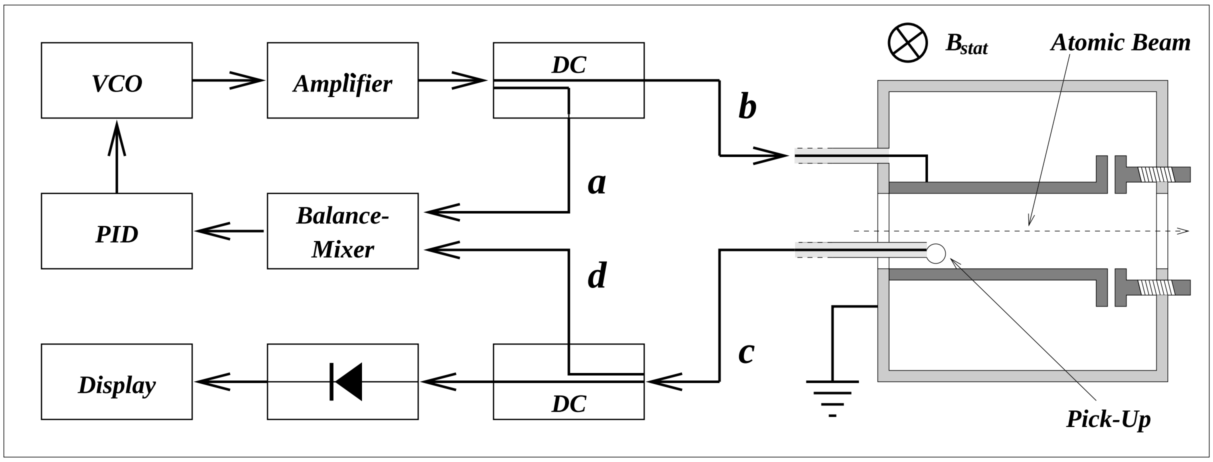

Fig. 4.4:
Structure of a strong field resonator with resonance control circuit. The labels mean:VCO – **V**oltage **C**ontrolled **O**szillator, DC – **D**irectional **C**oupler and PID – **P**roportional-, **I**ntegral- and **D**ifferential-Controller. The lengths of the conductors a, b, c and d have to fulfill the relation $b - a = c + d$.

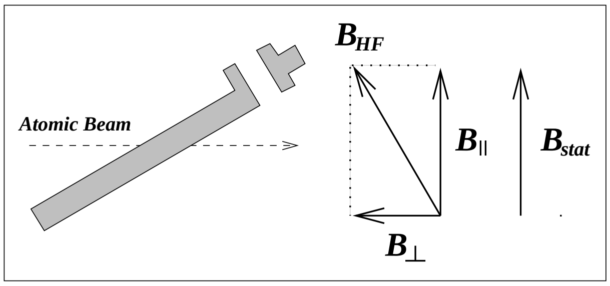

Fig. 4.5:
Band conductivity resonator with resonator rods that are tilted relative to the atomic beam axis and the static magnetic field. The HF-field consists of two components, one of which is parallel and one of which is perpendicular to the static magnetic field.

resonator and transferred to a balance mixer. The amplitude of the HF-field is monitored with a pick-up loop. The HF-signal induced in the loop is rectified by a diode and can be displayed by a voltmeter. From this pick-up part of the signal is coupled out and transferred to the balance mixer. If the length of the lines from balance mixer to the resonator rod and to the pick-up fulfill the condition $b - a = c + d$, the phase difference at the two inputs of the balance mixer will be 90^0 in the case of resonance. If the phase difference deviates from this ideal value, a correcting voltage generated by the balance mixer is used to tune the frequency of a voltage controlled oscillator (VCO) through a PID-regulator.

The band conductivity resonators with phase control proved to be very stable over the course of the measurements and they could be switched on and off without any problems. Without phase control the transitions performed significantly poorer. This can be see in the comparison of the efficiencies for the strong field transitions for deuterium in source and polarimeter (table 8.2). Of these two resonators only the one in the source was operated with phase control. The efficiencies measured for this transition are noticeably better than those for the unregulated one in the polarimeter. In the HERMES experiment all band conductivity resonators will be equipped with a phase control.

The fact that the frequency of the HF-field of a band conductivity resonator with phase control will shift during the warm-up phase due to this compensation is without consequence for the operation of the high frequency transition. The superposition of the static field with a gradient field leads to a widening of the resonance and thus creates a plateau in the resonance region (figure 5.4). As a result the transition can be operated efficiently over a sufficiently wide frequency band.

4.3.3 The Sextupole Magnet System

The separation of the beam atoms according to their magnetic moment in inhomogeneous magnetic fields goes back to W. Gerlach and O. Stern [113, 114].

In the Breit-Rabi polarimeter sextupole magnets are used to generate inhomogeneous magnetic fields. As opposed to the electrically excited sextupole in the source the ones in the polarimeter are permanent magnets made from a NdFeB alloy. Their magnetic field reaches a value of 1.43 T at the pole tips [115] (figure 4.6). The remanent field of the magnets is 1.13 T.

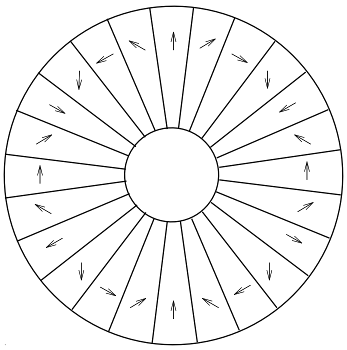

Fig. 4.6:
Cross section through a permanent sextupole magnet. The magnet consists of 24 trapezoid segments. The direction of the magnetization of a segment is rotated by 45^0 with respect to the radial direction relative to the neighbouring segment. The pole tip radius corresponds to the radius of the inner cylinder, it amounts to $12,5\,\mathrm{mm}$. The value of the magnetic field at the pole tip radius, the so-called pole tip field, is $1,43\,\mathrm{T}$.

A production based fill factor $\varepsilon = 0.98$ indicates the percentage to which the magnets are filled with the NdFeB alloy. The magnet system of the Breit-Rabi polarimeter consists of two sextupole magnets. The first magnet has a length of 70 mm, the second one is 110 mm. The drift length between the magnets is 135 mm which leads to a more effective separation of the states.

4.3.4 The Atomic Beam Detector

The atomic beam detection consists of three main components (figure 4.7): an atomic beam chopper, a quadrupole mass spectrometer and a data taking system. The atomic beam is periodically interrupted by the chopper before the detection by the mass spectrometer. The periodic structure of the measured signal generated in this way is used to distinguish between the atoms in the beam and the atoms from the rest gas in the detector chamber. The atoms from beam and rest gas are ionized in the formation volume of the mass spectrometer through collisions with thermally emitted electrons at 75 eV. They are then injected into the mass filter which separates the hydrogen or deuterium atoms from the rest gas atoms. After the mass filter the ions are accelerated to an energy of 2.1 to 2.5 keV and converted into an electron avalanche by a SEM. The electrons generate a charge pulse in the anode of the SEM that is further processed electronically.

The pulses from the SEM are first amplified by a fast amplifier, converted into normed NIM pulses using a discriminator with adjustable trigger threshold and then directed to the TRC module. This module can measure the time dependence of the counting rate, store it intermediately and further send it to the computer. To adjust the phase relation between the opening function of the chopper and the measurement cycles of the TRC module, each measurement cycle is started by a reference pulse from the chopper electronics. A detailed description of the electronic for the time resolved pulse counting can be found in [73, 116].

Figure 4.8 shows the result of such a time resolved counting rate measurement. The pulses from 100×4 chopper periods were added up and converted into the unit kHz. For both open and closed chopper four analysis windows each can be defined within which the mean counting

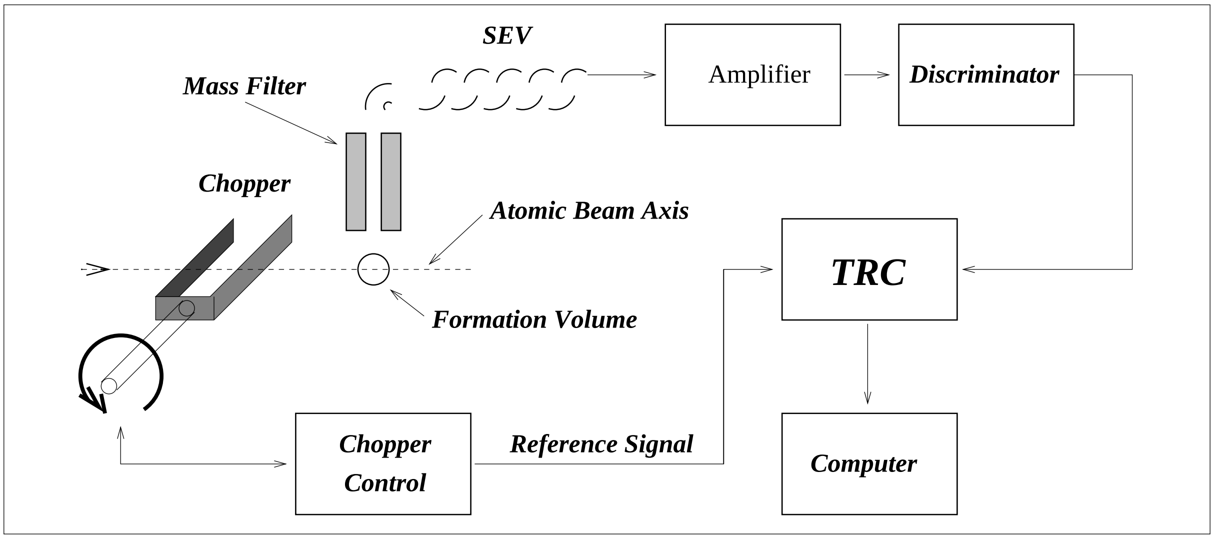

Fig. 4.7:
Scheme of the atomic beam detection with chopper, mass spectrometer, consisting of formation volume, mass filter and secondary electron multiplier (SEM), and electronic data taking system. TRC stands for **T**ime **R**esolving **C**ounter.

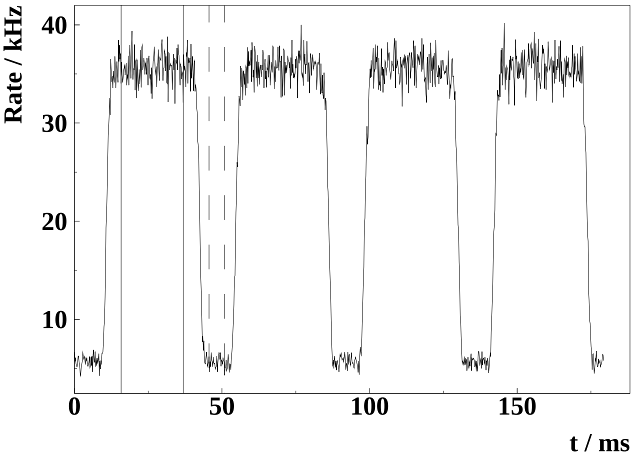

Fig. 4.8:
Opening function of the chopper measured by the TRC unit. Four chopper periods of $43,5\,\mathrm{ms}$ each are shown. The time resolution is $175\,\mu\mathrm{s}$. The vertical lines limit the analysis window, one for the open and one for the closed chopper. The measurement was performed with an atomic beam that effused from a storage cell. The high frequency transitions in the polarimeter were switched off, so that the beam counting rate was caused by the states $|\,1\,\rangle$ and $|\,2\,\rangle$. The effective length of the measurement is about $50\,\mathrm{s}$.

rates S_{open} and S_{closed} are determined as the mean value over the window. The difference of both gives a measure for the intensity of the atomic beam:

$$S_{beam} = S_{open} - S_{closed}. \tag{4.1}$$

The relative error of this difference depends on the relative errors of the measured counting rates as follows:

$$\frac{\Delta S_{beam}}{S_{beam}} = \sqrt{\left(\frac{S_{open}}{S_{open} - S_{closed}} \cdot \frac{\Delta S_{open}}{S_{open}}\right)^2 + \left(\frac{S_{closed}}{S_{open} - S_{closed}} \cdot \frac{\Delta S_{closed}}{S_{closed}}\right)^2}. \tag{4.2}$$

The relative error of the beam signal for signal to background ratios $R = S_{beam}/S_{closed} \ll 1$ is enlarged in proportion to $1/R$ due to the difference $S_{open} - S_{closed}$ in the denominator under the square root. In signal to background ratios of $R \gg 1$ the second term under the square root can be disregarded which leads to

$$\frac{\Delta S_{beam}}{S_{beam}} \approx \frac{\Delta S_{open}}{S_{open}}, \tag{4.3}$$

This means that the relative error of the beam signal is largely determined by the relative error of the counting rate with open chopper and that the relative error of the background counting rate $\Delta S_{closed}/S_{closed}$ may be disregarded. The signal to background ratio for the measurements is sufficiently good due to the excellent vacuum in the detector chamber. Therefore the ratio of open to closed time can be set strongly in favor of the open time of the chopper (figure 4.8). This was realized by using a geometry in the shape of a tuning fork (figure 4.7). The statistics of the measurement of S_{open} is improved and thus the error on S_{beam} is reduced.

5 High Frequency Transitions

It is the task of a high frequency transition to exchange the occupation of two hyperfine structure components in the atomic beam. It's functioning is based on the interaction of the beam atoms with an electromagnetic high frequency field and a superimposed static magnetic field. The frequency of the HF-field is determined through the energy difference of the involved hyperfine states in the Breit-Rabi diagram (figures 1.2 and 2.2) for a given static magnetic field. A complete exchange of occupation is achieved in adiabatic high frequency transitions, in which a gradient field is superimposed over the static field.

5.1 Adiabatic High Frequency Transitions

5.1.1 Classic Treatment

The processes in a high frequency transition are illustrated in figure 5.1. A magnetic moment **M** – more specifically: the expectation value of the magnetization of an ensemble – precesses under the influence of an external magnetic field B_z around the quantization axis given by the direction of the field (figure 5.1 a.). the description of the interaction with the HF-field can be simplified by using a system that rotates around the quantization axis with the Larmor frequency [95]. In such a system the external magnetic field vanishes and the precession of the magnetic moment **M** stops (figure 5.1 a.). A resonant high frequency field that is perpendicular

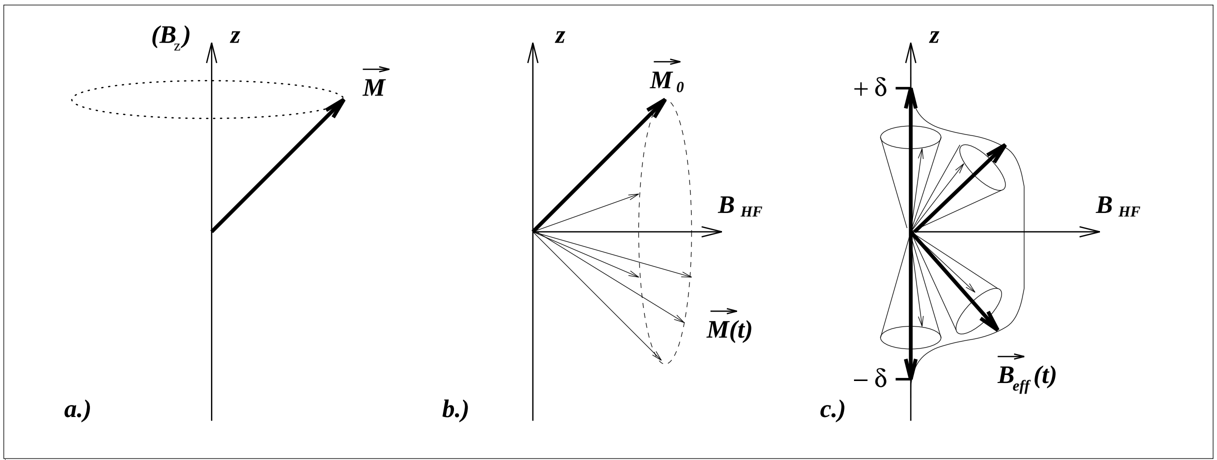

Fig. 5.1:
The functionality of an adiabatic *Abragam-Winter Transition*: a.) Precession of the magnetic moment in a magnetic field B_z. b.) Precession in a system that rotates around the resonant high frequency field B_{HF} with the Larmor frequency. c.) Precession in an adiabatic Transition in the co-rotating system.

to the static field can be decomposited into two counter-rotating fields, where one, fast rotating component, averages out and the other one appears as a constant magnetic field B_{HF} in the co-rotating system. The magnetic moment is at rest in this system without HF-field and under the influence of B_{HF} it starts to precess around this field (figure 5.1 b.). The precession angle after the transition depends on the interaction time of the beam atoms with the high frequency field. As the length of the interaction region is fixed for apparative reasons, the precession angle depends on the flight time of the beam atoms through the high frequency transition and therefore on the velocity of a beam atom. If the velocity of a beam atom matches the length of the high frequency transition, the magnetic moment is rotated by exactly 180^0. An atom whose velocity deviates from the ideal velocity, will leave the high frequency transition with a precession angle that differs from 180^0. For this reason it will be transformed incompletely into the other spin state with a probability that depends on this angle. As the velocities of the beam atoms in general follow a modified Maxwell distribution (6.18) the precession angle distribution will even be smeared for an optimal matching of interaction length and average beam velocity. An exact exchange of the occupations of two hyperfine structure components is not possible with this method. Due to the Maxwell distribution a theoretical limit of about 0.76 exists for the exchange efficiency of such a transition [117].

Using a high frequency transition is called method of *exact resonance*. It is used for a determination of the resonance frequency that is as precise as possible. This is for example the case for the experiments of I. Rabi [118].

In the construction of atomic beam sources high frequency transitions are of interest that induce an exchange of the involved states as completely as possible. High exchange efficiencies of the high frequency transitions mean large and well known analyzing powers for the Breit-Rabi polarimeter. The achievement of an exchange that is as complete as possible is at least for some of the used high frequency transitions a prerequisite for a precise calibration of the Breit-Rabi polarimeter.

Complete exchanges can be reached using adiabatic high frequency transitions following A. Abragam and J.M. Winter [119]. For transitions of this type the static magnetic field is superimposed with an additional gradient field. The magnetic field increases on the way through the transition from $B_0 - \delta$ to a value of $B_0 + \delta$ and decreases again accordingly. In a system that rotates with the frequency of the HF-field (figure 5.1c.) the magnetic moment initially experiences for a negative gradient a magnetic field parallel to the quantization axis of magnitude $+\delta$. After entry into the HF-field region a component slowly arises that is perpendicular to the quantization axis. As a result of the gradient field the effective magnetic field B_{eff} composed of the two above mentioned components is rotated *slowly* or *adiabatically* along the solid line downward until after leaving the HF-region it is antiparallel to the quantization axis and has the value $-\delta$. The magnetic moment permanently sees an effective magnetic field while flying through the transition. Therefore it follows this field on a narrow precession cone as long as the change in B_{HF} is sufficiently slow in comparison to the Larmor precession. As in a high frequency transition like this it is not the spin directly but rather an effective quantization axis that is rotated. This rotation of 180^0 is almost complete and practically independent of the velocity of the beam atoms. With an adiabatic high frequency transition exchange efficiencies very close to 100 % can be achieved.

5.1.2 Quantummechanic Treatment

The effect of an adiabatic high frequency transition can be understood completely with the classic treatment discussed above. However, the quantummechanic treatment following [120] gives a very graphic description of the adiabacity of a high frequency transition and also allows it's calculation. For simplicity a simple two-niveau-system is discussed that is equivalent to a spin-1/2-system and can be treated analytically .

A spin-1/2 particle can exist in two states that here are labelled as $|1\rangle$ and $|2\rangle$. The corresponding energy eigenvalues E_1 and E_2 depend on the external field as is shown in figure 5.2.a. The transformation into the co-rotating system leads to a global lowering or raising of the energy eigenstates (figure 5.2.b).

The interaction with a high frequency field can be treated as a perturbation [92], where the Hamilton operator has the form

$$H = H_0 + W \tag{5.1}$$

H_0 is the unperturbed Hamilton operator in the co-rotating system and W is the perturbation that results from the HF-field. The perturbed Hamiltonian is no longer diagonal and the states $|1\rangle$ and $|2\rangle$ are no longer eigenstates of the system, as the non-diagonal elements W_{12} and W_{21} of the perturbation matrix do not vanish. However, the eigenstates of the perturbed system can be expressed as a linear combination of unperturbed states:

$$\begin{aligned} |+\rangle &= \cos\varphi\,|1\rangle + \sin\varphi\,|2\rangle \\ |-\rangle &= \sin\varphi\,|1\rangle - \cos\varphi\,|2\rangle\,, \end{aligned} \tag{5.2}$$

where the mixing angle φ depends on the static field B and the amplitude of the HF-field. The energy eigenvalues of these states in the co-rotating system are shown as solid lines in the modified Breit-Rabi diagram (figure 5.2.c). The energy niveaus do not cross anymore but repel one another, leading to an energy barrier.

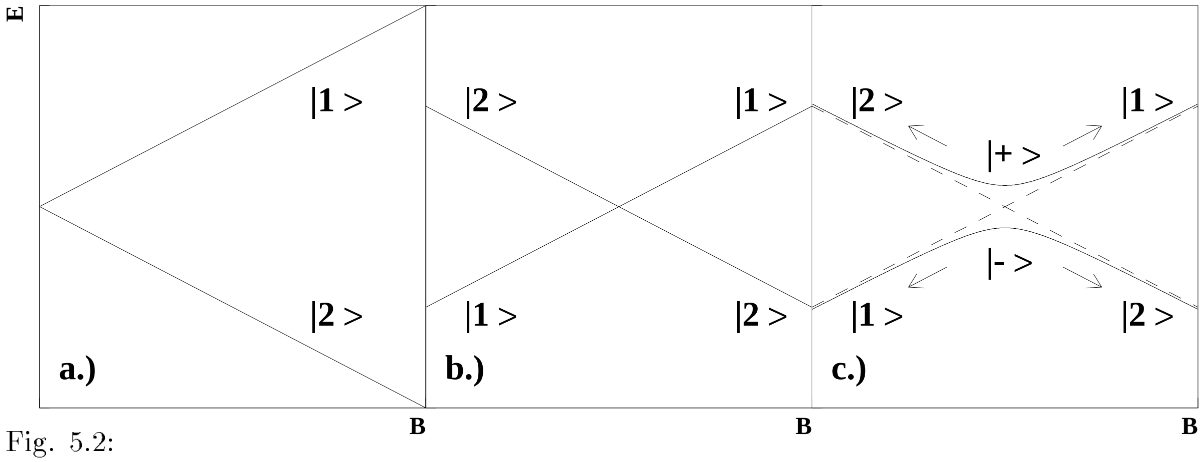

Fig. 5.2:
Quantummechanic treatment of adiabatic two-niveau transition: a.) Breit-Rabi diagram of a two-niveau system. b.) Breit-Rabi diagram in a co-rotating system. c.) Effect of the interaction with the high frequency field on the Breit-Rabi niveaus in the co-rotating system.

In the resonance field both niveaus reach their closest approach, the mixing of the states $|1\rangle$ and $|2\rangle$ becomes maximal and $\varphi = 45°$ applies. The behaviour of the states upon moving away from the resonance field is remarkable. The upper branch which belongs to the state $|+\rangle$ approaches for large fields asymptotically the state $|1\rangle$ at ($\varphi \to 0°$), while for smaller fields it approaches the state $|2\rangle$ ($\varphi \to 90°$).

Passing through the modified Breit-Rabi diagram from right to left, that is letting the magnetic field drop, just relates to the flight of an atom through an adiabatic transition where the static field has a negative gradient. A particle that at the beginning is in the state $|1\rangle$ will stay on the upper branch, as this is an eigenstate of the coupled system, and end as a particle in state $|2\rangle$.

If this pass happens too fast, the particle can migrate from the upper branch to the lower one and the particle leaves the transition in the same state in which it entered. This non-adiabatic transition probability gets smaller, the larger the barrier between upper and lower branch becomes. It can be calculated analytically following [120]:

$$p = \mathrm{e}^{-2\pi\kappa} \qquad \kappa = \left|\frac{\mu_J B_{HF}^2}{2\dot{B}\hbar}\right|. \tag{5.3}$$

This treatment can be transferred to systems with more than two states, however, in this case numerical methods are necessary to calculate the transition probabilities. Generally in these cases one has to require that in (5.3) $\kappa \gg 1$, that is:

$$\mu_J B_{HF}^2 \gg 2\dot{B}\hbar. \tag{5.4}$$

This inequality is called adiabatic condition. Essentially it's statement is that for the adiabatic operation of a high frequency transition an amplitude of the HF-field is needed that is as large as possible. With increasing HF-amplitude the efficiency of a transition asymptotically approaches the saturation value 1.

5.2 Strong Field Transitions for Hydrogen

High frequency transitions between different Zeeman-multiplets are for historical reasons called 'strong field transitions', because they were first described for strong static magnetic fields. They induced occupation changes that change the total angular momentum ($\Delta F = \pm 1$). However, they are not limited to the region of strong fields. In fact these transitions can be operated easier in the region of weak fields, as the necessary magnetic fields are smaller and therefore easier to realize.

Strong field transitions are divided into σ-transitions and π-transitions. σ-transitions follow the selections rule $\Delta m_F = 0$. In this case the HF-field has to oscillate in parallel to the static field. π-transitions follow the selection rule $\Delta m_F = \pm 1$ and the HF-field is perpendicular to the static field. Therefore the transition SFT 1-4 in hydrogen is a π-transition while the transition SFT 2-4 is a σ-transition.

The left side of figure 5.3 shows the resonances in the Breit-Rabi diagram for these two possible strong field transitions at the same frequency[5] as fat lines that connect the concerned hyperfine states. As both lines represent the same energetic distance, the resonance condition is fulfilled for different static magnetic fields.

The right hand side of figure 5.3 shows the resonance frequencies of the two possible strong field transitions as a function of the external magnetic field.

Before the installation in the vacuum chamber the band conductivity resonator for the strong field transition is tuned to a fixed resonance frequency of 1425 MHz that cannot be changed anymore from the outside. For the tuning of the transitions the storage cell between atomic beam source and polarimeter (figure 1.4) is moved out of the beam using a linear manipulator. This mode of operation of the apparatus is also used in the efficiency measurements (figure 8.1). The static field of the high frequency transition is varied while the high frequency is switched on. The resonances are marked by a drop in the measured beam intensity in the atomic beam detector (figure 5.4). The atomic beam source produces an atomic beam that after the first sextupole magnet consists mostly of the states $|1\rangle$ and $|2\rangle$. If the strong field transition is not in resonance, theses states are also focused in the sextupole system of the polarimeter and the atomic beam detector measures an intensity which is proportional to the sum of the intensities for the states $|1\rangle$ and $|2\rangle$. If the strong field transition between the sextupole systems fulfills a resonance condition, one of the upper states will be exchanged for a state $|4\rangle$. Because this one is not occupied any longer after the sextupole magnet in the source, the beam behind the transition consists of two states of which only one will be focused in the sextupole system of the polarimeter. The other in the high frequency transition to $|4\rangle$ transformed state is removed

[5] For reasons of a clearer presentation a frequency of 1734 MHz was chosen instead of the actual operation frequency of 1425 MHz.

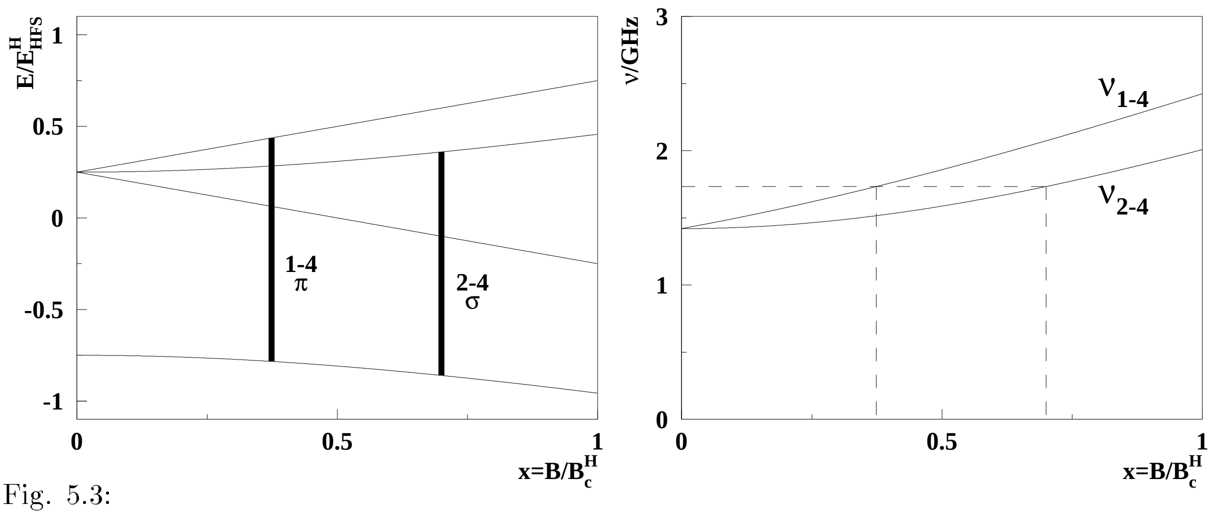

Fig. 5.3:
Resonances of a strong field transition for atomic hydrogen shown for a frequency of 1734 MHz. Left: Representation of the Transitions in the Breit-Rabi diagram. Right: Resonance frequencies as function of the external magnetic field. The dashed lines indicate the resonance condition.

from the beam and the intensity measured by the atomic beam detector is reduced to about half.

The top plot of figure 5.4 illustrates how the intensity of the atomic beam varies as a function of the static field for the strong field resonator if the high frequency is switched on. The resonance condition for the SFT 2-4 is fulfilled for both signs of the static field, therefore the resonance of the transition 2-4 appears once on the left and once on the right side. The gradient of the field is relatively weak, $70\,\mu\mathrm{T\,cm^{-1}}$, which leads to narrow resonances. The gradient field that is superimposed over the static field also leads to a shift of the zero point which moves all resonances somewhat further to the right. As expected, in case of a resonance the beam signal drops to about half the counting rate without resonance.

In the middle, close to zero field, an additional resonance appears, which using the lower plot can be unambiguously identified as resonance of the transition 1-4. For this second measurement additionally the weak field transition WFT 1-3 in the source was switched on (figure 8.1 and chapter 5.4). As a result, the state $|1\rangle$ is already emptied before the strong field transition and the signal is already reduced to half of the value without high frequency transition without a resonance condition being fulfilled in the strong field transition. If the resonance condition

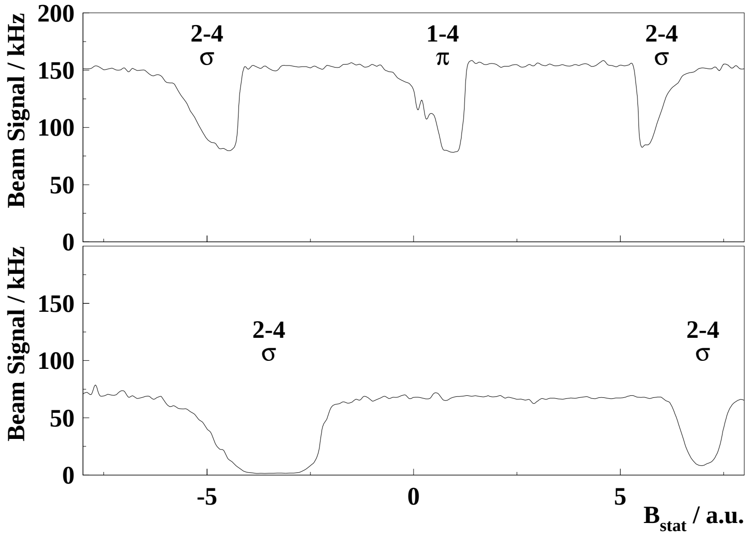

Fig. 5.4:
Identification of the strong field transition resonances for hydrogen. Top: The gradient of the field is about $70\,\mu\mathrm{T\,cm^{-1}}$. Bottom: For this measurement additionally the weak field transition WFT 1-3 is switched on in the source, therefore the resonance of the transition 1-4 vanishes. The gradient of the field is about $350\,\mu\mathrm{T\,cm^{-1}}$; this leads to a broadening of the resonance on the left relative to the upper plot.

for the SFT 2-4 is fulfilled, also the state $|2\rangle$ is depopulated and the signal measured by the atomic beam detector is reduced to close to zero. A SFT 1-4 has no effect on an atomic beam that only contains the states $|2\rangle$ and $|3\rangle$, the corresponding resonance vanishes. The remaining intensity in the plateau region of SFT 2-4 on the left side for active WFT 1-3 is only 0.3 % of the intensity without high frequency transition. This leads to the conclusion that the transitions SFT 2-4 and WFT 1-3 both are operating with an efficiency of at least 99.7 %. This can be concluded without any knowledge of the transmissions in the sextupole system (chapter 8.2). If this almost complete depopulation is not reached, the inefficiency cannot be easily related to one of the transitions. The efficiencies of these two high frequency transitions will be confirmed in a different way in chapter 8.

For the measurement in the lower figure a stronger field gradient of about $350\,\mu\mathrm{T\,cm}^{-1}$ was used. It can clearly be seen that the resonance is significantly broadened on the left side and that it shows a large plateau region. The resonance on the right side gets worse, indicating that the sign of the gradient field influences the efficiency of the transition.

5.3 Medium Field Transitions for Hydrogen

With a medium field transition occupation changes *within* a Zeeman-multiplet are induced. They were for the first time successfully used for occupation changes in the hyperfine structure of a polarized sodium atom beam [121]. The first medium field transitions for hydrogen were developed together with the Breit-Rabi polarimeter [50]. A medium field transition for deuterium for an atomic beam source at the IUCF in Bloomington is described in [122].

In the case of the hydrogen atom there are only two possible resonances which lead to the occupation changes 1-2 and 2-3 within the triplet with $F = 1$. The transition is operated in the lower medium field region, but close enough to B_C to be able to separate these two resonances well enough. However, there is no use to operate the transition 1-2 on its own, as the following sextupole magnet is not sensitive to this transition.

Nevertheless through one medium field transition two high frequency transitions can be operated, labelled MFT 1-3 and MFT 2-3. Both medium field transitions are operated at a frequency of 68.2 MHz. For reasons of clarity, a higher frequency of 308 MHz was chosen for figure 5.5.

The MFT 2-3 is in principle not different from the already discussed strong field transitions. For a given frequency of the HF-field the corresponding resonant static field is applied, superimposed by a gradient field. This is illustrated in figure 5.5. In adjusting the gradient field it must be considered that the field region passed through in the medium field transition does not include the resonance for the transition 1-2, so that the transition 2-3 is in fact the only one happening. For MFT 1-3 the static field is shifted in such a way that due to the superimposed gradient field both resonance conditions are fulfilled.

It is recommended for this purpose to increase the gradient field somewhat relative to MFT 2-3, so that the traversed field region is broadened, as is indicated in figure 5.5 through the somewhat longer fat line. For this setting of the fields both resonances are passed through after one another, that is separated in space and time. Therefore the effect of MFT 1-3 on the hyperfine occupation in the atomic beam depends on the direction of the gradient field. For a negative gradient, the resonance for the transition 1-2 is traversed first and then the transition

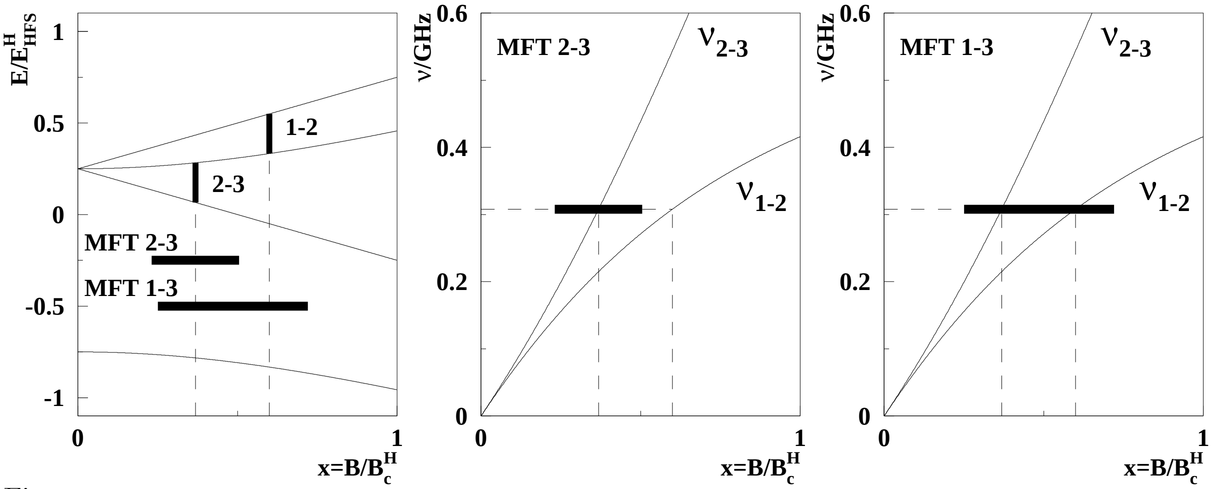

Fig. 5.5:
Resonances of a medium field transition for hydrogen depicted for a frequency of 308 MHz. Left: Representation of the occupation changes in the Breit-Rabi diagram. Middle and right: Resonance frequencies as a function of the external magnetic field. The resonance conditions for the transformations 1-2 and 2-3 are indicated by the dashed lines. The fat horizontal lines indicate the field region passed through as a result of the gradient field.

2-3 is traversed and vice versa for a positive gradient. The effect of a medium field transition for both gradient directions can be expressed through occupation tuples:

$$\text{neg.}: \begin{pmatrix} n_1 \\ n_2 \\ n_3 \\ n_4 \end{pmatrix} \xrightarrow{1\leftrightarrow 2} \begin{pmatrix} n_2 \\ n_1 \\ n_3 \\ n_4 \end{pmatrix} \xrightarrow{2\leftrightarrow 3} \begin{pmatrix} n_2 \\ n_3 \\ n_1 \\ n_4 \end{pmatrix} \quad \text{pos.}: \begin{pmatrix} n_1 \\ n_2 \\ n_3 \\ n_4 \end{pmatrix} \xrightarrow{2\leftrightarrow 3} \begin{pmatrix} n_1 \\ n_3 \\ n_2 \\ n_4 \end{pmatrix} \xrightarrow{1\leftrightarrow 2} \begin{pmatrix} n_3 \\ n_1 \\ n_2 \\ n_4 \end{pmatrix}, \tag{5.5}$$

In this representation it is apparent that in none of the two cases the effect of the MFT 1-3 is an exchange of the states $|1\rangle$ and $|3\rangle$, but that all three states in the triplet are exchanged cyclically in one or the other direction. Further it may be noted that only for a negative gradient field the state $|1\rangle$ is transferred from the two upper states into the two lower ones. Thus it can be removed from the atomic beam by the sextupole magnet in this case only. Therefore in a polarimeter a MFT 1-3 must be operated with a negative gradient. A positive gradient would effectively lead to a MFT 2-3. The label MFT 1-3 is sensible in as much as the transition

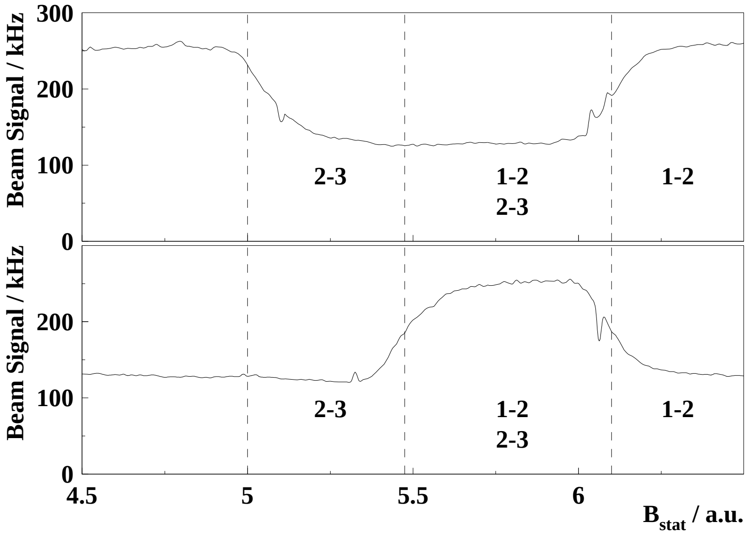

Fig. 5.6:
Identification of the resonances for a medium field transition for hydrogen. In the upper figure the medium field transition was switched on by itself, in the lower figure also the weak field transition WFT 1-3 in the source was operational. The dashed lines separate the regions in which only the transition 2-3 or 1-2 occur and the region where both transitions occur simultaneously in the medium field transition.

together with the following sextupole magnet removes the state $|1\rangle$ from the beam and instead focuses the original state $|3\rangle$.

As in the strong field transition the medium field transition is adjusted through variation of the static field for a given frequency and measurement of the beam signal. If a resonance condition is fulfilled, the signal drops to about half of the signal outside the resonance (figure 5.6 top). However, it is not possible to decide only from this measurement whether the medium field transition is operating as MFT 1-3 or as MFT 2-3, as the reduction of the signal is a result of the transition 2-3 alone. For this purpose an second high frequency transition in front of the medium field transition is necessary, for example the WFT 1-3 in the atomic beam source. It's influence on the measurement can again be expressed through occupation tuples.

If the medium field transition operates as MFT 2-3, the following scheme may be obtained for an active WFT 1-3 under the assumption of ideal behaviour of the sextuple magnets and the high frequency transitions:

$$\begin{pmatrix}1\\1\\1\\1\end{pmatrix} \xrightarrow{\text{sextupole}} \begin{pmatrix}1\\1\\0\\0\end{pmatrix} \xrightarrow{\text{WFT}1\leftrightarrow 3} \begin{pmatrix}0\\1\\1\\0\end{pmatrix} \xrightarrow{2\leftrightarrow 3} \begin{pmatrix}0\\1\\1\\0\end{pmatrix} \xrightarrow{\text{sextupole}} \begin{pmatrix}0\\1\\0\\0\end{pmatrix} \longrightarrow S = 1. \tag{5.6}$$

The resonance of the transition 2-3 in the medium field transition has no effect on the atomic beam prepared by the WFT 1-3, because it just exchanges the two still occupied states $|2\rangle$ and $|3\rangle$. If the transition 1-2 occurs in the medium field transition as well and the high frequency transition operates as MFT 1-3, the following scheme is arrived at:

$$\begin{pmatrix}1\\1\\1\\1\end{pmatrix} \xrightarrow{\text{sextupole}} \begin{pmatrix}1\\1\\0\\0\end{pmatrix} \xrightarrow{\text{WFT}1\leftrightarrow 3} \begin{pmatrix}0\\1\\1\\0\end{pmatrix} \xrightarrow{1\leftrightarrow 2} \begin{pmatrix}1\\0\\1\\0\end{pmatrix} \xrightarrow{2\leftrightarrow 3} \begin{pmatrix}1\\1\\0\\0\end{pmatrix} \xrightarrow{\text{sextupole}} \begin{pmatrix}1\\1\\0\\0\end{pmatrix} \longrightarrow S = 2. \tag{5.7}$$

Thus the MFT 1-3 just compensates the effect of the WFT 1-3 and the beam signal increases again to the value it has between the sextupole magnets without the high frequency transitions. Figure 5.6 illustrates this increase in conjunction with transition 1-2 in the lower plot. If the MFT were operated with positive field gradient the order of the transitions 1-2 and 2-3 would be switched and this increase would vanish.

Following the resonance curves in figure 5.6 from left to right, for a small static field the signal without WFT drops to half its value, while with WFT it remains constant. In this region only the transition 2-3 of the medium field transition works. Thus a static field is chosen in this region for the operation of the MFT 2-3. For a stronger static field due to the superimposed gradient field also the resonance condition for the transition 1-2 is fulfilled, while the transition 2-3 is active as well and the signal increases in the lower plot. In the upper plot the beam signal stays constant at half the maximal value. In this region of the static field the medium field transition operates as MFT 1-3. After a further increase of the static field the resonance condition for the transition 2-3 is not fulfilled any longer, the signal in the upper plot increases again and the signal in the lower plot decreases. The transition 1-2 is still active in this region , but it is not visible any longer as the sextupole magnets are not sensitive to a sole exchange of the states $|1\rangle$ and $|2\rangle$, if one neglects transmission corrections (chapter 8.2 and 9).

5.4 Weak Field Transitions

The weak field transition WFT 1-3 for hydrogen that is used in the atomic beam source is operated at a much lower frequency of 12.6 MHz compared to the medium field transition and thus also at a far lower static field. In the medium field transition, the transitions 1-2 and 2-3 which are normally spatially separated begin to move together as a result of a weak field and thus practically happen at the same point in space. The effect of an ideal and adiabatically operated WFT 1-3 on a hydrogen beam is and exchange of the states $|\,1\,\rangle$ and $|\,3\,\rangle$, independant of the sign of the field gradient:

$$\begin{pmatrix} n_1 \\ n_2 \\ n_3 \\ n_4 \end{pmatrix} \xrightarrow{\text{WFT } 1-3} \begin{pmatrix} n_3 \\ n_2 \\ n_1 \\ n_4 \end{pmatrix}. \tag{5.8}$$

In general a weak field transition changes the sign of the magnetic quantum number m_F for all states that are present in the atomic beam following the selection rule $m_F \leftrightarrow -m_F$. Thus in a weak field transition transitions also occur, in which the magnetic quantum number changes by more than one unit. These transitions are prohibited for single photon exchange with the HF-field, and therefore must be the product of multiple quantum transitions. In WFT 1-3 for hydrogen two photons are exchanged.

The most remarkable effect of WFT 1-3 on an atomic beam (5.8) is the fact that it behaves neither like a medium field transition with negative gradient nor like one with positive gradient. If the WFT 1-3 in the source is replaced with a medium field transition following (5.5), and under the assumption that the states $|\,3\,\rangle$ and $|\,4\,\rangle$ are entirely removed from the beam in the sextupole magnet, these occupations may be seen for the atomic beam:

$$\text{neg.Grad.}: \quad \xrightarrow{sextupole} \begin{pmatrix} n_1 \\ n_2 \\ 0 \\ 0 \end{pmatrix} \xrightarrow{1\leftrightarrow 2} \begin{pmatrix} n_2 \\ n_1 \\ 0 \\ 0 \end{pmatrix} \xrightarrow{2\leftrightarrow 3} \begin{pmatrix} n_2 \\ 0 \\ n_1 \\ 0 \end{pmatrix} \tag{5.9}$$

$$\text{pos.Grad.}: \quad \xrightarrow{sextupole} \begin{pmatrix} n_1 \\ n_2 \\ 0 \\ 0 \end{pmatrix} \xrightarrow{2\leftrightarrow 3} \begin{pmatrix} n_1 \\ 0 \\ n_2 \\ 0 \end{pmatrix} \xrightarrow{1\leftrightarrow 2} \begin{pmatrix} 0 \\ n_1 \\ n_2 \\ 0 \end{pmatrix}. \tag{5.10}$$

The assumption that the WFT 1-3 behaves like a medium field transition with negative gradient and therefore produces an occupation following (5.9) in the atomic beam can be excluded due to the measurements shown in figure 5.4. Otherwise in the lower measurement the resonances of the transition 2-4 would vanish instead of the resonance of the transition 1-4.

A medium field transition with positive gradient does produce an atomic beam in which the same states are occupied as after a weak field transition[6], but a comparison between (5.8) and (5.10) shows that the indices of both states in the beam after a medium field transition are just switched relative to a weak field transition. The indices indicate in which state the atoms were during their flight through the sextupole magnet in the source. Therefore the main difference between the two transitions is the *history* of the states in the atomic beam. This difference can only be of importance if the states $|\,1\,\rangle$ and $|\,2\,\rangle$ are focused differently in the first sextupole magnet.

In chapter 8 and 9.1 it will be shown that particularly the history of the states in the first sextupole is an important correction to the measurements of the efficiency of the high frequency

[6] Note that a medium field transition in a source has to be operated with a positive gradient to produce and occupation analogous to a WFT 1-3, while in the polarimeter a negative gradient is needed to operate a medium field transition as MFT 1-3 (5.5).

transitions, which may not be neglected. The assumption that WFT 1-3 behaves like a medium field transition with positive gradient leads to contradictions when the consistency method for the analysis of the efficiency measurements from chapter 8.6 is applied: There are no consistent solutions. On the other hand consistent solutions are obtained with very small errors from the treatment of WFT 1-3 according to (5.8) (chapter 8.7). This leads to the conclusion that this description of the effect of WFT 1-3 on the atomic beam is correct within the error margins.

The effect of the WFT 1-3 on an atomic beam can only be described by (5.8) if it is operated in a sufficiently weak field. For stronger static fields the effect of a weak field transition has to steadily merge into the effect of a medium field transition with positive or negative gradient field, depending on the choice of the gradient field. The behaviour of a high frequency transition in this transition region between weak and medium field transition is highly complex and experimentally only difficult to quantify. This was described for the case of deuterium in [123].

In the framework of this thesis the WFT 1-3 in the source was on the one hand used to produce a nuclear spin polarized atomic beam in strong magnetic fields. On the other hand it was also used for the identification of the resonances of the medium field transition in the polarimeter (figure 5.6) and for its calibration (chapter 8.4). During the course of the HERMES experiment a strong field transition SFT 1-4 or SFT 2-4 in the polarimeter will be used for this purpose (chapter 8.8). At the time of this writing this was not yet possible in the described test setup. The static fields for the strong and medium field transitions in the polarimeter were produced by the same magnet (figure 1.4) which prohibited a simultaneous operation of both transitions.

5.5 High Frequency Transitions for Deuterium

In the deuterium measurements in both the Breit-Rabi polarimeter and the atomic beam source exclusively strong and medium field transitions were used. In the case of strong field transitions band conductivity resonators with relative to the beam axis tilted resonator rods were used for the first time (figure 4.5). With these π- and σ-transitions could both be operated equally well. The band conductivity resonators in source and polarimeter were operated at a frequency of 419 MHz.

As in the case of the strong field transitions for hydrogen, the transitions are adjusted by measuring the beam intensity as a function of the static field above the resonator for active high frequency. Figures 5.7 shows the result of such a measurement with the strong field transition in the polarimeter. Four resonances are clearly visible. As only the three upper of the six hyperfine states of the deuterium are focused in a sextupole magnet and a simple transition transfers only one of these states into a defocussed state, the beam intensity in the resonance case drops only to 2/3 of the intensity without the resonance.

The transitions 2-5 and 3-6 are subject to the same resonance condition, so that in this case the beam intensity decreases to less than 2/3 of the intensity outside of the resonances. However, the transition 3-6 is a difficult transition according to the nomenclature following [124], because the transition's amplitude decreases proportionately to $1/x^2$. For this reason the intensity of the atomic beam does not drop to 1/3 of the intensity outside the resonances. This transition was not used for the measurements in the framework of this thesis. The other three transitions SFT 1-6, SFT 2-6 and SFT 3-5 were used both in the source to prepare different polarization states in the atomic beam (see table 4.1) and in the Breit-Rabi polarimeter.

Though a medium field transition in deuterium the three transitions 1-2, 2-3 and 3-4 can be induced. Similar to a medium field transition in hydrogen three sensible medium field transitions can be operated through the combination of these transitions. In a MFT 3-4 only the transition

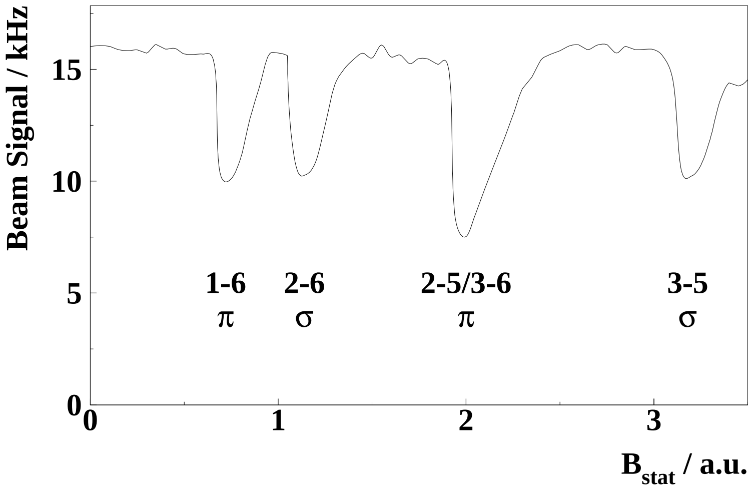

Fig. 5.7:
Identification of the resonances of a strong field transition for deuterium in the polarimeter. In contrast to the hydrogen transitions the signal in the region of the resonances drops only to 2/3 of the value outside the resonances. The π-transitions SFT 2-5 and SFT 3-6 operate for the same field and therefore lead to a decrease of the signal to a value below 2/3. This resonance was not used in the polarization measurements.

3-4 is functioning, in MFT 2-4 it is the transitions 2-3 and 3-4 and in a MFT 1-4 all three transitions operate one after the other. Because the medium field transition is used for the analysis of the polarization, it has to be operated with a negative field gradient.

Out of the three possible medium field transitions for deuterium only the transitions MFT 2-4 and MFT 3-4 were used for the polarization measurements. Together with the three strong field transitions the necessary number of five high frequency transitions is available for the measurement of the polarization of the atomic deuterium beams. In principle a MFT 1-4 could be used as well, however, it's effect on the atomic beam could not yet be quantified experimentally (chapter 8.5).

As in the case of medium field transitions for hydrogen, also for deuterium the adjustment of the medium field transitions relies on the use of additional transitions before the medium field transition. This follows from the decrease of the beam signal in the upper plot of figure 5.8 to 2/3 through the transition 3-4 alone. The region in which additionally the transition 2-3 is present can be made visible through a decrease of the signal to 1/3 with the help of a SFT 3-5 before the medium field transition (figure 5.8 bottom). A region in which the medium field transition can be functioning as MFT 1-4 is not apparent in figure 5.8. In this region the signal would drop to 1/3 if SFT 2-6 is switched on. For this high frequency transition to work the field gradient would have to be increased.

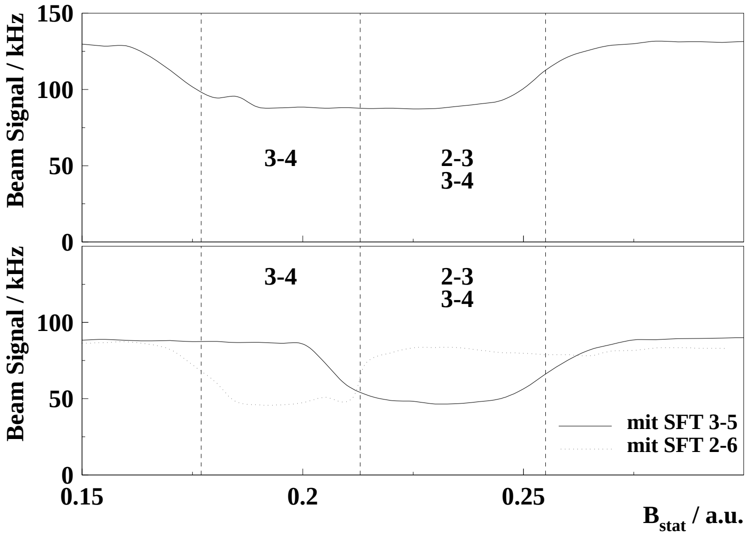

Fig. 5.8:
Identification of the resonances of a medium field transition for deuterium. In the upper figure the medium field transition switched on by itself. In the lower figure also SFT 3-5 or SFT 2-6 were switched on in the source. The dashed line separates regions in which either the transition 3-4 alone or the two transitions 2-3 and 3-4 are operational.

6 Monte Carlo Simulation of Sextupole Magnet Systems

It is the exact description of the effect of sextupole magnets on an atomic beam which provides the foundation for the calculation of corrections. These corrections must be given consideration as a result of not ideal sextupole magnet behaviour during polarisation and efficiency measurements. This leads in particular to the question with which probability an atom, that is emitted by a source, reaches a target as determined by the apparatus, for example the sensitive area of the particle beam detector, depending on its hyperfine state and speed. While it is possible in part to determine these so called transmission probabilities during the experiment (chapter 9), it is nonetheless necessary to perform Monte-Carlo-Simulations to calculate trajectories. The fundamentals of these will be addressed in this chapter.

6.1 Trajectories in Sextupole Magnets

The field distribution within a Sextupole magnet can be calculated using, [125]. The value of the magnetic field is given as:

$$B\left(r\right) := \left|\vec{B}\left(r\right)\right| = \frac{3}{2}J\left(\frac{r}{r_{pt}}\right)^2\left[1-\left(\frac{r_{pt}}{r_a}\right)^2\right]\frac{\sin\left(4\pi\varepsilon/M\right)}{4\pi/M} \tag{6.1}$$

J describes the magnetization, that is to say the remanent magnetic field, r_{pt} the internal radius, also called the pole tip radius, r_a describes the external radius, M the number of segments which comprise the magnets (figure 4.6) and ε is a factor describing to which degree the magnet is comprised of magnetized material.

Important for the calculation of trajectories is that a sextupole magnet, in respect to the magnetic field, has a completely rotation symmetric shape and that the value of the field rises quadratically with the distance r from the magnetic axis, the field gradient being proportional to r:

$$B\left(r\right) = B_{pt}\cdot\frac{r^2}{r_{pt}^2} \qquad \frac{\partial B}{\partial r} = 2B_{pt}\cdot\frac{r}{r_{pt}^2}. \tag{6.2}$$

B_{pt} describes the pole tip field, or rather the field at the tip of the pole radius. Since the value of the field within a sextupole magnet is only dependant upon r, it is possible to describe the energy affecting an atom in the state $|\,i\,\rangle$ and with a magnetic momentum of $\mu_{|\,i\,\rangle}$ as follows:

$$\mathbf{F}_i = -\mathrm{grad}_r U_i = -\frac{\partial U_i}{\partial r}\mathbf{e}_r = -\frac{\partial U_i}{\partial B}\cdot\frac{\partial B}{\partial r}\mathbf{e}_r = -\mu_{|\,i\,\rangle}(B)\frac{\partial B}{\partial r}\mathbf{e}_r. \tag{6.3}$$

U represents the potential in which an atom finds itself as a result of its magnetic momentum under the influence of a magnetic field. These potentials are given by the energy eigenvalues of the different hyperfine states (2.6) and (2.23. It is to be noted that the relationship is only for pure states $U = -\mu_{|\,i\,\rangle}B$ but does **not** apply for mixed states!

The effective magnetic momentum $\mu_{|\,i\,\rangle}$ of an atom generally depends on the value of the external field, following (6.3) it is determined by the increase of the energy eigenvalues in the Breit-Rabi diagram (figures 1.2 and 2.2). For example, using hydrogen:

$$\begin{aligned} \mu_{|\,1\,\rangle,|\,3\,\rangle} &= \pm\frac{g_S\mu_B}{2} &&\approx \pm\mu_B \\ \mu_{|\,2\,\rangle,|\,4\,\rangle} &= \pm\frac{g_S\mu_B}{2}\cdot\frac{x}{\sqrt{1+x^2}} &&\approx \pm\frac{\mu_B B}{\sqrt{B_C^2+B^2}}. \end{aligned} \tag{6.4}$$

As may be seen with the aid of the relationship (2.21) and in comparison with (2.20), the actual magnetic momenta, in units of electron magnetic momenta, are in agreement with the expected electron polarisation values of single hyperfine states.

The relationship

$$\mu_{|\,i\,\rangle} = \langle\, i \,|\, \mathcal{P}_e \,|\, i \,\rangle \cdot \frac{g_S \mu_B}{2} \tag{6.5}$$

applies for both hydrogen as well as for deuterium in as much as the interaction of the nucleon with the external field can be disregarded. The evolution of the effective magnetic momenta of the hyperfine states can thus be seen in the figures 2.1 and 2.3.

On hand of its symmetry, the trajectories of single atoms in a sextupole magnet are calculated in cylindrical coordinates using the Lagrangian

$$\mathcal{L}_i = \frac{m}{2}\left(\dot{r}^2 + r^2\dot{\varphi}^2 + \dot{z}^2\right) - \langle\, i \,|\, \mathcal{H} \,|\, i \,\rangle \tag{6.6}$$

wherein $\mathcal{H}$ represents the Hamilton operator (2.3). For the derivation of the equations of motion the following relationship is used:

$$\frac{\partial \langle\, i \,|\, \mathcal{H} \,|\, i \,\rangle}{\partial r} = -\mu_{|\,i\,\rangle}\,(B)\,\frac{\partial B}{\partial r}. \tag{6.7}$$

The equation of motion for the z-component along the magnetic axis is simple in the case of cylindrical sextupoles, v_z is constant and $z = v_z t$ applies.

If it is given that the effective magnetic momenta are constant, as is the case in pure states, then the atoms, aside from moving homogeneously in the z-direction, move in a two dimensional rotationally symmetrical parabolic potential.

The Lagrangian (6.6) allows the derivation of the equations of motion:

$$\ddot{r} = \frac{a}{r^3} - br, \tag{6.8}$$

with the constant values

$$\begin{aligned} a &= \frac{L^2}{m^2} & \qquad b &= \frac{2\gamma}{m} \\ L &= mr^2\dot{\varphi} & \qquad \gamma &= \operatorname{sgn}\left(\mu_{|\,i\,\rangle}\right)\frac{\mu_B B_{pt}}{r_{pt}^2}. \end{aligned} \tag{6.9}$$

The equations of motion (6.8) can be analytically integrated, and the following solutions are derived:

$$\dot{r} = \pm\sqrt{c - \frac{a}{r^2} - br^2} \tag{6.10}$$

$$r(z) = \sqrt{\frac{c}{2b} + 2A\left\{\begin{matrix}\cos\\ \cosh\end{matrix}\right\}(2\lambda z + \delta)}. \tag{6.11}$$

For amplitude A, wavelength λ, phase δ, and the integration constant c the following relationships can be established:

$$\begin{aligned} A &= \sqrt{\frac{c^2 - 4ab}{16b^2}} & \qquad \cos\delta &= \frac{y_0}{A} & \qquad c &= \dot{r}_0^2 + \frac{a}{r_0^2} + br_0^2 \\ \lambda &= \sqrt{\frac{|b|}{v_z^2}} & \qquad \sin\delta &= \frac{\operatorname{sgn}(\dot{r}_0)}{A}\cdot\sqrt{y_0^2 - A^2} & \qquad y_0 &= \frac{r_0^2}{2} - \frac{c}{4b}, \end{aligned} \tag{6.12}$$

or, with reference to the hyperbolic case

$$\sinh \delta = -\frac{\operatorname{sgn}(\dot{r}_0)}{A} \cdot \sqrt{y_0^2 - A^2}. \tag{6.13}$$

If the atom is injected into the sextupole without angular momentum ($\dot{\varphi}_0 = 0$), the first term on the right hand side of the equation of motion (6.8) vanishes and the solutions devolve into the purely harmonic or hyperbolic trajectories

$$r(z) = A \left| \begin{Bmatrix} \cos \\ \cosh \end{Bmatrix} (\lambda z + \delta) \right| \tag{6.14}$$

The trigonometric solution is valid for the state $|1\rangle$ with positive magnetic moment, for the state $|3\rangle$ the hyperbolic solution must be used.

The influence of the angular momentum on the trajectory of a hydrogen atom in the state $|1\rangle$ is illustrated in figure 6.1. The wavelength stays constant, independently of the angular momentum. With increasing angular momentum only the approach to the sextupole axis is more and more inhibited. For the trajectories of the mixed states of a hydrogen atom the equations of motion are given as

$$\ddot{r} = \frac{a}{r^3} - \operatorname{sgn}(\mu_{|i\rangle}) \cdot \frac{2\gamma^2 r^3}{m_{\mathrm{H}}\sqrt{\eta_{\mathrm{H}}^2 + \gamma^2 r^4}} \qquad \eta_{\mathrm{H}} = \frac{E_{\mathrm{HFS}}^{\mathrm{H}}}{2} = \mu_B B_C^{\mathrm{H}}, \tag{6.15}$$

So far no analytical solutions are known for these equations. However, they can be integrated numerically using a Runge-Kutta method described in appendix G.

Figure 6.2 compares the trajectories for the four hyperfine states of a hydrogen atom in a sextupole magnet for the same initial conditions. The mixed states $|2\rangle$ ad $|4\rangle$ experience smaller forces than the pure states $|1\rangle$ and $|3\rangle$, and their wavelength is correspondingly larger. For stronger pole tip fields the trajectories of the pure and the mixed states converge.

The calculation for deuterium atom is analogous. The trajectories for the pure states $|1\rangle$ and $|4\rangle$ as in the case of hydrogen fulfill the equation of motion (6.8), only the mass m must be set to the deuterium mass. For the calculation of the mixed states also the magnetic moments are needed, that can be obtained from (6.5) and (2.26). The following equations of motion result:

$$\ddot{r} = \frac{a}{r^3} - \operatorname{sgn}(\mu_{|i\rangle}) \cdot \frac{6\gamma^2 r^3 + 2\operatorname{sgn}(m_F)\,\eta_{\mathrm{D}}\gamma r}{m_{\mathrm{D}}\sqrt{9\eta_{\mathrm{D}}^2 + 6\operatorname{sgn}(m_F)\,\eta_{\mathrm{D}}\gamma r^2 + 9\gamma^2 r^4}} \quad \eta_{\mathrm{D}} = \frac{E_{\mathrm{HFS}}^{\mathrm{D}}}{2} = \mu_B B_C^{\mathrm{D}}. \tag{6.16}$$

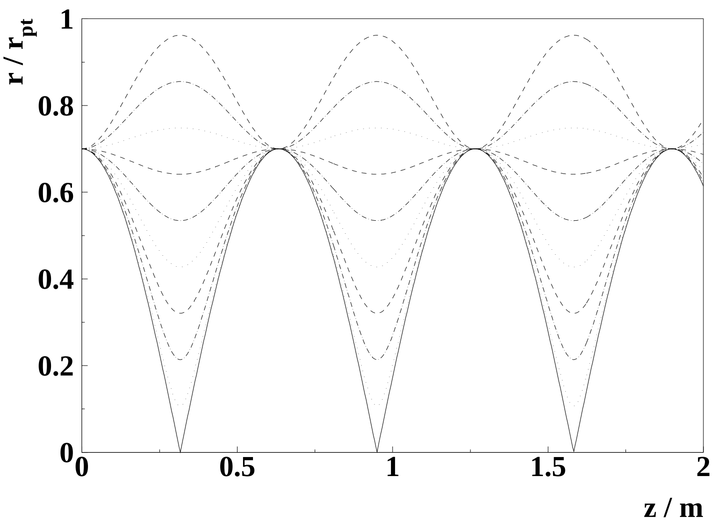

Fig. 6.1:
Influence of the angular momentum on the trajectories of hydrogen atoms in a sextupole magnet. A hydrogen atom in the state $|1\rangle$ is injected with a velocity of $v_z = 2500\,\mathrm{m\,s^{-1}}$ into a sextupole magnet with a pole tip field of $B_{pt} = 0.5\,\mathrm{T}$ and a pole tip radius of $r_{pt} = 6\,\mathrm{mm}$. Plotted are the radial projections $r(z)$ of the trajectories. The additional component of the velocity in azimuthal direction varies from $0\,\%$ of v_z (bottom) to $18\,\%$ of v_z (top) in steps of $2\,\%$.

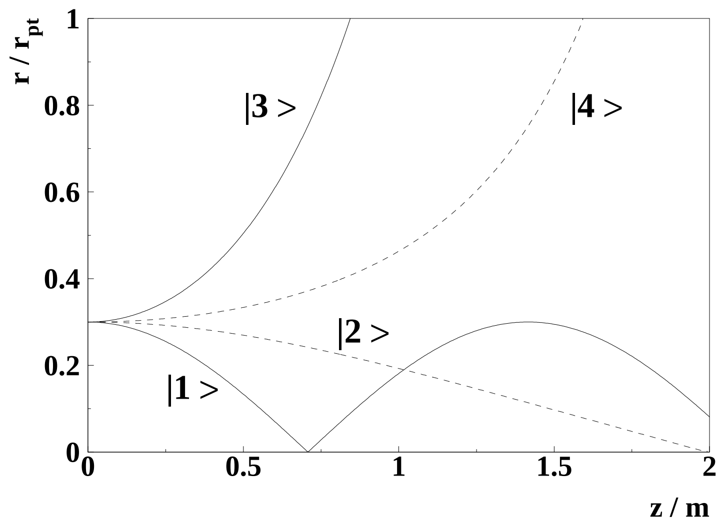

Fig. 6.2:
Comparison of the trajectories for the four hyperfine states of a hydrogen atom in a sextupole magnet. The hydrogen atoms are injected with a velocity of $v_z = 2500\,\mathrm{m\,s^{-1}}$ into a sextupole magnet. To emphasize the differences a pole tip field of only $0.1\,\mathrm{T}$ for a pole tip radius of $r_{pt} = 6\,\mathrm{mm}$ was assumed.

It is remarkable that the states $|\,3\,\rangle$ and $|\,5\,\rangle$ are focused or defocussed, depending on the magnetic field that they are in, because their effective magnetic field can change it's sign (figure 2.2).

In *tapered* magnets, that is magnets with varying pole tip radius, the z-component must also be taken into account. This leads to a system of coupled equations of motion of the form $\ddot{r} = f_r(r,z)$, $\ddot{z} = f_z(r,z)$. For all cases treated in this thesis $\ddot{z} \ll \ddot{r}$ is valid, so that the second equation can be solved to very good approximation by $z = v_z t$. In the solution of the radial equation the variation of B_{pt} with z must be considered. An analytical solution of this equation is not known. However, the tapering of the magnets can also be described by several cylindrical sextupole magnets.

6.2 Monte Carlo Generator for a Nozzle Beam

In addition to the calculation of trajectories the second fundamental component of a Monte Carlo simulation for the calculation of transmission probabilities is the random generation of initial conditions for atoms entering a sextupole system.

In general a Monte Carlo generator for particle trajectories consists of two parts, one of which generates a random velocity according to a predefined probability distribution, while the other one determines a random initial direction.

Atoms in an atomic beam source flow through the dissociator nozzle into the high vacuum region of the source where they are formed into an atomic beam by a skimmer and a collimator. The flow regime of the atoms can be characterized by the Knudsen parameter [126]

$$K_n = \frac{\lambda}{d} \tag{6.17}$$

where λ is the mean free path length and d the nozzle diameter. Under the typical pressures in the region between nozzle and collimator the interactions between the atoms can in general not be disregarded. The gas flow is in the so called transition region between laminar flow ($1/K_n > 110$), where the inter-atomic interaction dominates, and the molecular flow ($1/K_n < 1$), where the interaction of the atoms with the vessel walls determines the flowing behaviour.

In the nozzle region thermal energy is transformed into directed kinetic energy of the atoms as a result of the inter-atomic interaction. A velocity component v_{drift} in the direction of the atomic beam axis is superimposed over the thermal velocity distribution of the atoms as described by the Maxwell distribution. The velocities of the atoms exiting from the nozzle therefore follow a modified Maxwell distribution [127]

$$p(v)\,\mathrm{d}v \propto v^2 \exp\left(-\frac{m}{2kT_{\mathrm{beam}}}\left(v - v_{\mathrm{drift}}\right)^2\right)\mathrm{d}v, \tag{6.18}$$

parameterized by the drift velocity v_{drift} and the beam temperature T_{beam}. k is the Boltzmann constant and m the mass of the atom. A normalization factor does not have to be applied for the random generation of a velocity.

Drift velocity and beam temperature are related by the enthalpy balance before and after the expansion:

$$\frac{5}{2}kT_{\mathrm{nozzle}} = \frac{5}{2}kT_{\mathrm{beam}} + \frac{1}{2}mv_{\mathrm{rms}}^2. \tag{6.19}$$

Here it is assumed that the gas temperature before the expansion has assumed the nozzle temperature T_{nozzle}. $v_{\mathrm{rms}} = \sqrt{\bar{v}^2}$ is the quadratic average of the velocity, for the most probable velocity v_{prob} can be used as an approximation instead [108]. It is related to the drift velocity by

$$v_{\mathrm{prob}} = \frac{v_{\mathrm{drift}}}{2} + \sqrt{\left(\frac{v_{\mathrm{drift}}}{2}\right)^2 + \frac{2kT_{\mathrm{beam}}}{m}} \tag{6.20}$$

The equation (6.19) was found to be in good agreement with measurements with the atomic beam source for the HERMES experiment [108]. For known nozzle temperature and given drift velocity the beam temperature can be calculated, so that there is finally only one free parameter in the velocity distribution (6.18).

The flowing behaviour in the nozzle region also plays a crucial role in the generation of a random initial direction. The following describes a method for the generation of random directions for an arbitrary flow regime that is an extension of the method in [45] to generate a beam in the molecular flow regime. For both the opening surfaces of the nozzle and the collimator[7] an equally distributed random point is generated. The connecting line between both points then defines the random direction of the particle trajectory (figure 6.3a).

This method can also be used for the generation of a nozzle beam in the laminar flow regime. The first point is taken to be the intersection point between the enveloping surface of the cone, as defined by the real nozzle and the collimator with the atomic beam axis and the second point as a random point on the opening of the collimator as in the case of molecular flow (figure 6.3b) [129]. This method creates a maximal correlation between the the directions of the generated particles, which describes the laminar flow regime well. The obvious way to generate a nozzle beam in the transition region is to first generate a random point on a *virtual nozzle* which is chosen at an arbitrary position between the above described cone tip and the real nozzle. It's diameter is defined by the shape of the cone (figure 6.3c).

The parameter K_{mol}, which characterizes the flowing behaviour of the generated atomic beam, corresponding to the properties of the above described Monte Carlo can be defined as

$$K_{\mathrm{mol}} = \frac{\log\left(1 - \frac{d'_D}{d_K}\right)}{\log\left(1 - \frac{d_D}{d_K}\right)}. \tag{6.21}$$

d_D and d_K are the distances between nozzle and collimator to the cone tip, and d'_D is the distance between the virtual nozzle and the cone tip. Independent of the geometry of the beam formation

[7] The skimmer is not taken into consideration in this method, as its opening angle relative to the nozzle is larger than that of the collimator

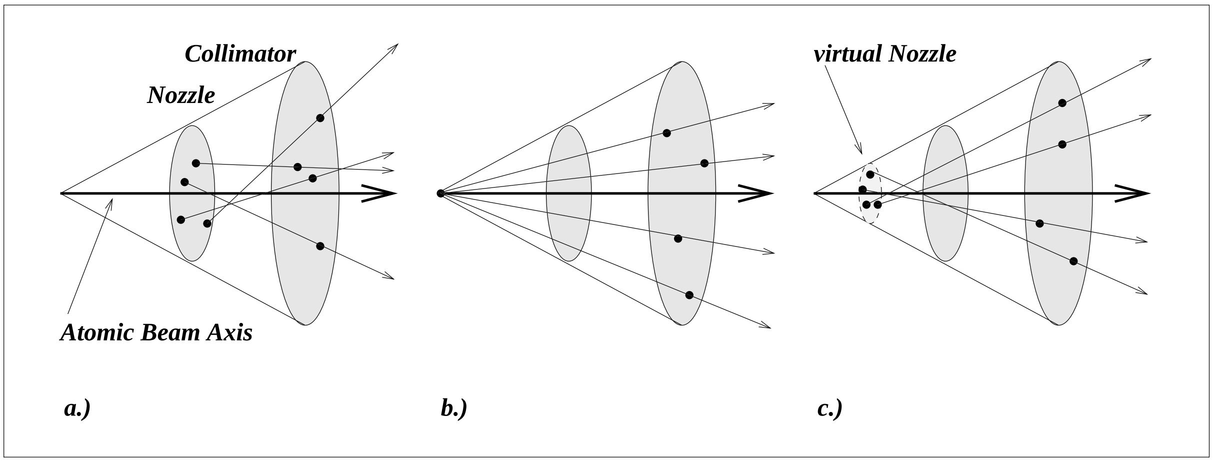

Fig. 6.3:
Direction generators for a nozzle beam. a.) Beam generation in the molecular flow regime, $K_{\mathrm{mol}} = 1$. b.) Beam generation in the laminar flow regime, $K_{\mathrm{mol}} = 0$. c.) Beam generation in the transition region, $0 < K_{\mathrm{mol}} < 1$.

system, this definition has the property, that for $K_{\mathrm{mol}} = 0$ all trajectories start at the cone tip and for $K_{\mathrm{mol}} = 1$ the virtual nozzle is at the position of the real nozzle. For values between 0 and 1 the virtual nozzle is positioned between cone tip and real nozzle and atomic beams are generated in the transition region.

K_{mol} controls the azimuthal as well as the radial beam temperature. If K_{mol} increases, more particles with larger azimuthal velocity are injected into the sextupole system, the average angular momentum increases and the focusing forces of the magnet are weakened (figure 6.1).

In summary, it can be said that the generation of a nozzle beam can be described by the geometry of the beam formation system and the parameters v_{drift}, T_{beam} and K_{mol}. The beam temperature can be be calculated by using (6.19), that is to say from the nozzle temperature, if it is know, and the drift velocity.

6.3 Monte Carlo Generator for an Effusive Beam

Inside the storage cell pressures in the range of $5.0 \cdot 10^{-7} - 1.0 \cdot 10^{-5}$ mbar (table B.2) exist, which result in mean free path lengths of several meters. These are large when compared to the dimensions of the storage cell, so that the beam formation in the exit tube of the storage cell happens in the molecular flow regime.

Due to the lack of interaction between the atoms there is no energy transfer to a directed velocity component as in the case of the nozzle beam. The drift velocity of the generated atomic beam vanishes and the velocity distribution devolves into a normal Maxwell distribution with $v_{\mathrm{drift}} = 0$. This distribution can be parameterized completely by the single parameter T_{beam}. The gas has assumed the temperature of the storage cell while diffusing through it. Therefore the beam temperature must be equal to the temperature of the storage cell, and the velocity distribution in the beam is thus unambiguously defined.

The direction generator for an effusive beam formed in the exit tube of a storage cell is based on a Monte Carlo simulation for molecular flow (appendix A.3). The atoms collide with the walls and desorb from there statistically with a $\cos\vartheta$-distribution with respect to the surface normal. All trajectories begin in the flat surface on the closed side of the tube. The initial direction for the calculation of the trajectories in the sextupole system is defined when the particle leaves the tube. The simulation of the entire storage cell is time consuming as a result of the large amount of wall collisions and the complex geometry. Limiting the simulation to the exit tube increases the efficiency of the direction generator - that is to say the number of particles generated per unit of time - by about two orders of magnitude.

The Monte Carlo generator for an effusive atomic beam is completely parameterized by the geometry of the exit tube and only one additional parameter $T_{\text{beam}} = T_{\text{cell}}$.

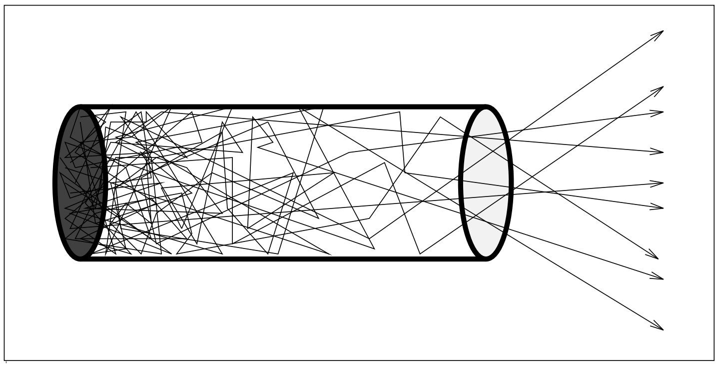

Fig. 6.4:
Direction generator for an effusive beam. Molecular flow is simulated inside the exit tube of the storage cell. All particles start from the flat surface on the closed side of the tube. The direction of the trajectory is defined when the particles leave the tube through the open other side.

7 Analyzing Power of the Breit-Rabi Polarimeter

For the determination of the polarization states in an atomic beam with the Breit-Rabi polarimeter independent measurements are necessary, in which different components of the polarimeter are used. Specifically these are in the case of hydrogen four and in the case of deuterium six measurements. This suggests that in order to describe the analyzing power of the Breit-Rabi polarimeter not a single parameter should be used, but rather the quality of the individual polarization analyzing components. Several components must even be described by more than one parameter.

Already in the introduction (chapter 1.5) a formalism was developed that allows the deduction of the hyperfine occupancy in an atomic beam from a measurement of intensity ratios. In this chapter the properties of the sextupole magnet in the form of transmission probabilities will be integrated into this formalism. The formalism is developed by mostly using the example of an atomic beam of hydrogen. The applicability to deuterium is only discussed if significant deviations to hydrogen arise.

For the interpretation of the measured signal ratios the properties of the high frequency transitions (chapter 5) and the sextupole magnets (chapter 6) have to be considered appropriately and the calculation of the occupation numbers must be modified accordingly. Those modifications include

- Modifications due to the sextupole magnets:
  - incomplete separation of the states $|3\rangle$ and $|4\rangle$ for hydrogen and $|4\rangle$, $|5\rangle$ and $|6\rangle$ for deuterium,
  - the states $|1\rangle$ and $|2\rangle$ for hydrogen and $|1\rangle$, $|2\rangle$ and $|3\rangle$ for deuterium are not focused in the same way,
  - the states$|3\rangle$ and $|4\rangle$ for hydrogen and $|4\rangle$, $|5\rangle$ and $|6\rangle$ for deuterium are not defocussed in the same way,
- Modifications due to the high frequency transitions:
  - incomplete occupation transfer in the transitions,
  - the medium field transitions for hydrogen MFT 1-3 and MFT 2-3 must be described by two occupation transfers 1-2 and 2-3 after one another
  - the medium field transitions for deuterium MFT 1-4, MFT 2-4 and MFT 3-4 must be described by a series of three occupation transfers 1-2, 2-3 and 3-4.

It will be seen in the following that these modifications, especially in the case of the sextupole modifications for deuterium, lead to corrections that are negligibly small. However, this is only true under certain conditions. However, this only applies under certain conditions and thus al the modifications desribed above are considered and introduced into the formalism. The negligibility of individual corrections will be pointed out separately later.

The following describes replacement of the operation (1.7) in the description of the effect of a sextupole magnet and the operation (1.8) describing the effect of a high frequency transition forms the basis for the description of the analyzing power of the Breit-Rabi polarimeter as well as for the entire calibration procedure described in the chapters 8 and 9.

7.1 Sextupole Magnets

The effect of a non-ideal sextupole magnet on the atomic beam can be described by introducing a transmission probability σ_i for each hyperfine state $|\, i\,\rangle$ to reach a target through the sextupole system. In the case of a polarization measurement, the exit tube of the storage cell is the source and the sensitive area of the atomic beam detector is the target. The transmissions can be determined with the Monte Carlo simulation for sextupole magnet systems as described in chapter 6.

To account for these transmissions in the effects that a sextupole magnet has on the atomic beam, the operation (1.7) from chapter 1.5 must be replaced by the operation

$$\begin{pmatrix} n_1 \\ n_2 \\ n_3 \\ n_4 \end{pmatrix} \xrightarrow{\text{Sechspol}} \begin{pmatrix} \sigma_1 n_1 \\ \sigma_2 n_2 \\ \sigma_3 n_3 \\ \sigma_4 n_4 \end{pmatrix} . \tag{7.1}$$

This describes the effect of a sextupole magnet completely with respect to the properties that are relevant for a polarization measurement.

In the case of relative measurements, i.e. measurements of intensity ratios, it is permissible to normalize the transmission arbitrarily. Usually the normalization $\sigma_1 = 1$ is chosen. The other transmissions only have to be known relative to σ_1.

7.2 Strong Field Transitions

In general four efficiencies ε_{ij}^+, ε_{ij}^-, ε_{ji}^+ and ε_{ji}^- are necessary to completely describe an occupation transfer in a high frequency transition. In the right picture of figure 5.2 they belong the the upper and lower branch, respectively, and to the two different signs of the field gradient, as marked by the upper indices $+$ and $-$. A transition in a two niveau system is symmetric, as shown in the picture. Therefore all four efficiencies are identical. In a four or six niveau system, like the hyperfine structure of hydrogen or deuterium, the non-involved states cause a perturbation that leads to an asymmetry. The absolute value of the slope of the two niveaus without interaction with the HF-field (dashed lines in figure 5.2 right) does not agree any longer and the niveaus can even have a curved evolution in the resonance region [120]. This breaks the symmetry in this picture and in the above efficiencies. After the definition of the field gradient an occupation transfer must in general be described by two efficiencies $\varepsilon_{ij} \neq \varepsilon_{ji}$.

In the framework of this thesis, asymmetries in the efficiencies of a high frequency transition are in general disregarded and it is assumed that $\varepsilon_{ij} = \varepsilon_{ji}$. This assumption does not lead to an error in the efficiency measurement described in chapter 8, because the defocussed states are entirely removed through the use of beam blocks in the sextupole magnets. However, only one of the two efficiencies ε_{ij} is measured, while in the analysis of the polarization measurements ε_{ji} is used. The order of magnitude of the systematic error on a polarization measurement introduced by neglecting asymmetric efficiencies can be estimated using the right resonance of SFT 2-4 in figure 5.4.

These efficiencies will have to be measured in the future, or the high frequency transitions will have to be operated with moderate field gradients and maximal HF-power, so that the adiabatic condition is sufficiently well fulfilled for both efficiencies. If the efficiencies of a high frequency transition in both directions approach the saturation value of 100 %, the relation $\varepsilon_{ij} = \varepsilon_{ji}$ is valid. In the relaxation measurements described in this thesis this condition was not yet sufficiently fulfilled, and it must be expected that the systematic errors on the relaxation measurements as discussed in chapter 11.5 are dominated by the neglection of these asymmetries.

In a strong field transition for a given setting of the static field and the field gradient always only one occupation transfer is ever present [8], under the assumption of symmetric efficiencies the introduction of only one transition efficiency ε_{ij} is sufficient to describe the effect of a non-ideal strong field transition.

The consideration of this transition efficiency for a SFT 2-4 leads to the replacement of the first operation in (1.8) by the following:

$$\begin{pmatrix} n_1 \\ n_2 \\ n_3 \\ n_4 \end{pmatrix} \xrightarrow{\text{SFT2}\leftrightarrow 4} \begin{pmatrix} n_1 \\ \varepsilon_{24} n_4 + (1-\varepsilon_{24})\, n_2 \\ n_3 \\ \varepsilon_{24} n_2 + (1-\varepsilon_{24})\, n_4 \end{pmatrix} . \tag{7.2}$$

The other strong field transitions can be treated analogously. Also the weak field transition WFT 1-3 for hydrogen can be described by an analogous operation, as long as it is operated in a sufficiently weak field (chapter 5.4).

7.3 Medium Field Transitions

A medium field transition for hydrogen consists of two simultaneous occupation transfers, one of which is suppressed by a suitable selection of the magnetic fields (chapter 5.3). The effect of a non-ideal medium field transition for hydrogen can be expressed as the successive application of two operations of the type (7.2). If the medium field transition is operated with a negative gradient the following occupation transfer scheme ensues:

$$\begin{pmatrix} n_1 \\ n_2 \\ n_3 \\ n_4 \end{pmatrix} \xrightarrow{1\leftrightarrow 2} \begin{pmatrix} \varepsilon_{12} n_2 + (1-\varepsilon_{12})\, n_1 \\ \varepsilon_{12} n_1 + (1-\varepsilon_{12})\, n_2 \\ n_3 \\ n_4 \end{pmatrix} \xrightarrow{2\leftrightarrow 3} \begin{pmatrix} \varepsilon_{12} n_2 + (1-\varepsilon_{12})\, n_1 \\ \varepsilon_{23} n_3 + (1-\varepsilon_{23}) \left[\varepsilon_{12} n_1 + (1-\varepsilon_{12})\, n_2\right] \\ \varepsilon_{23} \left[\varepsilon_{12} n_1 + (1-\varepsilon_{12})\, n_2\right] + (1-\varepsilon_{23})\, n_3 \\ n_4 \end{pmatrix} . \tag{7.3}$$

At this point the question of why it is not possible to describe the MFT 1-3 by an overall efficiency $\varepsilon_{13} = \varepsilon_{12} \cdot \varepsilon_{23}$ and to treat the MFT 1-3 like the WFT 1-3 arises. The difference between these two high frequency transitions was already discussed in chapter 5.4, with the result that the treatment of the WFT 1-3 in the source like the MFT 1-3 leads to inconsistencies in the efficiency measurements.

If on the other hand the MFT 1-3 in the polarimeter is treated like a WFT 1-3, the same injected states n_2 and n_3 end up in the upper states after the transition, however, their position is just switched. This can be seen by comparing (5.5) and (5.8). As a result the different focusing of the states $|\,1\,\rangle$ and $|\,2\,\rangle$ in the following sextupole system (figure 6.2) cannot be accounted for correctly. This makes a consistent interpretation of the efficiency measurements (chapter 8.6) impossible, just like in the case of treating WFT 1-3 like MFT 1-3. In a polarization measurement the transmissions of the two focused states in the sextupole system of the polarimeter differ by up to 10 % (figure 9.5), so that the treatment of the MFT 1-3 as a WFT 1-3 could lead to a significant error.

While the effect of a MFT 2-3 on an atomic beam can be described with only one efficiency, it is preferable to use the operation (7.3) and to take both efficiencies ε_{12} and ε_{23} into consideration in this high frequency transition. This treatment allows the measurement of the suppression of the occupation transfer 1-2 and to provide an uncertainty for the property $\varepsilon_{12} = 0$ of the MFT 2-3. This uncertainty can then be considered in the polarization measurements. Furthermore,

[8] With the exception of the strong field transition SFT 2-5/3-6 for deuterium

the measurement of ε_{12} gives an additional condition for the determination of the sextupole corrections using the consistency method for the efficiency measurements (chapter 8.6).

A medium field transition for deuterium consists of up to three occupation transfers, one after another. The effect of this high frequency transition can be described in analogy to (7.3) by three consecutive operations of the type (7.2). If the medium field transition is operated with a negative gradient, the following overall effect results for the atomic beam:

$$\begin{pmatrix} n_1 \\ n_2 \\ n_3 \\ n_4 \\ n_5 \\ n_6 \end{pmatrix} \xrightarrow{\text{MFT}} \begin{pmatrix} \varepsilon_{12}n_2 + (1-\varepsilon_{12})\,n_1 \\ \varepsilon_{23}n_3 + (1-\varepsilon_{23})\left[\varepsilon_{12}n_1 + (1-\varepsilon_{12})\,n_2\right] \\ \varepsilon_{34}n_4 + (1-\varepsilon_{34})\left\{\varepsilon_{23}\left[\varepsilon_{12}n_1 + (1-\varepsilon_{12})\,n_2\right] + (1-\varepsilon_{23})\,n_3\right\} \\ \varepsilon_{34}\left\{\varepsilon_{23}\left[\varepsilon_{12}n_1 + (1-\varepsilon_{12})\,n_2\right] + (1-\varepsilon_{23})\,n_3\right\} + (1-\varepsilon_{34})\,n_4 \\ n_5 \\ n_6 \end{pmatrix}. \tag{7.4}$$

7.4 Calculation of the Correction Matrices

In summary it can be said that the non-ideal properties of the high frequency transitions and of the sextupoles can be accounted for by introducing efficiencies ε_{ij} and transmission probabilities σ_i into the calculation of the occupation numbers n_i from the measured signal ratios R_{ij}. For this purpose the operations on the occupation tuples in (1.7) and (1.8) must be replaced by the above introduced operations (7.1), (7.2), (7.3) and (7.4), while the signal ratios are calculated as in chapter 1.5.

In a measurement using strong field transitions instead of (1.10) signal ratios of the form

$$R_{ij} = 1 - \frac{\varepsilon_{ij}\left(\sigma_i - \sigma_j\right)\left(n_i - n_j\right)}{\sum_i \sigma_i n_i}. \tag{7.5}$$

are obtained. These signal ratios also result from the application of a strong field transition for deuterium.

In the case of medium field transitions the ratios are somewhat more complex, due to the description using two or three efficiencies. For a medium field transition for hydrogen the signal ratio is

$$R_{ij} = 1 - \frac{\alpha_H n_1 + \beta_H n_2 + \gamma_H n_3}{\sum_{i=1}^{4} \sigma_i n_i} \tag{7.6}$$

with the coefficients

$$\begin{aligned} \alpha_H &= \varepsilon_{12}\left(\sigma_1 - \sigma_2\right) + \varepsilon_{12}\varepsilon_{23}\left(\sigma_2 - \sigma_3\right) \\ \beta_H &= \varepsilon_{12}\left(\sigma_2 - \sigma_1\right) + \varepsilon_{23}\left(\sigma_2 - \sigma_3\right) + \varepsilon_{12}\varepsilon_{23}\left(\sigma_3 - \sigma_2\right) \\ \gamma_H &= \varepsilon_{23}\left(\sigma_3 - \sigma_2\right). \end{aligned} \tag{7.7}$$

The operation (7.4) for the case of a medium field transition for deuterium gives the ratio

$$R_{ij} = 1 - \frac{\alpha_D n_1 + \beta_D n_2 + \gamma_D n_3 + \delta_D n_4}{\sum_{i=1}^{6} \sigma_i n_i} \tag{7.8}$$

with the coefficients

$$\begin{aligned} \alpha_D &= \varepsilon_{12}\left(\sigma_1 - \sigma_2\right) + \varepsilon_{12}\varepsilon_{23}\left(\sigma_2 - \sigma_3\right) + \varepsilon_{12}\varepsilon_{23}\varepsilon_{34}\left(\sigma_3 - \sigma_4\right) \\ \beta_D &= \varepsilon_{12}\left(\sigma_2 - \sigma_1\right) + \varepsilon_{23}\left(\sigma_2 - \sigma_3\right) + \varepsilon_{12}\varepsilon_{23}\left(\sigma_3 - \sigma_2\right) + \varepsilon_{23}\varepsilon_{34}\left(\sigma_3 - \sigma_4\right) + \varepsilon_{12}\varepsilon_{23}\varepsilon_{34}\left(\sigma_4 - \sigma_3\right) \\ \gamma_D &= \varepsilon_{23}\left(\sigma_3 - \sigma_2\right) + \varepsilon_{34}\left(\sigma_3 - \sigma_4\right) + \varepsilon_{23}\varepsilon_{34}\left(\sigma_4 - \sigma_3\right) \\ \delta_D &= \varepsilon_{34}\left(\sigma_4 - \sigma_3\right). \end{aligned} \tag{7.9}$$

The solution of the equations (7.5), (7.6) and (7.8) for the occupation numbers in turn leads to systems of linear equations, in which the elements of the coefficient matrix in (1.11) have to be replaced by corrected terms. The explicit shape of these corrected coefficient matrices for hydrogen and deuterium can be found in appendix E.

The following two chapters will describe how numerical values are obtained for efficiencies and transmissions. As efficiencies and transmissions together describe the analyzing power of the Breit-Rabi polarimeter, this procedure is actually the *calibration* of the polarimeter. The uncertainties of efficiencies and transmissions determine the systematic uncertainty of a polarization measurement.

8 Efficiency Measurements

8.1 Experimental Setup for Efficiency Measurements

For the efficiency measurements of the high frequency transitions of the apparatus, the storage cell is moved out of the atomic beam using a linear manipulator. The beam is injected directly from the source into the Breit-Rabi polarimeter. Figure 8.1 shows an overview of the apparatus used for the efficiency measurements (compare figure 1.4). This schematic setup almost completely corresponds to the classic setup of the Rabi-experiment [118] and consequently is called *Rabi setup* in the following. However, historically asymmetric dipole magnets were used for the generation of inhomogeneous magnetic fields, as in the experiments by W. Gerlach and O. Stern [113, 114], and the high frequency transitions were operated in exact resonance, because transition frequencies were measured to high resolution.

On the axes of the sextupole in the source and the first sextupole in the polarimeter beam blocks were installed, that prevent the direct course of the atoms through the apparatus. This completely suppresses the transmission of defocused states. Due to the small defocusing forces near the axis in the case of hydrogen the states $|3\rangle$ and $|4\rangle$ and for deuterium the states $|4\rangle$, $|5\rangle$ and $|6\rangle$ could still pass through a sextupole without beam block and thus could still be detected in the atomic beam detector. The beam blocks simplify the corrections due to non-ideal sextupole magnets considerably also for the efficiency measurements. This made it possible to determine the still remaining sextupole corrections experimentally, without the use of Monte Carlo simulations. For the efficiency measurements the

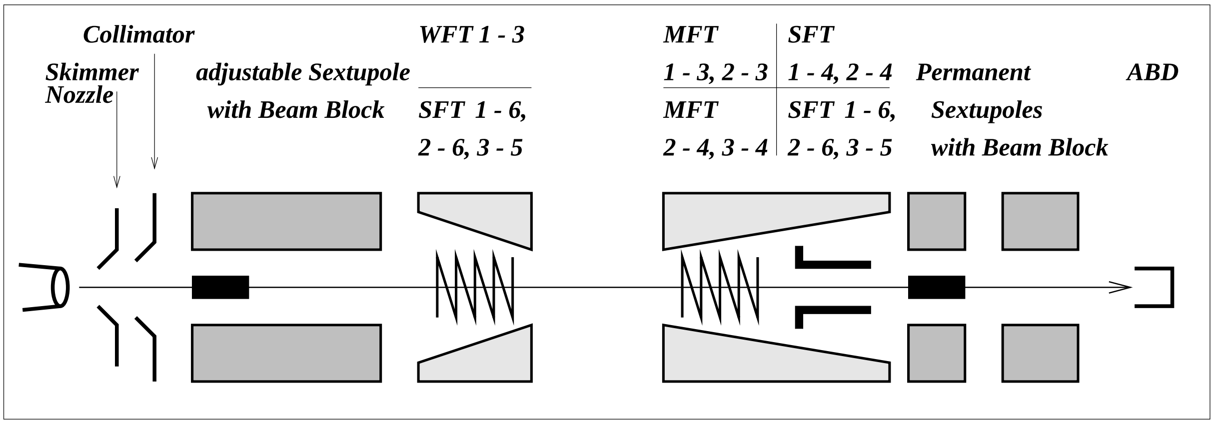

Fig. 8.1:
Rabi setup: Experimental setup for the efficiency measurement. The storage cell was removed from the atomic beam. Beam blocks have been installed on the axis of the sextupole of the source as well as in the first sextupole of the polarimeter to completely suppress the transmission of defocused states. The high frequency transitions listed at the top correspond to measurements with hydrogen, the ones at the bottom correspond to deuterium measurements.

apparatus shown in figure 8.1 should be regarded as a single unit with the essential scheme – *sextupole – high frequency transitions – sextupole* – A separation of the apparatus into source and polarimeter is irrelevant for the efficiency measurements at the high frequency transitions, even if these concepts will still be used in this chapter to identify the sextupoles and assign the high frequency transitions.

The changes in the intensity of the atomic beam when a high frequency transition is switched on are the basis for all efficiency measurements. The decrease or increase in intensity, that were also used to adjust the transitions (figure 5.4, 5.6, 5.7 and 5.8), are a measure for the efficiency of the high frequency transition.

8.2 Transmission Corrections for Efficiency Measurements

The operation (7.1) that was introduced in chapter 7.1, which was used in describing the effect of a sextupole magnet on an atomic beam, must be extended by one important point to also be valid for the treatment of sextupole corrections in efficiency measurements. After removal of the storage cell the sextupole sub-systems in the source and the polarimeter must be regarded as a coupled overall system, within which the hyperfine states can be altered by the high frequency transitions. Also, the transmission properties of a sextupole sub-system may depend on the properties of the source and the target in question.

In the case of the sextupole in the atomic beam source, the beam formation system consisting of nozzle and collimator acts as the source and the opening of the first sextupole in the polarimeter represents the target. For the polarimeter system the exit opening of the sextupole magnet in the atomic beam source represents the source, while the sensitive area of the atomic beam detector is the target.

The phase space distributions for the individual hyperfine states are different from one another after the first sextupole and the acceptance of the polarimeter system depends on these phase space distributions. Therefore, the trajectories of the atoms in the polarimeter sextupoles do not only depend on the state of the atom in the polarimeter system, but also on the state it was in while flying through the sextupole magnet inside the source. Thus, the history of the atoms in the earlier sextupole magnet influences the focusing properties of the sextupole magnet in the polarimeter via the phase space distributions in the atomic beam.

For the description of the polarimeter system transmissions were introduced that depend on two indices: σ'_{ij}. The first index refers to the hyperfine state while crossing through the source sextupole, the second index marks the state in the polarimeter system. As before, one index is sufficient to distinguish between the transmissions of the sextupole in the source.

The transmissions through the overall system therefore can be expressed as the product of two transmissions, a σ_i for the source sextupole and a σ'_{ij} for the polarimeter system. As the first index of the polarimeter transmission is by definition identical to the index of the source transmission, the nomenclature can be simplified by defining

$$\sigma_{ij} := \sigma_i \cdot \sigma'_{ij} \tag{8.1}$$

In the following, the total set of transmissions σ_{ij} for an atomic species is referred to as transmission matrix.

If the sextupole corrections for the efficiencies of all transitions are calculated according to the methods that will be introduced in the following chapters 8.3, 8.4 and 8.5, it becomes apparent that all of the 16 elements of the transmission matrix are necessary for the analysis of the efficiency measurements for hydrogen, with the exception of the transmissions σ_{34} and σ_{43}. As the transmissions only must be known relative to σ_{11}, a total of 13 normalized transmissions is needed. In the case of deuterium the transmission matrix even has 36 elements, of which 27 normalized transmissions are necessary for the analysis of the efficiency measurements.

This situation is considerably simplified if the sextupoles of source and polarimeter are equipped with beam blocks on the axis, which almost completely suppress the transmission of the states $|3\rangle$ and $|4\rangle$ for hydrogen and $|4\rangle$, $|5\rangle$ and $|6\rangle$ for deuterium (figure 8.1). The suppression of these transmissions is complete if the beam blocks block the sight between source and target. For the beam block in the polarimeter that is in fact the case. The beam block in the source sextupole does not completely cover the connection between the nozzle and the opening of the polarimeter system, so that the contributions of the defocused states to the corrections may only be neglected for pole tip fields above about $0,3 - 0,4\,\mathrm{T}$. Below this field, atoms in defocused states can still pass the source sextupole, be transferred into one of the upper states by one of the high frequency transitions and be focused again in the sextupole system of the polarimeter and finally be detected in the sensitive area of the atomic beam detector.

The shape of the transmission matrix of the overall system for hydrogen becomes the following, due to the introduction of the beam block and assuming a sufficiently high pole tip field in the source sextupole:

$$\sigma = \begin{pmatrix} \sigma_{11} & \sigma_{12} & 0 & 0 \\ \sigma_{21} & \sigma_{22} & 0 & 0 \\ 0 & 0 & 0 & 0 \\ 0 & 0 & 0 & 0 \end{pmatrix}. \tag{8.2}$$

The normalization is arbitrary, so that only the transmissions σ_{12}, σ_{21} and σ_{22} relative to σ_{11} are needed for the analysis of all efficiency measurements[9] In the case of deuterium the beam blocks reduce the number of necessary transmissions to eight. Without the measurement of the efficiency ε_{12} in the medium field transitions only four normalized transmissions are sufficient for the analysis of the efficiency measurements.

8.3 Efficiencies of the Strong and Weak Field Transitions

The measurement of the efficiency ε_{ij} of a strong or weak field transition affords the measurement of two beam intensities, the intensity for inactive and active high frequency transition.

The beam signal without high frequency transition is proportional to the trace of the transmission matrix of the overall system:

$$S_{OFF} = \mathrm{Tr}\,(\sigma) = \sum_i \sigma_{ii}. \tag{8.3}$$

The intensity of the detected beam with active SFT 2-4 is obtained by the successive application of the operations (7.1) (7.2) to an initially equally occupied atomic beam

$$\begin{pmatrix} 1 \\ 1 \\ 1 \\ 1 \end{pmatrix} \xrightarrow{\text{sextupole}} \begin{pmatrix} \sigma_1 \\ \sigma_2 \\ \sigma_3 \\ \sigma_4 \end{pmatrix} \xrightarrow{\text{SFT2}\leftrightarrow 4} \begin{pmatrix} \sigma_1 \\ \varepsilon_{24}\sigma_4 + (1-\varepsilon_{24})\,\sigma_2 \\ \sigma_3 \\ \varepsilon_{24}\sigma_2 + (1-\varepsilon_{24})\,\sigma_4 \end{pmatrix} \xrightarrow{\text{sextupole}} \begin{pmatrix} \sigma_{11} \\ \varepsilon_{24}\sigma_{42} + (1-\varepsilon_{24})\,\sigma_{22} \\ \sigma_{33} \\ \varepsilon_{24}\sigma_{24} + (1-\varepsilon_{24})\,\sigma_{44} \end{pmatrix} \tag{8.4}$$

and summation over all components of the last occupation tuple. The other high frequency transitions, within which an occupation transfer occurs, can be treated analogously.

By forming the ratio between both beam signals and calculating the efficiency a relation is obtained that is valid for all high frequency transitions that operate with an occupation transfer:

$$\varepsilon_{ij} = \kappa_{ij} \cdot \left(1 - \frac{S_{ON}}{S_{OFF}}\right) \tag{8.5}$$

The correction factor κ_{ij} contains all transmission corrections and has the form:

$$\kappa_{ij} = \frac{\mathrm{Tr}\,(\sigma)}{\sigma_{ii} + \sigma_{jj} - (\sigma_{ij} + \sigma_{ji})}. \tag{8.6}$$

[9] Despite the normalization the transmissions σ_1 and σ_{11} will be given explicitly in the following equations, because the normalization is arbitrary and the connection to the transmissions σ_{11} and σ_1 should not be forgotten. If all transmissions are determined by a Monte Carlo simulation, the transmissions σ_1 and σ_{11} must be determined as well.

For the sextupole corrections in the case of an ideal sextupole system for hydrogen transitions $\kappa_{ij} = 2$, which corresponds to a reduction of the beam signal with high frequency transition with complete occupation transfer to exactly half of the signal without the high frequency transition. For deuterium $\kappa_{ij} = 3$ is ideal, with a signal that is reduced by 1/3 when an ideally working high frequency transition is activated.

Through the use of the beam blocks in the sextupole magnets the shape of the correction factors (8.6) is simplified, because it is sufficient to know the upper half of the diagonal elements within the transmission matrix to determine the efficiencies of the strong field transitions and the weak field transition WFT 1-3. By inserting the transmissions from (8.2) into the relation (8.6) the corrections for the hydrogen transitions are obtained:

$$\kappa_{13} = \kappa_{14} = 1 + \frac{\sigma_{22}}{\sigma_{11}} \qquad \kappa_{24} = 1 + \frac{\sigma_{11}}{\sigma_{22}}. \tag{8.7}$$

If the transmissions from the deuterium matrix analogous to (8.2) are inserted in (8.6), the correction factors for the three strong field transitions FT 1-6, SFT 2-6 and SFT 3-5 result:

$$\kappa_{16} = 1 + \frac{\sigma_{22} + \sigma_{33}}{\sigma_{11}} \qquad \kappa_{26} = 1 + \frac{\sigma_{11} + \sigma_{33}}{\sigma_{22}} \qquad \kappa_{35} = 1 + \frac{\sigma_{11} + \sigma_{22}}{\sigma_{33}}. \tag{8.8}$$

Both efficiencies of the fourth strong field transition SFT 2-5/3-6 – ε_{25} and ε_{36} cannot be determined with the methods described in this chapter, because this high frequency transition consists of two simultaneous occupation transfers. In this case an additional high frequency transition with known efficiency must be used, as in the case of the efficiency measurement of a medium field transition, in order to be able to distinguish the two occupation transfers.

8.4 Efficiencies of a Medium Field Transition for Hydrogen

As was already pointed out in chapter 5.3, the measurement of the resonance with active medium field transition alone (figure 5.6) cannot decide whether the high frequency transition is operating as MFT 1-3 or MFT 2-3. For this reason an efficiency measurement on the sole basis of the measurement of the two beam signals with active and inactive medium field transition analogous to the procedure in chapter 8.3 cannot be sufficient to distinguish between the effects of the two medium field transitions onto an atomic beam in a quantitative fashion.

If this procedure is naively applied to a medium field transition, very high efficiencies for both settings of the medium field transition will be measured, because in both cases the occupation transfer 2-3 is working excellently, so that the beam signal in both cases is reduced to about half. However, these results alone are not sufficient for the calibration of the polarimeter, because they do not give any information about the quality of the transfer 1-2 within the medium field transition. The *quantitative* difference between the two medium field transitions MFT 1-3 and MFT 2-3 on the other hand is crucial for the analyzing power of the Breit-Rabi polarimeter with respect to nuclear polarization especially for polarization measurements in the strong field region ($B \gg B_C$). This is true, because in this case the states $|1\rangle$ and $|2\rangle$ carry opposite nuclear polarizations (figure 1.2 and 2.1). A method, that allows the discrimination between the occupation transfers 1-2 and 2-3 in a medium field transition for hydrogen was described and applied in [116] for the first time. This method is identical for the two medium field transitions MFT 1-3 and MFT 2-3, because the measurement in both cases determines the efficiencies of the occupation transfers 1-2 and 2-3 in the medium field transition.

The efficiency measurement of the medium field transition is carried out like the adjusting of the resonant static fields, by using an additional transition in front of the medium field transition.

To this purpose the WFT 1-3 in the source can be used. A total of four beam signals must be measured: without high frequency transition, with WFT 1-3, with the medium field transition and with both of the transitions.

From the ratio of the intensities for active WFT 1-3 to the beam signal without high frequency transition the efficiency of the weak field transition is obtained as described in chapter 8.3. The efficiencies of the medium field transitions then result from the intensity ratios of active medium field transition to inactive medium field transition, with and without the WFT 1-3. The calculation of these intensity ratios again follows from the application of the operations (7.1), (7.2) and (7.3) to an initially equally occupied atomic beam. Here a maximum of three operations of the type (7.2) must be carried out between the two sextupole systems.

The signal ratio between active and inactive MFT for inactive WFT 1-3 may be expressed as

$$R_M = \frac{S_{MFT\,on}}{S_{MFT\,off}} = 1 - \frac{a\varepsilon_{12} + b\varepsilon_{23} + c\varepsilon_{12}\varepsilon_{23}}{d}. \tag{8.9}$$

As sextupole corrections the coefficients a, b, c and d contain the elements of the transmission matrix for the overall system σ

$$\begin{array}{rcll} a & = & \sigma_{11} + \sigma_{22} - \sigma_{12} - \sigma_{21} & \longrightarrow \ 0 \\ b & = & \sigma_{22} + \sigma_{33} - \sigma_{23} - \sigma_{32} & \longrightarrow \ 1 \\ c & = & \sigma_{12} + \sigma_{23} - \sigma_{22} - \sigma_{13} & \longrightarrow \ 0 \\ d & = & \sigma_{11} + \sigma_{22} + \sigma_{33} + \sigma_{44} & \longrightarrow \ 2, \end{array} \tag{8.10}$$

where the cases in the limit of an ideal sextupole system are included.

Because a and c vanish in the limit of an ideal sextupole system and b goes to 1, this signal ratio is sensitive to the efficiency ε_{23} and corresponds to the drop of the beam signal in the upper picture of figure 5.6. A further analysis of the limiting case of an ideal sextupole shows that the signal ratio (8.9) leads to the relation (8.5). Therefore this measurement corresponds to an efficiency measurement for the transfer 2-3 in the medium field transition, while the transition 1-2 contributes only little through the sextupole corrections.

For an active WFT 1-3 the signal ratio of active to inactive medium field transition is

$$R_M^W = \frac{S_{MFT\,on}^{WFT\,on}}{S_{MFT\,off}^{WFT\,on}} = 1 - \frac{a'\varepsilon_{12} + b'\varepsilon_{23} + c'\varepsilon_{12}\varepsilon_{23}}{d'}. \tag{8.11}$$

The coefficients a', b', c' and d' contain the efficiency of the WFT 1-3 in addition to the transmissions:

$$\begin{array}{rcll} a' & = & a - \varepsilon_{13}\,(\sigma_{11} + \sigma_{32} - \sigma_{31} - \sigma_{12}) & \longrightarrow \quad 0 \\ b' & = & b - \varepsilon_{13}\,(\sigma_{12} + \sigma_{33} - \sigma_{32} - \sigma_{13}) & \longrightarrow \quad 0 \\ c' & = & c - \varepsilon_{13}\,(\sigma_{12} + \sigma_{33} - \sigma_{13} - \sigma_{32}) & \longrightarrow \ -1 \\ d' & = & d - \varepsilon_{13}\,(\sigma_{11} + \sigma_{33} - \sigma_{13} - \sigma_{31}) & \longrightarrow \quad 1. \end{array} \tag{8.12}$$

This signal ratio is a measure for the increase of the beam signal in the lower picture of figure 5.6. The coefficients a' and b' vanish in this case, while c' goes to -1. Thus for an active WFT 1-3 the product of the two efficiencies of the medium field transition is measured. As c' goes to -1, the beam signal rises instead of that it drops to half it's value as in (8.9).

The two signal ratios (8.9) and (8.11) can be combined into one quadratic equation for the efficiency ε_{23}

$$A\varepsilon_{23}^2 - B\varepsilon_{23} + C = 0, \tag{8.13}$$

with the coefficients

$$\begin{aligned} A &= b'c - bc' \\ B &= cd'\left(1 - R_M^W\right) - c'd\left(1 - R_M\right) + ab' - a'b \\ C &= ad'\left(1 - R_M^W\right) - a'd\left(1 - R_M\right), \end{aligned} \tag{8.14}$$

after whose solution the efficiency ε_{12} is also obtained:

$$\varepsilon_{12} = \frac{d'\left(1 - R_M^W\right) - \varepsilon_{23} b'}{a' - \varepsilon_{23} c'}. \tag{8.15}$$

Under the assumption that both the sextupole system and the WFT 1-3 behave in an ideal way, it follows that

$$\varepsilon_{12}\varepsilon_{23} = R_M^W - 1. \tag{8.16}$$

8.5 Efficiencies of a Medium Field Transition for Deuterium

A medium field transition for deuterium consists of up to three occupation transfers simultaneously – 1-2, 2-3 and 3-4 –, whose efficiencies ought to be determined separately, as in the medium field transition for hydrogen. For this purpose now two additional high frequency transitions before the medium field transition are necessary instead of one. However, it is found that the procedure in chapter 8.4, which for hydrogen leads to a quadratic equation for the efficiency ε_{23}, does not lead to a cubic equation when applied to a medium field transition for deuterium, but to an equation of higher order for the efficiency ε_{34} [130]. It was not yet possible to reduce this equation to a cubic equation. Thus the efficiency measurement for a medium field transition for deuterium can in principle be carried out, but at the moment no practical method exists to extract the efficiencies for all three occupation transfers from these measurements alone.

Nevertheless, the medium field transitions are necessary for the polarization measurements, since without them the minimum number of five high frequency transitions cannot be reached. Additional to the three strong field transitions SFT 1-6, SFT 2-6 ad SFT 3-5 at least two medium field transitions are needed. If the MFT 1-4 is avoided, the remaining medium field transitions MFT 2-4 and MFT 3-4 consist of maximally two simultaneous transfers. Assuming that the transfer 1-2 is completely suppressed in these cases and that $\varepsilon_{12} = 0$ is valid, it is sufficient to measure the efficiencies ε_{23} and ε_{34} for a quantitative analysis of the the effect of these two medium field transitions onto an atomic beam. However, this method does not allow a quantitative statement about how well the transfer 1-2 is suppressed in reality. In the case of hydrogen this was still possible through the measurement of the efficiency ε_{12} of the MFT 2-3. On the other hand, figure 5.8 shows that the MFT 1-4 cannot be operated for the chosen settings. The field gradient is set to such a weak value that the three transfers 1-2, 2-3 and 3-4 cannot occur simultaneously in the region of the high frequency field. Therefore the assumption $\varepsilon_{12} = 0$ can be justified for the chosen settings for the medium field transitions MFT 2-4 and MFT 3-4.

As the measurement of the two efficiencies ε_{23} and ε_{34} is sufficient for the transitions MFT 2-4 and MFT 3-4, it is possible to use the procedure from chapter 8.4 without any significant changes also in the case of a medium field transition for deuterium. As in the case of hydrogen, only for an efficiency measurement one additional high frequency transition with known efficiency is needed in front of the medium field transition. A total of four beam signals is measured. From these follow the efficiency of the additional high frequency transition and two signal ratios analogous to the equations (8.9) and (8.11):

$$R_M = \frac{S_{MFT\,on}}{S_{MFT\,off}} = 1 - \frac{a\varepsilon_{23} + b\varepsilon_{34} + c\varepsilon_{23}\varepsilon_{34}}{d} \tag{8.17}$$

$$R_M^S = \frac{S_{MFT\,on}^{SFT\,on}}{S_{MFT\,off}^{SFT\,on}} = 1 - \frac{a'\varepsilon_{23} + b'\varepsilon_{34} + c'\varepsilon_{23}\varepsilon_{34}}{d'}. \tag{8.18}$$

The coefficients a, b, c and d depend only on the transmission of the overall system:

$$\begin{aligned} a &= \sigma_{22} + \sigma_{33} - \sigma_{23} - \sigma_{32} && \longrightarrow \; 0 \\ b &= \sigma_{33} + \sigma_{44} - \sigma_{34} - \sigma_{43} && \longrightarrow \; 1 \\ c &= \sigma_{23} + \sigma_{34} - \sigma_{33} - \sigma_{24} && \longrightarrow \; 0 \\ d &= \sigma_{11} + \sigma_{22} + \sigma_{33} + \sigma_{44} + \sigma_{55} + \sigma_{66} && \longrightarrow \; 3. \end{aligned} \tag{8.19}$$

The primed coefficients a', b', c' and d' depend on the choice of the additional high frequency transition. Of the three possible strong field transitions in the source the SFT 2-6 or the SFT 3-5 could be used. If the SFT 2-6 is used, the coefficients become

$$\begin{aligned} a' &= a - \varepsilon_{26}\left(\sigma_{22} + \sigma_{63} - \sigma_{23} - \sigma_{62}\right) && \longrightarrow \; 0 \\ b' &= b && \longrightarrow \; 1 \\ c' &= c - \varepsilon_{26}\left(\sigma_{23} + \sigma_{64} - \sigma_{24} - \sigma_{63}\right) && \longrightarrow \; -1 \\ d' &= d - \varepsilon_{26}\left(\sigma_{22} + \sigma_{66} - \sigma_{26} - \sigma_{62}\right) && \longrightarrow \; 2, \end{aligned} \tag{8.20}$$

while for the SFT 3-5 the coefficients become

$$\begin{aligned} a' &= a - \varepsilon_{35}\left(\sigma_{33} + \sigma_{52} - \sigma_{32} - \sigma_{53}\right) && \longrightarrow \; 0 \\ b' &= b - \varepsilon_{35}\left(\sigma_{33} + \sigma_{54} - \sigma_{34} - \sigma_{53}\right) && \longrightarrow \; 0 \\ c' &= c - \varepsilon_{35}\left(\sigma_{34} + \sigma_{53} - \sigma_{33} - \sigma_{54}\right) && \longrightarrow \; 1 \\ d' &= d - \varepsilon_{35}\left(\sigma_{33} + \sigma_{55} - \sigma_{35} - \sigma_{53}\right) && \longrightarrow \; 2 \end{aligned} \tag{8.21}$$

The solution of a quadratic equation follows as described in chapter 8.4. Only the efficiencies ε_{12} and ε_{23} are replaced by the efficiencies ε_{23} and ε_{34}.

The results for the efficiencies of the medium field transitions that follow from the use of either of the two strong field transitions will be compared in chapter 8.7.

8.6 Analysis of the Efficiency Measurements

8.6.1 Interpretation of the Measured Signal Ratios

From the signal ratios measured with the apparatus as described in chapter 8.1 and according to the procedures in chapters 8.3 to 8.5 just as many independent equations may be formed as there are efficiencies to determine. However, the transmissions of the sextupole system appear as additional unknown parameters in theses equations. As will be seen in the following (figure 9.3), these may not be neglected especially in the hydrogen measurement, despite the presence of the beam blocks in the sextupole systems. Therefore it may not be possible in all cases to obtain all necessary parameters for the determination of the efficiencies from experiment.

This problem of an under-determinate system may be attacked in two different ways, that mostly differ in the interpretation of the measured signal ratios. These two interpretations are listed in the following together with their most important characteristics:

- Interpretation as efficiency measurements:
  - Determination of the transmission corrections by Monte Carlo simulation (chapter 6).
  - A direct beam from the atomic beam source is necessary.

+ Efficiencies $\varepsilon_{ij} < 1$ can in principle be measured.

- Interpretation as transmission measurements:
  - The efficiencies determine the quality of the measurement and result indirectly from the uncertainty of the transmission measurement.
  - For a large part of the occupation transfers only the verification of $\varepsilon_{ij} = 1$ is possible with a justifiable uncertainty.
  + If certain high frequency transitions are operated in an ideal way, all needed parameters can be determined experimentally.
  + No Monte Carlo simulation is needed.
  + The procedure can also be carried out for a beam of unknown hyperfine occupancy (chapter8.8).
  + It allows a precise check of the Monte Carlo simulation of sextupole magnet systems (chapter 9.1).

In the first variant an experimental determination of the transmission corrections is foregone. Instead they are determined with the help of Monte Carlo simulations (chapter 6). Although the results of this simulation could be experimentally verified by the second method (!) (chapter 9.1), the uncertainties on the results are large without this check.

For this method a direct beam from the atomic beam source is needed that guarantees an equal distribution of hyperfine occupancies in the atomic beam before it enters the first sextupole magnet to be able to determine the transmission corrections. However, this beam is a nozzle beam, whose properties following chapter 6.2 can be parameterized by three parameters v_{drift}, T_{beam} and K_{mol}. Extensive measurements of the velocity distribution of the generated beam were carried out on the source of the HERMES experiment [128, 131, 108] and the first two parameters were determined for a wide variety of running conditions. Unfortunately these measurements could not be carried out for the test source due to details of the construction and it seems to be at least questionable whether the results from the HERMES source can be transferred to the test source, as the geometries of the beam formation systems differ.

Until now no procedure is known for the direct measurement of the third parameter K_{mol}. But the molecularity of the beam determines the angular momentum distribution on entry into the sextupole magnet system and thus influences it's focusing properties (figure 6.1). The beam parameters needed for the Monte Carlo generator therefore are in general not completely known, so that the first variant should not be used if the transmission corrections exceed the statistical error of an efficiency measurement.

In the second variant the signal ratios are not interpreted as efficiency measurements in the direct sense of the word, but as transmission measurements. If for example in the case of hydrogen the WFT 1-3 is activated between the sextupole magnets in the source and the polarimeter, the state $|1\rangle$ is removed from the beam and the atomic beam detector measures the intensity of the state $|2\rangle$. The SFT 2-4 on the other hand depopulates the state $|2\rangle$, so that the intensity of the state $|1\rangle$ is measured. The ratio of these two intensities then directly corresponds to the transmission ratio σ_{22}/σ_{11}.

The uncertainty of the transmission ratio measurement is determined by the inefficiency of both high frequency transitions and thus can be evaluated according to the argument in chapter 8.6.2. The procedure is based on the requirement that the derived efficiencies must be physically *consistent*, i.e. all efficiencies must fulfill the condition

$$0 \leq \varepsilon_{ij} \leq 1 \tag{8.22}$$

In chapter 8.6.4 this requirement is applied to the total set of all efficiency measurements. The derived inefficiencies however cannot be unambiguously attributed to an individual occupation transfer. Therefore, with respect to the above example, in a measurement of the transmission ratio σ_{22}/σ_{11} it cannot be decided if it's uncertainty is caused by an inefficiency of the WFT 1-3, the SFT 2-4 or both transitions. The inefficiencies can always be the result of several, at least two, transfers.

If the concerned transitions are working nearly ideally, also the uncertainty of the transmission measurement becomes small. Additionally, the proof is given that the concerned occupation transfers occur within the same uncertainty with ideal efficiencies $\varepsilon = 1$. As soon as a transmission correction has been determined in this way, it can be used to measure the efficiencies of further transitions that use the same corrections with the same accuracy, independent of their efficiency. This would be an efficiency measurement in the proper meaning of the term.

The results compiled in chapter 8.7 support the idea that high frequency transitions can in fact be technically realized with efficiencies of $\varepsilon_{ij} = 1$. This makes the second variant technically viable. The results presented in this chapter were with no exception gained on the basis of the second variant, and are thus entirely based on purely experimental results, without the help of Monte Carlo simulations. A further advantage of this method is the possibility to also use a beam from a storage cell with unknown hyperfine occupancy (chapter 8.8) and to test the Monte Carlo simulation by comparison with the measured transmission ratios (chapter 9.1).

8.6.2 Ostensive Efficiencies and the Consistency Requirement

Before the consistency requirement (8.22) is applied to the entirety of all efficiency measurements, it's effective functionality will be discussed using the hydrogen transitions SFT 1-4, SFT 2-4 and WFT 1-3 as a simple and clear example. In each of these transitions only one occupation transfer occurs. Therefore only one transmission ratio σ_{22}/σ_{11} enters into the analysis of these efficiency measurements.

First the signal ratios needed for the efficiencies of these transitions are measured for sextupole currents between 100 and170 A[10]. Then the efficiencies are calculated according to (8.5), assuming that the sextupole system behaves ideally, i.e. that $\kappa_{ij} = 2$.

The *ostensive* efficiencies $\tilde{\varepsilon}_{ij}$ gained in this way are plotted in figure 8.6.2 versus the current of the sextupole in the source. This method of plotting only represents a suitable scaling of the measured signal ratios, in other words they are still completely uninterpreted raw data. The scaling only has the effect that for an ideal sextupole system the efficiency of the concerned transition would have been obtained. These seeming corrections do not yet contain any sextupole corrections and the efficiencies $\tilde{\varepsilon}_{ij} > 1$ that occur are of course non-physical and not equal to the real efficiencies ε_{ij}.

To clarify this way of plotting the data, it helps to look at the the mathematical relationship between ostensive and real efficiencies, that follows from (8.5) by explicitly replacing the correction factor κ_{ij} by 2 :

$$\tilde{\varepsilon}_{ij} = \frac{2}{\kappa_{ij}\left(B_{pt}\right)}\varepsilon_{ij}. \tag{8.23}$$

The real efficiencies ε_{ij} to a good approximation are intrinsic properties of the high frequency transitions and are thus independent of the properties of the sextupole system. The sextupole corrections on the other hand depend on the properties of the sextupole system and thus on the pole tip field of the source sextupole. This can be seen explicitly in (8.23). It is this dependency

[10]Despite the beam block in the sextupole magnet of the atomic beam source the contributions of the states $|3\rangle$ and $|4\rangle$ can only be neglected for currents above about 80 A

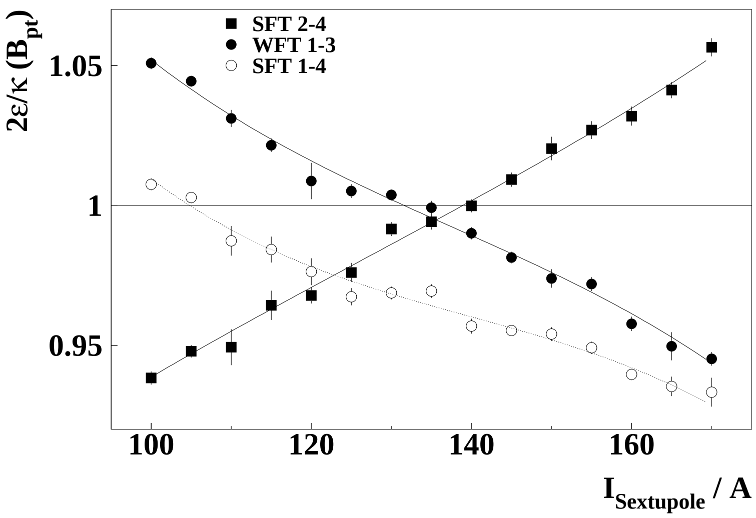

Fig. 8.2:
Ostensive efficiencies of the high frequency transitions WFT 1-3, SFT 1-4 and SFT 2 without consideration of the sextupole corrections as a function of the sextupole current. The measured data were fitted with third degree polynomials

that finds it's expression in the variation of the scaled signal ratios with the sextupole current as shown in figure 8.6.2. Therefore the transmission ratio σ_{22}/σ_{11} must vary with the sextupole current in exactly such a way, that the sextupole corrections according to (8.7) transform all ostensive efficiencies in figure 8.6.2 into horizontal lines for the real efficiencies.

Turther considerations will for now be concentrated on the transitions WFT 1-3 and SFT 2-4. There ostensive efficiencies depend in a roughly linear way on the pole tip field of the source sextupole. The transmission ratios enter reciprocally into the sextupole correction for these transitions (8.7), so that the slopes have opposite signs and the curves intersect at a sextupole current of about 135 A with an ostensive efficiency above 0.995.

If it is assumed that the WFT 1-3 operates with an efficiency of 0.95, then the sextupole correction for this transition for a sextupole current of 135 A that follows from (8.23) and figure 8.6.2 becomes $\kappa_{13} \approx 1.9$. According to (8.7) this implies immediately that the correction for the SFT 2-4 must be $\kappa_{24} \approx 2.1$, because the transmission ratio σ_{22}/σ_{11} that the corrections are based on must be the same in both cases. The actual efficiency found for the SFT 2-4 is $\varepsilon_{24} \approx 1.05$, so that $\varepsilon_{24} > 1$. The other way around the assumption of an efficiency of 0.95 for the SFT 2-4 leads to an efficiency of $\varepsilon_{13} \approx 1.05$ for WFT 1-3.

The phase space for the transmission ratio σ_{22}/σ_{11}, and thus the sextupole correction, is severely restricted by the fact that none of the real efficiencies may exceed 1. It follows that the sextupole system must be behaving almost ideally ($\sigma_{22}/\sigma_{11} \approx 1$) for 135 A and that the efficiencies of the transitions WFT 1-3 and SFT 2-4 must both be larger than 0.995. This result could already be deduced from the measurement shown in figure 5.4. The maximal or minimal correction that can be applied to both efficiencies without one of them exceeding the ideal value of $\varepsilon = 1$ leads to the overall inefficiency of the transitions and thus to the error on the transmission ratio.

This line of argument can be extended to other values of the sextupole current without difficulty. For each sextupole current a different transmission ratio ensues, but the efficiencies always stay the same. The results for the efficiencies are compiled for all high frequency transitions in chapter 8.7. In chapter 9.1 the dependence of the transmission ratios on the sextupole current, which can be measured to high accuracy with this method, will be compared to the Monte Carlo simulation from chapter 6.

Following the above interpretation of the measured data, the two equations (8.5) for the efficiencies of these two transitions result in only two parameters: A transmission ratio and an overall inefficiency for both transitions. However, it is not possible to decide how this inefficiency is distributed over the two transitions. Therefore efficiencies with sufficient precision follow from this method only when there is a depopulated state for each focused state in the beam and also when each one of the transitions is operating with nearly perfect efficiency. The error on this method increases linearly with the inefficiency of the transitions.

The dependence of the uncertainties on the efficiencies becomes apparent, when figure 8.6.2 is viewed under the assumption that the WFT 1-3 would not be available. In this case the analysis would have to be based on the results for the transitions SFT 1-4 and SFT 2-4 alone. They intersect at an ostensive efficiency of only about 0.975. The efficiencies of these transitions could therefore be corrected by ± 0.025 without running into inconsistencies.

After the analysis of the signal ratio for WFT 1-3 and SFT 2-4 the sextupole corrections are known to be highly accurate. This makes it possible to determine the efficiency of the transition SFT 1-4 directly according to (8.5) and (8.7), although the efficiency of this transition differs significantly from the ideal value of 1. This is a typical example for an actual efficiency measurement.

8.6.3 Dependence of the Efficiencies on the Sextupole System

In the previous subchapter it was assumed that efficiencies are intrinsic properties of the high frequency transitions. This assumption is also made when the results of the efficiency measurements are used for the polarization measurements. However, this is only permissible if the high frequency transitions are operated in saturation.

On the one hand, polarization measurements analyze a beam from a storage cell, which in general has a different velocity distribution than the beam from the test source as it is used in the efficiency measurements (chapter 9.2 and 9.4). However, the efficiency of a transition can also depend on the velocity of the atoms in the beam, as these enter into the adiabatic condition (5.4).

On the other hand, the amplitude of the HF-field does not have to be constant over the entire region of the transition, so that the diameter of the beam, which is also influenced by the focusing properties of the sextupole system, can change the efficiency of the transition.

The measurement of the efficiencies for different pole tip fields in the sextupole magnet of the source gives information about the quality of the above assumption, because different velocities are filtered out of the beam and focused into the sextupole system of the polarimeter, when the pole tip field is changed (figure 9.4).

Effects of the focusing properties on the efficiency of a transition could only be demonstrated for the SFT 1-4 for hydrogen. The efficiency of this transition in the region below 130 A is smaller by about 0.01 compared to the region above 130 A. This is visible in figure 8.6.2 in the light curvature of the fit in the region below 130 A. Here it must be taken into account that the SFT 1-4 represents a π-transition and that it was operated with a resonator that was specifically constructed for the σ-transition SFT 2-4. Therefore the component of the HF-field that is perpendicular to the static field and which is needed for the SFT 1-4 can only be weakly expressed. Variations of the HF-amplitude in the region of this transition thus have a far stronger effect than in the high frequency transitions. This effect on the efficiency of SFT 1-4 was accounted for by an additional uncertainty of 0.01 on the efficiency of this transition.

From the excellent results for the efficiency of the SFT 2-4 it may be concluded that the newly built band conductivity resonator with tilted resonator rods (figure 4.5) is suited to also operate the SFT 1-4 in an optimal way. In particular no dependency of it's efficiency on the properties of the sextupole system could be detected any more with the used setup. In general it may be assumed that effects of this kind may be neglected, if the high frequency transition is operated far into saturation, that is with the highest possible HF-power, so that efficiencies close to 1 are reached.

8.6.4 The Application of the Consistency Requirement to all Transitions.

The application of the consistency requirement to the total set[11] of all efficiency measurements is facilitated with the help of a computer program. This allows the consideration of all correlations between the efficiency measurements of the individual transitions in the analysis. Otherwise they might have a restrictive effect on the transmissions.

In the case of hydrogen, the three dimensional parameter space defined by the normalized transmissions σ_{12}, σ_{21} and σ_{22} is analyzed in search of consistent parameter sets according to (8.22)in the interval $[0,8;1,2]$[12] in steps of 0.001. For each one of these parameter sets sextupole corrections are calculated and together with the measured signal ratios the efficiencies are obtained. These are then checked for consistency. Only if all efficiencies for one given set of transmissions are within the allowed consistency interval these transmissions can be correct within the uncertainties for the given sextupole system. Consistent parameter sets are stored and returned at the end of the program.

The physically well defined interval for the efficiencies of $[0;1]$ is extended by the statistical errors of the efficiency measurements of the concerned transitions to $[0-\Delta\varepsilon_{ij};1+\Delta\varepsilon_{ij}]$ to account for the uncertainties of the measurement. A good approximation of theses uncertainties is obtained from the analysis of the efficiency measurements under the assumption that the sextupole system is in fact behaving ideally. In this case the statistical errors of the ostensive efficiencies are used to set $\Delta\varepsilon_{ij} \approx \Delta\hat{\varepsilon}_{ij}$.

The requirement that no efficiency must be negative leads to another restriction, because the efficiency ε_{12} of the MFT 2-3 ideally is zero. For all efficiencies and transmissions thus a consistency interval is defined, within which the parameter may vary without contradiction to the consistency requirement. The center of this interval is interpreted as the result for this parameter, the half-width of the interval as overall uncertainty i.e. the sum of statistical and systematic error.

A total of eight normalized transmissions is needed for the complete analysis of the efficiency measurements of the deuterium transitions. However, due to the fact that the MFT 1-4 is not used and the efficiency ε_{12} for the other two medium field transitions is waived, the number of needed normalized transmissions is reduced to four: σ_{22}, σ_{33}, σ_{23} and σ_{32}. Despite this reduction the method that was used for hydrogen cannot be directly applied to deuterium. Searching through a four-dimensional parameter space with the same resolution as for hydrogen would take up about one CPU-year. The searching of the three-dimensional parameter space for hydrogen on the other hand takes only a few hours.

For this reason the analysis of the efficiency measurements for deuterium is separated into to steps: First only the normalized transmissions σ_{22} and σ_{33} are determined together with the efficiencies of all strong field transitions. In the second step the two other transmissions σ_{23}

[11] Total set refers to the set of all efficiency measurements for a fixed sextupole system, in this case also a fixed value for the sextupole current. The information about the behaviour of the measured signal ratios on the variation of a parameter is not necessary for the analysis of the efficiency measurements. However, the examination of the variation in the sextupole system in this thesis shows, that the consistency method cannot only be applied to a particular sextupole system, but that it is generally applicable.

[12] This interval was chosen in such a way as to include all consistent parameter sets within it's boundaries. It does not restrict the possible solution in any way.

Tab. 8.1:
Efficiencies of the high frequency transitions for hydrogen. For the measurement of the high frequency power of the strong field transitions no suitable reflectometer for the concerned frequency range was available.

	Transition	Transfer	ν[MHz]	P[W]	ε_{ij}[%]	$\Delta\varepsilon_{ij}$[%]
Source	WFT 1–3		12.0	0.4	99.50	0.77
Polarimeter	SFT 1–4		1425.6	—	96.55	1.24
	SFT 2–4		1425.6	—	99.52	0.78
	MFT 1–3	1–2	68.2	3.6	99.16	1.82
	MFT 1–3	2–3	68.2	3.6	99.47	0.94
	MFT 2–3	1–2	68.2	1.0	1.40	1.75
	MFT 2–3	2–3	68.2	1.0	97.56	0.84

and σ_{32} are determined together with the efficiencies of the medium field transitions. Here the results for the other two transitions from the first step are assumed as given.

8.7 Results of the Efficiency Measurements

The results of the efficiency measurements that are compiled into tables in this chapter were determined exclusively on the basis of the consistency method and without the use of Monte Carlo simulations. The measured signal ratios were interpreted as transmission measurements and the efficiencies were derived indirectly from those. This must be considered in the interpretation of the results, especially in the interpretation of the listed uncertainties. The uncertainties in the tables contain the statistical and the systematic errors of the method and enter into the systematic uncertainty of a polarization measurement. All errors are given as absolute errors. Additionally, the frequencies and the power with which the transitions were operated are listed as well.

The efficiencies for the occupation transfers in the hydrogen transitions (table 8.1) are largely compatible with their ideal value with two exceptions. The efficiencies that result from the measurement of a single signal ratio have a maximal uncertainty of 0.85 %.

The uncertainties of the efficiencies ε_{12} of the middle field transitions are somewhat larger with values of 1.8 %, because it includes the analysis of further sextupole components, the uncertainty of the efficiency ε_{23} of the middle field transition itself and the uncertainty of the efficiency of WFT 1-3.

As in the cases of the transitions SFT 2-4 and WFT 1-3, the efficiency of the SFT 1-4 could be derived from the data with an uncertainty of 0.8 %. The value quoted in the table also includes an additional error of 1 % due to the dependency of its real efficiency on the properties of the sextupole system. However, it should be possible to further increase the somewhat lower efficiency of this transition by using a resonator with tilted rods (figure 4.5).

The efficiency ε_{23} of the MFT 2-3 is significantly lower than 100 %. The reason for this nonetheless small inefficiency can be found in the static magnetic field and the gradient field for this transition. In the time available no setting could be found that simultaneously fulfilled both conditions, $\varepsilon_{12} = 0$ and $\varepsilon_{23} = 1$, for an ideal MFT 2-3. Nevertheless, the important parameter for the error on a polarization measurement is the uncertainty on this efficiency, which despite the inefficiency of this transfer is only 0.84 %

The quoted total uncertainties for the efficiencies of the hydrogen transitions are roughly equal to twice the statistical error. The systematic errors resulting from the application of the consistency method are thus comparable to the statistical errors.

	Transition	ν[MHz]	P[W]	ε_{ij}[%]	$\Delta\varepsilon_{ij}$[%]
Quelle	SFT 1–6	405.3	3.5	98.59	1.89
	SFT 2–6	405.3	3.5	98.61	1.87
	SFT 3–5	405.3	3.5	98.68	1.92
Polarimeter	SFT 1–6	419.1	4.5	94.70	1.82
	SFT 2–6	419.1	4.5	93.32	1.77
	SFT 3–5	419.1	4.5	94.61	1.84

Tab. 8.2:
Efficiencies of the strong field transitions for deuterium

The same low systematic errors could not yet be achieved for the deuterium transitions. The total uncertainty for the efficiencies of the strong field transitions (table 8.2) are about 1.9 %, while the statistical errors of the measurements are as in the case of hydrogen only 0.4 %. The quoted uncertainties are thus predominantly caused by the systematic errors due to inefficient occupation transfers.

This fact leads to consequences for the interpretation of these uncertainties. Not all three occupation transfers can be ideal, although the values for the strong field transitions in the source that are listed in table 8.2 imply efficiencies that within errors are compatible with the ideal value of 100 %. The systematic error of about 1.8 % indicates that at least one of the three transfers, perhaps even two or three, are not working with full efficiency. It cannot be concluded from the experimental data alone, which transfers are inefficient and therefore cause the error. [13] The strong field transitions in the polarimeter had to be operated without a resonance feedback circuit (figure 4.4), because at the time of the measurements such a circuit was only available for the strong field transitions in the source. Significantly lower efficiencies were measured, whose total uncertainty corresponds to the error of the strong field transitions in the source, because the necessary sextupole corrections and their errors were already determined by the efficiency measurements on these transitions. The significantly lower efficiencies of the strong field transitions in the polarimeter illustrate, that a resonance feedback is a necessary precondition for the reliable and stable operation of a strong field resonator. In the HERMES experiment all strong field transitions are fitted with a resonance feedback.

The efficiency measurements for the medium field transitions for deuterium can be performed in two different ways according to chapter 8.5, using either SFT 2-6 or SFT 3-5. As illustrated by the results in table 8.3, both methods agree very well. The uncertainties of these efficiencies are mainly caused by the error of the efficiency of the additionally needed strong field transition. Therefore an improvement of the strong field transitions will also lead to a reduced error of the medium field transition efficiencies.

		mit SFT 2-6		mit SFT 3-5	
Transition	Resonance	ε_{ij}[%]	$\Delta\varepsilon_{ij}$[%]	ε_{ij}[%]	$\Delta\varepsilon_{ij}$[%]
MFT 2–4	2–3	99.64	2.31	99.13	2.68
MFT 2–4	3–4	99.01	2.50	98.28	3.09
MFT 3–4	2–3	1.94	1.87	1.65	1.92
MFT 3–4	3–4	99.75	1.87	99.74	1.92

Tab. 8.3:
Efficiencies of the medium field transitions for deuterium. The transitions were operated at a frequency of 17.0 MHz with a power of 4 Watt

[13] Monte Carlo simulations for the determination of sextupole corrections would of course allow to do so. However, for the deuterium measurements with the test stand no simulations were carried out (chapter 9.7).

8.8 Efficiency Measurements during the HERMES Experiment

For the H/D-target in the HERMES experiment a 30° tilt of source and polarimeter relative to the horizontal is envisaged (figure 1.3). Thus the collinear setup of atomic beam source and polarimeter used in the previous efficiency measurement (figure 8.1) cannot be reproduced.

This leads to the question, how the calibration of the polarimeter as described in this chapter can also be carried out under the circumstances determined by the HERMES experimental setup, without having to remove the polarimeter from the target area and calibrating it on an external test stand.

Up to now it was assumed for the efficiency measurements that in the first step a uniformly populated atomic beam enters into a sextupole magnet, which then defocuses the states $|3\rangle$ and $|4\rangle$ and thus removes them from the beam (8.4). If a beam block with sufficient diameter is placed on the axis of the magnet, the sextupole behaves in this sense ideally and the following occupancy is obtained from the magnet:

$$\begin{pmatrix} 1 \\ 1 \\ 1 \\ 1 \end{pmatrix} \xrightarrow{\text{sextupole}} \begin{pmatrix} \sigma_1 \\ \sigma_2 \\ 0 \\ 0 \end{pmatrix} \longrightarrow \ldots. \tag{8.24}$$

The transmissions σ_1 and σ_2 of the source sextupole as well as their ratio are not needed for the analysis of an efficiency measurement. Instead of them the normalized transmissions of the overall system σ_{12}, σ_{21} and σ_{22} enter into the sextupole corrections. These on the other hand can be determined experimentally by applying the consistency condition (8.22). Therefore efficiency measurements can be carried out even if the transmissions σ_1 and σ_2 of the source sextupole are not know, although the transmissions of the overall system depend on them. It is sufficient, to produce a beam that only contains the states $|1\rangle$ and $|2\rangle$. The ratio of these two occupancies is not needed for an efficiency measurement according to the consistency method.

According to this argument, also the knowledge of the occupancies before the first sextupole is not a necessary precondition for an experimental determination of the sextupole corrections for an efficiency measurement. A calibration of the Breit-Rabi polarimeter can also be carried out with an atomic beam of completely unknown hyperfine occupancy, e.g. a beam from a storage cell, if an additional sextupole magnet between storage cell and polarimeter ensures that the states $|3\rangle$ and $|4\rangle$ are entirely removed from the beam (figure 8.3).

For the complete suppression of these states the sextupole must be equipped with a beam block on it's axis that must be removable, so that polarization measurements can also be carried out.

After the additional sextupole between storage cell and polarimeter the occupancy becomes

$$\begin{pmatrix} n_1 \\ n_2 \\ n_3 \\ n_4 \end{pmatrix} \xrightarrow{\text{sextupole}} \begin{pmatrix} n_1\sigma_1 \\ n_2\sigma_2 \\ 0 \\ 0 \end{pmatrix} \longrightarrow \ldots. \tag{8.25}$$

instead of (8.24).

The methods for the efficiency measurements used with the straight setup can be transferred completely to the setup for the HERMES experiment, if in the calculation of the beam intensities the first sextupole operation (8.24) is replaced by (8.25). The corrections are not longer determined by the transmissions of the overall system alone, but also by the occupancies n_1 and

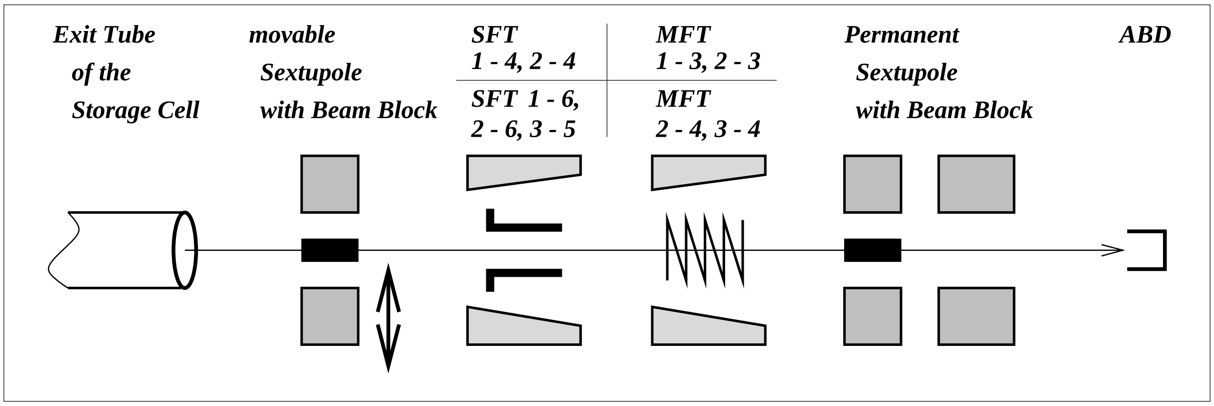

Fig. 8.3:
Setup of the Breit-Rabi polarimeter for the HERMES experiment. A movable sextupole magnet with beam block for calibration purposes is placed in front of the actual polarimeter. The strong and medium field transitions each have their own magnets for the static fields and field gradients. The strong field transitions must be positioned in front of the medium field transitions.

n_2 of the beam that is extracted from the storage cell. The transmission ratios are replaced as follows:

$$\frac{\sigma_{12}}{\sigma_{11}} \longrightarrow \frac{n_1\sigma_{12}}{n_1\sigma_{11}} \qquad \frac{\sigma_{21}}{\sigma_{11}} \longrightarrow \frac{n_2\sigma_{21}}{n_1\sigma_{11}} \qquad \frac{\sigma_{22}}{\sigma_{11}} \longrightarrow \frac{n_2\sigma_{22}}{n_1\sigma_{11}}. \tag{8.26}$$

The transmission ratios for deuterium can be extended by the occupancies n_1, n_2 and n_3 in an analogous way. These extended transmission ratios can be determined through the consistency condition with the same degree of precision as the original transmission ratios. This is true as long as certain high frequency transitions reach efficiencies of almost 100 %.

The WFT 1-3 is not available in the setup for the HERMES experiment. Therefore a transition in front of the medium field transition is needed to facilitate the measurement of it's efficiencies. This task of the WFT 1-3 can be taken over by one of the two strong field transitions SFT 1-4 or SFT 2-4. It only must be ensured that it can be operated separately from the medium field transitions, i.e. both transitions must be equipped with their own magnet for the generation of static fields and field gradients (see figure 8.1 and figure 8.3). The strong field transition must be positioned in front of the medium field transition.

A further condition for the realization of this method is that the atomic beam from the storage cell contains sufficient amounts of both states, $|1\rangle$ and $|2\rangle$. This condition can be fulfilled easily by operating the atomic beam source without a high frequency transition, so that exactly these states are injected into the storage cell.

As a result of the replacement of the WFT 1-3 by one of the two strong field transitions, the corrections listed in chapter 8.4 must be re-evaluated. The following coefficients for the SFT 1-4 replace the coefficients (8.12):

$$\begin{array}{rcllr} a' & = & a - \varepsilon_{14}\left(\sigma_{11}+\sigma_{42}-\sigma_{12}-\sigma_{41}\right) & \longrightarrow & 0 \\ b' & = & b & \longrightarrow & 1 \\ c' & = & c - \varepsilon_{14}\left(\sigma_{12}+\sigma_{43}-\sigma_{13}-\sigma_{42}\right) & \longrightarrow & -1 \\ d' & = & d - \varepsilon_{14}\left(\sigma_{11}+\sigma_{44}-\sigma_{14}-\sigma_{41}\right) & \longrightarrow & 1. \end{array} \tag{8.27}$$

If the SFT 2-4 is used instead, the coefficients become

$$\begin{array}{rcllr} a' & = & a - \varepsilon_{24}\left(\sigma_{22}+\sigma_{41}-\sigma_{21}-\sigma_{42}\right) & \longrightarrow & 0 \\ b' & = & b - \varepsilon_{24}\left(\sigma_{22}+\sigma_{43}-\sigma_{23}-\sigma_{42}\right) & \longrightarrow & 0 \\ c' & = & c - \varepsilon_{24}\left(\sigma_{23}+\sigma_{42}-\sigma_{22}-\sigma_{43}\right) & \longrightarrow & 1 \\ d' & = & d - \varepsilon_{24}\left(\sigma_{22}+\sigma_{44}-\sigma_{24}-\sigma_{42}\right) & \longrightarrow & 1 \end{array} \tag{8.28}$$

9 Transmissions

There are in total three different types of transmission probabilities that are relevant for the measurements described in this thesis. These transmission probabilities are compiled together with their most important properties in the following list.

- The transmissions of the sextupole magnet system of the source σ_i^Q:
  - They determine the hyperfine occupancy of the atomic beam injected into the cell
  - and they cannot be measured.[14]
  - The storage cell is located in the line of the beam (figure 1.4).
  - The nozzle serves as source and the cell entrance tube as target.
  - A Monte Carlo generator for a beam from a nozzle is needed (chapter 6.2).
- The transmissions of the sextupole system of the polarimeter σ_i^P:
  - They are needed as corrections for the calculation of the polarization from the measured signal ratios
  - and they also cannot be measured.[14]
  - The storage cell is located in the line of the beam (figure 1.4).
  - The cell exit tube serves as source and the atomic beam detector as target.
  - A Monte Carlo Generator for an effusive beam is needed (chapter 6.3).
  - There are no free parameters.
- The transmissions of the overall system of source and polarimeter σ_{ij}:
  - They are needed as corrections for the efficiency measurements
  - and they can be measured.
  - The storage cell is not located in the line of the beam. (figure 8.1).
  - The nozzle serves as source and the atomic beam detector as target.
  - A Monte Carlo generator for a beam from a nozzle is needed (chapter 6.2).

The most important goal of this chapter certainly is the determination of the transmissions in the sextupole system of the polarimeter σ_i^P (chapter 9.3), since these are needed as corrections in the analysis of the measured signal ratios (chapter 7.1) and thus contribute to the systematic error of the polarization measurement. These transmissions cannot be measured, so that their determination has to rely on a Monte Carlo simulation. However, as there are no free parameters in the generation of the starting conditions, these transmissions can be determined unambiguously by a correctly working Monte Carlo simulation.

The transmissions in the overall system σ_{ij} could be derived from the efficiency measurements due to the almost ideal operation of the high frequency transitions (chapter 8.6). They are used in chapter 9.1 for a high precision check of the simulation program used for the other transmissions

[14] If a sextupole system behaves ideally in the sense that the transmissions of the defocussed states completely vanish and the transmissions for the focused states are identical, this ideal behaviour may be experimentally detected within the measurement uncertainties. This is for example the case for the deuterium measurements (chapter 9.7). Deviations from this ideal case can only be quantified in a model dependant way (appendix C) or based on Monte Carlo simulations. At least for this apparatus this is the case.

before this program is used to determine σ_i^Q and σ_i^P The chapters 9.2 and 9.4 deal with the velocity profiles of the different sextupole systems for efficiency and polarization measurements. The transmissions and velocity profiles for the sextupole magnet of the source σ_i^Q are discussed in the chapters 9.5 and 9.6

As in the case of deuterium, no sextupole corrections have to be used in the light of the measurement uncertainties reached until now, the following will focus exclusively on the transmission of hydrogen atoms. However, there are some additional reasonings in chapter 9.7.

9.1 Transmissions in the Rabi setup

The main goal of this subsection is to prove that the transmissions extracted from efficiency measurements in the Rabi setup (chapter 8.6) can be reproduced with the help of the Monte Carlo simulation described in chapter 6. For the production of the necessary jet in the simulation program (chapter 6.2) the following parameterization is used:

$$K_{\mathrm{mol}} = 0.4 \qquad v_{\mathrm{drift}} = 1484\,\mathrm{m\,s^{-1}} \qquad T_{\mathrm{beam}} = 234\,\mathrm{K} \tag{9.1}$$

v_{drift} and T_{beam} were derived from measurements of velocity distributions carried out by B. Lorentz using an aluminum nozzle with a diameter of 5 mm and a gas flux of $0.5\,\mathrm{mbar\,l\,s^{-1}}$ together with the atomic beam source of the HERMES experiment[108]. Here it was assumed that the glass nozzle used at the test beam was at room temperature, about 300 K. The parameter K_{mol} was derived from fits to the following measurements.

Measurements of the velocity distribution in the produced atomic beam that would have at least yielded v_{drift} and T_{beam} would have involved considerable reconstruction of the test source. Thus it was decided to do without them.

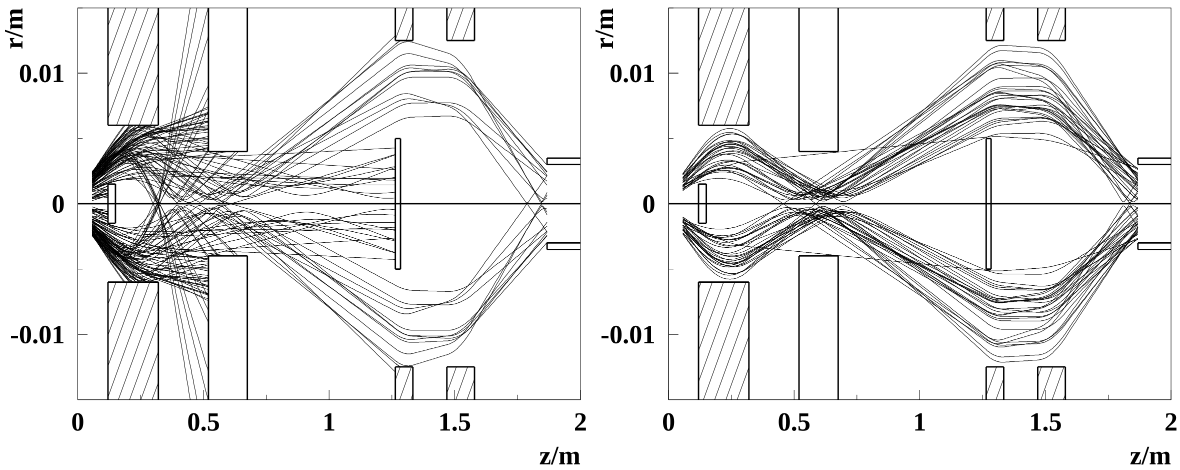

Fig. 9.1:
Radial projections from the trajectories of hydrogen atoms in the state $|1\rangle$ in the Rabi setup. The sextupole magnet in the source is operated with a current of 130 A. The trajectories were mirrored at the x-axis for a clearer picture. The sextupoles are shown as rectangles in hatches. The beam blockers in the first and second sextupole are shown as white rectangles. The two white rectangles between the first two sextupoles indicate the position of the injection tube and the two fat horizontal lines at the right edges of the pictures indicate the acceptance of the atomic beam detector. On the left side 2×60 random trajectories are shown, on the right side 2×30 trajectories that all reach the detector.

The test source is operated with a somewhat lower gas flow rate of about $0.3\,\mathrm{mbar\,l\,s^{-1}}$ and the nozzle diameter is only 3 mm. The resulting changes in the velocity distribution of the atomic beam should roughly compensate for one another. Nevertheless, it is not proven that the results from the measurements with the HERMES source can be transferred to the environment of the test source. The parameterization (9.1) should thus be understood as a working hypothesis only. The good agreement between the measurements and the results of the Monte Carlo simulation under the assumption of this hypothesis however shows that this procedure is legitimate.

Figure 9.1 shows several trajectories through the sextupole magnet of the Rabi setup that were calculated based on this parameterization. It should be noted that the vertical scale was stretched by a factor of 50 relative to the horizontal scale.

The beam block in the first two sextupole magnets and the cell entry tube strongly limit the phase space of trajectories that reach the atomic beam detector. Especially the strongly collimating effect of the cell entry tube on the atomic beam must be taken into account in the simulations. In the right picture that shows only trajectories that reach the detector, it is obvious that most of the atoms cross the sextupole system on a trajectory that corresponds to the first harmonic. The trajectories intersect the atomic beam axis once in the region of the cell entry tube. A trajectory belonging to the basic oscillation is visible as well.

There are two possibilities to check the results of the Monte Carlo simulations using the measurements from chapter 8. These are

- the comparison of absolute transmissions (figure 9.2) and
- the comparison of relative transmissions (figure 9.3).

For the comparison of absolute transmissions the SFT 2-4 between the first two sextupole magnets is switched on. As this high frequency transition has an efficiency of $99,52(78)\,\%$ (table 8.1), the state $|\,2\,\rangle$ is transferred almost completely into the state $|\,4\,\rangle$, which in turn is removed from the beam in the sextupole system of the polarimeter. The atomic beam detected in the detector therefore consists practically only of atoms in the state $|\,1\,\rangle$ and the measured intensity corresponds to the absolute transmission σ_{11} times a constant factor. This transmission can be determined by the simulation program for a given parameterization. The analytical calculation of trajectories of atoms in the state $|\,1\,\rangle$ according to (6.11) proves to be a large advantage. It allows the simulations to run much faster and with better statistics than the use of numerical methods alone would do. Figure 9.2 shows the measured intensity for the state $|\,1\,\rangle$ and the transmission σ_{11} plotted versus the sextupole magnet current.

Besides the three parameters for the atomic beam generator two additional scaling parameters have to be adjusted in tuning the Monte Carlo results to the measurements of the absolute transmissions. As already mentioned, these two parameters are the constant factor between σ_{11} and the measured counting rate and the relation between magnet current and pole tip field, the scaling of the abscissa.

The scaling factor for the ordinate is only of interest if the relation between the measured counting rate and the beam intensity is examined. It cancels out in measurements of intensity ratios and thus is not discussed further. For the scaling of the abscissa a linear relation between the magnet current and the pole tip field is assumed:

$$B_{pt}\,[\mathrm{mT}] = 4.78(35) \cdot I_{\mathrm{sextupole}}\,[\mathrm{A}]\,, \tag{9.2}$$

where saturation effects for high currents are disregarded. According to measurements of the pole tip fields as a function of the magnet current saturation effects should be only noticeable above 150 A [132]. Therefore the deviation of the measured values from the Monte Carlo simulation

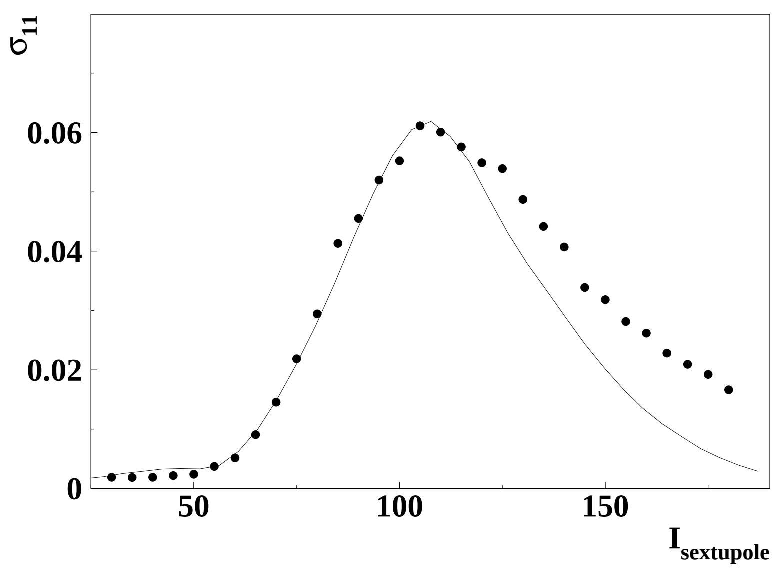

Fig. 9.2:
Transmission of the state $|1\rangle$ through the Rabi setup as a function of the sextupole magnet current in the atomic beam source. The points represent the intensity of the atomic beam for active SFT 2-4, the line shows the result of the Monte Carlo simulation. For each sextupole current value 2.000.000 trajectories were calculated. For the generation of the atomic beam the parameterization (9.1) was used.

in the region of 120 to 150 A in figure 9.2 must have other reasons. A sudden change in the intensity of the atomic beam or a change in the sensitivity of the atomic beam detector could be a possible explanation of why these measurements cannot be safely excluded.

In comparing the transmissions σ_{12}, σ_{21} and σ_{22} relative to σ_{11} (figure 9.3), which can be deduced from the efficiency measurements influences of this kind can be excluded. Thus they allow for a more precise verification of the Monte Carlo simulation than the determination of the absolute transmission σ_{11} alone.

As the trajectories of the state $|2\rangle$ cannot be calculated analytically but only numerically, the calculation of the transmissions σ_{12}, σ_{21} and σ_{22} requires a much larger calculation effort than the determination of σ_{11}. Also the requirements on the quality of the simulation program are much higher. Agreement between measurements and Monte Carlo simulations, as is apparent in figure 9.3, could first be reached with a newly developed simulation program about one year after the measurements were taken (chapter 6).

The results for the transmission ratio σ_{12}/σ_{11} deviate from the measurements by up to 5 % also below 150 A. The agreement in the case of the transmission ratios can possibly be further improved by a different beam parameterization. The transmissions σ_{21} and σ_{22} relative to σ_{11} however agree very well with the measurements, except in the region above 150 A. The increasing deviation of the Monte Carlo simulation from the measurements above 150 A can probably be explained by disregarding the saturation effects in (9.2).

The transmission ratio σ_{12}/σ_{11} is much less influenced by the sextupole current and also deviates less from 1 than the two other transmission ratios. Additionally, the two latter ratios do not differ very much from one another. This shows that the transmissions are far more determined by the state of the atom in the first sextupole magnet and that the transmission differences in the sextupole system of the polarimeter are small. The reason for this lies less in the sextupole of the source itself, but in the very long drift distance between the first two

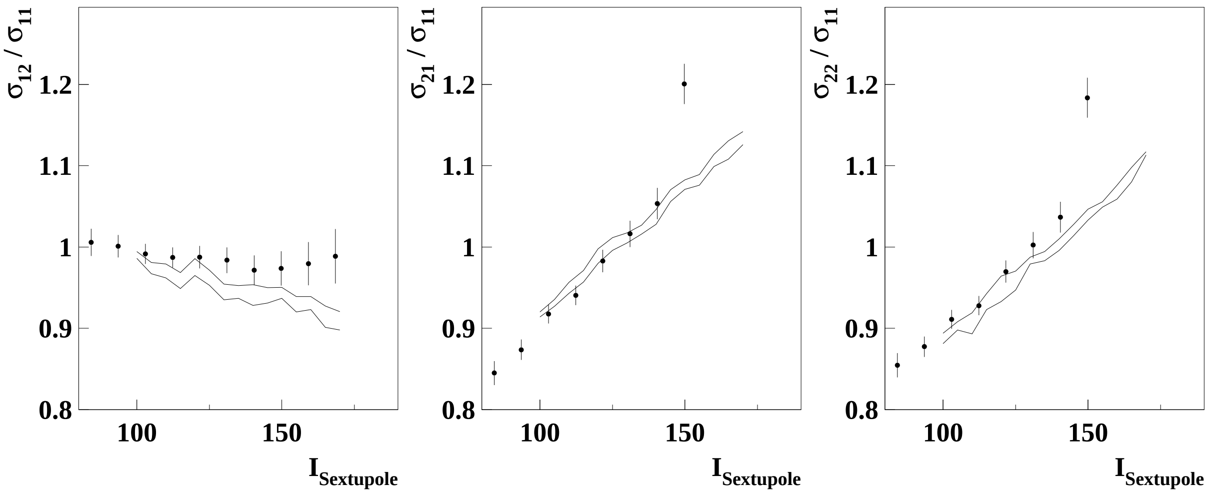

Fig. 9.3:
Transmission ratios in the Rabi setup. The two solid curves in the figures represent the upper and lower boundaries for the ratios as resulting from the consistency condition applied to the efficiency measurements (chapter 8.6). **The results of the Monte Carlo simulation are shown a points with error bars.** The results for σ_{22}/σ_{11} in the right figure can be deduced directly from figure 8.6.2. For each transmission and sextupole current value 200.000 trajectories were calculated.

sextupoles (figure 9.1). It amplifies the smallest differences in the radial velocity at the exit from the first sextupole in the sense that the atoms reach the second sextupole with very different distances to the atomic beam axis.

The overall agreement between the measurements and the results from the Monte Carlo simulations is absolutely satisfying and the most important goal of this subsection is reached. The reliability of the Monte Carlo simulation of sextupole magnet systems was experimentally verified and the simulation program can now be used for the determination of the transmissions in the polarimeter system that cannot be measured experimentally and for the determination of the initial polarization.

9.2 Transmitted Velocity Profile of the Rabi Setup

In addition to the determination of the transmissions, Monte Carlo simulations can also be used to examine the filter effect of a sextupole magnet system on the velocity distribution of an atomic beam. In viewing the velocity profile in front of the sextuple magnet system, that in general can be described by a modified Maxwell-distribution (6.18), only a small fraction reaches the target which depending on the setup is either the storage cell or the atomic beam detector. This fraction, the transmitted velocity profile, can be shifted along the velocity axis by the variation of certain parameters. This change under certain conditions can influence the measured efficiency of the high frequency transition, due to the fact that with increasing velocity of the atoms also the variation of the static field in the transitions over time increases and the adiabatic condition (5.4) for constant HF-amplitude is fulfilled less well. Thus the efficiencies of the high frequency transitions can decrease with increasing mean velocity in the transmitted atomic beam.

A parameter that leads to a change in the transmitted velocity profile in the Rabi setup and that is suited to examine the possible effects on the efficiencies of the high frequency transitions is the sextupole magnet current in the source. Figure 9.4 shows the transmitted velocity profiles for three different magnet currents. All of these profiles are dominated by the main peaks that belong to the first harmonic of the sextupole system. The contributions from the basic oscillation and the second harmonic are negligible. It is apparent that the center of the main peaks with increasing current shifts to higher velocities. For a current of 100 A the peak center is at about $1900\,\mathrm{m\,s^{-1}}$, while for 170 A it is at about $2300\,\mathrm{m\,s^{-1}}$.

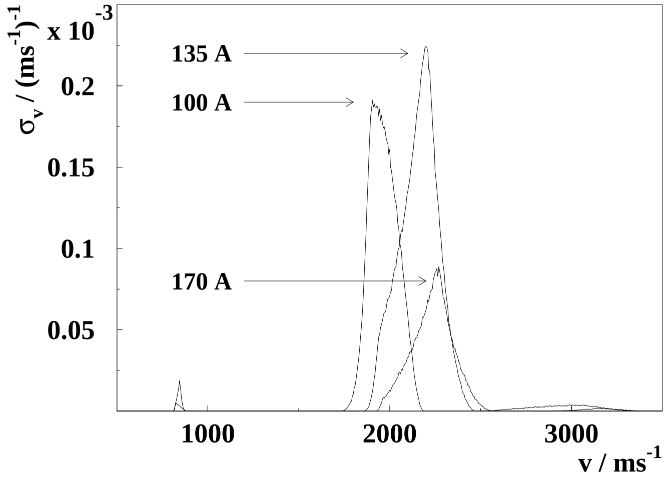

Fig. 9.4:
Transmitted velocity profiles for the state $|1\rangle$ in the Rabi setup for three different settings of the sextupole magnet current in the atomic beam source. The main peaks in the region of $2000\,\mathrm{m\,s^{-1}}$ belong to the first harmonic. In addition the wider and lower contributions from basic oscillation in the region around $3000\,\mathrm{m\,s^{-1}}$ and smaller peaks below $1000\,\mathrm{m\,s^{-1}}$ from the second harmonic can be seen. The integrals of the profiles are normalized to σ_{11}

The efficiency measurements used values in the same region of the current for the sextupole magnet. No changes in the measured efficiencies could be detected, with the exception of SFT 1-4 which has so far not been used for the polarisation measurements (chapter 8.6.3). Therefore the notion that a shift in the transmitted velocity profiles between $1900\,\mathrm{m\,s^{-1}}$ and $2300\,\mathrm{m\,s^{-1}}$ has any significant impact on the efficiencies of the high frequency transitions can be excluded from further consideration. In how far this result can assure the efficiencies in a polarization measurement will be discussed in chapter 9.4.

9.3 Transmissions in the Polarimeter System

According to chapter 6.3 the direction distribution of an atomic beam effusing from a storage cell is unambiguously determined by the geometry of the storage cell and it's velocity distribution can be parameterized by a single parameter, it's beam temperature T_{beam}. As the beam temperature must be equal to the cell temperature, there are no free parameters in the determination of the transmission probabilities of the sextupole system of the polarimeter. Thus the transmissions can be defined unambiguously.

For the determination of these transmissions a Monte Carlo generator was used to generate $200,000$ random directions for an effusive beam. These were used together with the also randomly generated velocity for the determination of the transmission probabilities for the polarimeter system in dependence of the storage cell temperature. Figure 9.5[15] shows the results of this simulation for the transmission of the four hyperfine states of a hydrogen atom.

The picture on the left shows the absolute transmission probabilities for the polarimeter system for the four hyperfine states of a hydrogen atom without a beam blocker in the case of a large storage cell with a 60 mm long exit tube. For a 30 mm long exit tube in general somewhat smaller transmissions result due to the different initial directions. These were not

[15] **One** randomly generated initial condition was used for the calculation of the trajectories for all hyperfine states. Thus the transmissions for the different states are statistically highly correlated. So far this correlation was not taken into account in the calculation of the uncertainties of the transmission ratios. Generally these uncertainties were therefore overestimated in chapter 9. This is particularly clear in the middle picture of figure 9.5.

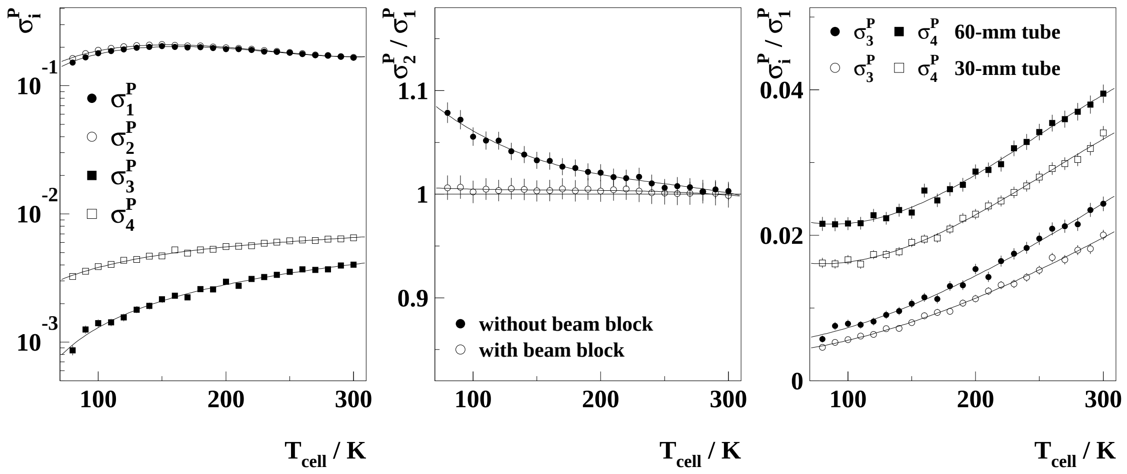

Fig. 9.5:
Transmission probabilities for the hyperfine states of hydrogen in the sextupole system of the polarimeter depending on the cell temperature. The results of the Monte Carlo simulation were fitted with third order polynomials which enter as corrections into the evaluation of the polarization measurements. Left: Absolute transmissions for a cell with a $60\,\mathrm{mm}$ long exit tube. The absolute values are to be understood relative to the number of atoms that coming from the exit of the storage cell reach the entrance of the first sextupole magnet. Middle: Normalized transmission for the state $|\,2\,\rangle$ for a cell with a $60\,\mathrm{mm}$ long exit tube without and with beam blocker in the first sextupole magnet. Right: Normalized transmissions for the states $|\,3\,\rangle$ and $|\,4\,\rangle$ for a $30\,\mathrm{mm}$ and a $60\,\mathrm{mm}$ long exit tube.

plotted. In this plot the differences between the focused states $|\,1\,\rangle$ and $|\,2\,\rangle$ are only visible at lower temperatures. The differences between the defocused states are far more obvious. The state $|\,4\,\rangle$ has a smaller magnetic moment as state $|\,3\,\rangle$ in weak fields, that is close to the axis of the sextupole magnet. Thus the deflecting forces in the region of the axis are a little weaker and an atom in state $|\,4\,\rangle$ can pass the sextupole system with a higher probability than in state $|\,3\,\rangle$ (see figure 6.2).

For the analysis of polarization measurements only the transmissions that are normalized to σ_1^P are needed. These are shown in the middle and on the right.

The middle picture shows the normalized transmission σ_2^P in the case of a sextupole system with and without a beam block on the axis for a 60 mm long exit tube. The results for the cell with the 30 mm long tube differ by maximally $0,3\,\%$ and thus are not shown. Without a beam block there are clear differences between state $|\,1\,\rangle$ and $|\,2\,\rangle$ at low temperatures that reach up to $8\,\%$, which is a non-negligible correction. With a beam block the transmission σ_2^P deviates from σ_1^P by maximally $0,6\,\%$ over the entire temperature range. The transmissions for the states $|\,3\,\rangle$ and $|\,4\,\rangle$ vanish in this case, so that the sextupole system with a beam block can be regarded as practically correction-free.

The normalized transmissions for the states $|\,3\,\rangle$ and $|\,4\,\rangle$ have to be taken into account only for a sextupole system without a beam block. They are shown in the right picture for the two different lengths of the cell exit tube. The length of the cell exit tube and thus the change in the direction distribution has a clearly visible impact on these transmissions.

The results of the Monte Carlo simulations suggest that the Breit-Rabi polarimeter should in principle be operated with a beam block in the sextupole system. The corrections due to the incomplete defocusing of the states $|1\rangle$ and $|2\rangle$ are significantly smaller than the systematic error induced by the efficiency measurement. Furthermore, the influence of the geometry of the cell exit tube can be disregarded and the intensity of the atomic beam is reduced by only about 30 %.

Another very important argument for the use of a beam block are molecular beams of molecules containing hydrogen like H_2 or H_2O, that can effuse from the cell as well. These pass through the sextupole system undisturbed and contribute to the H_1-counting rate due to dissociative ionization in the ion formation space of the mass spectrometer. As these molecules are not affected by the sextupole magnet, they cause an unpolarized background in the beam signal that cannot be separated by the chopper of the atomic beam detector. This may significantly reduce the measured polarization (figure 12.12). A beam block can completely suppress these effects.

Nevertheless, so far the polarization measurements with hydrogen atom beams were carried out without beam block in the sextupole magnets, in particular to also examine molecular beams like H_2 or H_2O that effuse from the cell (chapter 12.1). The transmissions of the states $|3\rangle$ and $|4\rangle$ are small, so that their errors hardly contribute to the systematic error of a polarization measurement. The influences on the measured atomic beam signal due to unpolarized background of molecular beams from the storage cell are smaller than 0.2 %, with the exception of the effect shown in figure 12.12 (table B.2).

Also during the HERMES experiment the necessity exists to determine the intensity of the molecular hydrogen effusing from the cell to measure the degree of dissociation in the storage cell. This measurement can be carried out with a second mass spectrometer in front of the polarimeter [133], so that there is no reason against the use of a beam block in the sextupole system.

9.4 Transmitted Velocity Profile in the Polarimeter System

The purpose of this subsection is to clarify whether the results from chapter 9.2 with respect to the insensitivity of the high frequency transitions towards shifts in the transmitted velocity profile in the sextupole system of the Rabi setup, which was used for the efficiency measurements, can be transferred to polarization measurements that use a different sextupole system with a different filter effect on the initial velocity distribution. The significant parameter that can cause a shift in the transmitted velocity profile is the temperature of the storage cell.

In figure 9.6 several transmitted velocity profiles are compiled, for different cell temperatures, for focused and defocused states and for a sextupole system with and without beam block. The profiles for the focused states (left) consist of two peaks for all examined cell temperatures. The dominant peak (right) belongs to the basic oscillation, it is practically independent of the cell temperature at about $2000\,\mathrm{m\,s^{-1}}$. This is just the velocity that was also filtered out dominantly by the Rabi setup (figure 9.4). The side peaks (left) belong to the first harmonic. Their position is also practically independent of the cell temperature and their contributions to the integral of the distributions is below 13 %, as can be seen in table 9.1.

Theses side peaks could lead to an increase of the efficiencies, due to the fact that they give contributions at smaller velocities in the atomic beam. However, for almost all high frequency transitions the efficiencies are practically 100 % within the measurement uncertainties, so that the side peaks should not lead to significantly different efficiency values for the polarization measurements than those given in table 8.1. However, the main peaks reach far into the region of high velocities, which could lead to a reduction of the efficiencies. The part of the profile above the limit for the adiabatic equation of $2300\,\mathrm{m\,s^{-1}}$, as estimated in chapter 9.2, is listed

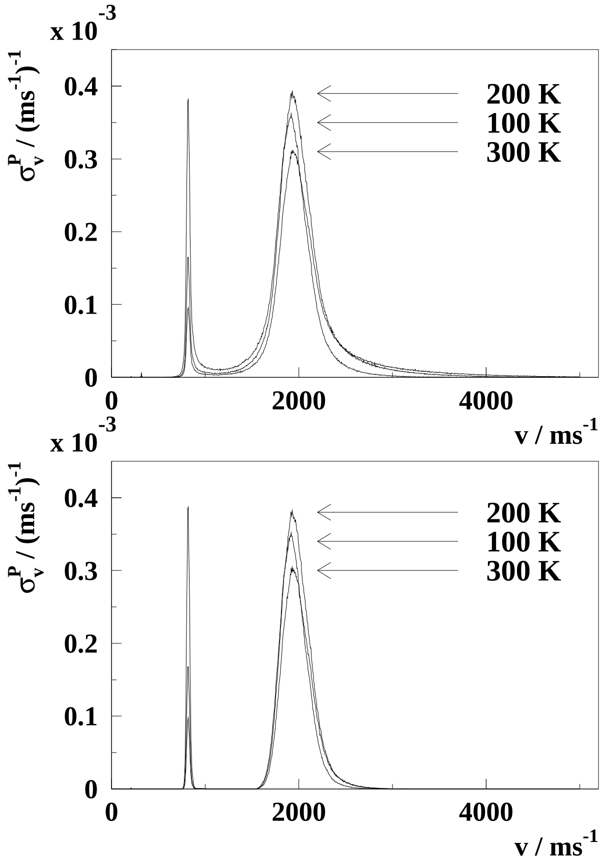

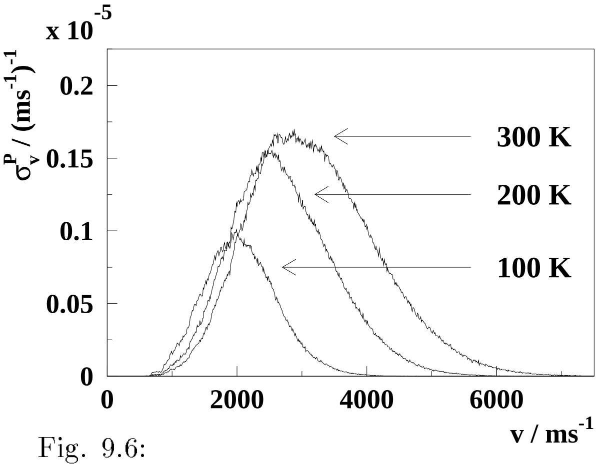

Fig. 9.6:
Transmitted velocity profiles in the sextupole system of the polarimeter for different cell temperatures. On the left for the state $|1\rangle$ without beam block (top) and with beam block (bottom), on the right for the state $|3\rangle$ without beam block in the first sextupole of the polarimeter system. The initial direction was generated by the Monte Carlo generator for an effusive beam (chapter 6.3) with a 60 mm long exit tube. The integrals of the distributions were normalized to the corresponding transmission.

in table 9.1. It increases strongly with increasing cell temperature and reaches almost 19 % at 300 K.

In a sextupole system without beam block also the states $|3\rangle$ and $|4\rangle$ can reach the detector. In this case therefore also their velocity profiles must be examined. The right side of figure 9.6 shows profiles for the state $|3\rangle$ in such a system. A clear shift is visible for the center of the distribution from about 2000 m s^{-1} at a cell temperature of 100 K to about 3000 m s^{-1} at 300 K. Furthermore, the distributions are very wide and reach far into the region of high velocities, up to about 7000 m s^{-1}. Following the results of chapter 9.2, an influence on the efficiencies cannot be excluded in this region. The different shape of the velocity profiles for focused and defocused states may also lead to weakly asymmetric efficiencies of the high frequency transitions (see chapter 7.2).

In comparing the different scales of the ordinates in the pictures on the left and on the right it becomes apparent that the contributions from defocused states are about two orders of magnitude smaller than the contributions of the focused states (see also figure 9.5 left). Although the shift of the velocity profile is far more significant for the defocused states, the

Limit	< 1000 m s^{-1}		> 2300 m s^{-1}		
Beam Block	without	with	without		with
State	$|1\rangle$	$|1\rangle$	$|1\rangle$	$|3\rangle$	$|1\rangle$
100 K	12.3 %	11.8 %	5.2 %	32.6 %	2.0 %
200 K	4.9 %	4.8 %	13.2 %	68.6 %	4.0 %
300 K	3.4 %	3.4 %	18.9 %	82.4 %	4.8 %

Tab. 9.1:
Critical regions of transmitted velocity profiles in the sextupole magnet system of the polarimeter. The limit 1000 m s^{-1} marks the contributions of the side peaks, 2300 m s^{-1} the fulfilled adiabatic equation (5.4) according to chapter 9.2.

absolute contribution to the integral due to the defocused states above 2300 m s^{-1} is only 5.3 % of the absolute contribution from the focused states; it thus is negligible.

According to these results a weak influence of the cell temperature on the efficiency of the high frequency transitions is to be expected in the polarization measurements without the beam block in the sextupole magnets. This can lead to a seeming reduction of the polarization with increasing cell temperature. An effect of this kind was in fact observed in the measurements of the temperature dependence of the polarization (chapter 12.4). However, in chapter 11.4 a different, dominating, reason for this behaviour is described. The overall agreement of the velocity profile in the Rabi setup and the polarimeter system is satisfactory, after all the efficiency of a high frequency transition above the limit does not drop to zero immediately, but slowly.

As can be seen in figure 9.6 (bottom left) and table 9.1, the use of a beam block leads to a further improvement of this situation. The contributions of the defocused states vanish completely and the share of the focused states above the limit reaches less than 5 % at 300 K. The efficiencies above this limit decrease only slowly, so that this value is innocuous. This is an additional convincing argument to always use a beam block with the Breit-Rabi polarimeter in the future.[16] Another possibility to counteract the reduction of the efficiency of high frequency transitions can be read out of the adiabatic equation (5.4) directly. Any inefficiency due to a shift in the velocity profiles can be compensated by increasing the strength of the high frequency field, as long as this stays inside the technical and financial limits.

[16] After the many arguments in this chapter it is probably not easy to understand why the polarization measurements for hydrogen were carried out without a beam block. However, the results of this chapter where reached long after this decision had been made. This is mostly due to the fact that for quite some time the transmission measurements with the Breit-Rabi setup (figure 9.3) could not be reproduced by Monte Carlo simulations. This lead to justified doubt about the reliability of the simulation programs used at the time. However, it should be noted that the results from the transmission measurements in the meantime could also be reproduced with a corrected version of this program. Furthermore, in the early phase of the polarization measurements serious problems with the detection of the atomic beam did not allow a reduction of the intensity due to the beam block. These problems have by now been solved.

9.5 The Initial Polarization

The different high frequency transitions have different phase space distributions after the sextupole magnet in the atomic beam source. As a result they enter the storage cell with different directions. Atoms that are focused enter further into the cell before they collide with a wall for the first time, compared to atoms that are defocused. Therefore the probability to reach the polarimeter via the cell is a little larger for the focused states than for the defocused ones. Thus it is not sufficient for the determination of the initial polarization to simply measure the hyperfine occupancy in the atomic beam at the entrance into the storage cell, but additionally the transmission probability through the storage cell must be determined for each hyperfine state. This can be done using a Monte Carlo simulation for molecular flow (appendix A.3). The initial polarization or the initial occupancy, respectively, which is important for the relaxation measurements, is therefore given by the products of two transmissions:

$$n_{i0} = \frac{\sigma_i^Q \sigma_i^{\text{cell}}}{\sum_i \sigma_i^Q \sigma_i^{\text{cell}}}, \tag{9.3}$$

where σ_i^Q is the probability to reach the sextupole magnet through the storage cell, and σ_i^{cell} is the probability to leave the cell through the exit tube in the direction of the polarimeter. The hyperfine occupancy defined by (9.3) is the one which would be measured by the polarimeter if no relaxation processes would take place within the storage cell. In general it is not identical to the occupancy that is injected into the cell.

The determination of the σ_i^{cell} is very involved. Therefore it was only carried out for one parameterization (9.1) and only for one sextupole current. The influences of the parameterization on the initial polarization are discussed using the hyperfine occupancies that are injected into the cell. For this purpose the transmission σ_i^Q through the sextupole is determined for every hyperfine state. From these transmissions the hyperfine occupancy in the atomic beam at the entrance to the storage cell can then be calculated. Figure 9.7 shows the transmissions on the left and the resulting occupancies as a function of the sextupole current in the source on the right.

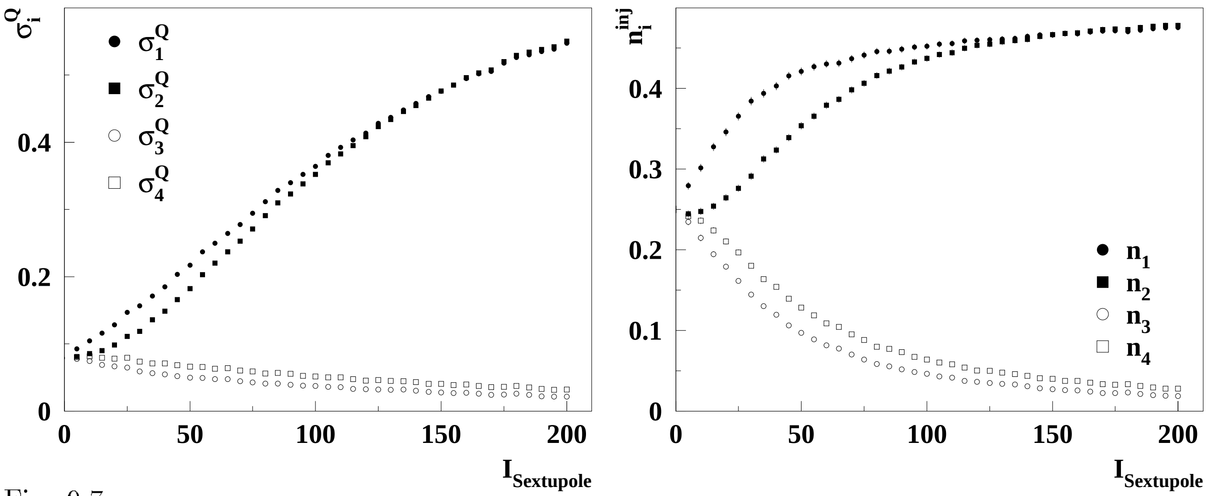

Fig. 9.7:
Left: Absolute transmissions σ_i^Q in the sextupole magnet of the source as a function of the magnet current. Right: The resulting calculated hyperfine occupancies of the atomic beam that is injected into the cell. The values refer to the entrance of the entry tube of the storage cell, the transmissions through the storage cell σ_i^{cell} are not taken into account. The Monte Carlo generator was parameterized by (9.1).

The pictures illustrate that the ideal setting for the sextupole current would be at a constant 170 A. It is clearly visible how the states $|\,3\,\rangle$ and $|\,4\,\rangle$ are more and more removed from the beam with increasing sextupole current, while at the same time the focusing of the states $|\,1\,\rangle$ and $|\,2\,\rangle$ is improved. This leads to a higher polarization on the one hand and to an increased flow injected into the cell on the other hand. The differences between the states $|\,1\,\rangle$ and $|\,2\,\rangle$ get smaller as well and are hardly noticeable above 130 A.

From the hyperfine occupancy nuclear and electron polarization can be calculated following (2.22). Figure 9.8 shows the results for the nuclear polarization again as a function of the sextupole current. For the relaxation measurements a sextupole current of 170 A was selected. This value is marked by a vertical line. The efficiency of the WFT 1-3 was taken into account in the calculation of the nuclear polarization and the maximal field of 750 mT was assumed for the storage cell. Additionally, the influence of the drift velocity and of the parameter K_{mol} on the polarization was examined. The drift velocity has a clearly visible influence on the polarization for sextupole currents below 150 A. Above this current the differences become small. For K_{mol} the behaviour is similar.

The parameterization of the Monte Carlo generator at 170 A has hardly any influence on the initial polarization. The variation of the initial polarization depending on the sextupole current is very flat in this region and the reliability of the simulation program has been proven through comparison with measurements (chapter 9.1). Therefore it can be assumed that the values for the injected polarization in the region of 170 A shown in figure 9.8 have a small systematic uncertainty of only about 2 %.

If also the different transmission probabilities through the storage cell are also taken into consideration, an injected polarization of $P_z^{inj} = 0.883(7)$ together with a holding field of 750 mT and a sextupole current of 170 A lead to an initial polarization of $P_{z0} = 0.900(8)$. This value is valid for the small as well as for the large storage cell. The given errors contain only the

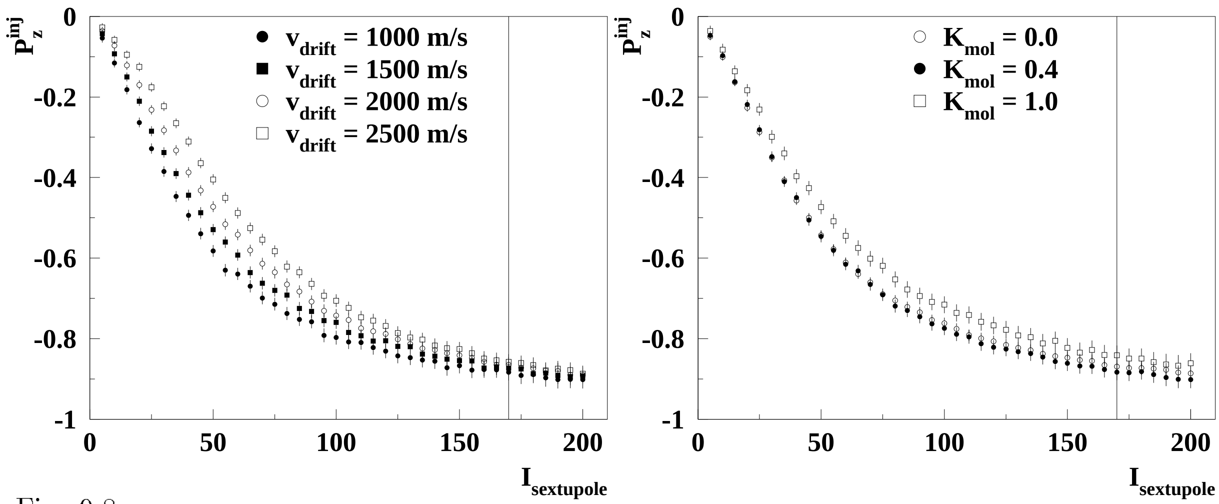

Fig. 9.8:
Nuclear polarization of the atomic beam that is injected into the storage cell at the entrance of the cell entry tube as a function of the magnet current in the sextupole of the source. For the calculation of the polarization from the hyperfine occupancy a field of 750 mT was assumed for the storage cell. The efficiency of the WFT 1-3 was taken into account, the transmissions through the storage cell σ_i^{cell} were not considered. The vertical line marks the sextupole current that was set for the polarization measurements. Left: Influence of the drift velocity at $K_{\mathrm{mol}} = 0.4$. The beam temperature was calculated from the drift velocity according to (6.19) with the approximation $v_{\mathrm{rms}} \approx v_{\mathrm{drift}}$. The nozzle temperature was assumed to be 300 K. Right: Influence of K_{mol} at $v_{\mathrm{drift}} = 1484\,\mathrm{m\,s^{-1}}$ and $T_{\mathrm{beam}} = 234\,\mathrm{K}$.

statistical errors of the transmission determination and the efficiency of the WFT 1-3. Further data to the initial occupancy can be found in table C.1.

9.6 Transmitted Velocity Profile in the Sextupole Magnet of the Source

In contrast to the transmitted velocity profiles for the sextupole system of the Breit-Rabi polarimeter (chapter 9.4) the profiles for the sextupole magnet of the test source are almost completely above the limit of $2300\,\mathrm{m\,s^{-1}}$ estimated in chapter 9.2 (figure 9.9). This is the case for focused and defocused states and for sextupole magnets with beam block and without. In the case of the state $|\,1\,\rangle$ the profiles with and without beam block in the sextupole reach up to about $6000\,\mathrm{m\,s^{-1}}$. For the state $|\,3\,\rangle$ they even exceed this value significantly. As in the case of the polarimeter (chapter 9.4) systems the influence of this velocity profile becomes negligible as a result of the far lower overall transmission for this state.

The high velocities in the part of the beam that is focused into the entry tube of the storage cell do not allow anymore to exclude a violation of the adiabatic condition for the high frequency transitions within the uncertainties. A reduction of the efficiencies at the injection of an atomic beam into the storage cell compared to those measured in the Rabi setup (chapter 8.7) has to be expected.

In addition to the analysis in chapter 11 the results of an alternative analysis of the relaxation measurements may be found in appendix C. This analysis allows conclusions to be drawn about the injected hyperfine occupancies as well as about the efficiencies in the source, which indicate that at least the efficiency of the WFT 1-3 for hydrogen is not influenced in the slightest by the shift of the velocity profile. However, these results can be transferred to the case of the strong field transitions in the source for deuterium by simple scaling. In this analysis they indicate a reduction of the efficiencies.

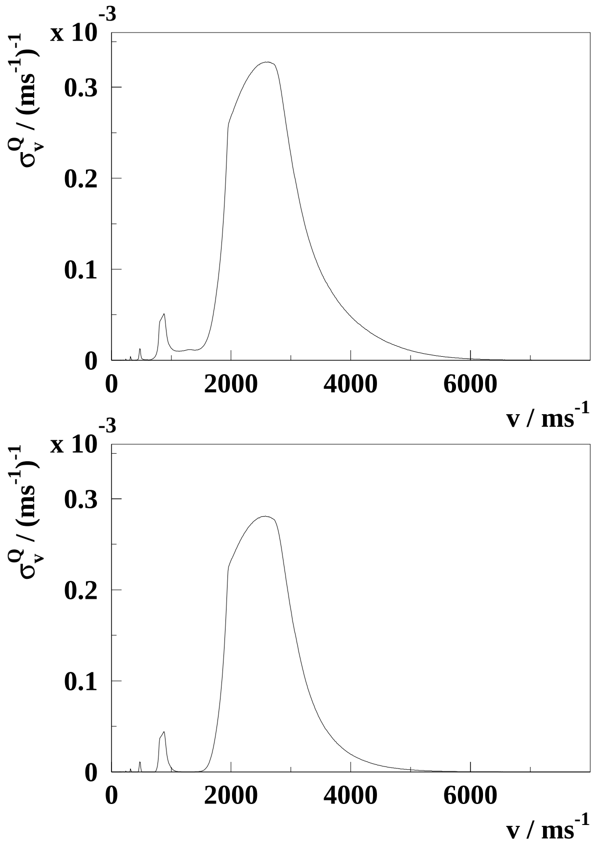

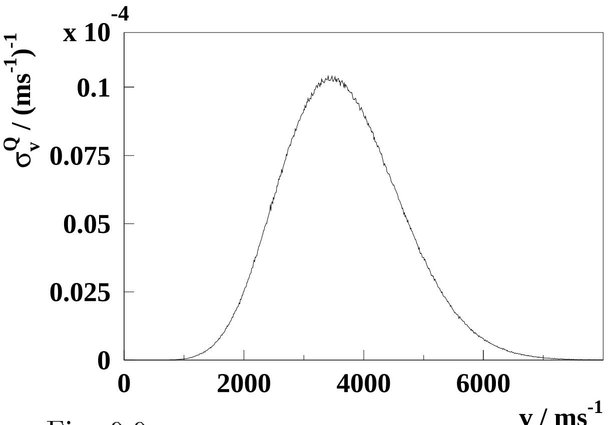

Fig. 9.9:
Transmitted velocity profile in the sextupole magnet of the atomic beam source. Left for the state $|\,1\,\rangle$, top without beam block an bottom with, right for the state $|\,3\,\rangle$ without beam block in the sextupole magnet. The initial conditions were generated with the Monte Carlo generator for a jet beam (chapter 6.2) and the parameterization (9.1). The sextupole current is $170\,\mathrm{A}$. The distributions are normalized to the respective transmission.

9.7 Transmission of Deuterium Atoms

The analysis of the efficiency measurements with the deuterium transitions shows no differences in the transmissions of the focused states $|1\rangle$, $|2\rangle$ and $|3\rangle$. However, this is valid within the measurement uncertainties that are somewhat larger than in the case of hydrogen [112]. This result can be explained by the beam blocks in source and polarimeter and by the critical field of the deuterium atoms, a factor of 4.5 smaller. The differences in the transmission of the focused states are better suppressed by a factor of 20 by the beam blocks than in the case of hydrogen, because the magnetic field inside a sextupole magnet increases quadratically with the distance from the axis

Nevertheless, the transmission corrections have to be considered in the analysis of the efficiency measurements as in the case of hydrogen, because the assumption of an ideal sextupole system does not lead to consistent results. Apparently the long drift distance between the first two sextupole magnets leads to small differences between the transmissions of the focused states. However, due to the lower efficiencies of the deuterium transitions these could not yet be resolved.

Contrary to the hydrogen measurements, the polarization measurements for deuterium were carried out with a beam block in both the sextupole of the source and the first sextupole of the polarimeter. The transmission corrections for the polarimeter system are due to the use of the beam block already below 0.6 % for hydrogen (figure 9.5 middle). Therefore they could be completely disregarded for deuterium. Also the transmissions for the sextupole system in the source, which determine the hyperfine occupancies of the beam that is injected into the storage cell, have to behave ideally within the uncertainties. For deuterium the states $|1\rangle$, $|2\rangle$ and $|3\rangle$ after the sextupole magnet in the source must be occupied to one third each. The sextupole systems of source and polarimeter within negligible errors do not need any corrections in polarization measurements with deuterium.

10 Uncertainties of the Polarization Measurements

10.1 Statistical Errors

The statistical errors of a polarization measurement are determined by the errors on the beam intensity measurements. These are calculated as follows: The measured opening functions of the chopper (figure 4.8) are added up bin-wise for individual measurement cycles and switch cycles of the high frequency transitions and are finally converted into a counting rate. With every additional measurement cycle the variations within the analysis windows, that determine the statistical error for the counting rates with open and closed chopper, become smaller. The statistical error of the beam signal results from regular error propagation for the difference of these two counting rates.

Another possibility consists of the calculation of the mean over time for all observables that are derived from the beam signals. Here the individual values that enter the mean calculation are determined from a single switch cycle of the high frequency transitions. The errors calculated from both methods are in agreement. The errors presented in this chapter were calculated according to the first method.

As will be discussed in chapter 11, in the future, in addition to the atomic beam signal also the beam signals for hydrogen containing molecules will also have to be measured and the atomic beam signal accordingly corrected. This will increase the statistical error as well as the necessary duration of the measurement. This error is not taken into account in the following. As the background signal is small compared to the atomic beam signal, according to the arguments of chapter 4.3.4 a short measuring time is sufficient for this background signal and the error may be large compared to the error of the atomic beam signal without any significant impact on the statistical errors and measuring times listed here. Figure 10.1 shows the decrease of the statistical error as a function of the duration of the polarization measurements with hydrogen (left) and deuterium (right).

The statistical errors of a polarization measurement are significantly larger for deuterium than for hydrogen measurements. This is due to the fact that for hydrogen four and for deuterium six beam intensities must be measured for the determination of the hyperfine occupancy. Furthermore, for the deuterium measurement beam blocks were installed in both the sextupole magnet of the source and the first sextupole of the polarimeter. The hydrogen measurements

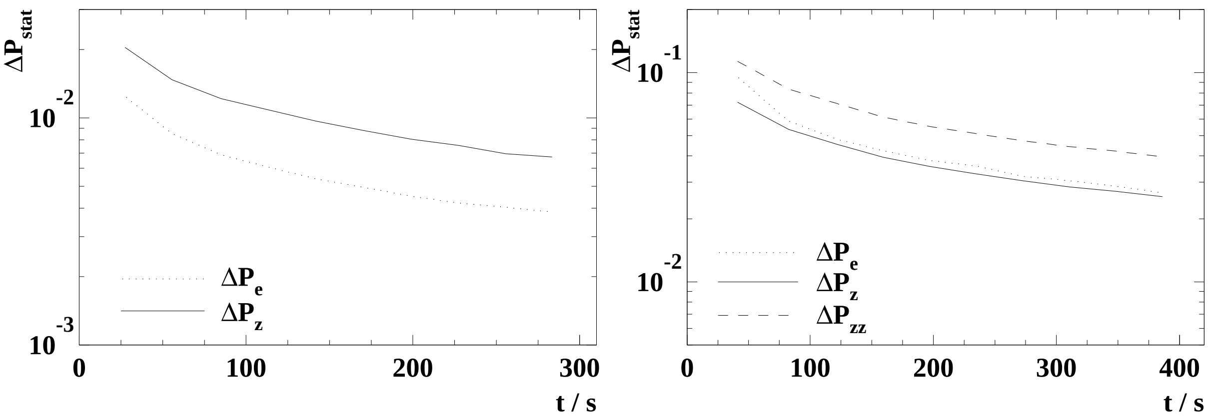

Fig. 10.1:
Statistical error of a polarization measurement as a function of the duration of the measurement. Left: Polarization measurement with hydrogen. $B = 350\,\mathrm{mT}$, $T_{\mathrm{cell}} = 101\,\mathrm{K}$ and drifilm coating. Right: Polarization measurement with deuterium. $B = 300\,\mathrm{mT}$, $T_{\mathrm{cell}} = 110\,\mathrm{K}$ and teflon coating. The measurement with hydrogen was taken without and the measurement with deuterium with beam blocks in the sextupole magnets.

were taken without beam blocks in the sextupole magnets. As a result of the beam blocks the beam intensity was reduced to about 1/3.

In the case of the hydrogen measurements an absolute error of about 0.02 for P_z was arrived at after one switch cycle of 30 seconds for the high frequency transitions. This is already clearly lower than the required error for HERMES of 0.03. The measurements for the results for hydrogen that are compiled in chapter 12 were reached with a measuring time of about 5 minutes per point. After this time a statistical error of 0.007 is reached for the nuclear polarization. The error on the electron polarization even is only 0.004.

The deuterium measurements reach an error of 0.03 for the vector polarization after about 300 seconds. For the tensor polarization this error was not yet reached after 400 seconds. If ΔP_{zz} is extrapolated in figure 10.1, it can be estimated that a measuring time of about 600 seconds would be necessary for this uncertainty.

Assuming that the density in the HERMES storage cell will be about a factor of 10 larger than in the test storage cell with operation without beam block in the sextupole of the test source (see tables 14.3, 14.4 and B.2), and further, taking the smaller diameter of the exit tube of 5 mm for the HERMES storage cell into account, the intensity of the atomic beam that is injected from the storage cell into the polarimeter is higher by a factor of five. The beam block in the polarimeter reduces the intensity by about 30 %, which again increases the measuring time for hydrogen. The beam block in the test source leads to a reduction by a factor of two, which in turn reduces the measuring time in HERMES for the case of deuterium compared to the test stand measurements.

If the polarimeter in the HERMES experiment is operated with beam block and the atomic beam source without it, the following estimate is obtained for the measuring time that is required to reach a statistical error of 0.03 in the HERMES experiment. For the nuclear polarization of hydrogen about ten seconds are needed, for the vector polarization of deuterium about 30 seconds and for the tensor polarization about 60 seconds. For the densities in the test storage cells as quoted in table B.2 a large systematic error has to be expected. This may lead to measuring times that deviate from theses expectations by up to a factor of two.

10.2 Systematic Errors

The systematic errors of a polarization measurement depend on the accuracy reached in the calibration of the polarimeter. The uncertainties of the efficiencies (chapter 8.7) and the uncertainties of the transmissions (chapter 9.3) are included here. For the hydrogen measurements only one transmission correction had to be taken into account. For deuterium transmission corrections can be disregarded if a beam block is installed in the sextupole system. Therefore the systematic errors are dominated by the uncertainties of the efficiency measurements.

As a result from further improvements in the high frequency transitions, it can be expected that the adiabatic condition (5.4) will be even better fulfilled in HERMES, so that the efficiencies will be even closer to 1. The systematic error of a polarization measurement will be reduced accordingly. The following data relate to the results from the test stand.

As the contribution from mixed states to the polarization in the atomic beam increases with the holding field, also the systematic error of a polarization measurement increases with increasing field. This field dependence is shown in figure 10.2 left for hydrogen and right for deuterium.

In the case of hydrogen and for the used configuration of high frequency transitions the systematic error for the nuclear polarization at a holding field of 350 mT lies a little below the required error of 0.03.

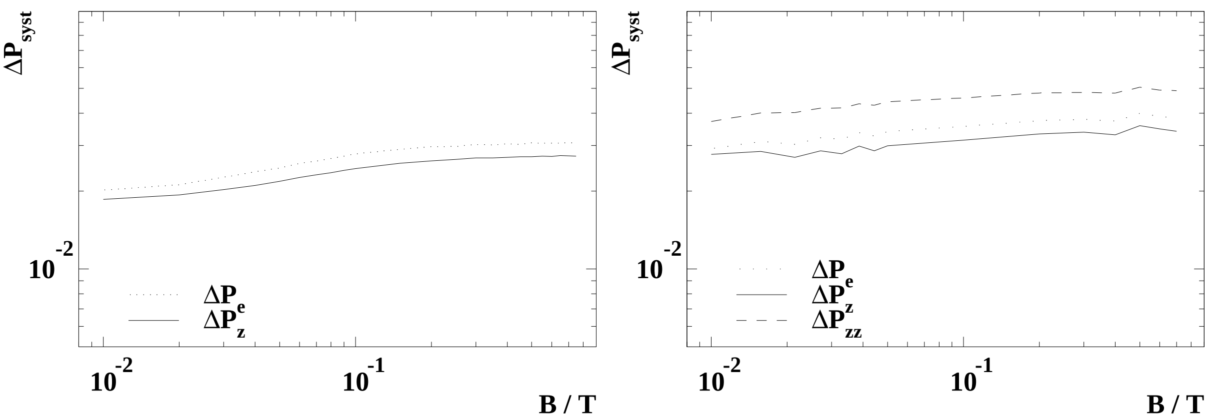

Fig. 10.2:
Systematic error of a polarization measurement as a function of the holding field in the storage cell. Left: Uncertainty of the electron and nuclear polarization of hydrogen using the high frequency transitions SFT 2-4, MFT 1-3 and MFT 2-3. For the electron polarization the WFT 1-3 was switched off, for the nuclear polarization it was switched on. Right: Error of the electron, vector and tensor polarization for deuterium with active SFT 2-6 in the atomic beam source.

The uncertainty for the vector polarization of deuterium is smaller than the required 0.03 over almost the entire field range. For the tensor polarization however, only an uncertainty of 0.05 could be reached until now. However, the strong field transitions in the polarimeter for deuterium had to be operated without a phase control until now. It may be expected that the use of such a control will lead to a significant improvement of the systematic errors of a deuterium measurement.

The polarization for a given hyperfine occupancy depends on the holding field, so that finally also the uncertainty on the holding field value or the field inhomogeneity enters into the uncertainty of a polarization observable. This uncertainty however has nothing to do with the precision of the Breit-Rabi polarimeter, but depends on the accuracy with which the polarization in the storage cell is defined in the first place. It was therefore not taken into consideration. The field inhomogeneity for example is only 0.45 % for the transverse holding field in the HERMES experiment [134], so that this contribution to the systematic error may be disregarded.

The systematic error resulting from the neglection of asymmetric efficiencies (chapter 7.2) is not included here. If it is insured that the high frequency transitions are operated in sufficient saturation and that the not yet measured efficiencies ε_{ji} reach 100 % within the statistical errors, as the already measured efficiencies ε_{ij} do, then the systematic error is further reduced.

The error bars of the measurement results shown in chapter 12 contain only statistical, not systematic, errors.

10.3 Comparison of the Analysis Methods

In the case of hydrogen altogether four high frequency transitions are available, but only three are needed for the analysis. Therefore there are four possibilities for the analysis of a polarization measurement, one for each transition that is not used in the given analysis. Figure 10.3 shows the results for all four analysis methods in comparison. On the left side the electron and nuclear polarizations for all four analysis methods are shown together in one picture. The physics meaning of these results will be discussed in detail in chapter 12.3.2, here only the comparison of the different methods is important. Differences between the methods can only be seen for very few points at all, and even in these cases the differences are smaller than the statistical

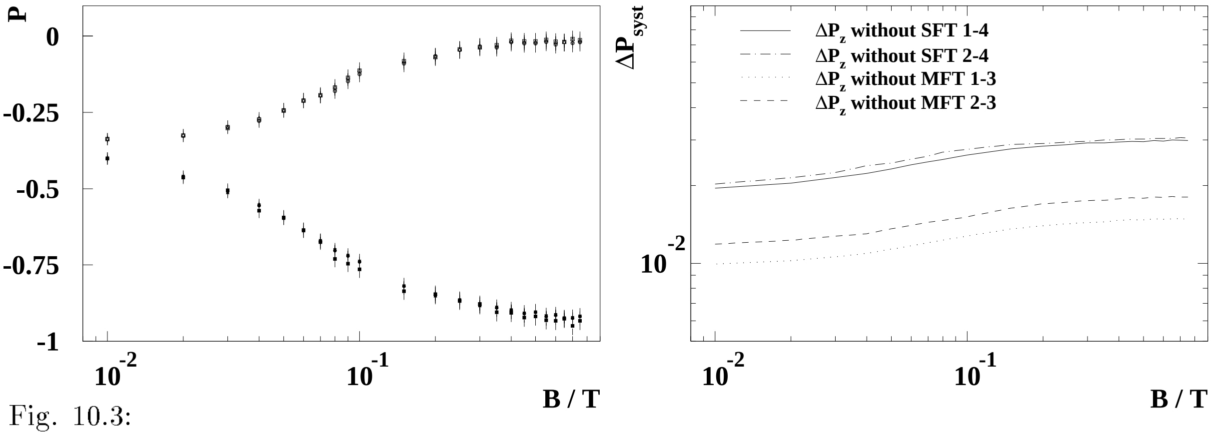

Fig. 10.3:
Comparison of the four possible analysis methods for hydrogen. On the left side the results for nuclear polarization (lower branch) and the electron polarization (upper branch) are shown. A legend was waived as the markers cannot be distinguished from one another. On the right side the systematic errors for the nuclear polarization are shown for the four methods. The measurement was taken with drifilm coating at 101 K and 3505(14) wall collisions. The states $|2\rangle$ and $|3\rangle$ were injected into the cell.

errors. The different markers for the methods cannot be distinguished, because almost all points lie on top of one another. Therefore no legend is shown.

However, there are differences between the methods with regard to the systematic errors, as can be seen in the right picture. Not using one of the medium field transitions leads to smaller errors, as for these transitions always two efficiencies and thus also two errors enter into the analysis. The best results are obtained in leaving MFT 1-3 out, that is in using the transitions SFT 1-4, SFT 2-4 and MFT 2-3. In a strong field this combination leads to a systematic error of less than 0.014.

However, there are some doubts about the time stability of the efficiency of SFT 1-4, because it was used with a resonator for σ-transitions and in a very weak static field. For the results shown in chapter 12 therefore the combination SFT 2-4, MFT 1-3 and MFT 2-3 was used for the analysis. In this case the systematic error in a strong field lies just below 0.03, still fulfilling the requirements of the HERMES experiment. In the HERMES experiment a resonator with tilted rods is also used for hydrogen, so that the SFT 1-4 can be operated with high stability and efficiency. Therefore it is realistic to assume a systematic error of 0.015 for hydrogen measurements.

For the analysis of the deuterium measurement no additional high frequency transition is available so far, so that there is only one possible analysis method. While the possibility to include either the SFT 2-5/3-6 or the MFT 1-4 into the analysis exists, time constraints have not enabled this to occur. The use of an additional high frequency transition for the deuterium measurements would be advantageous, as several analysis procedures could be executed simultaneously.

The different analysis methods are not completely independent of one another, but differences in the results of the procedures can help to discover mistakes in the calibration or suddenly appearing technical problems in one or several high frequency transitions also during a polarization measurement. On the other hand, the agreement of all methods does not directly mean that the calibration is correct. Certain inferences can be made only in the other direction: If there are significant differences between the different methods, there must be an error either in the efficiencies of the high frequency transitions or in the transmissions of the sextupole system. In the measurements described in chapter12 no such differences were observed.

11 Analysis of the Relaxation Measurements

11.1 Results from the Relaxation Measurements

In chapter 12.3 the results from the measurements of the dependence of the spin relaxation on a static field over the region of the storage cell are compiled. They are compared to calculations that are based on the theoretical description of wall and spin exchange collisions that is discussed in chapter 3 and appendix F. Some parameters in the master equation (3.1) for the description of the relaxation processes in the storage cell and for the definition of the initial occupancies have to be fitted to the results using a χ^2-minimization [135]. These parameters are collected in table 11.1. Their selection and the connection to the parameters of the master equation will be explained in separate subsections.

For the fitting procedure the master equation (3.1) is integrated over two seconds for every measured value of the static magnetic field. After this time a sufficiently accurate equilibrium between injection and relaxation has been reached and the occupancies do not change anymore within the uncertainties.

The neglection of some apparatus related effects and additional relaxation mechanisms, for example the recombination, and the orders of magnitude of the systematic errors resulting from this, will be discussed in the following in chapter 11.5.

Tab. 11.1:
Compilation of the fit parameters for the measurements of the field dependence. The relaxation due to wall collisions is parameterized by τ_C and C (3.6). The injected flux $\dot{n}_{\text{inj}}$ determines the density inside the cell and is proportional to the spin exchange collisions rate T_{AA}^{-1}. The correction counting rate $S_{\text{korr.}}$ was adapted as well, it gives the counting rate due to the dissociative ionization of chopped molecular beams. The aluminum cell was ice coated (chapter 12.1). The given numbers for the wall collision rate in principle refer to state $|\,1\,\rangle$ (appendix A.3) and the parameterization (9.1) for the generation of the initial conditions. Systematic errors are not contained in the table.

	Hydrogen				**Deuterium**
Surface	Aluminum	Drifilm	Teflon	Teflon	Teflon
No. of Collisions	3505(14)	3505(14)	3505(14)	1456(6)	3505(14)
Temperature [K]	90(5)	101(5)	95(5)	90(5)	110(5)
χ^2	0.76	2.94	5.80	4.83	1,12
τ_c $[10^{-12}\,\text{s}]$	4.37(46)	5.41(27)	4.63(12)	4.68(26)	$2{,}26(56)\cdot 10^2$
C $[\text{s}^{-1}]$	84.7(19)	2.70(6)	21.8(2)	7.49(19)	7.28(59)
$\dot{n}_{\text{inj}}$ $[10^{14}\,\text{s}^{-1}]$	2.30(50)	3.24(4)	10.13(17)	13.09(16)	20.2(8)
$S_{\text{korr.}}$ [kHz]	1.441(28)	2.850(39)	3.449(56)	3.959(50)	0.679(34)

11.2 Parameterization of the Relaxation due to Wall Collisions

The correlation time τ_C and the amplitude C (3.6) were used as free parameters in the description of the wall collision relaxation. These parameters enter directly and without conversion into the fit.

The fit gives similar correlation times for the hydrogen measurements for all storage cells. For deuterium on teflon however the correlation time was longer by a factor of 50. Based on the measured data it is difficult to decide, whether this difference between hydrogen and deuterium results from the interactions on the surface or from systematic errors due to the neglections that are discussed in chapter 11.5. However, if the correlation time is interpreted as the mean length of stay on the surface and the Arrhenius law (3.2) is applied, then the large difference for τ_C at 100 K relates to a difference of about 30 meV in the binding energy E_S.

The order of magnitude of the correlation times also agrees well with the results measured by D.R. Swenson and L.W. Anderson for the relaxation of polarized sodium on a drifilm surface: $\tau_C = 4.0 \cdot 10^{-11}$ s for a fresh drifilm coating and $\tau_C = 1.5 \cdot 10^{-10}$ s for a drifilm coating that was exposed to the sodium vapor in the storage cell for a longer time. These two correlation times differ by about a factor of four that can be ascribed to the aging of the surface [43].

The polarization losses due to wall collisions in the cell mainly depend on the amplitude C. The measurement with the aluminum cell showed the largest value for C and the lowest electron polarization. The measurement with the drifilm cell has the lowest value of C and the highest electron polarization (see chapter 12.3.5). Neglecting the recombination leads to a systematic error in the fitting of C to the measured data (chapter 12.2). It may be assumed that the estimated values for C here are in general to low. In the case of the ice coated aluminum cell (see chapter 12.1) an especially large error is to be expected due to the high recombination rate. Without a measurement of the recombination rate no more precise statements are possible.

The amplitude does not exclusively depend on the surface conditions. In comparing results for the amplitude differences in the storage cell geometry and the temperature have to be taken into consideration. The results from table 11.1 can also not simply be compared to the values measured by D.R. Swenson and L.W. Anderson. This is of course also true if the results from the two teflon cell or the results for hydrogen and deuterium are being compared.

Assuming that the correlation time is roughly equal to the length of stay on the surface ($\tau_C \approx \tau_S$) which in turn may be neglected compared to the mean time of flight between two wall collisions ($\tau_S \ll \tau_F$), the following approximation is obtained for the the amplitude from (3.6):

$$C \approx \frac{2}{3}\gamma_S^2 b^2 \frac{\tau_C^2}{\tau_F}, \tag{11.1}$$

This may be used to estimate the strengths of the fluctuating magnetic fields that cause the relaxation. The mean time of flight can be taken from table A.3, for τ_C and C the fitted values from table 11.1 may be taken.

The strength of these fields is a surface specific parameter that allows a comparison between the different measurements. The results are compiled in table 11.2. The order of magnitude of the fields is in the region of the critical field of 50.7 mT for hydrogen, which speaks for the assumption that the fields are caused by the nuclear spins of hydrogen atoms that are bound to the surface. This conclusion was also drawn by M.A. Bouchiat and J. Brossel from the comparison of the relaxation on deuterized and normal paraffin [66].

The values for the measurements with teflon coating should largely agree in this table also in the comparison of hydrogen and teflon, because it is not to be expected that the strength of the

Tab. 11.2:
Estimate of the strengths of the fluctuating fields on the different surfaces. Systematic errors are not included.

	Hydrogen				**Deuterium**
Surface	Aluminum	Drifilm	Teflon	Teflon	Teflon
collision number	3505(14)	3505(14)	3505(14)	1456(6)	3505(14)
Temperature [K]	90(5)	101(5)	95(5)	90(5)	110(5)
b_{rms} [mT]	68.1(53)	9.38(38)	31.64(84)	16.85(77)	0.429(77)

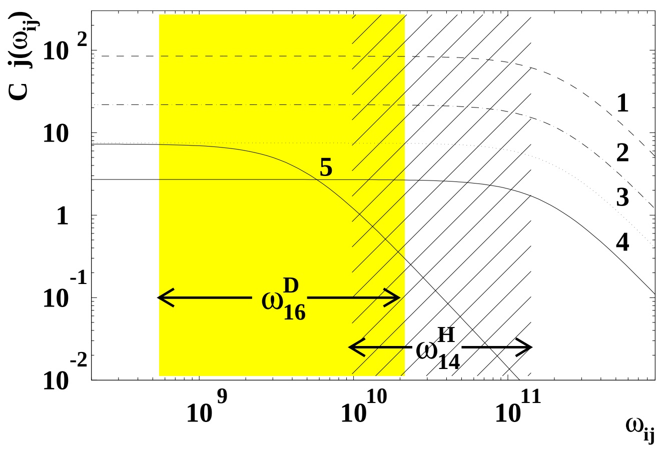

Fig. 11.1:
Wall collision relaxation as a function of the transition frequency. 1.-4.: Results for hydrogen. 1.) Ice coated aluminum (3505). 2.) Teflon, (3505). 3.) Teflon, (1456). 4.) Drifilm (3505). 5.) Deuterium on teflon, (3505). The hashed region marks the frequency region, which using fields between 10 and 350 mT for the transition 1-4 is covered by the hydrogen. The dotted region shows the analogous region for the 1-6 transition for deuterium.

fluctuating fields depends strongly on the used probe. The value for the deuterium measurement however is considerably smaller, due to the large correlation time that was found from the fit to this measurement. A possible reason for the size of this difference is perhaps that the assumption $\tau_C \approx \tau_S$ is not quite justified.

Figure 11.1 shows the wall collision relaxation rate according to (3.7) as a function of the transition frequencies ω_{ij} that are defined by the holding field over the storage cells. The individual curves are parameterized by the amplitude C and the correlation time τ_C that were taken from table 11.1. C describes the level of the constant regions and τ_C^{-1} is roughly the limiting frequency above which the transition probabilities decrease. The hashed and dotted areas illustrate the frequency region covered by holding fields between 10 and 750 mT for the transition 1-4 for hydrogen and 1-6 for deuterium. Transitions within the Zeeman-multiplets also happen at far lower frequencies. For the measurement of the correlation times sufficiently high magnetic fields must be reached. This condition is clearly better fulfilled for deuterium than for hydrogen. With the used holding fields the limiting frequency is reached for hydrogen as well as for deuterium which demonstrates that the measurements are in fact sensitive to the correlation time.

11.3 Parameterization of the Relaxation due to Spin Exchange Collisions

The fit of the theoretical calculation of the spin exchange relaxation to the measured data can be done with a single free parameter. The spin exchange collision rate T_{AA}^{-1} (3.10) is an obvious choice. As the entrance tube of the storage cell is not cooled, the collision rate depends on the storage cell temperature through the conductance values of entrance and exit tube (A.4). The temperature dependence of the density does not cancel itself out anymore with the temperature dependence of the mean velocity. As not all measurements were taken with the same cell temperature, the choice of collision rate as free parameter does not allow a direct comparison between the different cells.

By neglecting the thermal averaging $\langle \sigma_{SE} v \rangle$, in (3.10) the following approximation for the spin exchange collision rate is obtained:

$$T_{AA}^{-1} \approx n \sigma_{SE} \bar{v}, \tag{11.2}$$

It shows a simple relation between the spin exchange cross section and the spin exchange collision rate deduced from the measurements. For known density inside the storage cell now the spin exchange cross section can be determined and vice versa.

If the flux that is injected into the cell is known, the density inside the cell may be determined using the relations (A.1) and (A.4). The mean velocity is obtained from equation (A.9).

However, the apparatus used with the test source measured mostly flux ratios. The flux that is injected into the cell gained its absolute value from rough estimates with an error margin of about 50 % [136]. Therefore the cross section was set to the literature value of $\sigma_{SE} = 23.1 \cdot 10^{16}\,\mathrm{cm}^2$ [101] and the collision rate that was fitted to the measured data was converted into the injected fluxes using the following equation

$$\dot{n}_{[\mathrm{s}^{-1}]} = \frac{2.040 + C''_{\mathrm{off}}\sqrt{T_{[\mathrm{K}]}}}{3.338 \cdot \sqrt{T_{[\mathrm{K}]}}} \cdot 10^{14} \cdot T^{-1}_{AA\,[\mathrm{s}^{-1}]} \tag{11.3}$$

Values for C''_{off} can be taken from the table A.2 in the appendix. If the temperature is constant over the storage cell, the temperature dependence cancels itself out. However, according to theoretical calculations the spin exchange cross section falls drastically for values below 70 K [101], so that the spin exchange collision rate becomes temperature dependent if the thermal averaging $\langle \sigma_{SE} v \rangle$ is included. The approximation (11.2) is really only applicable for high temperatures.

In the application of equation (A.1) the recombination at the cell walls was not yet taken into account. There are also no data about the degree of dissociation inside the cell available so far, that would allow direct conclusions about this. Recombination leads to a reduction of the partial pressure for atomic hydrogen or deuterium, respectively, so that the technique introduced here leads to seemingly lower fluxes with increasing degrees of recombination. The other way around the measured fluxes allow the deduction of information about the degree of recombination.

A comparison of both cells with teflon coating in the case of hydrogen measurements in table 11.1 shows a somewhat lower flux for the larger cell, which is compatible with the assumption of a higher recombination resulting from the longer duration of stay in this cell. In the case of the deuterium measurement the gas throughput at the dissociator was set to twice the value. However, the flux in the cell is again reduced to half the value by the beam block in the sextupole magnet of the source. Therefore this value should be in agreement with the value for the hydrogen flux for the larger teflon cell. The difference of more than a factor of two indicates a systematic error rather than a higher recombination rate in hydrogen. A plausible explanation for the large differences in the injected gas fluxes was not found up to now.

The flux for an ice covered aluminum cell again agrees very well with the assumption that in this cell about 75 % of the atomic hydrogen recombines to molecules. This atomic hydrogen is still present in the teflon cell even under the assumption of a possible recombination. This value is also estimated in chapter 12.1 from the, compared to the teflon cell, smaller counting rate. However, for the cell with drifilm coating the same counting rate as for the teflon cell was measured, so that the small value resulting from the fit for the drifilm cell cannot be explained by a higher recombination.

11.4 The Correction due to Molecular Beams

Molecular beams containing hydrogen and deuterium contribute to the detected atomic beam signal through dissociative ionization in the formation volume of the mass spectrometer. As this background signal is not caused by the restgas in the detector chamber, but by a molecular beam, it is not possible to separate it from the atomic beam signal by chopping the beam.

Background contributions from molecular hydrogen (or deuterium) that is already injected into the storage cell or that results from recombination were already early taken into consideration. As the molecular beam exiting from the cell is not focused in the sextupole system of the Breit-Rabi polarimeter, the background signals caused are extremely small and can in general be disregarded. Following the estimate in appendix B.3 (table B.2) they maximally contribute 0.2 % to the atomic beam signal. Effects on the measured polarisation can only be demonstrated if large amounts of water thaw off from the walls during warming up of the storage cells (chapter 12.1 and 12.4). Background contributions of molecular beams from the storage cells can be completely removed through the deployment of a beam block in the sextupole system of the polarimeter.

Only after the relaxation measurements were complete, it was discovered that molecular beams are produced as a result of the pressure gradient in the differential pumping system and conductance limiting connection pipes between the chambers of the Breit-Rabi polarimeter and that their contribution to the atomic beam signal may not be disregarded. It was found that at least for the measurements of the holding field dependence of the relaxation, a subsequent fit is possible, using a constant background counting rate $S_{\text{corr.}}$ for the measurement of the concerned storage cell. These fitted background counting rates agree well with estimates of gas fluxes in the polarimeter (table B.2). As is shown in appendix B, this correction counting rate can depend only weakly on the setting of the high frequency transitions. In the measurements of the dependence on the storage cell temperature however, the conductance in the region of the storage cell changes and thus also the vacuum conditions in the first chambers of the polarimeter. Therefore the assumption of a constant background signal leads to a visible degradation of the quality of these measurements (chapter 12.4).

It is a disadvantage of this fit method that the measured values of the Breit-Rabi polarimeter are not absolute polarization values, because they were adapted to the relaxation model through $S_{\text{corr.}}$. Therefore the results of an alternative adaptation are compiled in appendix C. This method starts with the assumption that the initial occupancy derived from the efficiency measurements (chapter 8.7) and the transmission calculations (chapter 9.5) are not correct. In this adaptation all transmissions and efficiencies that are relevant for the initial occupancies are treated as free parameters and included in the fit. Despite the significantly higher number of free parameters this adaptation gives comparable results. As is apparent from the comparison of the tables 11.1 and C.1, the choice of fit method has practically no effect on the parameters of the relaxation model. With few exceptions the values in both tables agree within the given statistical errors. Table C.1 lists both the calculated parameters for the initial occupancy for the used adaptation method and the ones resulting from the fit.

It is apparent from figure 11.2 which effect both fit methods have on the plot of the polarization results. On the left side the initial occupancy and on the right side the background counting rate was adapted. Besides the scale of the ordinate both pictures agree almost completely. This simple relation is true for all polarization results shown in chapter 12.3, including the deuterium measurements. The depiction of measured results of hyperfine occupancies however cannot be transformed from one fit method to another in this simple fashion, because here the differences between the occupancies n_i change.

There are several good arguments to prefer the adaptation of the background counting rate:

- The background correction can be based on flux estimates (appendix B).
- A loss of more than 10 % in all nuclear polarization observables in strong fields, that cannot explained by the relaxation model, disappears (see table C.1).
- For the uncoated aluminum cell an adaptation of the initial occupancy leads to a by 0.07 smaller initial polarization for P_z compared to the coated cells. This contradiction is avoided if the background counting rate is adapted.
- In measurements of the dependence on the storage cell temperature (chapter 12.4) the polarization decreases again for temperatures above 150 K. This behaviour cannot be

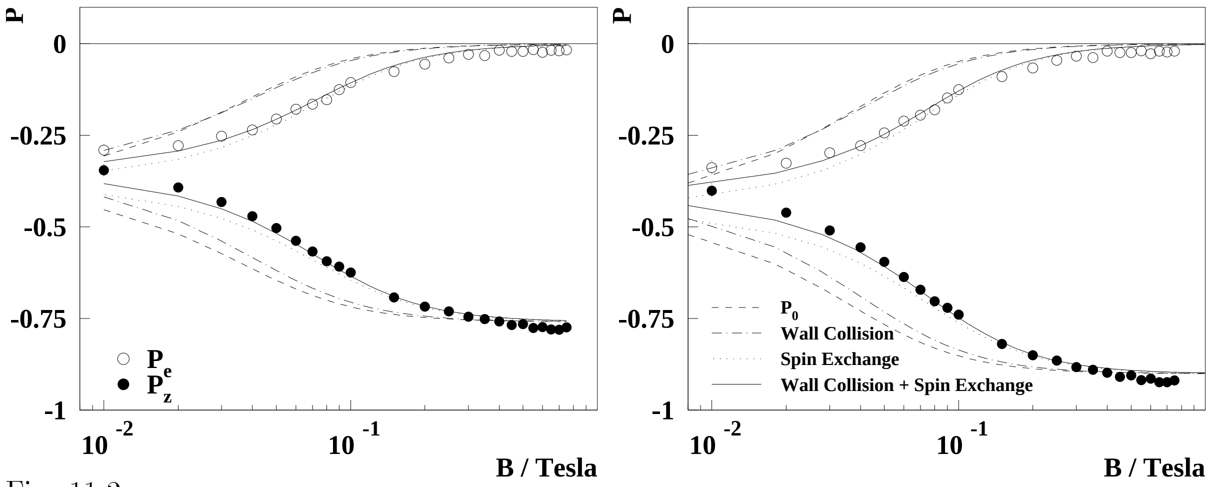

Fig. 11.2:
Comparison of the fit methods with respect to the results of the polarization measurements. The nuclear and electron polarization values are shown as a function of the magnetic field in a cell with drifilm coating for an average number of wall collisions of $3505(14)$ and a cell temperature of $101(5)\,\mathrm{K}$. At the injection of of the states $|2\rangle$ and $|3\rangle$. On the left side the initial occupancy and on the right side the background counting rate was adapted, this picture agrees with the right side of figure 12.4. The meaning of the different curves is explained there as well.

understood in the framework of the relaxation model, but can be understood assuming a molecular background beam.

In the following subsection it will be shown, that especially in deuterium measurements large errors still have to be expected in the determination of the initial occupancies. Therefore the adaptation in appendix C is at least partially justified. Both fit methods therefore only determine an upper and a lower limit for the initial polarization, the real initial polarization lies somewhere in between.

In future measurements an adaptation of the background counting rate may be waived if the counting rates for the contributing molecules at the masses 2 (H_2), 4 (D_2) and 18 (H_2O) are measured during a polarization measurement as well. A determination of the probability for the dissociative ionization of these molecules is possible for any setting of the mass spectrometer with the method that was used in the measurement shown in figure 12.2.

11.5 Causes of Systematic Errors

Systematic errors in the adaptation of the relaxation model to the measured data can result from some neglections as well as from errors in the initial occupancy or the polarization measurement. Several possible causes are listed and discussed in the following.

- Incomplete description of the relaxation inside the storage cell:
  - Neglections in the integration of the master equation:
    - differing conditions in the injection tube
    - linearly decreasing density in the injection and exit tubes
    - polarization distributions.
  - Additional relaxation mechanisms:
    - spin dependence of the recombination.

- Errors in the determination of the initial polarization:
  - Errors in the simulation calculations:
    - differences between real sextupole system and the computer model
    - the parameterization of the beam production (9.1).
  - Reduced efficiencies of the high frequency transitions due to high beam velocities
- Errors in the polarization measurements:
  - Reduced efficiencies of the high frequency transitions
    - due to high beam velocities and
    - due to the missing phase control in the strong field transitions (deuterium).
  - Asymmetric efficiencies of the high frequency transitions
    - as a result of the different velocity profiles for focused and defocused states and
    - as a result of interference from noninvolved states (chapter 7.2).
  - Unpolarized background in the chopped beam.

The master equation (3.1) is integrated under the assumption that the physical conditions are identical throughout the storage cell. This assumption is only partly justified. Especially the weaker holding field in the injection tube of the storage cell can lead to a stronger relaxation compared to the rest of the cell

The atoms detected by the Breit-Rabi polarimeter in the case of the small cell have maximally 7 % of their wall collisions in the injection tube (table A.3), for the large cell it is only 4 %. The maximal loss of polarization for all measurements for the entire storage cell is 80 % for holding fields in the region of the critical field (chapter 13). Assuming that the magnetic field that is worst for keeping the polarization is present over the entire injection tube, the injection tube could cause a loss of polarization of maximally 5.6 % for the small cell and 3.2 % for the large cell. Especially for measurements with strong fields over the region of the storage cell, the field in the injection tube is also strong, at least in the part close to the actual cell. The systematic error caused by the injection tube therefore should be significantly smaller. Simulation calculations [136] show values of less than 2 % for holding fields of more than 400 mT. The effects of the teflon coating and the higher temperature in the injection tube should be comparatively negligible.

The decreasing density in injection and exit tube and the spatial variation of the polarization are relevant for the relaxation within the HERMES storage cell, because in some sense it only consists of injection and exit tubes (figure A.2). Following the above argument the atoms spend only a short time in the injection and exit tubes compared to the total duration of stay in the test storage cells. Therefore the assumption of spatially constant physical conditions, besides the weaker field in the injection tube, should be justified.

The possibility of additional relaxation mechanisms besides wall and spin exchange collisions should in principle be taken into consideration. However, so far there are only hints that the recombination of the atoms on the surface influences the electron polarization due to it's dependence on the relative spin orientation of the electrons (chapter 12.2). As already discussed in chapter 11.2, this effect causes an underestimation of the amplitude C for the wall collision relaxation. The other parameters of the relaxation model remain mostly unaffected. Whether further relaxation mechanisms influence the hyperfine occupancies will only become apparent when systematic differences between relaxation model and measured data remain after all other potential errors have been eliminated.

The initial occupancy is fairly well known, at least for hydrogen. The efficiency of the WFT 1-3 is insensitive against the calculated changes in the velocity profile of the atomic beam (compare figures 9.4 and 9.9), because the transition was operated far into saturation, i.e. with a sufficiently strong high frequency field. The simulation program used for the determination of the sextupole transmissions was tested by comparison to measured data (figures 9.2 and 9.3) and can be regarded as reliable. Possible deviations of the real sextupole system from the computer model can be kept within narrow limits by thoroughly gauging the apparatus. The parameterization of the Monte Carlo generator for the beam production in the test source is not known from measurements; however, figure 9.8 that the polarization of the atomic beam that is injected into the storage cell at a sextupole current of 170 A is practically independent of the chosen parameterization. Also a higher nozzle temperature has only a very limited effect (figure C.1). The error on the determination of the initial polarization should therefore be less than 3 %.

In the case of deuterium measurements errors in the sextupole transmissions can be completely disregarded for the determination of the initial occupancy, because a beam block was installed in the sextupole magnet. However, a reduction of the efficiencies of the strong field transitions in the source due to the change in the velocity profiles (figures 9.4 and 9.9) has to be considered. For these transitions the saturation behaviour was significantly worse than in the case of WFT 1-3 for hydrogen. Also the results of the alternative fit in appendix C indicate that the efficiencies of these transitions were smaller in the polarization measurements than in the efficiency measurements. However, the comparison between the tables 11.1 and C.1 shows that this does not lead to a large error in the adaptation of the relaxation parameters.

Also for the high frequency transitions in the polarimeter a reduction of the high frequency transitions due to shifts in the velocity profiles has to be taken into consideration. A comparison between figure 9.4 and 9.6, however, shows that the different sextupole systems for efficiency and polarization measurements only have a minor impact on the efficiency of these transitions. By using a beam block in the first sextupole of the polarimeter a reduction of the efficiencies can be completely excluded. In the polarimeter the strong field transitions for deuterium on the other hand were still operated without phase control (figure 4.4), so that their efficiencies are not necessarily stable. This flaw has already been corrected and only concerns the relaxation measurements with deuterium that are presented here. To first order, it is of no consequence whether the efficiency of a high frequency transition is changed before or after the storage cell, so that the reduction of efficiency of a transition in the polarimeter has a similar effect as one in a transition in the source. Therefore an upper limit for the reduction of the efficiencies of the strong field transitions in the polarimeter can also be taken from table C.1. Large errors in the adaptation of the relaxation parameters cannot result from a reduction in the efficiencies in the polarimeter.

Asymmetric efficiencies due to differences in the transmitted velocity profiles can be excluded completely as a cause of systematic errors in the deuterium measurements by installing beam blocks in the sextupole magnets. In the hydrogen measurements, that were carried out without the beam blocks, they are negligible. However, this is not true for the asymmetry described in chapter 7.2. This asymmetry can only be reduced to a minimum by the high frequency transition operating in saturation, but it cannot be eliminated completely. This effect probably gives a large contribution to the systematic errors, that were created in the adaptation of the relaxation model to the relaxation measurements that will be described in the following.

The background signal from molecular beams discussed in chapter 11.4 is in itself a systematic error of the polarization measurement if it is not taken into account. In the adaptation of this background signal to the measurements a systematic error also results from the assumption of a constant background signal over the entire measurement.

In the comparison of different storage cells changes in the surface structure due to adsorbates from the restgas have to be considered. The pressure in the region of the storage cell is about 10^{-7} mbar without gas. Even for identical coating, temperature and holding field it cannot be expected that the surface conditions are identical. In chapter 12.1 the growth of an ice layer in the uncoated aluminum cell is described and in chapter 12.4 obvious indications are given that and ice layer also freezes out on the walls of coated cells. Due to this ice layer the wall collision relaxation can depend on how long the cell temperature is kept below about 150 K. From this point of view there is an excellent agreement between the two teflon coated cells with different wall collision rates. Only the results for the strengths of the fluctuating fields that are responsible for the wall collision relaxation are different by a factor of two (tables 11.1 and 11.2).

12 Relaxation Measurements

12.1 Measurement with an Uncoated Aluminum Cell

In 1993 measurements of the relaxation of tensor polarized deuterium in uncoated aluminum cells were published by J.S. Price and W. Haeberli [74] that suggested that it would be possible to use uncoated aluminum storage cells also in the HERMES experiment. The measurements were carried out using an ion extraction polarimeter (chapter 1.6) in a strong holding field, using T-shaped storage cells with several hundred wall collisions. Especially for temperatures above 120 K the maximal loss of tensor polarization in these measurements is only 9 % in the atomic part of the gas, though including the recombination to molecular deuterium it is already up to 28 %.

Uncoated aluminum cells would be of great interest to the HERMES experiment, because the target cell is affected by the 27.5 GeV positron beam, even if the cell is protected from the synchrotron radiation by a collimator system. For this reason the Breit-Rabi polarimeter was used also to examine the relaxation behaviour in an uncoated aluminum storage cell. However, due to time constrictions the measurements could only be done for hydrogen.

After strong hysteresis effects regarding the cell temperature were seen in several test measurements a 'longtime' measurement was carried out to clarify the reasons. The storage cell, in which the atoms experience 3505(14) wall collisions, was cleaned with acetone in an ultrasound bath before installation and it was heated in vacuum up to a temperature 480 K before the measurement started to remove contaminants from the surface. Afterwards, the cell was cooled down to a temperature of 90 K and kept stable at this temperature for about one hundred hours. During this time the polarization of the exiting atomic beam was monitored continuously.

Figure 12.1 shows the results of this longtime measurement. The top picture shows the storage cell temperature, the second one the beam counting rate without high frequency transitions, the third one the electron polarization at the injection of the states $|\,1\,\rangle$ and $|\,2\,\rangle$ and the bottom one the nuclear polarization at the injection of the states $|\,2\,\rangle$ and $|\,3\,\rangle$.

After the bake-out, the cell cools down to about 270 K within about 20 hrs with the help of some nitrogen cooling. Then the flow of liquid nitrogen is increased, so that the cell reaches the final temperature of 90 K after two additional hours. During this cooling phase an electron polarization of about 0.1 and a nuclear polarization of -0.1 is measured. The counting rate, and thus the intensity of the H_1 beam exiting from the cell, is ery low with a value of 1 kHz. This leads to the conclusion of a high recombination rate within the storage cell. The low counting rate also leads to large statistical errors and to fluctuations in the measured polarization. After this cooling phase the cell is at first stable. Beam intensity, electron and nuclear polarization stay at the same values measured during the cooling process. Only after about twenty hours after the cell has reached it's final temperature the counting rate starts to rise and after seventy hours reaches a value of 7 kHz, without any apparent saturation. The electron polarization initially starts to rise to 0.2, but drops again to 0.15. The nuclear polarization increases [17] continuously and reaches a saturation value of about -0.65.

[17] In the following the phrase 'increase in polarization' is also used for negative polarization values that become more negative.

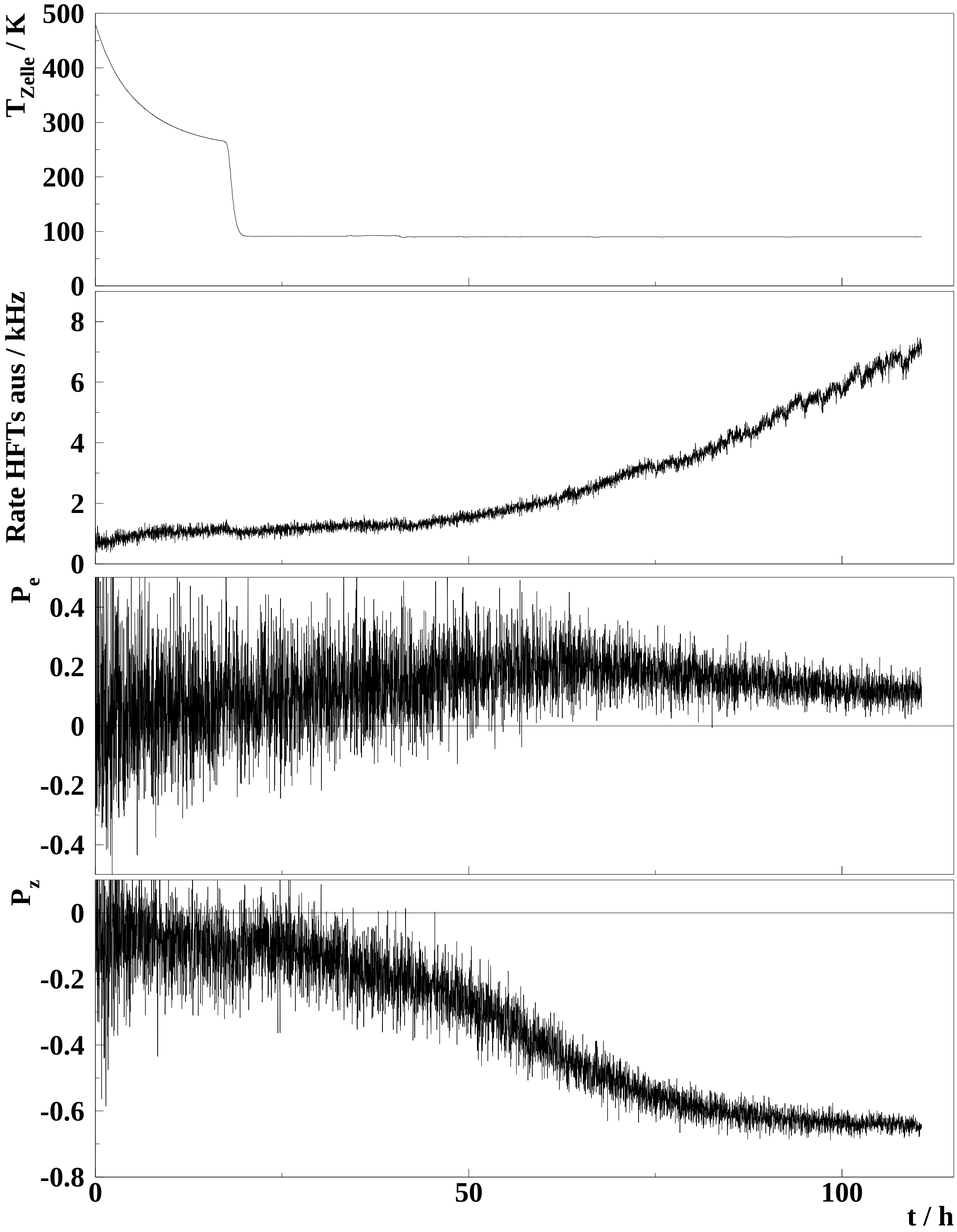

Fig. 12.1:
Longtime measurement with an uncoated aluminum storage cell for a holding field in the storage cell region of $350\,\mathrm{mT}$ and an average number of wall collisions of 3505(14). From top to bottom: 1.) temperature of the storage cell 2.) counting rate without high frequency transitions 3.) electron polarization without WFT 1-3, injection of the states $|1\rangle$ and $|2\rangle$ 4.) proton polarization with active WFT 1-3, injection of the states $|2\rangle$ and $|3\rangle$. All parameters are plotted versus the time of the measurement. The two injection modi were switched about every 30 seconds. The polarization was calculated without background correction (table 11.1).

This behaviour of the aluminum storage cell can be explained by a layer of ice that slowly freezes out on the cell surface at 90 K. This ice layer gradually reduces the recombination as well as the depolarization of the injected gas within the cell. The water for this ice layer probably comes from the restgas in the atomic beam source, whose vacuum chambers cannot be baked out. Without this ice layer a high depolarization as well as a high recombination rate is measured in the aluminum storage cell. Above 200 K no remaining polarization can be detected in the atomic fraction. This obviously constitutes a certain contradiction to the results of J.S. Price and W. Haeberli [74], even if the tensor polarization of deuterium in these measurements was measured for much smaller wall collision numbers.

It can be shown from mass spectra that the layer growing inside the cell is, in fact, ice or water, respectively. To this purpose the cell is warmed up slowly after the polarization measurements are finished and the mass spectrometer of the beam detector is used to measure the composition of the beam exiting from the cell and of the chopped beam as a function of the cell temperature. Figure 12.2 shows the intensity of the water beam exiting from the cell as a function of the cell temperature. Up to a temperature of 130 K the counting rate stays below 1 kHz. Above 140 K the intensity of the water beam increases and reaches a maximum of about 470 kHz at 200 K. Above 200 K about 3 kHz are measured. This counting rate can be traced to water that enters the cell from the atomic beam source, passes through the cell without freezing out and then is detected as water beam in the beam detector.

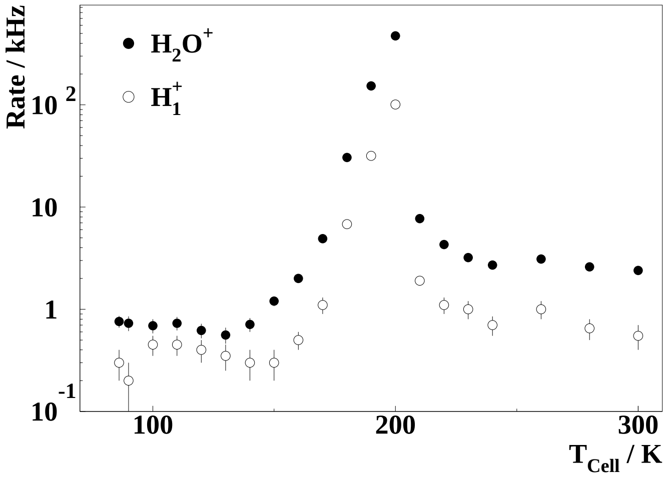

Fig. 12.2:
Intensity of the water beam exiting from the uncoated aluminum cell as a function of the storage cell temperature. Simultaneously also the H_1 counting rate from the dissociative ionization of water molecules is shown. The measurements were carried out during the warming up of the cell, after the cell had been kept at a temperature of 90 K for about 150 hours. Within the error bars further components could not be found in the mass spectra.

Even if the measured nuclear polarization of the atomic hydrogen beam exiting from the cell with -0.65 is relatively high despite the ice layer inside the aluminum storage cell, it is of limited usefulness for the HERMES experiment. If the H_1 counting rate after more than a hundred hours of about 7 kHz is compared to the counting rates of about 30 kHz, as they are measured with teflon or drifilm coated cells under identical conditions, it has to be concluded that at least 75 % of the injected hydrogen recombines to molecules in the ice coated aluminum storage cell. Assuming that the nuclei completely lose their polarization in the recombination to molecules, the nuclear polarization of atoms and molecules together is only about 15 % of the injected polarization.

Figure 12.2 shows the intensity of the water beam and additionally also the H_1 counting rate created by dissociative ionization of water molecules in the formation volume of the mass spectrometer. Both counting rates differ by a factor of four or five over the entire temperature range, resulting in a estimated probability of 20 % for the dissociative ionization of a water molecule. This H_1 counting rate cannot be separated from the atomic beam by the beam chopper in the same way the restgas background is separated. Therefore it contributes to an unpolarized background in the polarization measurements, that becomes noticeable in measurements of the temperature dependence between 150 and 200 K (figure 12.12). This kind of background contributions due to molecular beams from the storage cell can be completely avoided through the use of a beam block in the sextupole system of the polarimeter.

The aluminum cell is described in comparison to teflon and drifilm coated cells in chapter12.3.5. The necessary measurements were done after the longtime measurement described, while the storage cell temperature was kept constant after the ice layer was grown, and the electron and nuclear polarizations of the atomic beam exiting the cell had become stable.

12.2 Recombination

There is a further reason why the results shown in figure 12.1 are interesting. It is apparent that in the period between 50 to 100 hours after begin of the measurement the nuclear polarization rises steadily while the electron polarization decreases at the same time. This cannot be due to the polarization transfer from the electrons to the nuclei expected as a result of spin exchange collisions, because both lower plots show two independent measurements. In the upper picture the states $|\,1\,\rangle$ and $|\,2\,\rangle$ were injected into the cell, while in the lower picture $|\,2\,\rangle$ and $|\,3\,\rangle$ were used. The opposite behaviour of nuclear and electron polarization in this measurement cannot be explained within the framework of the relaxation model as described in chapter 3. However, if the recombination of the atoms on the walls of the storage cell is taken into account, this conspicuous behaviour can be understood very well, at least qualitatively.

The recombination of atoms to molecules depends on the relative orientation of the two electron spins before they are absorbed by the surface. Two atoms can recombine only if their electron spins are antiparallel so that together they carry no electron polarization. Thus atoms with depolarized electrons are permanently removed from the atomic fraction of the gas due to recombination, which depending on the recombination rate can lead to a significant reduction of the electron polarization.

In fact the decrease of electron polarization happens at the same time as the increase of the H_1 counting rate, which can be interpreted as a decrease of the recombination rate in the storage cell. Following the above argument this must lead to a reduction of the measured electron polarization, which is indeed observed.

If the recombination is integrated into the relaxation model, it becomes apparent that the recombination rate is strongly correlated to the amplitude for the wall collision relaxation C. The assumption of a high recombination rate leads to a higher wall collision amplitude in the fit. However, these two parameters cannot be set to fixed values. The other parameters of the relaxation model, especially the nuclear polarization in strong holding fields, remain uninfluenced.

The recombination therefore causes a systematic error in the fit of the wall collision amplitude, which especially for an ice coated aluminum cell due to the high recombination rate must be significantly higher than listed in table 11.1. The size of this effect for the coated storage cells cannot be estimated without a measurement of the recombination rate.

The measurement of the degree of dissociation of the beam exiting from the cell with an additional mass spectrometer between the cell and the Breit-Rabi polarimeter [133] thus becomes important not only for the correct measurement of the target polarization, but also for an exact determination of the relaxation parameters. Effects due to the spin dependence of the recombination are well known for very cold surfaces; they are in fact used in ultracold sources to avoid the recombination by polarizing the electrons [137, 138].

12.3 Measurements of the Dependence on the Holding Field in the Storage Cell

The parameters for the relaxation model in table 11.1 only in part agree within one order of magnitude. However, if the different cells are compared, still the measured results agree very well with the theoretical relaxation model from chapter 3 if every cell is considered alone. As will be shown in this subsection by comparing these sets of parameters directly to the measured results, the dependence of the relaxation on the holding field in the storage cells can be well described by this model.

12.3.1 The Field Dependence of the Hyperfine Occupancy for Hydrogen

The ability of the Breit-Rabi polarimeter to completely resolve the hyperfine occupancy in the analyzed atomic beam makes it possible to detect relaxation processes that cannot be seen by polarimeters that are only directly sensitive to the nuclear or electron polarization. The relaxation of the difference between the occupation numbers n_2 and n_4 in weak magnetic fields is mostly caused by spin exchange collisions and can be unambiguously detected by the Breit-Rabi polarimeter, although both states carry no polarization in a weak field (figure 2.1). The relaxation behaviour of the hyperfine occupancy of hydrogen as a function of the external magnetic field is shown in figure 12.3 for the example of a drifilm coated cell. The first two pictures show the effects of spin exchange collisions and wall collisions separately. In the last plot the theory including both effects is compared to the measured values. As can be seen clearly in the first picture, the relaxation in the difference of the occupancies of the states $|\,2\,\rangle$ and $|\,4\,\rangle$ can be attributed to the spin exchange collisions alone.

The wall collisions, whose effects can be seen in the second picture, also lead to a convergence of the two occupation numbers n_2 and n_4. However, this convergence is small compared to the effect of the spin exchange collisions. The effect of the wall collisions on the states $|\,1\,\rangle$ and $|\,3\,\rangle$ is far more significant. Their convergence in a weak field leads to a loss of polarization and thus cannot be explained by spin exchange collisions alone, as these cannot influence the difference in the occupation of these two states. In spin exchange collisions no loss of polarization may occur,

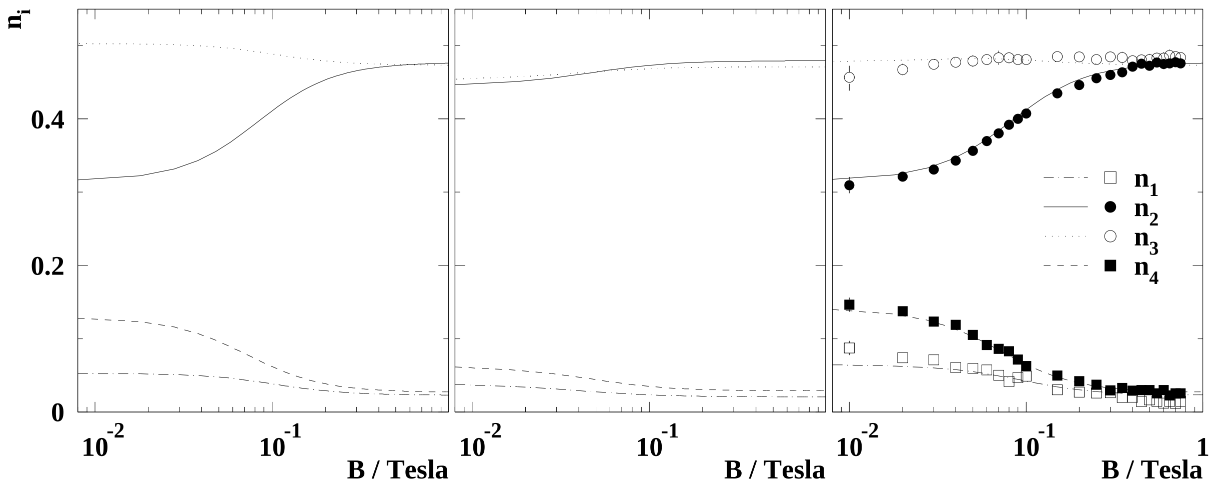

Fig. 12.3:
Hyperfine occupancy as a function of the magnetic field in a cell with drifilm coating for an average number of wall collisions of $3505(14)$ and a cell temperature of $101(5)\,\mathrm{K}$. Injection of the states $|\,2\,\rangle$ and $|\,3\,\rangle$. 1.) Effect of spin exchange collisions. 2.) Effect of wall collisions. 3.) Comparison of theory and measurement including both effects.

as the sum of nuclear and electron polarization must be conserved. Therefore the difference in the occupancies of the states $|1\rangle$ and $|3\rangle$ for hydrogen must also stay constant. The convergence of these two occupation numbers in weak fields thus illustrates the effect of the wall collisions.

12.3.2 The Field Dependence of the Polarization in Hydrogen

From the hyperfine occupancies measured by the Breit-Rabi polarimeter the nuclear and electron polarization can be calculated using (2.22). The results of this calculation are shown in figure 12.4 for the case of a drifilm coated cell. They are compared to the theoretical description through wall and spin exchange collisions using the parameterization from table 11.1 and the initial polarization from chapter 9.5.

Two cases are discerned: In the left figure the WFT 1-3 in the source was switched off and the states $|1\rangle$ and $|2\rangle$ were injected into the cell. In strong fields this means that a high positive electron polarization is injected into the cell, the injected nuclear polarization on the other hand tends towards 0. In the right figure the WFT 1-3 was activated; therefore the states $|2\rangle$ and $|3\rangle$ were injected, which for strong fields relates to a high negative nuclear polarization and a negligible electron polarization. As a result of the increasing hyperfine structure coupling for weak external fields in the first case both polarizations converge towards a value just below $+0.5$, in the second case towards a value just above -0.5. The comparison of the measured values with the initial polarization shows that the variation with the holding field for the measured nuclear and electron polarization results from the hyperfine structure coupling largely.

The electrons experience a significant depolarization also in the case of a strong field (figure 12.4 left), the nuclear polarization on the other hand converges towards the initial polarization (figure 12.4 right). This behaviour is in good agreement with the expectations for the relaxation due to wall collisions (see also figure 3.1). In the left figure it also can be seen that the depolarization of the electrons in a strong field cannot be explained by spin exchange collisions and that it must be assigned almost completely to wall collisions.

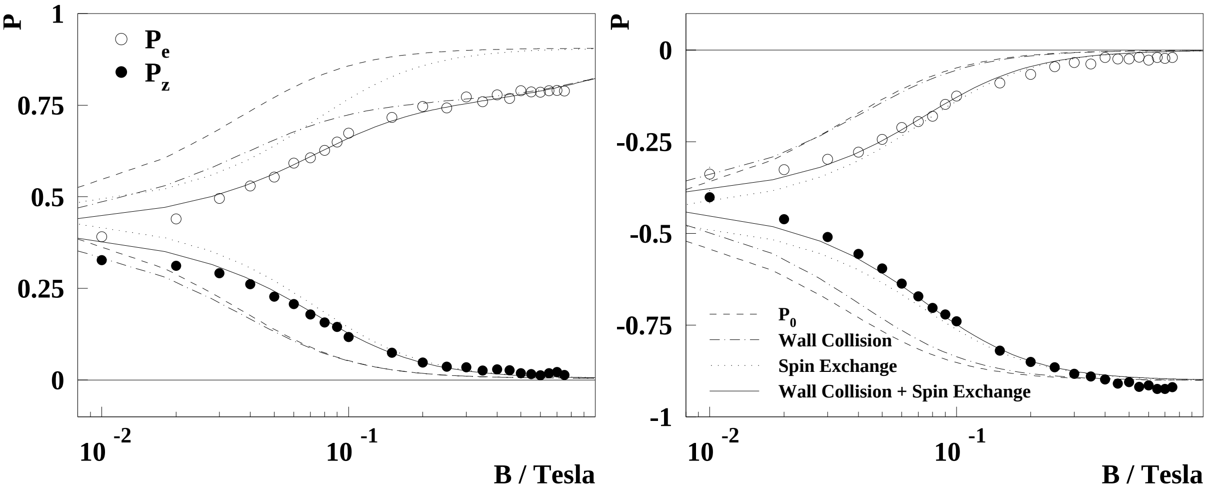

Fig. 12.4:
Nuclear and electron polarization as a function of magnetic field in a drifilm coated cell for an average number of wall collisions of $3505(14)$ and a cell temperature of $101(5)\,\mathrm{K}$. Left: Injection of the states $|1\rangle$ and $|2\rangle$. Right: Injection of the states $|2\rangle$ and $|3\rangle$. The fitted initial polarization is indicated by the dashed line, the effects due to wall and spin exchange collisions are shown as dotted and dash-dotted lines, the effects of both mechanisms are shown as solid curves, where no difference is made between nuclear and electron polarizations, because both can be assigned easily by comparison with the measured data.

12.3.3 The Field Dependence of the Hyperfine Occupancy for Deuterium

The relaxation behaviour in the hyperfine occupancy of deuterium was until now only examined for the case of a teflon coated storage cell with about 3500 wall collisions. By using a strong field resonator with tilted rods (figure 4.5) a total of five different hyperfine occupancies can be prepared for the atomic beam that is injected into the cell. However, only four of these were examined.

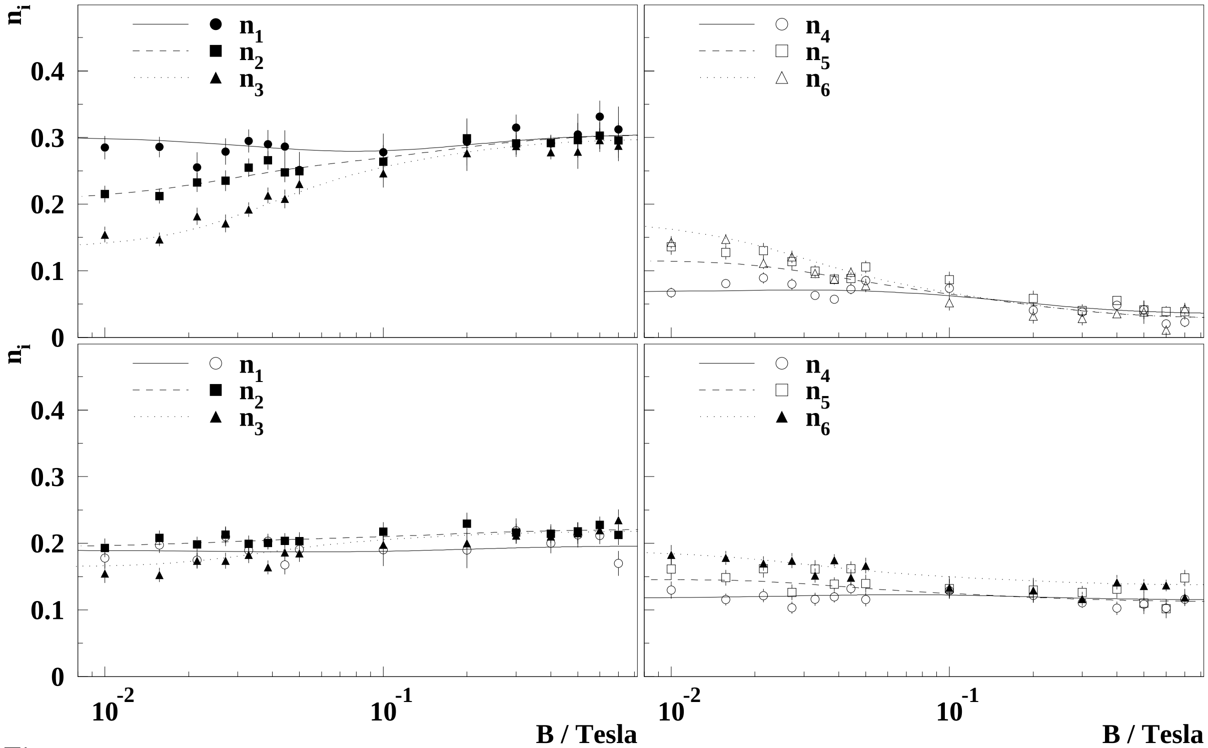

Fig. 12.5:
Hyperfine occupancy for deuterium as a function of the magnetic field in a teflon coated cell for an average number of wall collisions of 3505(14) and a cell temperature of 110(5) K. Top: Injection of the states $|1\rangle$, $|2\rangle$ and $|3\rangle$. Bottom: Injection of the states $|2\rangle$, $|3\rangle$ and $|6\rangle$. Left: Occupancy of the states $|1\rangle$ to $|3\rangle$. Right: Occupancy of the states $|4\rangle$ to $|6\rangle$. The filled markers indicate the injected states.

Figure 12.5 top shows the relaxation behaviour for inactive high frequency transition. The states $|1\rangle$, $|2\rangle$ and $|3\rangle$ are injected into the cell. This relates in a strong field to an electron polarization of $P_e \approx +1$, because for this measurement a beam block was installed inside the sextupole magnet of the source so that contributions of defocused states can be excluded. In a strong field the relaxation is weak and the injected populations are predominantly conserved. In a weaker field the occupancies of the states $|3\rangle$ and $|6\rangle$ show the strongest convergence. The populations of the states $|2\rangle$ and $|5\rangle$ also converge, but the effect is less expressed. The difference between the pure states $|1\rangle$ and $|4\rangle$ shows the smallest relaxation.

If the SFT 1-6 is activated (figure 12.5 bottom), in a strong field only the injected electron polarization is reduced to about 1/3, but no polarization is transferred to the nuclei (table 4.1). The effects are thus strongly reduced when compared to the case of inactive high frequency transition and the hyperfine occupancy is nearly constant and flat over the entire examined field range.

The most interesting effects on the hyperfine occupancy are observed if either the SFT 2-6 or the SFT 3-5 is activated in the source (figure 12.6). In these cases the possibility arises to experimentally detect spin exchange collisions in a strong field. Due to the decoupling fron the

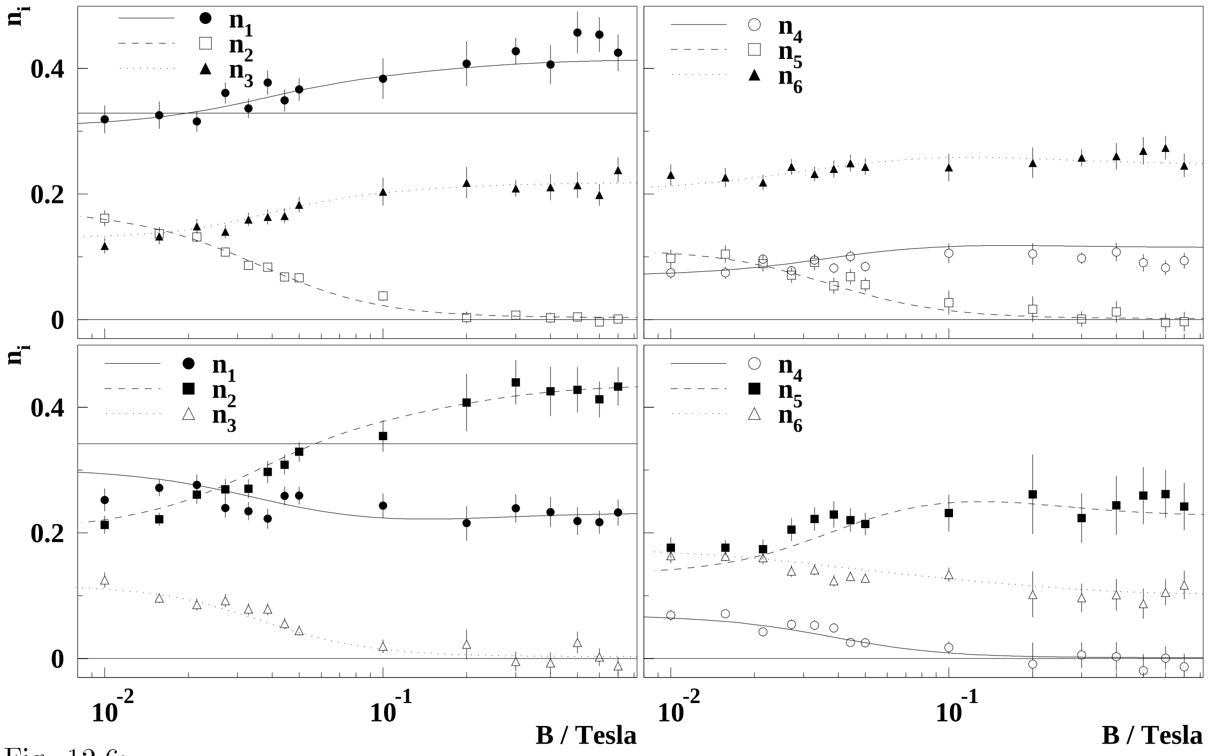

Fig. 12.6:
Hyperfine occupancy of deuterium as a function of the magnetic field in a teflon coated cell for an average number of wall collisions of $3505(14)$ and a cell temperature of $110(5)\,\mathrm{K}$. Top: Injection of the states $|\,1\,\rangle$, $|\,3\,\rangle$ and $|\,6\,\rangle$. Bottom: Injection of the states $|\,1\,\rangle$, $|\,2\,\rangle$ and $|\,5\,\rangle$. Left: Occupancy of the states $|\,1\,\rangle$ to $|\,3\,\rangle$. Right: Occupancy of the states $|\,4\,\rangle$ to $|\,6\,\rangle$. The filled markers indicate the injected states. The horizontal lines on the left mark the initial population of the state $|\,1\,\rangle$ (top) and the state $|\,2\,\rangle$ (bottom).

electron spins the nuclei can be regarded as spectators in these collisions, while the electron spins of the atoms are exchanged in the collision and thus the population of the hyperfine states is changed (chapter 3.2.2). However, these spin exchange collisions have no impact on the polarization observables.

In both cases the spin exchange collisions populate a state that is already injected into the cell. As no collision partner for this state is injected that could lead to a depopulation due to spin exchange, in a strong field a significant increase in the population of this state is observed to values above the injection value of 1/3.

In the first case, where the SFT 2-6 is activated, the states $|\,1\,\rangle$, $|\,3\,\rangle$ and $|\,6\,\rangle$ are injected into the cell and in the strong field the population of the state $|\,1\,\rangle$ increases as a result of the reaction mechanism (3.24). This increase is clearly visible in figure 12.6 top. If the SFT 3-5 in the source is activated, the states $|\,1\,\rangle$, $|\,2\,\rangle$ and $|\,5\,\rangle$ are injected into the cell (figure 12.6 bottom). In this case the reaction mechanism (3.25) in a strong field leads to an increase of the population of state $|\,2\,\rangle$.

Reactions of this kind occur in every second collision and they represent unambiguous proof for the existence of spin exchange collisions at low densities. Every atom experiences between 1.5 and 15 spin exchange collisions during its time in the storage cell, which is sufficient to lead to this effect. For a higher average number of spin exchange collisions (> 20) this effect would vanish again (figure 3.4).

12.3.4 The Field Dependence of the Polarization of Deuterium

Electron, vector and tensor polarization of deuterium are calculated from the measured hyperfine occupancy according to (2.30).

The behaviour of the electron polarization is examined as in the case of hydrogen with inactive high frequency transitions in the atomic beam source, so that the states $|\,1\,\rangle$, $|\,2\,\rangle$ and $|\,3\,\rangle$ are injected into the cell. This case is shown in figure 12.7. The solid curve in this plot represents the result of the theoretical calculations including wall and spin exchange collisions and is in good agreement with the experimental values. The dashed curve shows the injected electron polarization, while the other two curves describe the effects of wall collisions and spin exchange collisions separately.

The critical field of deuterium is only 11.7 mT, so that the examined magnetic fields are almost completely within the region of strong fields. The strongest examined magnetic field of 700 mT relates to about sixty times the critical field. Nevertheless, the electrons at this field still show a depolarization of more than 20 %, which still increases significantly for weaker fields. A comparison of the influence of both relaxation mechanisms on the electron polarization shows that this is mostly due to wall collisions, as in the case of hydrogen. Spin exchange collisions only play a secondary role for the electron polarization.

The atomic beam source used here is only suited for the examination of the relaxation behaviour of the vector polarization in a limited way, because the maximally obtainable vector polarization in a strong field is only 1/3. It can be obtained by activating the SFT 2-6 as well as the SFT 3-5 for the injected beam. With a weak field transition WFT 1-4 a beam with $P_z = 2/3$ could be prepared. A vector polarization of $P_z = \pm 1$ can only be reached with a second sextupole magnet after the high frequency transition in the source, because an additional state must be removed from the atomic beam. This ideally becomes possible with the source used in the HERMES experiment (see appendix D). Figure 12.8 shows the behaviour of the vector polarization in dependence of the holding field in the storage cell. In the left picture the vector polarization is nearly constant over the entire field range, a significant depolarization is not visible in this picture. The effects of the single relaxation mechanisms on the vector polarization can only distinguished from one another up to about 100 mT, for stronger fields the vector polarization calculated according to the relaxation model basically agrees with the injected polarization. The small size of these changes in comparison to the hydrogen measurements can be explained by the fact that for the injected initial occupancies $P_e \approx P_z$, so that almost no exchange between the vector polarization of the nuclei and the electron polarization is possible. According to the theoretical calculations in figure 3.4 spin exchange collisions under these conditions would even lead to a small increase in the vector polarization, which is in turn compensated by the wall collisions.

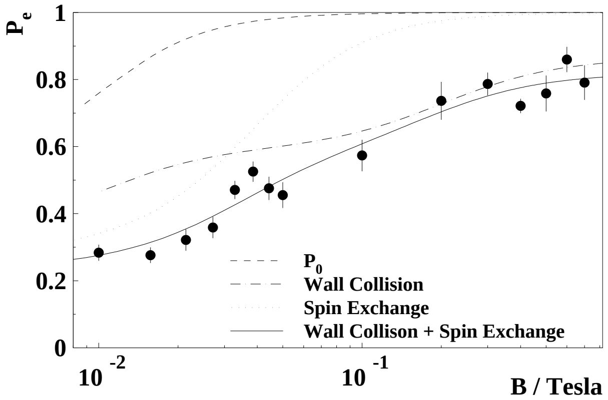

Fig. 12.7:
Electron polarization of deuterium as a function of the holding field in the storage cell for an average number of wall collisions of 3505(14) and a cell temperature of 110(5) K. Injection of the states $|\,1\,\rangle$, $|\,2\,\rangle$ and $|\,3\,\rangle$.

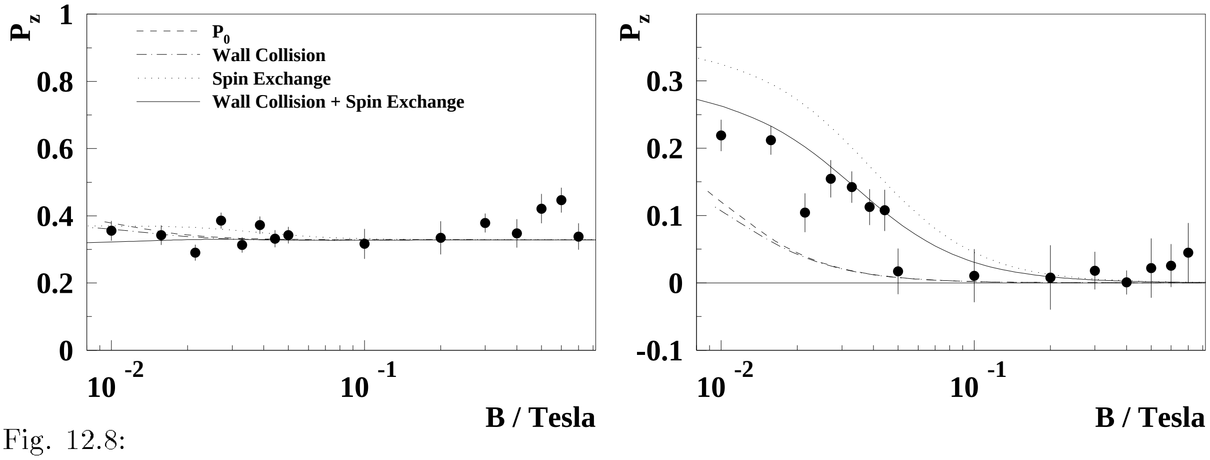

Fig. 12.8:
Behaviour of the vector polarization of deuterium as a function of the holding field in the storage cell for an average number of wall collisions of 3505(14) and a cell temperature of 110(5) K. Left: Injection of the states $|1\rangle$, $|3\rangle$ and $|6\rangle$. Right: Injection of the states $|1\rangle$, $|2\rangle$ and $|3\rangle$.

The best possibility to examine the behaviour of the vector polarization with the test source is to operate the source without high frequency transition and to inject a beam with high electron polarization, but without vector polarization. Under these conditions the polarization is transferred from the electrons to the nuclei by spin exchange collisions and the vector polarization increases, as can be seen on the right side of figure 12.8. The relaxation rates for increase and decay of the vector polarization due to spin exchange collisions is the same, so that an injected, high vector polarization without electron polarization decays as quickly as it increases in the shown measurement.

The behaviour of the tensor polarization could be examined in two cases. In the first case, for active SFT 2-6, the states $|1\rangle$, $|3\rangle$ and $|6\rangle$ are injected into the cell, which in a strong field relates to a tensor polarization of $P_{zz} \approx +1$ (figure 12.9 left). In the second case, for active SFT 3-5, the states $|1\rangle$, $|2\rangle$ and $|5\rangle$ are injected, relating to a negative tensor polarization of $P_{zz} \approx -1$ for strong fields (figure 12.9 right). The maximally possible negative tensor polarization of $P_{zz} = -2$ cannot be reached with the used source, because to obtain such an atomic beam again one state would have to be removed from the beam after the high frequency transition, which again requires a second sextupole magnet in the atomic beam source.

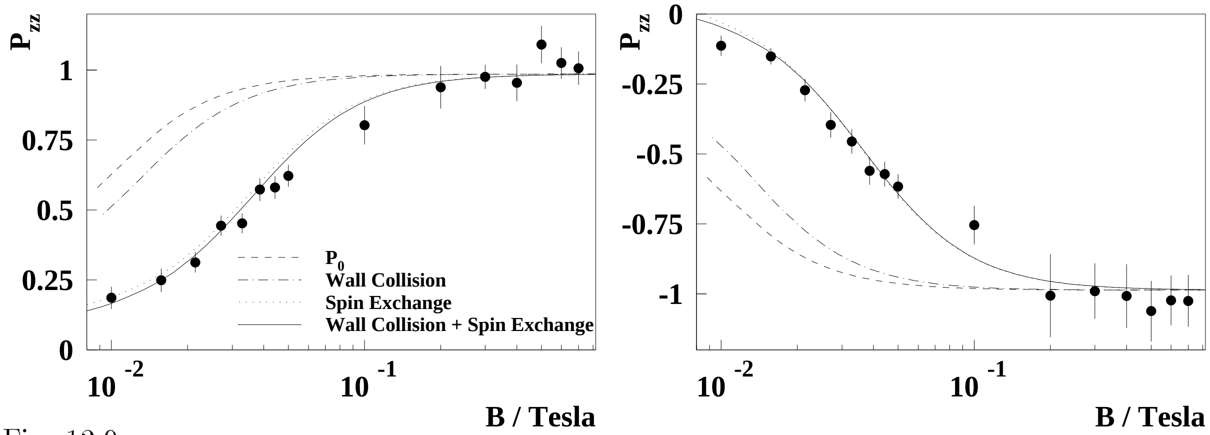

Fig. 12.9:
Behaviour of the tensor polarization of deuterium as a function of the holding field in the storage cell for an average number of wall collisions of 3505(14) and a cell temperature of 110(5) K. Left: Injection of the states $|1\rangle$, $|3\rangle$ and $|6\rangle$. Right; Injection of the states $|1\rangle$, $|2\rangle$ and $|5\rangle$.

The relaxation of the tensor polarization as a function of the holding field is basically symmetric with respect to the orientation of the field. However, a closer observation reveals that in weaker fields the measured tensor polarization is somewhat higher for a positive sign than for negative sign. Furthermore the right side of figure 12.9 illustrates that the theoretical calculation of the relaxation due to spin exchange collisions alone in weak fields leads to positive values, despite the injected negative tensor polarization. This can be attributed to the fact that according to [106] spin exchange collisions in deuterium lead to an equilibrium with positive tensor polarization, which explains the asymmetry between the two algebraic signs (see also figure 3.4).

The calculations for the relaxation of deuterium which are illustrated by the figures of this and the previous subsection are, as in the case of hydrogen, based on a parameterization which is obtained through a fit of the theory summarized in chapter 3 to the measured results for the occupation numbers. The analysis was done simultaneously for the four possible initial occupancies. This means that all theoretically calculated curves relating to the deuterium measurements described in this thesis are based on a single set of parameters. These parameters can be found in table 11.1.

12.3.5 Comparison of Surface Coatings

The relaxation behaviour in storage cells with different surface coatings was examined for hydrogen only, using an uncoated aluminum cell, a cell with teflon coating and a cell with drifilm coating. In all these cells the average number of wall collisions per atom is 3505(14).

Aluminum generally develops an oxide layer, so that in the case of the uncoated aluminum cell the surface is not really metallic. Nevertheless this cell without coating shows a high depolarization and also recombination. As described in chapter 12.1, when at low temperature an ice layer grows on the cell surface a polarization can be detected in the atomic beam exiting from the cell. The measurements described in this chapter were done with an ice layer left in place and compared to the other surface coatings.

Figure 12.10 left shows how the electron polarization behaves depending on the holding field for the injection of the states $|1\rangle$ and $|2\rangle$. The right side shows the behaviour of the nuclear polarization for the injection of the states $|2\rangle$ and $|3\rangle$.

The electron polarization shows a much greater sensitivity to the surface properties. The strongest depolarization is observed for the iced aluminum surface. For the teflon coating the electron polarization is already significantly higher, while the cell with drifilm coating shows the smallest losses of electron polarization.

The behaviour of the nuclear polarization is similar, here also the lowest polarization is measured for ice coated aluminum and the highest for drifilm coating. The nuclei are only indirectly influenced through the hyperfine interaction, so that the depolarization of the nuclei is for all cases smaller than the electron depolarization (compare also figure 3.1).

The results regarding the two coatings teflon and drifilm are in disagreement with the result of J.S. Price and W. Haeberli [81, 80], who found better results, i.e. higher polarization values, for teflon coatings than for drifilm. It may be possible that due to different vacuum conditions in the set-ups different adsorbates form on the surfaces, which could explain the different behaviour. However, for the HERMES experiment the described behaviour would be of advantage, as a teflon coating would not survive the radiation inside the HERA ring. Drifilm so far is the only known acceptable alternative.

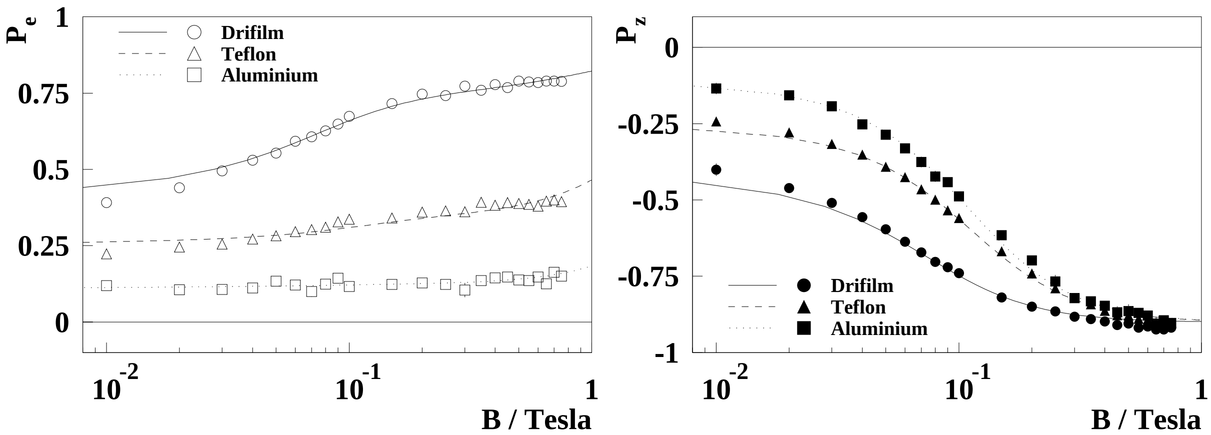

Fig. 12.10:
Polarization of hydrogen as a function of the holding field in the storage cell. Comparison of different surfaces at an average number of wall collisions of 3505(14). The cell temperatures during the measurements were: drifilm 101(5) K, aluminum 90(5) K and teflon 90(5) K. Left: Behaviour of the electron polarization for inactive WFT 1-3, injection of the states $|1\rangle$ and $|2\rangle$. Right: Behaviour of the nuclear polarization for active WFT 1-3, injection of the states $|2\rangle$ and $|3\rangle$.

12.3.6 Comparison of Cells with different Wall Collision Numbers

The comparison of relaxation measurements for different cell geometries is another possibility to check how well the model based on spin exchange collisions and wall collisions describes the experimental results. For this reason relaxation measurements were done with two different storage cells, both of them coated with teflon. The first cell is the storage cell described before. For the second cell the cell volume was reduced by about a factor of two, while the cell exit tube was also shortened from 60 mm to 30 mm. The reduction of the cell volume leads to a smaller average number of wall collisions and to a smaller average travel distance inside the cell. These effects can be determined precisely with a Monte Carlo simulation of molecular flow (appendix A.3). The shortening of the exit tube also leads to a smaller number of wall collisions and a shorter mean travel distance. Additionally, also the conductance of the exit tube is increased which reduces the density inside the cell. A difference in the average number of collisions obviously influences the relaxation due to wall collisions. The relaxation due to spin exchange collisions is influenced by the longer travel distance and the correspondingly longer time inside the cell as well as by the higher density in the cell with 3505 wall collisions compared to the cell with 1456 wall collisions.

The behaviour of the polarization in dependence of the holding field for both cells is shown in figure 12.11. The average number of wall collisions is used to identify the cells. The differences between the two cells affect the relaxation of the electrons in a particularly strong way over the entire examined field range for the injection of the states$|1\rangle$ and $|2\rangle$ (figure 12.11 left). Even for a field of 750 mT the electron polarization in the cell with 1456 wall collisions is more than 0.3 higher than in the cell with 3505 wallcollisons.

Also the nuclear polarization (figure 12.11 right) shows significant differences between both cells. However, these differences decrease for increasing holding field due to the decoupling of electron and nucleon spin. For both storage cells the nuclear polarization with increasing field strength approaches the value of the injected polarization of about-0.9.

The compatibility of the relaxation model with a change in the cell geometry can best be checked by comparing the fitted relaxation parameters in the tables 11.1 and 11.2 that were derived from the here described measurements. They are in good agreement, with the sole

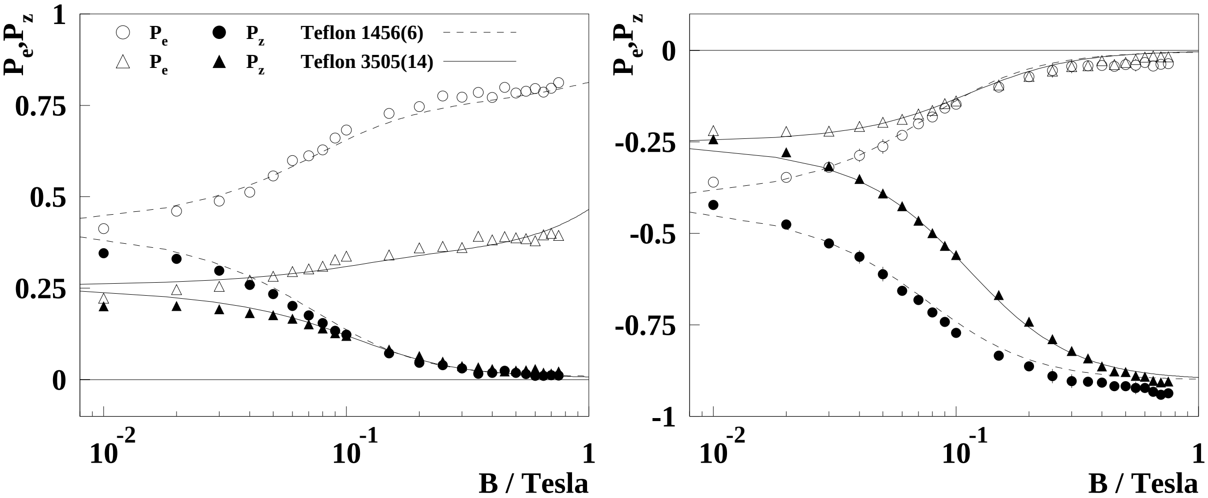

Fig. 12.11:
Polarization of hydrogen as a function of the holding field in the storage cell. Comparison of cells with different wall collision numbers. The average number of wall collisions is 3505(14) and 1456(6), respectively. In the left plot the WFT 1-3 was inactive, the states $|1\rangle$ and $|2\rangle$ were injected. In the right plot the WFT 1-3 was activated, the states $|2\rangle$ and $|3\rangle$ were injected.

exception of the strength of the fluctuating fields on the surface which differ by a factor of two. The differences can perhaps be attributed to different amounts of water that adsorbed on the surface prior to the measurements.

12.4 Measurements on the Dependence on the Storage Cell Temperature

Certainly the best way to examine the relaxation behaviour in the storage cells in dependence of the storage cell temperature would be to repeat the field dependence measurements for several temperatures, to fit the relaxation model to the results and to create a table of the form 11.1 for each temperature. In this way reliable information about the temperature dependence of wall collision amplitude and correlation time would be collected. At the moment however only the results obtained for hydrogen in a holding field of $B = 350\,\mathrm{mT}$ can be discussed here. The measurements were only executed with coated storage cells, because the ice layer in the uncoated aluminum cell started to thaw above 150 K and no atomic beam leaving the cell could be detected anymore.

Figure 12.12 shows the temperature dependence of electron and nuclear polarization for all coated cells. In the pictures on the left side the strong relaxation of the electron polarization at the injection of the states $|1\rangle$ and $|2\rangle$ can be seen. The nuclear polarization at the injection of the states $|2\rangle$ and $|3\rangle$ is approximately constant over the entire examined temperature range. In comparison to the magnetic field measurements the low value for P_z of about -0.75 is a result of the missing correction due to the molecular background in the beam (chapter 11.4).

The drops in the region of 175 K in the measurement with drifilm coating that are clearly visible both in the electron and in the nuclear polarization, are probably caused by a water beam from the cell at this temperature (see also chapter 12.1). The water beam contributes to the molecular background in the beam and reduces the measured polarization. This is a rather direct hint that also in the coated cells at low temperatures a coat of ice develops, which certainly also changes the conditions at the cell surfaces. In the other measurements these drops were not seen, because they were done during the cooling down of the cells.

The characteristic drop of polarization towards low temperatures that is known from several previous measurements [46, 57, 71, 74, 80, 81] that can be attributed to the decrease in the average duration of stay in the cell (3.2) is only clearly visible in the case of the large teflon cell. For the small teflon cell only the beginning of the drop is seen. The nuclear polarization is stable up to the temperatures of 90 and 100 K, respectively. This allows the expectation that also the storage cell in the HERMES experiment can be cooled to below 100 K without a loss of polarization. For constant polarization the density and thus the quality of the target ($\rho \cdot P^2$) increase proportionally to $1/\sqrt{T_{\text{cell}}}$.

In all measurements a slow decrease in electron and nuclear polarization can also be observed towards higher temperatures. This has not been observed in this way in other experiments before. This behaviour also disagrees with the relaxation model, because the adhesion time of the atoms on the surface (3.2) and thus the wall collision amplitude should decrease with increasing temperature.

This decrease can be explained as an effect of the molecular background beam and the decreasing transmission of the sextupole magnet system (figure 9.5). As a result of the decreasing intensity of the transmitted atomic beam the background increases relative to the atomic beam signal and the measured polarization decreases. Inclusion of a correction for this effect lets the decrease vanish, as can be seen in figure 12.13 for the case of the large teflon cell. Because the molecular background beam was not measured, a constant correction of ($S_{\text{corr}} = 3.45\,\text{kHz}$ from

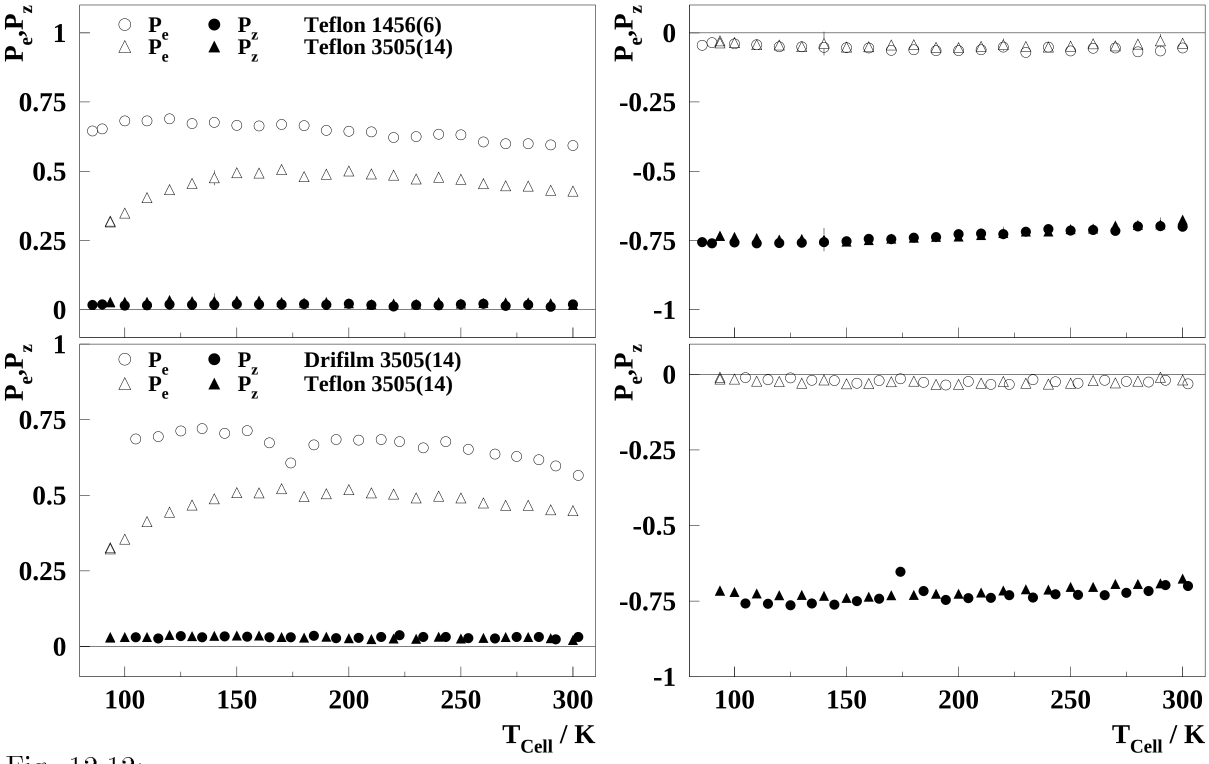

Fig. 12.12:
Polarization of hydrogen as a function of the storage cell temperature for a holding field in the storage cell of $350\,\text{mT}$. Top: Comparison between the teflon coated cells with different wall collision numbers. Bottom: Comparison between teflon and drifilm. The average number of wall collisions in both cases is $3505(14)$. In the left figure the WFT 1-3 was inactive, the states $|1\rangle$ and $|2\rangle$ were injected. In the right figure the WFT 1-3 was activated, the states $|2\rangle$ and $|3\rangle$ were injected. The measurement with drifilm was done during the warming up, the measurements with teflon during the cooling down of the cell. The measurements do not contain a correction due to the molecular background beam.

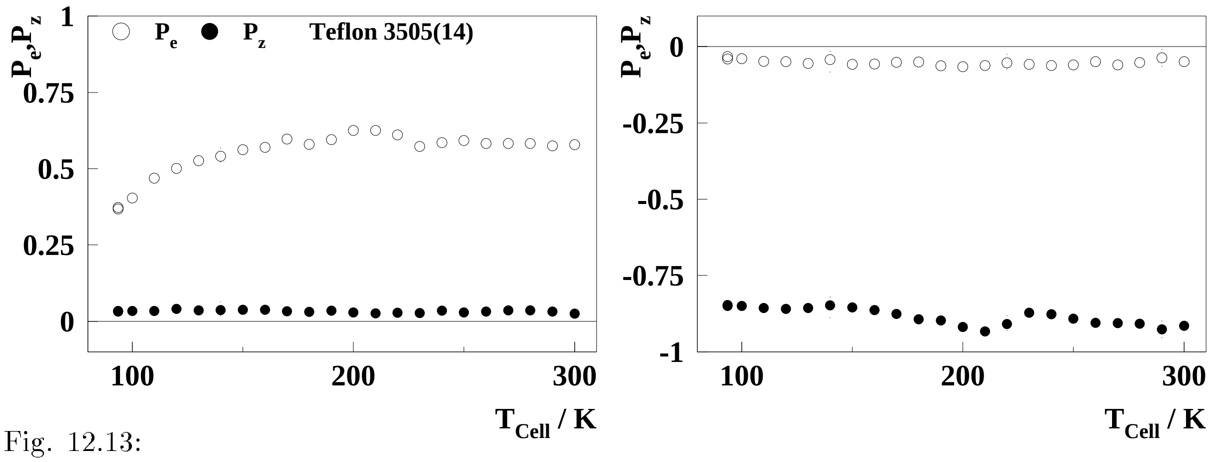

Fig. 12.13:
Polarization of hydrogen as a function of the storage cell temperature for a holding field of $350\,\mathrm{mT}$ in the storage cell with teflon coating after correction due to the molecular background beam. The average number of wall collisions is $3505(14)$. Left the WFT 1-3 was inactive, injection of the states $|1\rangle$ and $|2\rangle$. Right the WFT 1-3 was active, injection of the states $|2\rangle$ and $|3\rangle$.

table 11.1) was assumed for all temperatures. However, this assumption is only partially justified, as the variation of the storage cell temperature changes, conductance values in the apparatus and thus also the vacuum conditions that cause the background (appendix B). Furthermore, as a result of the decreasing intensity of the atomic beam signal also the uncertainty of this correction increases; however, it should be possible to improve it again by measuring the background signal. Due to the uncertain background correction a fit of the relaxation model to these data was foregone.

13 Polarization Losses

In this chapter the polarization losses $(1-P/P_0)$ will be shown on a logarithmic scale as a function of the magnetic field in order to make the effects of the individual relaxation mechanisms on the nuclear and electron polarization more easily visible. The curves were calculated based on measured data using the parameterization in table 11.1. according to the theory outlined in chapter 3. The chosen representation allows detection and quantification of the extremely small losses in nuclear polarization in strong holding fields. A further advantage of this representation is the relative independence of the used fit method (chapter 11 or appendix C).

However, the given results are not generally applicable, because they may strongly depend on the injected hyperfine occupancies. The effects of the relaxation mechanisms on nuclear and electron polarization are considered separately; the effects of wall and spin exchange collisions are examined separately as well. It must be remembered that due to this procedure the influences of the two mechanisms on one another are being disregarded. This will become apparent through ostensive contradictions in some plots.

13.1 Polarization Losses in Hydrogen

In the left plot of figure 13.1 the polarization loss of the electrons for the injection of the states $|1\rangle$ and $|2\rangle$ is compared with the polarization loss of the nuclei for the injection of the states $|2\rangle$ and $|3\rangle$. The depolarization of the nuclei for a field of 350 mT – this corresponds to the longitudinal holding field in the storage cell of the HERMES experiment – is already an order of magnitude smaller than the depolarization of the electrons. This is a result of the decoupling of nuclei and electrons. It is remarkable that the polarization losses for electrons as well as for nuclei become smaller again for field strengths below 40 mT.

The plot in the middle illustrates, how the electron polarization is affected by wall and spin exchange collisions. The right plot shows the influence of the relaxation mechanisms on the nuclear polarization. In both cases the effects of only one single relaxation mechanism onto the

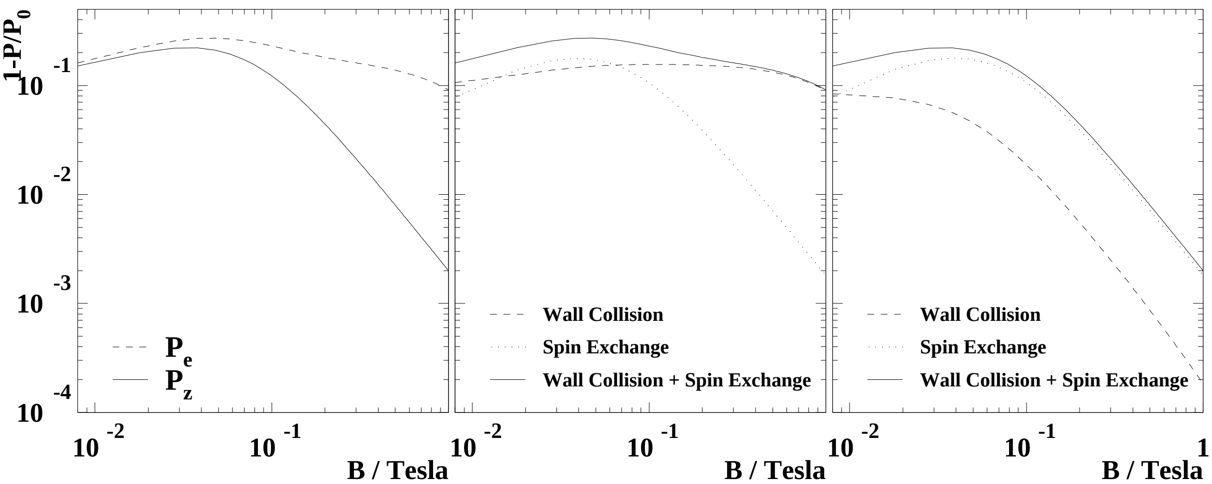

Fig. 13.1:
Nuclear and electron polarization as a function of the magnetic field in a cell with drifilm coating, an average number of wall collisions of $3505(14)$ and a cell temperature of $101(5)\,\mathrm{K}$. 1.) Comparison between the loss of electron polarization for the injection of the states $|1\rangle$ and $|2\rangle$ and the loss of nuclear polarization for the injection of the states $|2\rangle$ and $|3\rangle$. 2.) Contribution of the relaxation mechanisms to the loss of electron polarization for the injection of the states $|1\rangle$ and $|2\rangle$. 3.) Contribution of the relaxation mechanisms to the loss of nuclear polarization for the injection of the states $|2\rangle$ and $|3\rangle$.

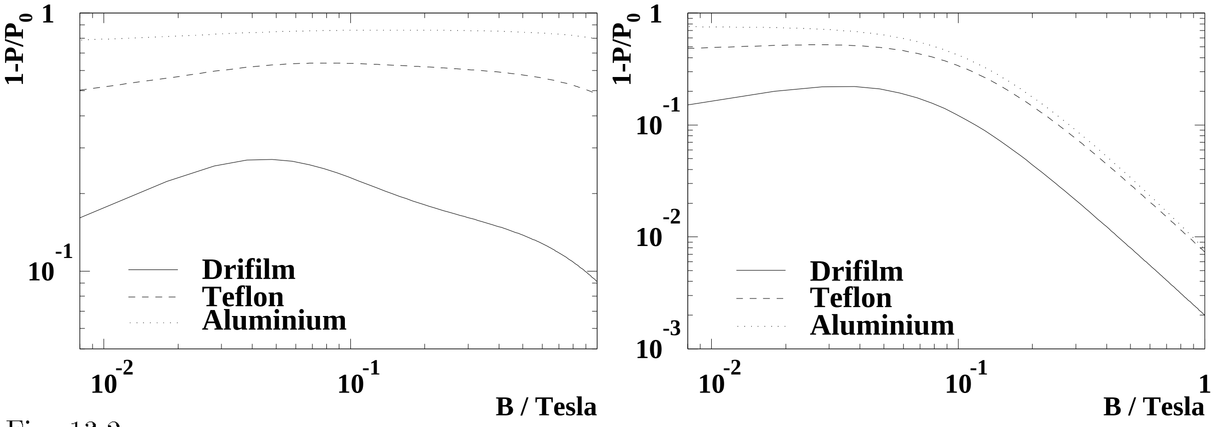

Fig. 13.2:
Polarization losses as a function of the magnetic field for an average number of wall collisions of $3505(14)$. Comparison between different surface coatings. Left: Electron polarization loss for the injection of the states $|1\rangle$ and $|2\rangle$. Right: Nuclear polarization loss for the injection of the states $|2\rangle$ and $|3\rangle$.

hyperfine occupancy and the polarization were calculated, under exclusion of the other mechanism. The flux term in the master equation (3.1) was always included. In this representation it is easy to see that the depolarization of the electrons is mostly a result of wall collisions. The depolarization of the nuclei on the other hand is well described by spin exchange collisions. However, it must be considered that the nuclear polarization is not simply lost, but that it is at first is transferred to the electrons, that in turn lose it in wall collisions.

Figure 13.2 shows the polarization losses for the three different surfaces that were examined. The differences between teflon and drifilm can be seen particularly well in this representation. The polarization loss for nuclei in strong fields is for a drifilm coating a factor of four lower than for a teflon coating.

13.2 Polarization Losses in Deuterium

Figure 13.3 compares the losses of electron, vector and tensor polarization in deuterium as a function of the holding field. Wall and spin exchange collisions are included in the evaluation.

The extremely small loss of vector polarization at the injection of the states $|1\rangle$, $|3\rangle$ and $|6\rangle$ is a result of the injection of an about equally high electron polarization. This case cannot be realistically used to predict the expected losses of vector polarization in the HERMES storage cell. Therefore, as already done in chapter 12.3.4, the increase of P_z for inactive high frequency transitions was analyzed. In this injection mode spin exchange collisions lead to a polarization transfer from the polarized electrons to the unpolarized nuclei. The loss of vector polarization

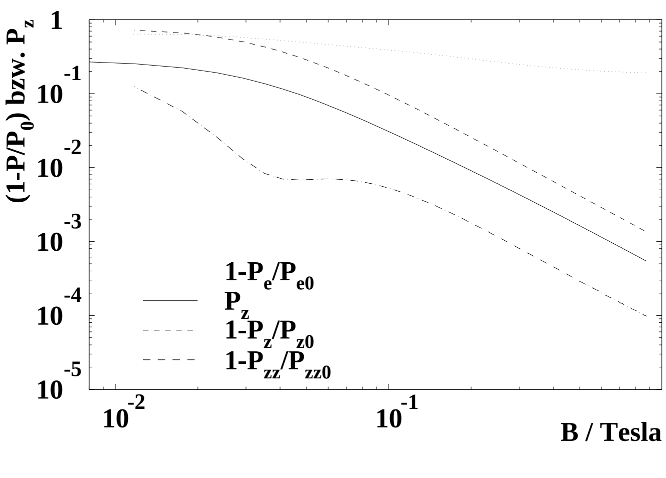

Fig. 13.3:
Polarization losses and polarization gains in deuterium as a function of the holding field in a teflon coated cell for a wall collision number of $3505(14)$ and a cell temperature of$110(5)\,\mathrm{K}$. Polarization loss of the electrons and increase of the vector polarization for inactive high frequency transitions. Injection of the states $|1\rangle$, $|2\rangle$ and $|3\rangle$. Loss of vector and tensor polarization for active SFT 2-6. Injection of the states $|1\rangle$, $|3\rangle$ and $|6\rangle$.

for the injection of a high vector polarization and a low electron polarization would behave similarly to the increase in the given case. The loss of tensor polarization is in strong fields somewhat higher than the increase in vector polarization for the injection of the states $|1\rangle$, $|2\rangle$ and $|3\rangle$, and somewhat smaller than the loss in vector polarization in hydrogen. For deuterium the polarization losses in weak fields are significantly higher than for hydrogen.

Figure 13.4 illustrates the effects of wall and spin exchange collisions onto the polarization separately for the four cases shown in figure 13.3. For the electrons (upper left), whose depolarization is mainly caused by wall collisions, the curves of wall collision depolarization and total depolarization converge with increasing fields. This is to be expected, as the effect of the spin exchange collisions decreases monotonously. However, the curves separate again for fields above 200 mT although the loss due to spin exchange collisions is still decreasing. This ostensive contradiction is a result of the influences of both relaxation mechanisms on one another.

Spin exchange collisions even lead to and increase in vector polarization for the injection of the states $|1\rangle$, $|3\rangle$ and $|6\rangle$ (upper right) (see also figure 3.4). Therefore, in this plot the gain in polarization, i.e. $-(1 - P/P_0)$, is shown. The wall collisions lead to a loss over the entire

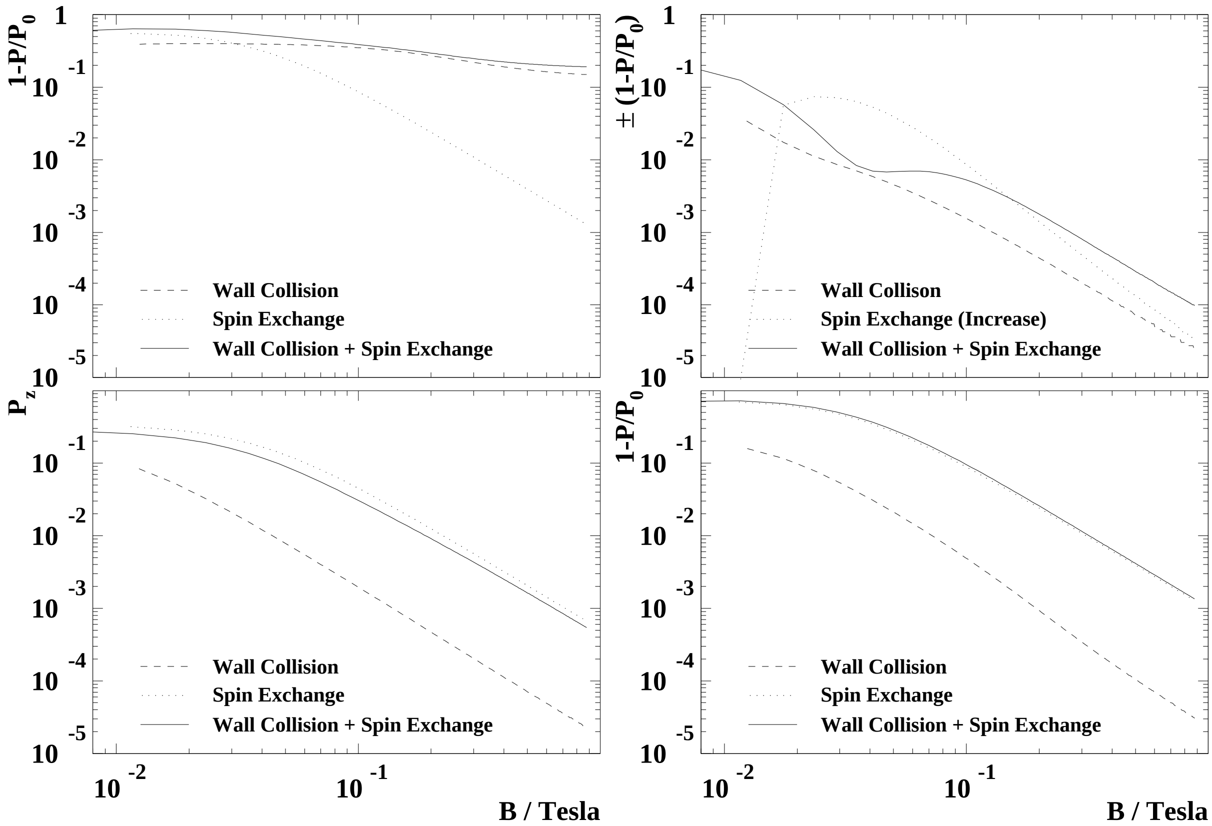

Fig. 13.4:
Polarization loss mechanisms as a function of the magnetic field in a teflon coated cell with an average number of wall collisions of $3505(14)$ and a cell temperature of $110(5)\,\mathrm{K}$. Upper left: Contribution of the relaxation mechanisms to the loss of electron polarization for the injection of the states $|1\rangle$, $|2\rangle$ and $|3\rangle$. Upper right: Contribution of the relaxation mechanisms to the loss of vector polarization for the injection of the states $|1\rangle$, $|3\rangle$ and $|6\rangle$. Spin exchange collisions lead to an increase in vector polarization. Lower left: Contribution of the relaxation mechanisms to the behaviour of the vector polarization for the injection of the states $|1\rangle$, $|2\rangle$ and $|3\rangle$. Wall collisions as well as spin exchange collisions lead to an increase in vector polarization. Lower right: Contribution of the relaxation mechanisms to the loss in tensor polarization for the injection of the states $|1\rangle$, $|3\rangle$ and $|6\rangle$.

field range. The increase in vector polarization for the injection of high electron polarizations is shown in the lower left picture. It is noteworthy that also wall collisions can lead to a small increase in vector polarization through a transfer of polarization from the electrons.

The loss in tensor polarization (lower right) shows a similar behaviour as the vector polarization as can be seen by comparison to it's increase in the lower left plot. As for hydrogen, the losses in the observables of nuclear polarization are predominantly caused by spin exchange collisions. Wall collisions only play a minor role. The curves for spin exchange collisions and for the total polarization loss or gain are practically indistinguishable in both of the lower plots.

14 Application of the Relaxation Model to Target Storage Cells

The relaxation model that was used for the polarization measurements with the test storage cells will now be applied to two target storage cells. Their relaxation behaviour is substantially different, as will be seen in the following. The first case is the storage cell of the FILTEX test experiment, this is the application to an experiment that was already completed in 1992 at the test storage ring (TSR) in Heidelberg [56, 57]. For the second storage cell, for the HERMES experiment, a model will be used to predict polarization in this storage cell target.

In both cases detailed information about the hyperfine occupancy is needed, with which the beam is injected from the atomic beam source into the storage cell target. It's determination is treated in detail in appendix D.

The storage cells themselves are described in appendix A. They differ from test storage cells examined up to now in one important detail: They exclusively consist of tubes within which the density decreases linearly to the edges (figure 1.1). As a result the relaxation conditions inside these cells are not constant and even the polarization itself varies over the cell. These properties could not yet be accounted for in the relaxation calculations, as the used programs up to now were only developed for spatially constant conditions. The parameters of the storage cells, e.g. the mean duration of stay, always refer to the atoms that are just leaving the cell through one of it's openings (tables A.4 and A.5). In the case of the FILTEX test experiment the values were averaged over all openings, for the HERMES experiment only those atoms were considered that leave the cell in the direction of the polarimeter. In principle these parameters would have to be averaged over the length of the beam pipe of the concerned storage cell to arrive at a correct determination of the target polarization.

The spin exchange collision rate is determined from the average density $\bar{\rho}$, which corresponds to half the density at the center of the cell $\rho_0/2$. The spin exchange cross section is set to the literature value of $\sigma_{SE} = 2.31(28) \cdot 10^{-15}\,\mathrm{cm}^2$ [101]. The density in the cell can be calculated from the gas flow that is injected into the cell from the source, as is described in appendix A. This flow is known from measurements [46, 140]. Thus there is no parameter concerning the spin exchange collision rates that needs to be taken from the measurements on test storage cells.

14.1 The Target of the FILTEX Test Experiment

It was the goal of the FILTEX test experiment, to polarize a proton beam, that was stored in the TSR. This was done successfully by employing the asymmetry in the cross section for both spin components by scattering on a polarized internal hydrogen target [58, 59]. Before and after the actual experiment the polarization of the gas target was measured by scattering stored α-particles with an energy of 27 MeV on the polarized protons. As a result of the target nucleon polarization the angle distribution of the from the target backscattered protons shows an asymmetry. This asymmetry can be detected through the difference in the counting rates of two detectors on the left and right side of the α-beam. The analyzing power for the αp-scattering is known [141, 142], so that in this way the polarization of the target could be measured [46].

The hydrogen target was operated in two modi at a holding field of only 0.5 mT, only about one hundredth of the critical field. The storage cell was coated with the same teflon that was used for the test storage cells. In the first case the source injected the two hyperfine states $|\,1\,\rangle$ and $|\,2\,\rangle$ into the storage cell. Because the state $|\,2\,\rangle$ in this weak field does not contribute to the polarization the maximal value of the polarization in this case is 0.5. For the preparation of such an atomic beam a sextupole system without high frequency transitions is sufficient. To produce a completely polarized target in a weak field it is necessary to inject a beam with only one hyperfine state into the cell. This is done by activating a SFT 2-4 after the first part of the source sextupole magnet system. This transfers the state $|\,2\,\rangle$ into $|\,4\,\rangle$, which then is removed from the beam in the second part of the magnet system. Thus only the pure state $|\,1\,\rangle$ is injected into the cell. This allows a maximal polarization of $+1.0$ in the target to be reached, at the price of a density reduction by a factor of two. However, as the polarization enters quadratically into the quality of the target $(n \cdot P^2)$, a factor of two is gained. The gas flow that is injected from the source into the cell as well as the target polarization is given in table 14.1 for both operation modes.

The atomic beam source was operated at a nozzle temperature of 80 K. Both the drift velocity and the beam temperature are known for this source as a function of the nozzle temperature from earlier measurements (appendix D) [108]. In addition only the parameter K_{mol} is needed for the determination of the injected hyperfine occupancies from simulations. This parameter characterizes the flowing behaviour of the beam in the region between nozzle and collimator (chapter 6.2).

The left side of figure 14.1 depicts the target polarization for the injection of two hyperfine states as a function of this as yet unknown parameter. The relaxation within the storage cell was already taken into account. The information in this figure that is the most important for the following argument is, that the target polarization in this case does **not** depend on K_{mol}.

The spin exchange rate can be calculated from the injected flow. Therefore the wall collision amplitude C and the correlation time τ_C are the only free parameters that can affect the target polarization in this case. The choice of the correlation time is not critical, as it is practically independent of the surface coating of the storage cell. For the calculation of the relaxation a value of $\tau_C = 4.63 \cdot 10^{-12}\,\mathrm{s}$ was used, which was derived from the polarization measurements with the test storage cells with a teflon coating (table 11.1).

For the wall collision amplitude C changes in the average flight time τ_F between two wall collisions, that result from geometry and temperature changes, must be considered (tables A.3 and A.4). The value of about 3500 from the test storage cell measurement would lead to a value of $C = 55.2(5)\,\mathrm{s}^{-1}$ for the storage cell of the FILTEX test experiment at $T_{\mathrm{cell}} = 115\,\mathrm{K}$. As the wall collision amplitude is the last unknown parameter for the target polarization for the

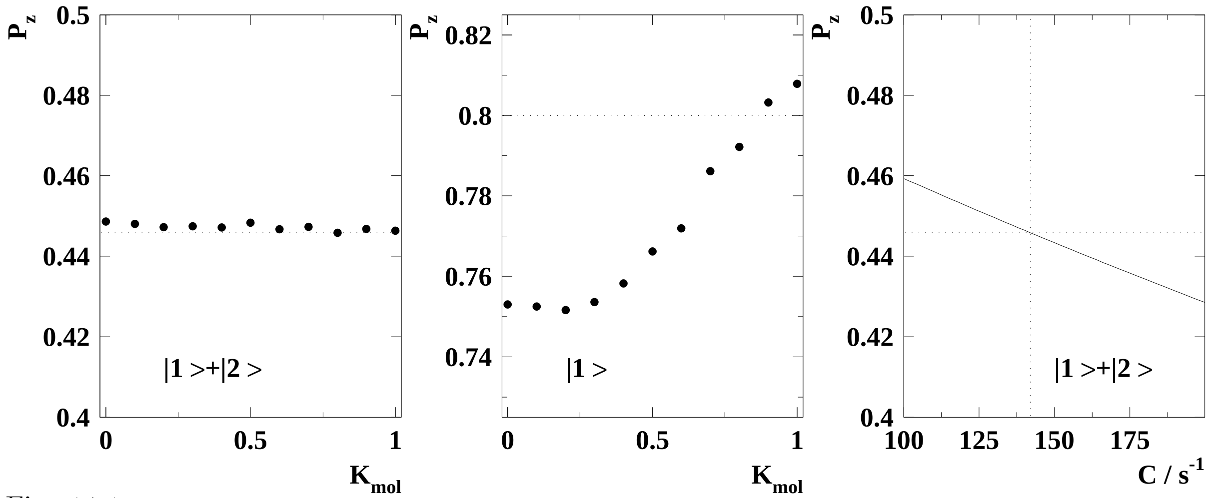

Fig. 14.1:
Polarization in the storage cell of the FILTEX test experiment at the TSR in Heidelberg. Left as a function of K_{mol} for the injection of two hyperfine states, in the middle for the injection of only one hyperfine state and on the right as a function of the wall collision amplitude C for the injection of two hyperfine states. The values correspond to a storage cell temperature of $115\,\mathrm{K}$. The efficiency of the high frequency transition SFT 2-4 was assumed to be $\varepsilon_{24} = 100\,\%$. The dotted lines indicate the experimentally measured values.

Tab. 14.1:
Hyperfine occupancies, polarization and quality factors of the atomic beam source and the storage cell of the FILTEX experiment. Parameters for the atomic beam source: $T_{\mathrm{nozzle}} = 80\,\mathrm{K}$, $T_{\mathrm{beam}} = 23.2\,\mathrm{K}$, $v_{\mathrm{drift}} = 1839\,\mathrm{m\,s^{-1}}$, $K_{\mathrm{mol}} = 1.0$ and $\varepsilon_{24} = 99.5(10)\,\%$. Parameters for the relaxation in the storage cell: $C = 142\,\mathrm{s^{-1}}$, $\tau_C = 4.36 \cdot 10^{-12}\,\mathrm{s}$ and $T_{\mathrm{cell}} = 115\,\mathrm{K}$. Σ is the transmission of the sextupole system and Ω refers to the opening angle of the collimator with respect to the nozzle. The relevance of these parameters is explained in the text. ρ_0 is the density in the center of the storage cell, $\bar{\rho}$ is the average density and n is the aerial target density.

	Atomic Beam Source			**Storage Cell**	
States	$\lvert 1\rangle, \lvert 2\rangle$	$\lvert 1\rangle$	States	$\lvert 1\rangle, \lvert 2\rangle$	$\lvert 1\rangle$
P_z^{soll}	+0.5	+1.0	P_z^{soll}	+0.5	+1.0
n_1	0.498(2)	0.893(3)	n_1	0.498(4)	0.814(8)
n_2	0.501(2)	$2.04(90) \cdot 10^{-2}$	n_2	0.333(2)	$7.80(96) \cdot 10^{-2}$
n_3	$1.42(36) \cdot 10^{-4}$	$2.56(64) \cdot 10^{-4}$	n_3	$4.94(16) \cdot 10^{-2}$	$9.35(95) \cdot 10^{-3}$
n_4	$4.99(71) \cdot 10^{-4}$	$8.7(16) \cdot 10^{-2}$	n_4	0.119(5)	$9.9(16) \cdot 10^{-2}$
P_z	0.493(2)	0.893(3)	P_z	0.446(5)	0.805(9)
			P_z^{mess}	0.446(9)	0.800(16)
			$(1 - P/P_0)$	$9.5(11) \cdot 10^{-2}$	$9.9(11) \cdot 10^{-2}$
Σ	0.841(2)	0.469(9)	ρ_0 $[\mathrm{cm^{-3}}]$	$7.13(18) \cdot 10^{12}$	$4.05(9) \cdot 10^{12}$
$\Sigma \cdot \Omega$ [sr]	$1.765(4) \cdot 10^{-2}$	$9.84(19) \cdot 10^{-3}$	$\bar{\rho}$ $[\mathrm{cm^{-3}}]$	$3.57(9) \cdot 10^{12}$	$2.03(5) \cdot 10^{12}$
$\dot{n}_{\mathrm{mess}}$ $[\mathrm{s^{-1}}]$	$8.1(2) \cdot 10^{16}$	$4.6(1) \cdot 10^{16}$	n $[\mathrm{cm^{-2}}]$	$8.93(23) \cdot 10^{13}$	$5.08(13) \cdot 10^{13}$
$\dot{n}P_z^2$ $[\mathrm{s^{-1}}]$	$1.97(5) \cdot 10^{16}$	$3.67(6) \cdot 10^{16}$	nP_z^2 $[\mathrm{cm^{-2}}]$	$1.77(5) \cdot 10^{13}$	$3.29(10) \cdot 10^{13}$

injection of two hyperfine states, it can also be derived from the measured polarization. Figure 14.1 shows the calculated target polarization as a function of the wall collision amplitude. The measured target polarization is shown as a dotted horizontal line, it can be reproduced with a wall collision amplitude of $C = 142(15)\,\mathrm{s^{-1}}$. This value was used for the relaxation calculation. Thus all relaxation parameters are known, also for the injection of only one hyperfine state. The factor of three between the deduced wall collision amplitude and the expected value from the test stand measurements can perhaps be explained by the different occupation of the surfaces by adsorbates from the restgas in the concerned vacuum chambers.

Two additional parameters concerning the polarization of the injected atomic beam occur in the calculation of the target polarization in the case of the injection of only one hyperfine state. These are the efficiency of the high frequency transition SFT 2-4 and the parameter K_{mol}. For the efficiency of the SFT 2-4 a value of $\varepsilon_{24} = 95\,\%$ was quoted in [59]. However, this value was calculated without a correction by sextupole transmissions. The parameter K_{mol} has a significant impact on the target polarization as can be seen in the middle plot of figure 14.1. This can be attributed to the fact that a high frequency transition is operated within the sextupole magnet system, i.e. between two magnets. The deflection of the undesirable and transferred hyperfine state in the second part of the magnet system depends strongly on the angular momentum of the atoms in the sextupole magnet and thus on K_{mol}. This is discussed in detail for the case of the HERMES sextupole system in appendix D.1.

A very molecular beam as well as a high efficiency are necessary to reach a high target polarization at the injection of only one hyperfine state. This fact together with the measured high target polarization of $P_z = 0.800(16)$ make it possible to determine both parameters within narrow boundaries (figure 14.1 center). The lower boundaries are

$$K_{\mathrm{mol}} > 0.85 \qquad \varepsilon_{24} > 99.0\,\%. \tag{14.1}$$

This means that the measured polarizations in this experiment can only be explained if an almost ideal status of the atomic beam source is assumed. This result is even more remarkable, as only the polarization of the atomic fraction of the beam was considered. The recombination in the storage cell, which was discussed as a partial explanation of the observed polarization losses, found no consideration.

In the HERMES experiment the value of K_{mol} that was extracted from this measurement is crucial for the maximal possible quality of the deuterium target. This is the case, because in the preparation of a polarized deuterium beam always a high frequency transition must be operated within the sextupole magnet system. A laminar beam would reduced the maximal possible polarization of the deuterium target in three out of four operation modes by about 20 % (appendix D.1).

Table 14.1 contains all important parameters concerning the target in the FILTEX test experiment, both for the source and for the storage cell. The table lists the measured gas flows $\dot{n}$ that are injected by the atomic beam source into the cell as well as the target polarization according to [46, 140]. All other parameters were calculated. Σ is the transmission of the sextupole system. It is defined as the sum of the non-normalized occupation numbers in the occupation tuples. They are listed for the calculation of the polarization in appendix D. They contain the efficiencies of the high frequency transitions and the transmissions for individual hyperfine states, which represent the probability for an atom to pass trough the sextupole system from the collimator up to the storage cell. Determining for the flux injected into the cell is the product of transmission and opening angle of the collimator with respect to the nozzle: $\Sigma \cdot \Omega$. Based on this parameter different sextupole magnet systems can be compared with one another. However, in this comparison the number of injected hyperfine states must be taken into account. In this table n stands for the aerial target density.

The cell properties enter into the calculation of the target polarization in the form of the average duration of stay, which was determined by Monte Carlo simulations (appendix A.3). Here the average over all openings of the storage cell was calculated (table A.4). The given polarization values therefore refer to atoms that are just leaving the cell. The measured value actually was the average polarization of the atoms within the beam pipe of the cell. The polarization inside the cell is mainly reduced as a result of wall collisions, as will be discussed in the following. For this reason it is permissible to use an estimate of the resulting correction, like the one in [136] for a previous version of the HERMES storage cell. While these corrections were not calculated for the storage cell of the FILTEX test experiment, it still should be possible to transfer the results for the HERMES cell, because the geometries of both cells are sufficiently similar. The simulations show that the polarization of the atoms that are just leaving the cell is about $1 - 2$ % higher than the average, density weighted polarization of the atoms in the beam pipe. This correction increases as the polarization decreases. This makes it seem possible that the SFT 2-4 is operating with an efficiency of 100 %, while also K_{mol} reaches the maximal value of 1.0. The discrepancy of about 1 % between measured and calculated polarization could be explained by this correction.

Although the target in the FILTEX test experiment was only operated in a weak field of 0.5 mT, it is still very interesting to examine the dependency of the hyperfine occupancies and polarization on the holding field up to the strong field region (figure 14.2). Despite the large similarities there are significant differences between the relaxation behaviour of this target and the one of the HERMES experiment if only one hyperfine state is injected into the storage cell.

For the injection of two states the typical strong relaxation between the states $|\,2\,\rangle$ and $|\,4\,\rangle$ in the weak field (top left) can be seen, that was already observed in the measurements with the test storage cells (figure 12.3). These states carry no polarization in a weak field and thus the target polarization is not affected. As can be seen in figure 3.3, spin exchange collisions have in general no effect on the polarization of hydrogen in weak fields. The rise of the electron polarization and the decrease of the nuclear polarization, that are shown in the center, are mainly caused by the hyperfine structure coupling and not by the relaxation. The changes in the polarization that are caused by wall and spin exchange collisions can again be best seen from the polarization losses. Because the nuclear polarization vanishes in strong fields, in figure 14.2 (top left) the loss of electron polarization is plotted. Besides a somewhat smaller loss due to the smaller number of wall collisions, the behaviour agrees with the one shown in figure 13.1 (center). Furthermore, figure 14.2 also illustrates the behaviour in very weak fields. Spin exchange collisions contribute to the polarization losses only in the region of the critical field. As in the measurements on the test storage cells, the polarization loss for the electrons is almost completely caused by wall collision.

For the injection of only one hyperfine state dependencies in the hyperfine occupancy and the polarization are only visible above the critical field. The relaxation in the hyperfine occupancies that is typical for spin exchange collisions does not appear any more. On the right side the losses in the nuclear polarization are plotted. It is clearly visible that the the nuclear polarization is not affected by spin exchange collisions over almost the entire field range. Only in strong fields are the contributions from wall collisions and spin exchange collisions comparably large. The relaxation behaviour is also in this case determined almost completely by the wall collisions and

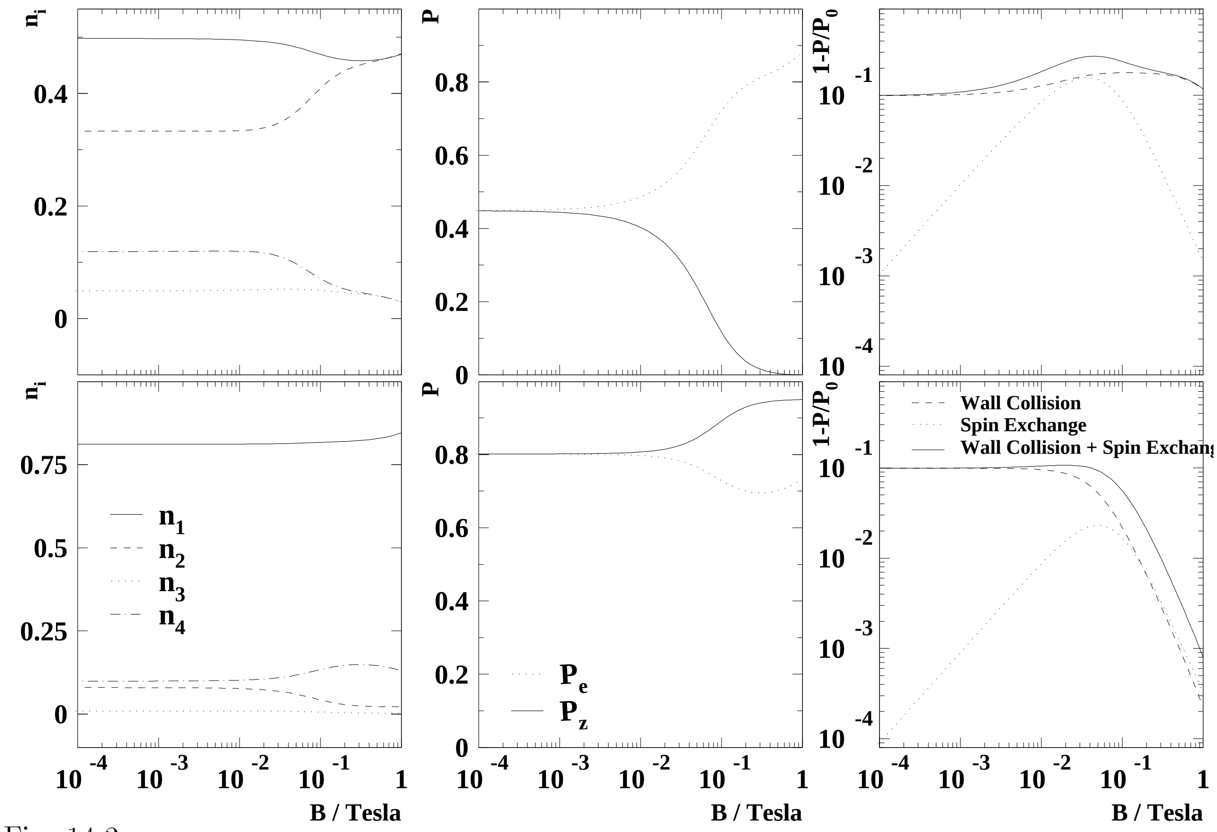

Fig. 14.2:
Hyperfine occupancy (left), polarization (center) and polarization losses (right) for the storage cell of the FILTEX test experiment at the TSR in Heidelberg. Top: Injection of the states $|1\rangle$ and $|2\rangle$, showing the polarization loss of the electron polarization P_e. Bottom: Injection of the state $|1\rangle$, showing the polarization loss of the nuclear polarization P_z. The target was operated with a holding field of $0.5\,\mathrm{mT}$. The cell temperature was $115\,\mathrm{K}$.

the field dependency of the polarization losses can be compared directly to the behaviour of the wall collision relaxation rate in figure 11.1.

There is a simple explanation for the small size of the contributions from the spin exchange collisions to the relaxation in this target. Only the pure state $|1\rangle$ was injected. As a result of angular momentum conservation (3.14), spin exchange collisions between atoms in the same pure hyperfine state cannot change the hyperfine occupancy (table 3.1). Thus the relaxation through spin exchange collisions is blocked. The fact that there is a contribution to the relaxation from them at all is due to a small admixture of other states as a result of an incomplete separation in the sextupole magnet system. Additionally as a result of wall collisions states are populated that in turn allow for spin exchange relaxation. The losses due to spin exchange collisions depicted in figure 14.2 however, only contain the contributions from already injected states, because the loss contributions from the different mechanisms were always calculated under exclusion of the other one.

14.2 The Hydrogen Target for the HERMES Experiment

Figure 14.3 illustrates that the relaxation behaviour in the storage cell of the HERMES experiment, and in contrast to the FILTEX test experiment, is almost entirely determined by spin exchange collisions. This behaviour can be traced to the injection of two hyperfine states. The contributions to the polarization losses due to wall collisions are for strong fields about two orders of magnitude lower than the contributions due to spin exchange collisions. For a cell temperature of 100 K and the expected average density in the cell (table 14.3) a spin exchange collision rate of $T_{HH}^{-1} = 668\,\mathrm{s}^{-1}$ can be estimated. For an average duration of stay of $T_{\mathrm{res}} = 2.4$ ms (table A.5) this corresponds to an average of only 1.5 spin exchange collisions per atom during it's entire time in the storage cell. The entire expected polarization loss in the target must be attributed to these, if beam-target interactions and recombination are neglected.

The calculation of the relaxation behaviour shown is based on a hyperfine occupancy of the injected atomic beam, that was calculated from the data in appendix D.3. The transmission probabilities in the sextupole system of the atomic beam source and the efficiencies of the high frequency transitions were taken into account. The results for the source are compiled in table 14.2 The relaxation calculation assumes a correlation time of $\tau_C = 5.41 \cdot 10^{-12}\,\mathrm{s}$ and a wall collision amplitude of $C = 8.5\,\mathrm{s}^{-1}$. These values were taken from the measurement on the drifilm coated test storage cell. The change in average flight time between two wall collisions that results from the geometry was included as well. As was seen in the discussion of the FILTEX target, the value of the wall collision amplitude can differ from the expected value by more than a factor of three. However, even a wall collision amplitude that would be larger by a factor of ten would have no effect on the nuclear polarization in strong fields. Only in weak fields, far below the critical field strength, a larger wall collision amplitude would lead to a behaviour that is different from the one shown here. These weak fields are of no interest to the HERMES experiment.

The injection of the two hyperfine states $|2\rangle$ and $|3\rangle$ was also examined for the test storage cells, see the figures 14.3 bottom, 12.3 right, 12.4 right and 13.1 right. There are significant differences in the geometry of the test storage cells and the storage cell of the HERMES experiment as well as in the average number of wall collisions. Nevertheless, there are no obvious differences with regard to the behaviour of the hyperfine occupancy, the polarization and the polarization losses. This is due to the fact that in both cases the relaxation is dominated by the spin exchange collisions. The atoms remain longer in the test storage cells, by about a factor between ten and thirty, then in the HERMES storage cell (tables A.3 and A.5). On the

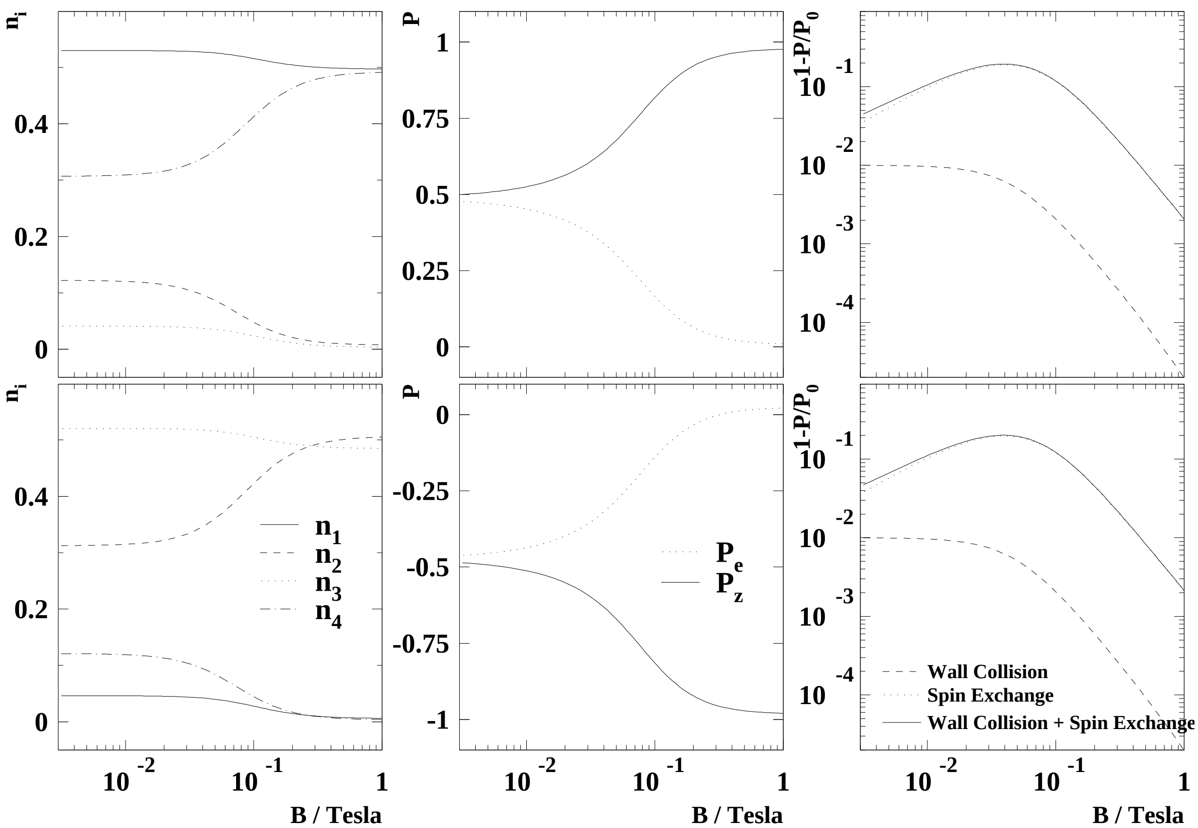

Fig. 14.3:
Hyperfine occupancy (left), polarization (center) and polarization losses (right) for hydrogen in the storage cell of the HERMES experiment. The losses due to spin exchange collisions are in fact plotted!. However, only in weak fields it is possible to distinguish them from the total loss. Top: Injection of the states $|1\rangle$ and $|4\rangle$. Bottom: Injection of the states $|2\rangle$ and $|3\rangle$.

other hand also the density in the HERMES storage cell is higher by a factor of ten to thirty compared to the test storage cells (tables B.2 and 14.3). This makes the overall effect of spin exchange collisions in both cells about comparable. Only the relaxation due to wall collisions is significantly higher for the test storage cells. This difference can be proven by injecting a beam with high electron polarization into the HERMES cell. However, this has no effect on the nuclear polarization in strong fields.

The HERMES target can be operated with a longitudinal as well as with a transverse holding field. High field strengths are desirable to limit the effects of beam-target interactions that may lead to bunch field depolarization [48]. However, the transverse holding field deflects the positron beam and thus leads to a large amount of synchrotron radiation. Therefore the transverse field was limited to a value of $B_{\perp} = 154\,\mathrm{mT}$, while the longitudinal field is chosen at $B_{\parallel} = 350\,\mathrm{mT}$ [23, 143].

Table 14.3 lists numerical values for the expected hyperfine occupancy, polarization, polarization losses and quality of the target for these field strengths. The hyperfine occupancies that are injected by the source serve as initial occupancies for the relaxation calculation. Spin exchange collisions and wall collisions are included. The storage cell temperature at which the target is operated is not yet finally defined. This allows the assumption of a cell temperature of 101 K to stay in agreement with the conditions for the test storage cells. Bunch field depolarization and recombination in the cell are not included, so that the given values do not actually agree with the target polarization expected for the experiment. It is not yet possible to determine

States	$\|1\rangle, \|4\rangle$	$\|2\rangle, \|3\rangle$
P_z^{soll}	$+1.0$	-1.0
n_1	$0.4938(13)$	$7.7(49)\cdot 10^{-3}$
n_2	$1.02(50)\cdot 10^{-2}$	$0.5048(13)$
n_3	$2.94(50)\cdot 10^{-4}$	$0.4864(51)$
n_4	$0.4957(52)$	$1.1(1)\cdot 10^{-3}$
$P_{z\perp}$	$0.9547(73)$	$-0.9572(72)$
$P_{z\parallel}$	$0.9741(73)$	$-0.9772(72)$
Σ	$1.192(9)$	
$\Sigma\cdot\Omega$ [sr]	$1.534(12)\cdot 10^{-2}$	
$\dot{n}$ [s^{-1}]	$7.0(2)\cdot 10^{16}$	
$\dot{n}P_{z\perp}^2$ [s^{-1}]	$6.4(2)\cdot 10^{16}$	$6.5(2)\cdot 10^{16}$
$\dot{n}P_{z\parallel}^2$ [s^{-1}]	$6.7(2)\cdot 10^{16}$	$6.7(2)\cdot 10^{16}$

Tab. 14.2:
Hyperfine occupancies, polarization and quality factors of the atomic beam source of the HERMES experiment for hydrogen. $T_{\text{nozzle}} = 80\,\text{K}$, $T_{\text{beam}} = 23.2\,\text{K}$, $v_{\text{drift}} = 1839\,\text{m}\,\text{s}^{-1}$, and $K_{\text{mol}} = 1.0$.

the target polarization for the atomic fraction alone. The method for the determination of the corrections applied in [136] only includes the relaxation due to wall collisions; spin exchange collisions are not included. Nevertheless, the significantly smaller polarization losses should lead to a correction that is smaller than the $1-2\,\%$ estimated for the FILTEX test experiment, especially at a field of 350 mT.

The uncertainties listed in table 14.3 are about equally based on the uncertainties of the determination of the injected hyperfine occupancies and the uncertainties on the relaxation. They contain the statistical error of the transmissions and the errors on the efficiency measurements that determine the uncertainty on the injected hyperfine occupancy as well as an uncertainty in the relaxation behaviour that was estimated from a calculation at a 30 % higher target density. This should account in a sufficient way for differences in the injected gas flux as well as for differences in the assumed spin exchange cross section. The parameter K_{mol} has a negligible effect on the hyperfine occupancy of the injected hydrogen atom beam, because all occupation transfers occur only after the entire sextupole magnet system. Thus it cannot cause any uncertainties that would have to be considered here. The neglections in the spatial density and polarization

Tab. 14.3:
Hyperfine occupancies, polarization and quality factors of the storage cell of the HERMES experiment for hydrogen. The uncertainties of the transmissions and efficiencies were included in the estimates of the uncertainties on the calculation of the injected hyperfine states. For the injected flux a difference of 30 % was included. Parameters for the relaxation in the storage cell: $C = 8.5\,\text{s}^{-1}$, $\tau_C = 5.41\cdot 10^{-12}\,\text{s}$ and $T_{\text{cell}} = 101\,\text{K}$.

	$B_\perp = 154\,\text{mT}$			$B_\parallel = 350\,\text{mT}$	
States	$\|1\rangle, \|4\rangle$	$\|2\rangle, \|3\rangle$	States	$\|1\rangle, \|4\rangle$	$\|2\rangle, \|3\rangle$
P_z^{soll}	$+1.0$	-1.0	P_z^{soll}	$+1.0$	-1.0
n_1	$0.5081(35)$	$1.87(34)\cdot 10^{-2}$	n_1	$0.4997(18)$	$9.0(9)\cdot 10^{-3}$
n_2	$2.86(68)\cdot 10^{-2}$	$0.4596(90)$	n_2	$1.20(23)\cdot 10^{-2}$	$0.4953(34)$
n_3	$1.55(35)\cdot 10^{-2}$	$0.4968(61)$	n_3	$6.4(13)\cdot 10^{-3}$	$0.4877(52)$
n_4	$0.448(13)$	$2.48(53)\cdot 10^{-2}$	n_4	$0.4820(62)$	$8.0(15)\cdot 10^{-3}$
P_z	$0.891(17)$	$-0.891(18)$	P_z	$0.9584(84)$	$-0.9610(85)$
$(1-P/P_0)$	$6.7(16)\cdot 10^{-2}$	$6.9(17)\cdot 10^{-2}$	$(1-P/P_0)$	$1.61(45)\cdot 10^{-2}$	$1.66(47)\cdot 10^{-2}$
ρ_0 [cm^{-3}]	$4.03(12)\cdot 10^{12}$		ρ_0 [cm^{-3}]	$4.03(12)\cdot 10^{12}$	
$\bar{\rho}$ [cm^{-3}]	$2.02(6)\cdot 10^{12}$		$\bar{\rho}$ [cm^{-3}]	$2.02(6)\cdot 10^{12}$	
n [cm^{-2}]	$8.08(24)\cdot 10^{13}$		n [cm^{-2}]	$8.08(24)\cdot 10^{13}$	
nP_z^2 [cm^{-2}]	$6.41(40)\cdot 10^{13}$	$6.41(40)\cdot 10^{13}$	nP_z^2 [cm^{-2}]	$7.42(32)\cdot 10^{13}$	$7.46(32)\cdot 10^{13}$

distributions also should be accounted for in a sufficient way by the assumed uncertainty in the target density of 30 %.

All data in table 14.3 can be verified experimentally by measuring the polarization of the atomic fraction in the cell with the Breit-Rabi polarimeter while no positron beam is in the HERA ring.

One of the listed parameters, the hydrogen flux that is injected into the cell by the source, could already be confirmed. This parameter depends mainly on the quality of the simulation calculations concerning the sextupole systems (appendix D). For a nozzle temperature of 110 K a flux of $\dot{n} = 6.8(2) \cdot 10^{16}\,\mathrm{s}^{-1}$ was measured [139], which is in excellent agreement with the quoted flux of $7.0(2) \cdot 10^{16}\,\mathrm{s}^{-1}$ at a temperature of 80 K listed in table 14.2.

The reasons for the observed shift in the optimal nozzle temperature were examined by U. Funk [139]. The HERMES source uses a novel dissociator for which the temperature is measured directly at the nozzle. In the source of the FILTEX test experiment an older type of dissociator was used, where the nozzle temperature was measured at the copper fitting for the nozzle. The *true* nozzle temperature in this case was about 15 K higher than the measured one. Following [139] this also leads to corrections in the parameterization of beam temperature and drift velocity according to B. Lorentz [108]. Furthermore, the sextupole magnets of the HERMES system have a higher magnetization of 1.25 T compared to 1.13 T for the FILTEX system, which again leads to a shift towards higher temperatures. This only became known after these calculations and thus could not be taken into account any more. An additional new calculation will be needed, to show if deviations from the assumed state of operation lead to deviations in the behaviour of the target polarization.

14.3 The Deuterium Target for the HERMES Experiment

A precise and reliable check of the simulation calculations will be made possible by comparing the calculated polarization and the measured data. The predictions in table 14.4 differ from earlier ones, which is the most apparent in the negative tensor polarization of deuterium. In [46] a value of $P_{zz} = -1.876$ is quoted, which is significantly different from the value of $-1.788(15)$ in table 14.4. This difference is partly caused by the incomplete treatment of the MFT 1-4 in [46]. In a correct calculation of the injected hyperfine occupancy according to appendix D.4 the efficiency of this three-step transition enters cubically into the the occupation numbers.

The polarization of the deuterium target for the HERMES experiment is defined almost completely by the injected hyperfine occupancy. In their calculation the transmission probabilities in the sextupole magnet system and the efficiencies of the high frequency transitions were taken into account (appendix D.4). The polarization losses due to relaxation are in the region of parts per million for the anticipated holding fields. Thus they are below the detection limit of the Breit-Rabi polarimeter. A measurement of the polarization of the atomic beam that leaves the storage cell therefore allows for a practically direct measurement of the injected polarization and thus also for an accurate check of the simulation calculations for the sextupole magnet systems.

The objective of the deuterium target is to reach an optimal vector polarization (figure 14.4 upper half and table 14.4 left side) as well as an optimal tensor polarization (figure 14.4 lower half and table 14.4 right side) while in the second case the vector polarization should vanish.

Figure 14.4 shows once again the dependency of the hyperfine occupancy, the polarization and the polarization losses on the holding field in the storage cell. As in the case of hydrogen, the relaxation is clearly dominated by spin exchange collisions, where the expected polarization losses are additionally reduced as a result of the lower critical field compared to hydrogen. The predictions about the relaxation can be checked in the weak field region by examining the behaviour of the hyperfine occupancy. A further possibility is the injection of the states $|3\rangle$ and $|6\rangle$. In this case the relaxation in the hyperfine occupancy is also for strong holding fields not suppressed. This relaxation process is caused by the *fast* spin exchange reaction (3.22), but it has no effect on the polarization observables. The sudden drop of the polarization losses for the injection of the states $|3\rangle$ and $|4\rangle$ can be explained by an increase in vector polarization below about 2 mT. The behaviour for the injection of the states $|3\rangle$ and $|6\rangle$ is caused by a zero crossing of the tensor polarization.

Table 14.4 lists the parameters for the injected atomic beam and for the expected values for the storage cells at the two planned holding fields under consideration of the relaxation by wall and spin exchange collisions. The values were calculated according to appendix D.4. Bunch field depolarization and recombination are not included. For this reason the quoted values do not refer to the actually expected target polarization, but to the properties of the atomic fraction in the cell that can be measured with the Breit-Rabi polarimeter with no positron beam in the ring.

For the calculation of the relaxation a correlation time of $\tau_C = 2.26 \cdot 10^{-10}\,\mathrm{s}$ and a wall collision amplitude of $C = 6.0\,\mathrm{s}^{-1}$ were assumed. The correlation time was taken from the deuterium measurement with the teflon cell (table11.1), assuming that the correlation time for the different surface coatings will be similar, as is the case for hydrogen. The value of the wall collision amplitude was derived from the hydrogen measurement with the drifilm cell, accounting for the change in average flight time between two wall collisions. This choice can be motivated by the similarity of the amplitudes for hydrogen and deuterium for identical coating. As in the case of the hydrogen target, the choice of these parameters is completely uncritical for the vector and tensor polarizations at the foreseen fields, even if a large uncertainty is assumed. Due to the small polarization losses, the listed uncertainties were determined almost entirely from the uncertainties of the injected hyperfine occupancies. The assumption of a by 30 % increased density does not lead to a notable difference in the polarization observables. Only for the relaxation in the hyperfine occupancy for the injection of the states $|3\rangle$ and $|6\rangle$ does this uncertainty contribute significantly. For the uncertainties of the injected hyperfine occupancies and the polarization it must be remembered, that the parameter K_{mol} determines the polarization of the deuterium target and that in chapter 14.1 only a lower boundary could be determined. Assuming a value of 0.85 for K_{mol} the reduction in vector polarization becomes about 1 %, the positive tensor polarization does not change and negative tensor polarization also decreases by about 1 %. The deviations observed for the occupation numbers are also in the same order of magnitude. The possibly smaller value of K_{mol} is not included in the error listing in table 14.4.

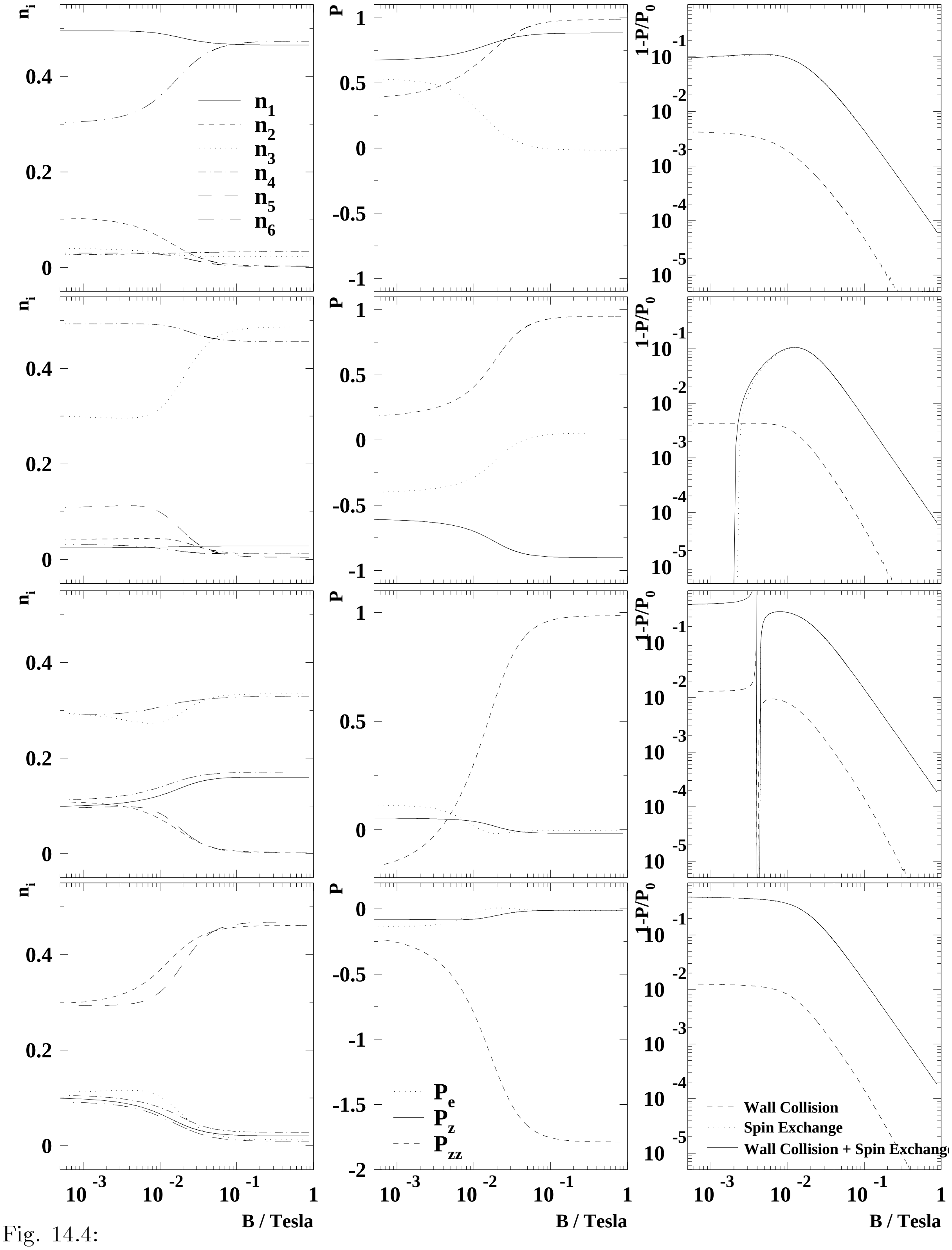

Fig. 14.4:
Hyperfine occupancy (left), polarization (center) and polarization losses (right) for deuterium in the storage cell of the HERMES experiment. The upper two plots on the right show the losses in vector polarization, the lower two show the losses of tensor polarization. From top to bottom: 1.) Injection of the states $|1\rangle$ and $|6\rangle$, $P_z^{\rm soll}=+1$, $P_{zz}^{\rm soll}=+1$. 2.) Injection of the states $|3\rangle$ and $|4\rangle$, $P_z^{\rm soll}=-1$, $P_{zz}^{\rm soll}=+1$. 3.) Injection of the states $|3\rangle$ and $|6\rangle$, $P_z^{\rm soll}=0$, $P_{zz}^{\rm soll}=+1$. 4.) Injection of the states $|2\rangle$ and $|5\rangle$, $P_z^{\rm soll}=0$, $P_{zz}^{\rm soll}=-2$.

Tab. 14.4:

Hyperfine occupancies, polarization and quality factors for the atomic beam source and and the storage cell of the HERMES experiment for deuterium. Parameters of the source: $T_{\mathrm{nozzle}} = 80\,\mathrm{K}$, $T_{\mathrm{beam}} = 21.4\,\mathrm{K}$, $v_{\mathrm{drift}} = 1346\,\mathrm{m\,s^{-1}}$ and $K_{\mathrm{mol}} = 1.0$. Parameters for the relaxation: $C = 6.0\,\mathrm{s^{-1}}$, $\tau_C = 2.26 \cdot 10^{-10}\,\mathrm{s}$ and $T_{\mathrm{cell}} = 110\,\mathrm{K}$. The quality factors on the left side contain P_z, on the right side P_{zz}.

States	$\vert 1\rangle, \vert 6\rangle$	$\vert 3\rangle, \vert 4\rangle$	$\vert 3\rangle, \vert 6\rangle$	$\vert 2\rangle, \vert 5\rangle$
P_z^{soll}	$+1.0$	-1.0	0.0	0.0
P_{zz}^{soll}	$+1.0$	$+1.0$	$+1.0$	-2.0
Atomic Beam Source				
n_1	$0.4715(13)$	$4.02(19) \cdot 10^{-2}$	$3.0(10) \cdot 10^{-2}$	$3.0(10) \cdot 10^{-2}$
n_2	$4.17(60) \cdot 10^{-3}$	$1.59(63) \cdot 10^{-2}$	$4.1(74) \cdot 10^{-3}$	$0.4639(62)$
n_3	$1.59(60) \cdot 10^{-2}$	$0.4715(49)$	$0.4656(62)$	$5.3(10) \cdot 10^{-4}$
n_4	$4.02(9) \cdot 10^{-2}$	$0.4715(49)$	$4.00(9) \cdot 10^{-2}$	$4.00(9) \cdot 10^{-2}$
n_5	$5.28(63) \cdot 10^{-4}$	$5.28(63) \cdot 10^{-4}$	$5.25(63) \cdot 10^{-4}$	$0.4656(86)$
n_6	$0.4677(49)$	$4.02(55) \cdot 10^{-4}$	$0.4602(85)$	$4.00(55) \cdot 10^{-4}$
$P_{z\perp}$	$0.8825(79)$	$-0.9017(96)$	$-1.6(16) \cdot 10^{-2}$	$-1.1(15) \cdot 10^{-2}$
$P_{zz\perp}$	$0.9842(79)$	$0.9489(96)$	$0.983(16)$	$-1.785(15)$
$P_{z\parallel}$	$0.8830(79)$	$-0.9022(96)$	$-1.6(16) \cdot 10^{-2}$	$-1.1(15) \cdot 10^{-2}$
$P_{zz\parallel}$	$0.9856(79)$	$0.9504(96)$	$0.985(16)$	$-1.788(15)$
Σ	$1.269(15)$		$1.276(16)$	
$\Sigma \cdot \Omega$ [sr]	$1.633(19) \cdot 10^{-2}$		$1.642(21) \cdot 10^{-2}$	
$\dot{n}$ [$\mathrm{s^{-1}}$]	$5.00(14) \cdot 10^{16}$		$5.02(14) \cdot 10^{16}$	
$\dot{n}P_\perp^2$ [$\mathrm{s^{-1}}$]	$3.89(12) \cdot 10^{16}$	$4.07(13) \cdot 10^{16}$	$4.85(18) \cdot 10^{16}$	$4.00(12) \cdot 10^{16}$
$\dot{n}P_\parallel^2$ [$\mathrm{s^{-1}}$]	$3.90(12) \cdot 10^{16}$	$4.07(13) \cdot 10^{16}$	$4.87(18) \cdot 10^{16}$	$4.01(12) \cdot 10^{16}$
Storage Cell at $B_\perp = 154\,\mathrm{mT}$				
n_1	$0.4661(14)$	$2.87(18) \cdot 10^{-2}$	$0.160(13)$	$2.12(71) \cdot 10^{-2}$
n_2	$4.12(62) \cdot 10^{-3}$	$1.23(49) \cdot 10^{-2}$	$4.1(75) \cdot 10^{-3}$	$0.4594(61)$
n_3	$2.31(87) \cdot 10^{-2}$	$0.4842(50)$	$0.334(14)$	$1.36(14) \cdot 10^{-2}$
n_4	$3.30(10) \cdot 10^{-2}$	$0.4567(49)$	$0.170(13)$	$2.89(11) \cdot 10^{-2}$
n_5	$2.44(38) \cdot 10^{-3}$	$6.14(76) \cdot 10^{-3}$	$2.79(43) \cdot 10^{-3}$	$0.4664(86)$
n_6	$0.4713(49)$	$1.19(11) \cdot 10^{-2}$	$0.329(14)$	$1.04(12) \cdot 10^{-2}$
P_z	$0.8808(79)$	$-0.8997(96)$	$-1.6(16) \cdot 10^{-2}$	$-1.1(15) \cdot 10^{-2}$
P_{zz}	$0.9785(81)$	$0.9427(98)$	$0.977(16)$	$-1.774(15)$
$(1 - P/P_0)$	$1.93(52) \cdot 10^{-3}$	$2.22(67) \cdot 10^{-3}$	$6.1(21) \cdot 10^{-3}$	$6.2(17) \cdot 10^{-3}$
ρ_0 [$\mathrm{cm^{-3}}$]	$3.90(11) \cdot 10^{12}$		$3.92(11) \cdot 10^{12}$	
$\bar{\rho}$ [$\mathrm{cm^{-3}}$]	$1.95(6) \cdot 10^{12}$		$1.96(6) \cdot 10^{12}$	
n [$\mathrm{cm^{-2}}$]	$7.80(24) \cdot 10^{13}$		$7.84(24) \cdot 10^{13}$	
nP^2 [$\mathrm{cm^{-2}}$]	$6.05(20) \cdot 10^{13}$	$6.31(22) \cdot 10^{13}$	$7.48(29) \cdot 10^{13}$	$6.17(20) \cdot 10^{13}$
Storage Cell at $B_\parallel = 350\,\mathrm{mT}$				
n_1	$0.4657(14)$	$2.88(18) \cdot 10^{-2}$	$0.160(13)$	$2.07(70) \cdot 10^{-2}$
n_2	$3.26(47) \cdot 10^{-3}$	$1.16(46) \cdot 10^{-2}$	$3.2(58) \cdot 10^{-3}$	$0.4607(62)$
n_3	$2.30(87) \cdot 10^{-2}$	$0.4865(53)$	$0.335(13)$	$1.27(12) \cdot 10^{-2}$
n_4	$3.30(10) \cdot 10^{-2}$	$0.4561(49)$	$0.171(13)$	$2.82(13) \cdot 10^{-2}$
n_5	$1.82(18) \cdot 10^{-3}$	$5.16(50) \cdot 10^{-3}$	$1.85(18) \cdot 10^{-3}$	$0.4681(86)$
n_6	$0.4731(50)$	$1.19(11) \cdot 10^{-2}$	$0.329(14)$	$9.61(96) \cdot 10^{-3}$
P_z	$0.8826(79)$	$-0.9018(96)$	$-1.6(16) \cdot 10^{-2}$	$-1.1(15) \cdot 10^{-2}$
P_{zz}	$0.9844(79)$	$0.9492(96)$	$0.984(16)$	$-1.786(15)$
$(1 - P/P_0)$	$4.5(11) \cdot 10^{-4}$	$4.4(11) \cdot 10^{-4}$	$1.02(10) \cdot 10^{-3}$	$1.12(56) \cdot 10^{-3}$
nP^2 [$\mathrm{cm^{-2}}$]	$6.08(20) \cdot 10^{13}$	$6.34(22) \cdot 10^{13}$	$7.59(29) \cdot 10^{13}$	$6.25(21) \cdot 10^{13}$

15 Discussion and Outlook

15.1 Operation of the Breit-Rabi Polarimeter in the HERMES Experiment

By the introduction of a time resolution into the readout of the atomic beam detector in combination with a single ion detection (chapter 4.3.4), it was possible to increase the sensitivity of the detector enough, so that under the conditions that are to be expected for the intensities in the HERMES experiment maximally 60 s will be needed to reach a statistical error of 0.03 on the tensor polarization of deuterium. For the nuclear polarization of hydrogen atoms only 10 s should be sufficient (chapter 10). The technique of time-resolved single ion detection even makes it possible to switch the polarization of the target with a frequency that is higher than the necessary time for a polarization measurement normally would allow. In this case the polarization must be averaged over several switch cycles for the target polarization.

The procedure that was developed for the calibration of the polarimeter (chapters 7, 8 and 9) does not in general allow the measurement of any arbitrary setting of the polarimeter that is far from the ideal. However, if the ideal setting is approximately achieved, it can be verified experimentally to high precision without using simulation programs for the determination of transmission corrections. The systematic error on the vector polarization that results from this calibration procedure reach under the conditions in the test apparatus for both hydrogen and deuterium the uncertainty of $\Delta P_z = 0.03$ that is required for the HERMES experiment. Only for the tensor polarization of deuterium with $\Delta P_{zz} = 0.05$ this value was not yet reached. However, these figures do not include uncertainties that might result from possible asymmetric efficiencies of the high frequency transitions.

The calibration procedure may utilize an atomic beam of unknown polarization (chapter 8.8). This allows the repetition during the HERMES experiment with the beam that exits the storage cell. For this purpose it is not necessary to build a setup in which the axes of atomic beam source and polarimeter agree, although this was the case in the test setup.

Several possibilities for further technical improvements of the Breit-Rabi polarimeter were already pointed out in the text of this thesis. However, the different points should be collected once more in this summary:

- Examination of asymmetric efficiencies of the high frequency transitions, both in theory and experiment (chapter 7.2). It should be possible to largely suppress these asymmetries through the use of minimal field gradients for maximal HF power.

- Measurement of the molecular background in the detected beam by measurement of the individual counting rates for all molecules that contribute to the atomic beam signal through dissociative ionization. This makes the adaption of a correction counting rate unnecessary and the measured polarization values should then be also correct with respect to their absolute value.

- Replacement of the resonator for the strong field transitions SFT 1-4 and SFT 2-4 for hydrogen by a resonator with tilted rods. This will improve the efficiency and stability of the SFT 1-4 significantly. According to figure 10.3 this will allow the further reduction of the systematic errors on hydrogen measurements.

- Operation of the strong field transitions for deuterium using a resonance feedback circuit (figure 4.4). This should improve efficiency and stability of the high frequency transitions. There is reason to expect that this would make it possible to reduce the systematic error on the tensor polarization to < 0.03.

- Bringing a further deuterium transition into operation, either the MFT 1-4 or the SFT 2-5/3-6. This will allow the use of several analysis methods also for deuterium measurements and the high frequency transitions can be monitored during a polarization measurement. For the MFT 1-4 three efficiencies would have to be measured, whose errors would enter into the analysis. Therefore the use of SFT 2-5/3-6 would be preferable.

- Installation of a beam block in the first sextupole magnet of the polarimeter also for measurements on hydrogen. According to the results from chapter 9.3 this provision would, also for hydrogen, mean that the sextupole system becomes practically free of corrections. Furthermore, possible sources of errors due to high velocities in the transmitted atomic beam are mostly removed (chapter 9.4).

- Separate magnets for the generation of the static fields and field gradients for the medium and strong field transitions [144]. This is necessary to allow the measurement of the medium field transitions during the HERMES experiment (chapter 8.8). At the moment medium and strong field transitions cannot be operated independently of one another. While the high frequency transitions in the test source could be used, this was also not necessary.

- Installation of an additional mass spectrometer between storage cell and Breit-Rabi polarimeter to measure the degree of dissociation in the storage cell [133]. For the measurement an angle of about $9°$ relative to the axis of the exit tube is used, so that the polarization measurement at $0°$ is not affected. The Breit-Rabi polarimeter is only sensitive to the polarization of the atomic fraction inside the storage cell. Therefore the measured polarization must also be corrected by the degree of dissociation.

Further technical improvements concern the operation of the apparatus in the HERMES experiment, where the polarimeter is in the vicinity of the interaction region inside the ring tunnel. The synchrotron radiation in this region causes a high radiation level, so that during the operation of the accelerator the target and thus also the polarimeter are inaccessible. Therefore all important parameters of the polarimeter must be remote controlled by computer. This was already mostly the case at the test stand in Heidelberg. Part of the technical improvements collected above were already implemented.

15.2 Applicability of the Relaxation Model

The very good agreement between the relaxation model from chapter 3 and the field dependency measurements in chapter 12 illustrates, that the most important relaxation processes for the hyperfine occupancies in the gas within the storage cell are known and well understood.

In chapter 14.1 the model could successfully be applied to measurements that were already carried out in 1992 at the TSR in Heidelberg. The measured target polarizations from this experiment were reproduced within their error bars.

In the chapters 14.2 and 14.3 simulations of sextupole magnet systems and the relaxation model were used to make a prediction for the parameters that are relevant for the polarization of the HERMES target. However, they do not yet account for the beam-target interaction and the recombination in the storage cell. Nevertheless, this prediction can be used to check the the reliability of the simulation calculations as well as the relaxation model by measuring the target polarization with the Breit-Rabi polarimeter while no beam is in the ring.

15.3 Software for the Calculation of the Relaxation in Target Storage Cells

The measurement of the target polarization during the running of the HERMES experiment uses an atomic beam, which is fed from a tube in the side of the storage cell to the Breit-Rabi polarimeter. The positrons in the ring on the other hand see a polarization that is averaged over the length of the storage cell. This may be different from the measured target polarization. The exact corrections on the measured target polarization can only be taken from computer calculations. At the moment there are three programs that may be used to solve partial aspects of this problem:

- A Monte Carlo simulation for molecular flow (appendix A.3),
- A program for the numerical integration of the master equation (3.1) and
- A Monte Carlo simulation for the bunch field depolarization [48].

The simulation program for molecular flow is best suited for the simulation of the relaxation due to wall collisions, because it actually describes the interaction of the atoms with the walls. So far this is a pure single particle simulation, so that spin exchange collisions that represent an interaction between atoms cannot be included without a significant extension of the program. A big advantage of the program is the inclusion of the storage cell geometry. This allows the determination of the important polarization distributions inside the HERMES storage cell, especially within the beam pipe.

The numerical integration of the master equation is certainly a valid ansatz for the description of the relaxation processes. However, in it's present form the program is not suited to describe the behaviour of the polarization inside the HERMES storage cell completely. For the integration it is assumed that polarization and density are constant over the extension of the storage cell. Polarization distributions therefore cannot be described. Also the density inside the HERMES storage cell actually is not constant, and this must be considered for the spin exchange collisions.

The simulation program for the bunch field depolarization was developed independently of the first two programs. As in the first program the interaction of individual atoms in the target is simulated. The integration of spin exchange collisions into this program leads to similar problems as in the case of the molecular flow simulation.

The corrections for the target polarization as measured with the Breit-Rabi polarimeter are probably smaller than the required maximal error on the target polarization of $\Delta P = 0.03$, due to the small polarization losses in the storage cell of the HERMES target (chapter 14.2 and 14.3). Nevertheless it is certainly a good idea to develop a program that simultaneously includes all relaxation processes, the recombination of atoms to molecules and the storage cell geometry. Without such a program it will not be possible to precisely determine the correction factor between the measured and the real value of the polarization as seen by the positrons. Such a program will probably be developed by combining the three programs discussed above.

15.4 Surface Interaction and Spin Exchange Cross Section

The precision that was achieved with respect to the determination of the relaxation parameters with the used apparatus is certainly not yet high enough to allow reliable statements about the spin exchange cross section or the interactions at the surface. However, it is imaginable that an improved setup will make these measurements possible.

Several of the necessary improvements will already be included in the construction of the target for the HERMES experiment:

- Velocity and temperature of the atomic beam in the source are known from measurements. This allows a reliable determination of the hyperfine occupancies that are injected into the cell.
- The gas flux that the source injects into the cell is monitored as well, so that the density inside the cell is known and statements about the spin exchange cross section become possible.
- The degree of dissociation in the storage cell is monitored. This allows a significant reduction of the systematic error especially in the determination of the wall collision amplitude. The recombination can be integrated into the relaxation model and measured.
- The magnetic field and the temperature are homogeneous inside the storage cell. Systematic errors like those generated for the test storage cells due to the entry tube, do not occur any more.
- The vacuum in the region of the storage cell will be significantly better than in the test setup, so that the conditions at the surfaces are controlled better.

It is not the main interest of the HERMES experiment to do surface physics or to measure spin exchange cross sections. Still, every improvement in these areas also leads to a better understanding of the relaxation processes in the storage cell and thus to a reduction of systematic uncertainties in the target polarization. This means that all of the improvements discussed above are also of interest for the HERMES experiment.

A Data about the Storage Cells

In this part of the appendix all data about the storage cells are collected. The foundations of their calculation were treated before. Appendix A.1 contains drawings to scale for the test storage cells, the target storage cell of the FILTEX test experiment at the TSR in Heidelberg [58, 59] and for the target storage cell of the HERMES experiment [23]. Appendix A.2 treats the calculation of flow conductance values that are needed for the calculation of the density within the storage cells from the injected gas flows. Appendix A.3 contains Monte Carlo results for the molecular flow.

A.1 Dimensions of the Storage Cells

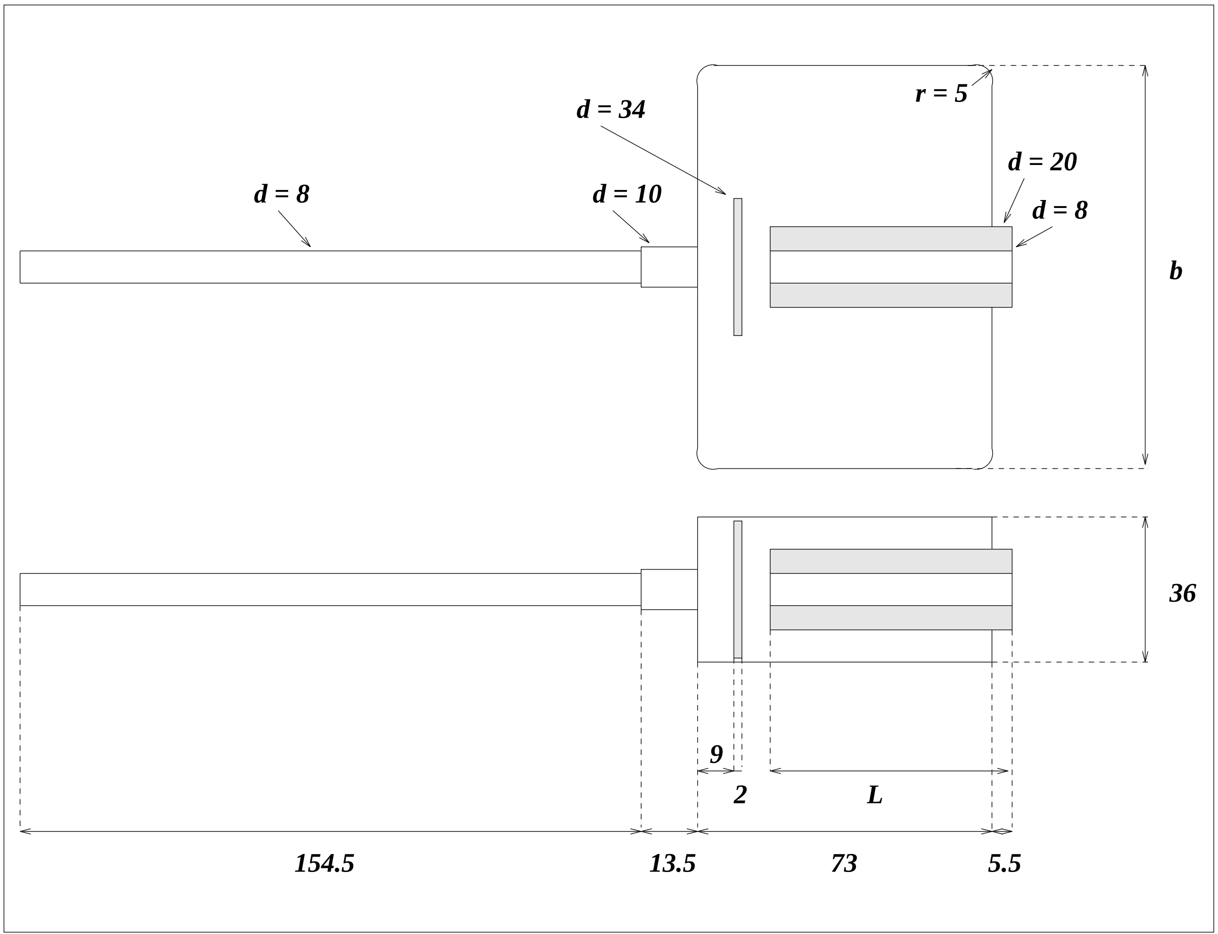

Fig. A.1:
Dimensions of the test storage cells. Top: Horizontal cut. Bottom: Vertical cut. Scale 1 : 1.875. All dimensions are given in mm. For the small cell: $L = 30\,\mathrm{mm}$ and $b = 50\,\mathrm{mm}$. For the large cell: $L = 60\,\mathrm{mm}$ and $b = 100\,\mathrm{mm}$. d stands for diameter, these are given for the entry tube (8), the entry opening of the cell (10), the beam block (34) and for the inner and outer diameter of the cell exit tube (8 and 20). The beam block is welded to the base plate.

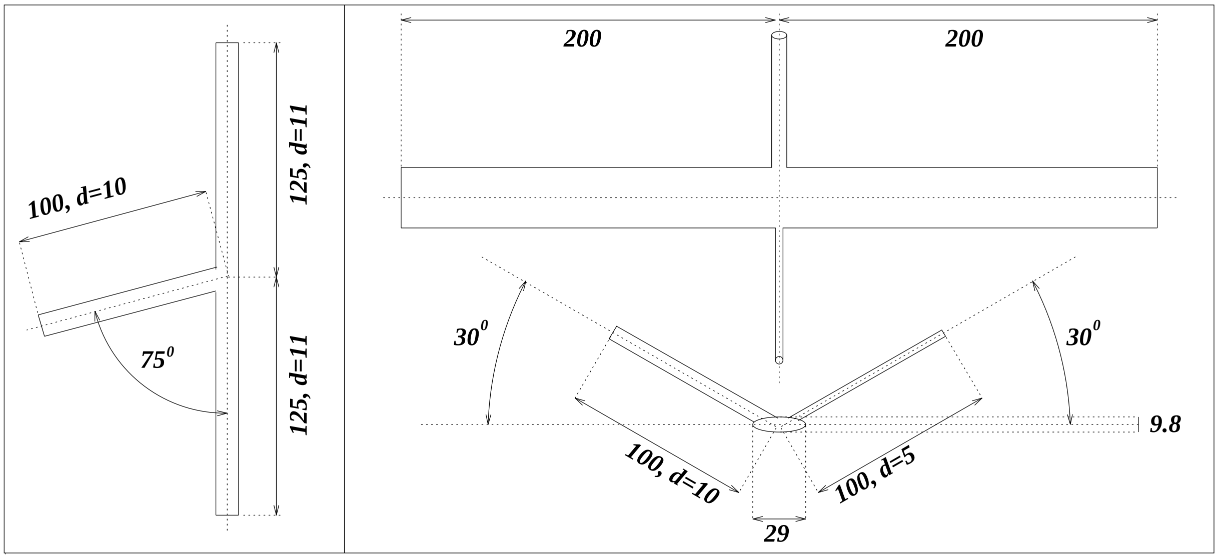

Fig. A.2:
Dimensions of the target storage cells. Scale $1:40$. All data in mm. d is the diameter. Left: Target storage cell of the FILTEX test experiment at the TSR in Heidelberg [58, 59]. The cell consists of a cylindrical beam tube and an also cylindrical injection tube, that is connected to the side of the beam tube under an angle of $75°$. Right: Target storage cell of the HERMES experiment. The cell consists of a beam tube with an elliptical cross section and two cylindrical tubes that are connected to the main tube under an angle of $30°$ relative to the horizontal plane. The first of the two tubes has a diameter of $10\,\mathrm{mm}$ and is used for the injection of the polarized atomic beam, the second one has a diameter of $5\,\mathrm{mm}$ and produces the test beam for the polarization measurement with the Breit-Rabi polarimeter.

A.2 Conductances

The density ρ inside the storage cell is determined by the injected gas flux $\dot{n}_{\mathrm{inj}}$ and the conductance values C_i for injection and exit tubes according to

$$\rho = \frac{\dot{n}_{\mathrm{inj}}}{C_{\mathrm{gesamt}}} = \frac{\dot{n}_{\mathrm{inj}}}{\sum_i C_i} \tag{A.1}$$

In the region of molecular flow the conductance of a tube with arbitrary cross section can be calculated as [105]

$$C_{[\mathrm{l\,s^{-1}}]} = C' \cdot \sqrt{\frac{T_{[\mathrm{K}]}}{M_{[\mathrm{amu}]}}}. \tag{A.2}$$

T is the temperature and M the mass of the atoms or molecules in atomic mass units (amu). C' is a factor that depends only on the geometry of the tube, it can easily be calculated with the formulae in table A.1.

Figure A.3 compares the formulae for short and long tubes with the results of the Monte Carlo simulation for molecular flow. The Monte Carlo simulation will be described in more detail in appendix A.3. The simulation program determines the ratio of the conductance of a tube with the given length to the conductance of a very long reference tube ($L = 500\,\mathrm{mm}$, $d = 8\,\mathrm{mm}$). Both tubes are connected to a very large start vessel, a direct flight of the atoms from tube to tube is made impossible by a beam block. The final conductance of this start vessel causes the deviations of the simulation results from the calculation according to (A.2) for short tubes.

Tab. A.1:
Calculation of conductance values C' for short and long tubes according to [105]. The parameters are: d diameter, L length, S cross section area and U circumference of the tube. The unit for these parameters is either mm or mm^2.

C'	long tubes	short tubes
circular	$3.82 \cdot 10^{-2} \cdot \dfrac{d^3}{L}$	$2.85 \cdot 10^{-2} \cdot \dfrac{d^2}{0.75 \cdot \frac{L}{d} + 1}$
arbitrary	$19.4 \cdot 10^{-2} \cdot \dfrac{S^2}{L \cdot U}$	$3.64 \cdot 10^{-2} \cdot \dfrac{S}{0.19 \cdot \frac{L \cdot U}{S} + 1}$

The results demonstrate that the formulae for short tubes principally give better results for the conductance values while the formulae for long tubes represent an approximation that really should only be used for very long tubes. On the other hand the reliability of the simulation program is illustrated by this example. Table A.2 lists the conductance values for all injection and exit tubes of the test storage cells and the two target storage cells. All values were calculated according to the formulae for short tubes (table A.1). Cross section area and circumference of the elliptical beam pipe of the target storage cell were calculated as

$$S = ab\pi \qquad U \approx \pi \left[\frac{3}{2}(a+b) - \sqrt{ab} \right] \tag{A.3}$$

In the case of a storage cell with homogeneous temperature distribution the total conductance values C'_{total} can be simply taken from table A.2. For the test storage cells it must be taken into account that the injection tube is not being cooled, and therefore is at room temperature ($\approx 300\,\mathrm{K}$). The rest of the cell, including the exit tube, is being cooled. In this case the total conductance of both tubes of the test storage cells can be calculated as

$$C_{\mathrm{total}} = \frac{2.040 + C'_{\mathrm{out}}\sqrt{T_{[\mathrm{K}]}}}{\sqrt{M_{[\mathrm{amu}]}}}. \tag{A.4}$$

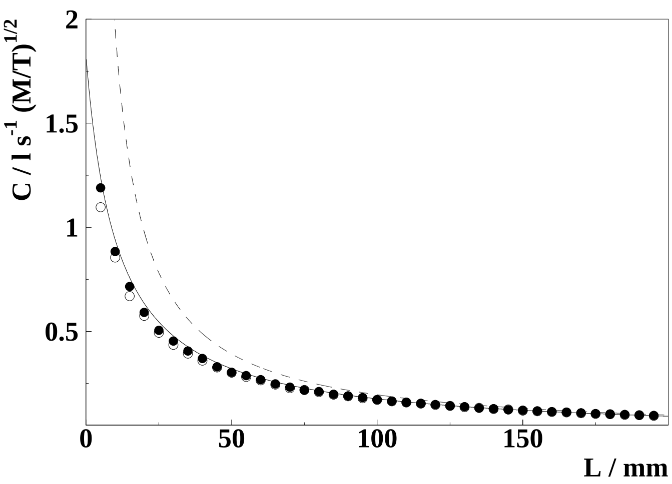

Fig. A.3:
Conductance of a tube with a circular cross section and a diameter of 8 mm as a function of it's length. The solid line was calculated with the formula for short tubes and the dashed line with the formula for long tubes. The points represent the results of the Monte Carlo simulation for molecular flow (chapter A.3). The open points were determined for a smaller start volume and deviate for short tubes somewhat more strongly from the analytical calculations (see also in the text).

Tab. A.2:
Conductance factors C' for injection and exit tubes of the storage cell given in units of $\mathrm{l\,s^{-1}} \cdot \sqrt{M/T}$. This means that for the calculation of the actual conductance values these numbers still must be multiplied by the factor $\sqrt{T_{[\mathrm{K}]}/M_{[\mathrm{amu}]}}$. In the case of the HERMES storage cell with elliptical cross section the lengths of the two semiaxes of the ellipse are given instead of the diameter.

		L [mm]	d [mm]		C'
Test Storage Cells					
injection tube	C'_{in}	154.5	8.0		0.1178
short exit tube	C'^{30}_{out}	30.0	8.0		0.4784
long exit tube	C'^{60}_{out}	60.0	8.0		0.2753
Storage Cell for the FILTEX Test Experiment					
		L [mm]	d [mm]		C'
half beam tube	C'_{beam}	125.0	11.0		0.3621
injection tube	C'_{in}	100.0	10.0		0.3353
total	C'_{total}	—	—		1.0595
Storage Cell for the HERMES Experiment					
		L [mm]	d [mm]		C'
half beam tube	C'_{beam}	200.0	$a = 14.5$	$b = 4.9$	0.6740
injection tube	C'_{in}	100.0	10.0		0.3353
exit tube	C'_{out}	100.0	5.0		0.0445
total	C'_{total}	—	—		1.7278

A.3 Monte Carlo Simulations of the Storage Cells

A Monte Carlo simulation was developed to determine several important key parameters for the storage cells. This Monte Carlo can simulate the trajectories of individual atoms through the storage cells in the molecular flow regime (chapter 6.2). In this flow regime the trajectories are determined by the interactions of the atoms with the walls of the storage cell while the interatomic interactions can be neglected. The single particle simulation thus is an appropriate approximation of the actual flowing behaviour.

The simulation program is based mainly on the definition of a suitable data structure, within which the geometry of the storage cells can be represented in the computer as two-dimensional surfaces within a three-dimensional space. The basic elements for the surfaces are planes, cylinders, cones, tubes with elliptic cross section, spheres and tori that can be arbitrarily placed and connected. The program uses a class of functions for the calculation of the intersection points between lines (trajectories of atoms) and simulated surfaces (storage cell walls) as well as several geometry parameters that are necessary for a correct running of the program.

An individual particle starts with an initial location and an initial direction, that together define a straight line. In general these values are generated by another program, e.g. the simulation program for the sextupole magnet in the atomic beam source (chapter 6). The initial location is located on the surface of the opening of the injection tube. The velocity of the particle is irrelevant. From this straight line the intersection with the storage cell walls is calculated. Then the normal direction in this point relative to the concerned surface is calculated and a new random direction is generated relative to this normal direction. This simulates the desorption of the atom from the surface.

In a thermal equilibrium the intensity distribution of the desorption due to isotropy arguments has to follow a $\cos\vartheta$ distribution [145, 146]:

$$\frac{\mathrm{d}\sigma}{\mathrm{d}\Omega} \propto \cos\vartheta. \tag{A.5}$$

This means that the trajectory after the desorption can be generated as an azimuthal angle φ with a flat distribution between 0 and 2π and a polar angle ϑ with a probability distribution of the form

$$\frac{\mathrm{d}\sigma}{\mathrm{d}\vartheta} \propto \sin 2\vartheta \tag{A.6}$$

Equation (A.6) follows from (A.5) by integration over the azimuthal angle φ.

This procedure is repeated until the atom hits one of the *open* surfaces that connect the injection and exit tubes with the *outside world*. From the simulation of a large number of trajectories some of the key parameters of the storage cells may be determined. The statistical accuracy is only limited by the finite cycle of the random number generator.

Table A.3 lists some of the key parameters for the geometries of the two test storage cells that were examined in this thesis. These parameters are the average number of wall collisions, the average length of the trajectories inside the storage cell, the average duration of stay and the average flight time of the atoms between two wall collisions, the relative fraction of the collisions of the atoms with the wall of the injection tube, where the physical conditions are different from the inside of the rest of the cell, and the transmission through the cell, which gives the probability that a particle that starts at the beginning of the injection tube leaves the cell through the exit tube towards the polarimeter instead of leaving it again through the injection tube towards the source.

As a result of the different phase space distributions of the individual hyperfine states after the sextupole of the atomic beam source the initial conditions are different, and so are the results of the simulations for the different states. The values in the table always refer to the state of the atoms inside the sextupole magnet of the source. The average duration of stay is calculated from the average length of the trajectory and the average speed according to

$$T_{\text{res}} = \frac{\bar{s}}{\bar{v}}, \tag{A.7}$$

where the average velocity is given as:

$$\bar{v} = \sqrt{\frac{8kT}{m\pi}}. \tag{A.8}$$

T is the storage cell temperature and m the atomic mass. The following is obtained:

$$\bar{v}_{[\mathrm{m\,s^{-1}}]} = 144,5 \cdot \sqrt{\frac{T_{[\mathrm{K}]}}{M_{[\mathrm{amu}]}}} \tag{A.9}$$

Tab. A.3:
Results of the Monte Carlo simulations for the test storage cells. The simulation program was used to generate 100.000 initial trajectories at the entrance of the injection tube of the storage cell for each state for the sextupole magnet in the atomic beam source (chapter 6), based on the parameterization (9.1). Only those atoms that also leave the cell again through the exit tube towards the polarimeter were taken into consideration. The values for duration of stay and flight time still must be multiplied by the factor $\sqrt{M_{[\mathrm{amu}]}/T_{[\mathrm{K}]}}$.

large storage cell with 60 mm exit tube					
state		$\|1\rangle$	$\|2\rangle$	$\|3\rangle$	$\|4\rangle$
avg. number of collisions $\bar{c}$		3505(14)	3534(14)	3547(16)	3526(15)
avg. length of trajectory $\bar{s}$	[m]	100.36(41)	101.19(42)	101.29(47)	100.82(44)
avg. duration of stay T_{res}	$[\mathrm{ms} \cdot \sqrt{T/M}]$	694.5(28)	700.3(29)	701.0(32)	697.7(30)
avg. flight time τ_F	$[\mu\mathrm{s} \cdot \sqrt{T/M}]$	198.1(11)	198.2(11)	197.6(13)	197.9(12)
inj. tube collisions	[%]	3.72	3.73	4.06	3.87
transmission σ_i^{cell}	[%]	57.96(24)	58.60(24)	45.59(21)	51.06(23)
small storage cell with 30 mm exit tube					
state		$\|1\rangle$	$\|2\rangle$	$\|3\rangle$	$\|4\rangle$
avg. number of collisions $\bar{c}$		1456(6)	1453(6)	1471(6)	1456(6)
avg. length of trajectory $\bar{s}$	[m]	34.20(13)	34.16(12)	34.37(15)	34.11(14)
avg. duration of stay T_{res}	$[\mathrm{ms} \cdot \sqrt{T/M}]$	236.7(9)	236.4(8)	237.9(10)	236.1(10)
avg. flight time τ_F	$[\mu\mathrm{s} \cdot \sqrt{T/M}]$	162.6(9)	162.7(9)	161.7(9)	162.2(10)
inj. tube collisions	[%]	6.35	6.27	7.05	6.72
transmission σ_i^{cell}	[%]	66,81(26)	67.08(26)	52.42(23)	58.47(24)

Tab. A.4:
Results of the Monte Carlo simulations of the storage cell of the FILTEX test experiment at the TSR. 1.600.000 atoms were injected into the cell along the axis of the cell entry tube. The values for the duration of stay and the flight time must still be multiplied by a factor of $\sqrt{M_{[\mathrm{amu}]}/T_{[\mathrm{K}]}}$. **I** is the entry opening of the injection tube, **A** the exit opening of the beam tube in figure A.2 top and **B** bottom.

exit		**all**	**I**	**A**	**B**
avg. number of collisions $\bar{c}$		211.6(1)	195.2(2)	217.5(2)	221.9(2)
avg. length of trajectory $\bar{s}$	[m]	2.395(2)	2.177(3)	2.479(3)	2.528(3)
avg. duration of stay T_{res}	$[\mathrm{ms} \cdot \sqrt{T/M}]$	16.57(1)	15.07(2)	17.16(2)	17.49(2)
avg. flight time τ_F	$[\mu\mathrm{s} \cdot \sqrt{T/M}]$	78.31(6)	77.20(13)	78.89(12)	78.82(11)
relative fraction	[%]	100.0	33.0	34.1	32.9
C'/C'_{total}	[%]	100.0	31.6	34.2	34.2

The average flight time between two wall collisions is obtained from the average duration of stay and the average number of wall collisions.

$$\tau_F = \frac{T_{\mathrm{res}}}{\bar{c}}. \tag{A.10}$$

The tables A.4 and A.5 list the results of the simulation program for the two target storage cells, whose relaxation behaviour was examined in chapter 14. Instead all atoms were injected into

Tab. A.5:
Results of the Monte Carlo simulations of the storage cell of the HERMES experiment. 1.000.000 atoms were injected into the cell along the axis of the injection tube. The values for the duration of stay and the flight time must still be multiplied by a factor of $\sqrt{M_{[\mathrm{amu}]}/T_{[\mathrm{K}]}}$. **I** is the entry opening of the injection tube, **P** the exit of the exit tube and **A** and **B** are the openings of the beam tube.

exit			all	I	P	A	B
collisions	$\bar{c}$		308.8(3)	253.9(6)	380.5(16)	319.3(4)	319.6(4)
trajectory	$\bar{s}$	[m]	4.129(3)	3.252(7)	3.450(19)	4.366(5)	4.370(5)
duration of stay	T_{res}	$[\mathrm{ms} \cdot \sqrt{T/M}]$	28.57(2)	22.51(4)	23.88(13)	30.21(3)	30.24(3)
flight time	τ_F	$[\mu\mathrm{s} \cdot \sqrt{T/M}]$	92.52(11)	88.66(26)	62.76(43)	94.61(15)	94.62(15)
relative fraction		[%]	100.0	19.0	2.91	39.1	38.9
C'/C'_{gesamt}		[%]	100.0	19.4	2.58	39.0	39.0

the cells along the axis of the injection tube. In the case of the storage cell for the FILTEX test experiment a transmission correction of the form used for the test storage cells (chapter 9.5) would not make sense. Instead, the influence of the different phase space distributions of the hyperfine states at injection onto their contribution to the density along the beam tube must be included as a correction to the initial occupancy. This is of course also true for the target polarization of the HERMES storage cell. The initial polarization of the test beam analysed by the Breit-Rabi polarimeter is given by equation (9.3). In the case of deuterium however it would be necessary to determine the cell transmissions $\sigma_{ij}^{\mathrm{cell}}$ for a total of 15 different sextupole transmissions (see appendix D.4). Due to the large necessary expenditure this was not done.

The key parameters in the tables A.4 and A.5 were differentiated by the opening through which the atoms leave the storage cell. For the HERMES storage cell there are significant differences in this regard, as the tubes are different in their geometry. Furthermore, the relative fraction of atoms was determined that leave the cell through a certain opening. This value can, in turn, be compared to the contribution of the conductance of the concerned tube to the total conductance (appendix A.2). These values are also listed and serve for the checking of the simulation results. Here it must be taken into account, that the lengths of the injection and exit tubes are given with respect to the axis of the beam tube (figure A.2). The calculation of the conductances for these lengths is therefore not exactly correct. As a result of the tilted injection tube of the FILTEX storage cell (figure A.2) and the assumed injection mode of the simulation a small asymmetry between the two halves of the beam tube is observed.

B Estimation of Gas Fluxes in the Breit-Rabi Polarimeter

B.1 Generation of Molecular Beams in Cylindrical Tubes

In the following some approximations are collected that can be used to estimate the intensities of molecular beams that have been generated in cylindrical tubes. For a more exact theoretical treatment of intensity distributions [147, 148] may be referred to.

The gas flux from a cylindrical tube into a certain spatial angle $\Delta\Omega$ can be approximated as

$$Q\,(\vartheta) = Q_0 \frac{\Delta\Omega}{\Omega} \cos^n \vartheta \tag{B.1}$$

ϑ is the angle with respect to the tube axis and Ω contains the normalization. Q_0 is the total gas flux from the tube, which is determined from the pressure difference Δp between the high and the low pressure end of the tube and it's conductance value C:

$$Q_0 = \Delta p \cdot C. \tag{B.2}$$

The calculation of conductance values was treated in appendix A.2. The tube changes the $\cos\vartheta$ distribution that otherwise is typical for effusive flows from holes or desorption from surfaces. The intensity on the beam or tube axis is increased and the intensity for large angles is largely reduced. This effect is included in the exponent n of the $\cos\vartheta$-distribution. n depends on the Klausing-factor κ for the tube, which is calculated from the inner radius r and the length L of the tube as follows:

$$\kappa = \frac{1}{\frac{\gamma}{3} + 2\gamma u} \tag{B.3}$$

$$u = \frac{1}{4\gamma} + \frac{1}{6\gamma^3}\left(1 - \sqrt{1+\gamma^2}^3\right) \tag{B.4}$$

$$\gamma = \frac{2r}{L}. \tag{B.5}$$

For $L \gg r$ κ may be approximated as

$$\kappa = \frac{3}{\gamma} = \frac{3L}{2r} \tag{B.6}$$

The effective total opening angle Ω and the exponent n are given as

$$\Omega = \frac{4\pi}{\kappa + 2} \qquad\qquad n = \frac{\kappa + 2}{2} - 1. \tag{B.7}$$

For $L = 0$ is also $\kappa = 0$ and thus $\Omega = 2\pi$. The intensity increase on the beam axis generated by the tube is described by the so-called *peaking factor* f which also may be calculated from the Klausing factor:

$$f = \frac{\pi}{\Omega} = \frac{\kappa + 2}{4} = \frac{n+1}{2}. \tag{B.8}$$

For long tubes ($L \gg r$) the length of the tube to a first order approximation enters linearly into both the peaking factor and the conductance (table A.1). This means that the length of the tube has only a small effect on the intensity on the beam axis, while it increases quadratically with the tube radius.

The molecular and atomic beams in the Breit-Rabi polarimeter are detected by a mass spectrometer that is sensitive to the density or the partial pressure for the concerned gas species.

Therefore all gas flows must be converted into an equivalent beam pressure to arrive at a parameter that is proportional to the measured counting rate. This parameter p_{ABD} is obtained by using the relation

$$p_{\mathrm{ABD}} = \frac{Q}{\bar{v} F_{\mathrm{ABD}}} \tag{B.9}$$

F_{ABD} is the sensitive area in the ion formation volume of the mass spectrometer. However, this does not have to be known for the beam pressure calculation; it also enters into the spatial angle $\Delta\Omega$ and thus cancels out.

B.2 Pressure Distribution in the Breit-Rabi Polarimeter

Tab. B.1:
Pressures in the Breit-Rabi polarimeter, all values in mbar. Both the lowest and highest pressure readout during the measurements are listed. $p^{\mathrm{H_2}}_{\mathrm{HFT}}$ is the pressure in the volume with the high frequency transitions, $p^{\mathrm{H_2}}_{\mathrm{6-Pol}}$ is the pressure in the volume with the sextupole magnets and $p^{\mathrm{H_2}}_{\mathrm{Det}}$ is the pressure in the detector chamber (figure4.2). The upper index $\mathrm{H_2}$ indicates, that the cell is not on the axis of the atomic beam and the beam goes directly from the source into the polarimeter (figure 8.1).

	without gas		with gas				
			with cell			direct beam	
	min.	max.	min.	typical	max.	min.	max.
$p^{\mathrm{H_2}}_{\mathrm{HFT}}$	$2.6 \cdot 10^{-8}$	$1.0 \cdot 10^{-6}$	$6.2 \cdot 10^{-8}$	$2 \cdot 10^{-7}$	$3.3 \cdot 10^{-6}$	$7.9 \cdot 10^{-8}$	$1.4 \cdot 10^{-6}$
$p^{\mathrm{H_2}}_{\mathrm{6-Pol}}$	$8.7 \cdot 10^{-10}$	$3.4 \cdot 10^{-9}$	$1.8 \cdot 10^{-9}$	$5 \cdot 10^{-9}$	$1.9 \cdot 10^{-8}$	$2.3 \cdot 10^{-9}$	$1.2 \cdot 10^{-8}$
$p^{\mathrm{H_2}}_{\mathrm{Det}}$	$6.3 \cdot 10^{-11}$	$1.7 \cdot 10^{-9}$	$3.1 \cdot 10^{-10}$	$8 \cdot 10^{-10}$	$4.3 \cdot 10^{-9}$	$4.0 \cdot 10^{-9}$	$3.5 \cdot 10^{-8}$

The pressure values listed in table B.1 give a rough overview of the vacuum in the Breit-Rabi polarimeter, as seen during the measurements. Higher pressures above 10^{-9} mbar inside the detector chamber were only seen directly after measurements with the direct beam from the atomic beam source. After the cell was moved back into the beam it took a few minutes before the typical pressure for measurements with storage cells of $8 \cdot 10^{-10}$ mbar was reached again.

The pressure inside the sextupole chamber is of particular importance. The pressure in this chamber as well as in the connection pipe between sextupole and detector chamber (see figure 4.2) produces a beam of molecular hydrogen or deuterium. This molecular beam hits the sensitive area of the atomic beam detector like the beam from the storage cell and by dissociative ionization produces a background signal in the detection of the atomic beam. This background cannot be suppressed by using the chopper, because the molecular beam is being chopped as well.

The pressure in the sextupole chamber can be explained very well by the gas load from the HFT-chamber. The first sextupole magnet of the polarimeter, which in addition also functions as a conductance limiter between the two chambers, has at room temperature ($\approx 300\,\mathrm{K}$) a conductance of about $70\,\mathrm{l\,s^{-1}}$ for molecular hydrogen. From the typical pressure for the HFT-chamber in table B.1 according to (B.2) a gas load of $1.4 \cdot 10^{-5}\,\mathrm{mbar\,l\,s^{-1}}$ may be calculated for the sextupole chamber. For an effective evacuation power of $S_{\mathrm{eff}} = 2000\,\mathrm{l\,s^{-1}}$ it follows from

$$p = \frac{Q}{S_{\mathrm{eff}}} \tag{B.10}$$

that the pressure is about $p^{\mathrm{H_2}}_{\mathrm{6-Pol}} = 7 \cdot 10^{-9}$ mbar, in good agreement with the value in table B.1.

B.3 Gas Fluxes from the Storage Cells

Also the beam from the storage cell leads to a gas ballast in the sextupole chamber. It can be estimated from the partial pressure of hydrogen in the storage cell (table B.2) together with the relation (B.1), where the spatial angle of the first sextupole magnet relative to the cell exit tube is assumed to be the target. Assuming a degree of dissociation of 50 % inside the storage cell and considering both the atomic and the molecular fraction in the beam, fluxes between $6 \cdot 10^{-9}$ and $5 \cdot 10^{-8}$ mbar l s^{-1} are obtained.

Therefore the beam from the cell contributes only about 0.35 % to the gas load in the sextupole chamber of the polarimeter. From this it can be deduced that the background in the measured beam signal caused by the rest gas pressure in this chamber hardly depends on the switching state of the high frequency transitions. This is an important precondition for the fit described in chapter 11 using a background signal that is constant over the duration of the measurement.

The flux of molecular hydrogen from the sextupole chamber into the atomic beam detector caused by the about 210 mm long connection tube with a diameter of 35 mm between sextupole chamber and detector chamber can also be estimated using the relation (B.1). For the typical pressure of $5(1) \cdot 10^{-9}$ mbar in table B.1 the flux of molecular hydrogen into the ion formation volume of the mass spectrometer of becomes $4.5(9) \cdot 10^{-9}$ mbar l s^{-1}. The sensitive area of 25 mm^2 is about 60 mm away from the end of the connection tube between both chambers. The temperature of the tube was assumed to be 300 K. Due to the smaller conductance value for deuterium also the flux of $3.2(7) \cdot 10^{-9}$ mbar l s^{-1} is smaller. Assuming a probability of 3.0(5) % [149] for the dissociative ionization of molecular hydrogen or deuterium in the formation volume, according to (B.9) the equivalent beam pressure becomes

$$p_{\mathrm{diss}}^{\mathrm{H}_1^+/\mathrm{D}_1^+} = 3,1(9) \cdot 10^{-12}\,\mathrm{mbar} \tag{B.11}$$

both for hydrogen as well as for deuterium. This value is to be compared with the beam pressures that are to be expected from the atomic beam from the storage cell into the atomic beam detector. These are estimated individually on the basis of the calculations presented in appendices A.2 and B.1 for the measurements with differently coated test storage cells . The results are collected in table B.2. As starting values for these estimates the gas fluxes that are injected into the cell $\dot{n}_{\mathrm{inj}}$ are used that are obtained from the fit of the relaxation model to the results of the polarization measurements (table 11.1). The fluxes in units of mbar l s^{-1} are converted into s^{-1}, and pressures into densities, by the expressions

$$\begin{aligned} Q_{[\mathrm{mbar\,l\,s^{-1}}]} &= 10 \cdot kT \cdot \dot{n}_{[\mathrm{s^{-1}}]} && \text{(B.12)} \\ p_{[\mathrm{mbar}]} &= 10^4 \cdot kT \cdot n_{[\mathrm{cm^{-3}}]} && \text{(B.13)} \end{aligned}$$

The estimation furthermore assumes that no occupation transfers occur inside the storage cell and that always two hyperfine states (three for deuterium) are transmitted through the sextupole system of the polarimeter with the probability σ_1. For hydrogen this assumption is justified, as can be seen by comparing the measured results to the beam signal for the case that both the WFT 1-3 in the source and the MFT 1-3 in the polarimeter are active. In this case the relaxation rate for strong holding fields in the storage cell is the lowest. For deuterium the *fast* spin exchange reactions (3.24) and (3.25) cause hyperfine occupation transfers even in strong holding fields. These were not considered in the estimate for the beam signal, which at least partially accounts for the discrepancy between the expected and the measured background to signal ratio (U/S_{total}) for deuterium. A comparison between hydrogen and deuterium on the other hand already reveals inconsistencies between the expected beam signals from the fit ($\dot{n}_{\mathrm{inj}}$ and $p^{\mathrm{D}_1}_{\mathrm{ABD}}$) and the actually measured signals ($S^{\mathrm{H}_1/\mathrm{D}_1}_{\mathrm{cell}}$). This indicates the order of magnitude of the systematic error of the fit.

Table B.2 furthermore contains an estimate of the fluxes of molecular hydrogen from the storage cells into the atomic beam detector. The degree of dissociation inside the cell is assumed to be $\alpha = 50(10)\,\%$. It is defined as

$$\alpha = \frac{n^{\mathrm{H}_1}}{2n^{\mathrm{H}_2} + n^{\mathrm{H}_1}} \tag{B.14}$$

As can be seen from the table, the background contributions of the cell are negligible compared to the contributions from the sextupole chamber of the polarimeter. For deuterium they vanish completely, because a beam block was installed in the first sextupole magnet of the polarimeter.

The background to signal ratios are taken from the correction counting rates from the fit (table 11.1) and from the measured beam counting rates for the strongest measured holding field of 750 mT. For hydrogen the counting rate for active high frequency transitions WFT 1-3 and MFT 1-3 is used, for deuterium the counting rate for the case that the SFT 2-6 is activated in both the source and the polarimeter.

The expected background to signal ratios for hydrogen in part agree within the error bars, for measurements with teflon they differ by about three standard deviations. The deuterium measurements show the largest discrepancies, as was already discussed previously. However, it must be taken into account, that the values in table B.2 are estimates of absolute fluxes that are not as stable as the flux ratios during the measurements that are needed for the polarization measurements. Furthermore, the errors for the injected fluxes do not include systematic uncertainties.

Despite the existing discrepancies between expected and measured background to signal ratios the results are sufficient to justify the background correction to the measured beam signals from chapter 11. It is without question that in future measurements with the Breit-Rabi polarimeter the contributions from molecular beams must be included in the measurements. This is possible through the measurement of the counting rates for the masses of 2 (4 for deuterium) and 18 (H_2O). The relative probabilities for the dissociative recombination, that are needed for the correction, can be measured for every setting of the mass spectrometer, in the way that is illustrated in figure 12.2.

Tab. B.2:
Estimate of the gas fluxes of hydrogen and deuterium from the storage cells into the atomic beam detector (ABD) and comparison to the unpolarized background in the chopped beam caused by molecular beam generation in the differential pumping system of the Breit-Rabi polarimeter. $\dot{n}_{\mathrm{inj}}$ and Q_{inj} are the flux of hydrogen or deuterium that is injected from the atomic beam source into the storage cell, the values for $\dot{n}_{\mathrm{inj}}$ were taken from table 11.1. C_{total} is the total conductance of injection and exit tube of the storage cell. From flux and conductance it is possible to calculated the density (ρ_{cell}) and the partial pressure (p_{cell}) according to (A.1). From the density and the conductance of the exit tube C_{out} follow the fluxes through the exit tube Q_{out} and $\dot{n}_{\mathrm{out}}$. κ, n, f and Ω are explained in the text (appendix B.1), $\Delta\Omega_{\mathrm{sextupole}}$ is the spatial opening angle of the first sextupole magnet in the polarimeter with respect to the exit tube. σ_1 is the transmission through the sextupole system for the state $|1\rangle$. Q_{ABD} and $\dot{n}_{\mathrm{ABD}}$ give the flux into the atomic beam detector, p_{ABD} is the resulting beam pressure according to (B.9). For the deuterium measurement he reduction of the D_1-fluxes by $30\,\%$ due to the beam block was taken into account. For the estimate of the background contributions from molecular beams from the cell a degree of dissociation of $\alpha = 0,5(1)$ was assumed inside the cell. For the calculation of the induced atomic beam signal also the probability for the dissociative ionization of molecular hydrogen of $3.0(5)\,\%$ [149] must be considered. Finally, the expected and according to table 11.1 fitted background to signal ratios (U/S) are listed as well.

		Hydrogen				**Deuterium**
Surface		Aluminum	Drifilm	Teflon	Teflon	Teflon
Number of Collisions		3505(14)	3505(14)	3505(14)	1456(6)	3505(14)
Temperature	[K]	90(5)	101(5)	95(5)	90(5)	110(5)
$\dot{n}_{\mathrm{inj}}$	$[10^{14}\,\mathrm{s}^{-1}]$	2.30(50)	3.24(4)	10.13(17)	13.09(16)	20.2(8)
Q_{inj}	$[10^{-6}\,\mathrm{mbar\,l\,s}^{-1}]$	2.86(64)	4.52(23)	13.29(73)	16.27(93)	30.7(19)
C_{total}	$[\mathrm{l\,s}^{-1}]$	4.65(7)	4.81(7)	4.72(7)	6.58(13)	3.48(3)
ρ_{cell}	$[10^{10}\,\mathrm{cm}^{-3}]$	5.0(11)	6.74(13)	21.5(5)	19.9(5)	58.1(24)
p_{cell}	$[10^{-7}\,\mathrm{mbar}]$	6.2(14)	9.4(5)	28.2(16)	24.7(15)	88.2(55)
C_{out}	$[\mathrm{l\,s}^{-1}]$	2.61(7)	2.77(7)	2.68(7)	4.54(13)	2.04(5)
Q_{out}	$[10^{-6}\,\mathrm{mbar\,l\,s}^{-1}]$	1.62(37)	2.60(16)	7.57(49)	11.2(8)	18.0(12)
$\dot{n}_{\mathrm{out}}$	$[10^{14}\,\mathrm{s}^{-1}]$	1.30(29)	1.87(6)	5.77(20)	9.02(33)	11.86(56)
κ		23.68			12.48	23.68
n		11.84			6.24	11.84
f		6.42			3.62	6.42
Ω		0.489			0.868	0.489
$\Delta\Omega_{\mathrm{sextupole}}$	$[10^{-3}\,\mathrm{sr}]$	1.99			1.99	1.99
σ_1	[%]	16.6(6)	17.8(6)	17.2(6)	16.8(6)	13.0(4)
$Q_{\mathrm{ABD}}^{\mathrm{H_1/D_1}}$	$[10^{-10}\,\mathrm{mbar\,l\,s}^{-1}]$	5.5(13)	9.40(66)	26.4(19)	21.6(17)	47.4(35)
$\dot{n}_{\mathrm{ABD}}^{\mathrm{H_1/D_1}}$	$[10^{10}\,\mathrm{s}^{-1}]$	4.4(10)	6.74(31)	20.2(10)	17.4(9)	31.2(18)
$p_{\mathrm{ABD}}^{\mathrm{H_1/D_1}}$	$[10^{-11}\,\mathrm{mbar}]$	1.62(39)	2.63(20)	7.62(58)	6.39(53)	17.9(13)
$Q_{\mathrm{ABD}}^{\mathrm{H_2/D_2}}$	$[10^{-11}\,\mathrm{mbar\,l\,s}^{-1}]$	2.38(72)	3.82(80)	11.1(23)	9.5(20)	—
$\dot{n}_{\mathrm{ABD}}^{\mathrm{H_2/D_2}}$	$[10^{9}\,\mathrm{s}^{-1}]$	1.91(57)	2.74(56)	8.5(17)	7.6(15)	—
$p_{\mathrm{ABD}}^{\mathrm{H_2/D_2}}$	$[10^{-12}\,\mathrm{mbar}]$	1.00(30)	1.51(32)	4.53(95)	3.97(84)	—
U/S_{cell}	[%]	0.185(76)	0.172(48)	0.178(50)	0.186(52)	—
U/S_{restgas}	[%]	19.1(72)	11.8(35)	4.1(12)	4.9(15)	1.73(52)
$U/S_{\mathrm{total}}^{\mathrm{expected}}$	[%]	19.3(72)	12.0(35)	4.3(12)	5.1(15)	1.73(52)
$S_{\mathrm{cell}}^{\mathrm{H_1/D_1}}$	[kHz]	11.195(57)	31.662(35)	43.19(15)	40.02(14)	6.041(65)
$S_{\mathrm{corr.}}^{\mathrm{H_1/D_1}}$	[kHz]	1.441(28)	2.850(39)	3.449(56)	3.959(50)	0.679(34)
$U/S_{\mathrm{total}}^{\mathrm{Fit}}$	[%]	12.87(26)	9.00(12)	7.99(13)	9.89(13)	11.24(58)

C Alternative Analysis of the Relaxation Measurements

As an alternative to the analysis in chapter 11, where the results of the polarization measurement were fitted to the theory through the correction for molecular background in the beam (chapter 11.4), an analysis without this correction was carried out and the initial occupancy was fitted later. The results of this alternative analysis are collected in table C.1.

On the one hand the results of this fit demonstrate that the parameters of the relaxation model in comparison to those in table 11.1 do not depend significantly on whether a correction

Tab. C.1:
Compilation of the fit parameters for the alternative fit. In the upper part the parameters relating to the relaxation are listed. The wall collision relaxation is parameterized by τ_C and C (3.6). The flux $\dot{n}$ determines the density inside the cell and affects the spin exchange collision rate. In the second and third part the hyperfine occupancies after the sextupole of the source and the efficiencies of the high frequency transitions are listed. They determine the initial occupancies and were fitted as well. The fourth part lists the resulting initial polarization values for 750 mT. For comparison the fifth and sixth parts give the values for the initial occupancy and polarization that are based on the sextupole transmissions (chapter 9.5 and 9.7) and the measured efficiencies from chapter 8.7. Systematic uncertainties are not included.

	Hydrogen				**Deuterium**	
Surface	Aluminum	Drifilm	Teflon	Teflon	Teflon	
Collisions	3505(14)	3505(14)	3505(14)	1456(6)	3505(14)	
Temperature [K]	90(5)	101(5)	95(5)	90(5)	110(5)	
χ^2	0.67	3.12	5.66	4.78	1.31	
τ_c $[10^{-12}\,\mathrm{s}]$	4.65(46)	5.58(29)	4.83(12)	5.60(29)	$1.58(21) \cdot 10^2$	
C $[\mathrm{s}^{-1}]$	88.1(21)	2.72(6)	22.4(2)	7.90(19)	12.7(6)	
$\dot{n}$ $[10^{14}\,\mathrm{s}^{-1}]$	1.61(56)	3.25(5)	10.23(19)	12.50(18)	21.2(8)	
n_1 [%]	42.06(28)	44.18(7)	43.78(13)	43.93(7)	32.40(25)	
n_2 [%]	43.24(29)	44.12(8)	45.32(14)	44.32(8)	34.19(26)	
n_3 [%]	6.11(29)	5.64(7)	4.25(14)	5.60(7)	—	
ε_{16} [%]	—	—	—	—	97.52(224)	
ε_{26} [%]	—	—	—	—	86.74(74)	
ε_{35} [%]	—	—	—	—	84.66(109)	
Transition	WFT 1-3	WFT 1-3	WFT 1-3	WFT 1-3	SFT 2-6	SFT 3-5
P_e w/o HFT	0.705(7)	0.765(2)	0.781(3)	0.764(2)	1	1
P_z	−0.702(8)	−0.761(5)	−0.777(6)	−0.760(5)	0.286(5)	0.273(5)
P_{zz}	—	—	—	—	0.864(9)	−0.874(11)
n_1 [%]	47.27(43)			47.44(43)	33.33	
n_2 [%]	48.01(44)			47.84(43)	33.33	
n_3 [%]	1.77(5)			1.77(5)	33.33	
n_4 [%]	2.95(7)			2.94(7)	—	
Transition	WFT 1-3			WFT 1-3	SFT 2-6	SFT 3-5
P_e w/o HFT	0.905(6)			0.905(6)	1	1
P_z	−0.900(8)			−0.900(8)	0.329(6)	0.329(6)
P_{zz}	—			—	0.986(14)	−0.987(14)

is fitted to the polarization measurement or to the initial occupancy. On the other hand, they show that at least in the present case it is possible to perform a fit for all parameters of the atomic beam source that are relevant for the initial occupancy, despite their large number. This allows the indirect measurement of the polarization of the atomic beam that is injected into the cell. However, this measurement is model dependent, because assumptions about the relaxation inside the storage cell enter into it. At the transition from one fit to the other mainly only the scale of the polarization in the figures in chapter 12 is changed. This was shown in figure 11.2, where the left side was produced using the parameters from table C.1. This fit however leads to a series of inconsistencies, which finally can only be resolved by the assumption of a molecular background in the detected beam. This was also the reason why the other analysis was preferred. The inconsistencies include an initial value for the nuclear polarization that is about 0.07 lower for the measurement with the ice coated aluminum cell compared to the other cells (table C.1), as well as the drop of nuclear and electron polarization with increasing cell temperature (figure 12.12). The high degree of reliability of the simulation programs that has been shown in comparisons to the measured data (figure 9.3) makes it improbable that the fitted initial occupancy for hydrogen in table C.1 is correct. As can be seen from figure C.1, the nozzle temperature would have to be above 400 K to explain the fitted initial polarization. The shown results for the initial polarization correspond to the left picture in figure 9.8. The horizontal line marks the fitted initial polarization for the teflon cell with 3505 wall collisions according to table C.1, the vertical line indicates the current in the sextupole magnet of the source. Even for a nozzle temperature of 400 K the simulation calculations are not consistent with the fit results. Additionally it should be noted, that the correction due to the different cell transmissions (9.3), which increase the initial polarization by another 2 %, are not yet included in this figure.

Although the results from this fit in part contradict the simulation calculations for the determination of the initial occupancy, it is worth to have a closer look at the results, because they also show agreement with the expectations in several points.

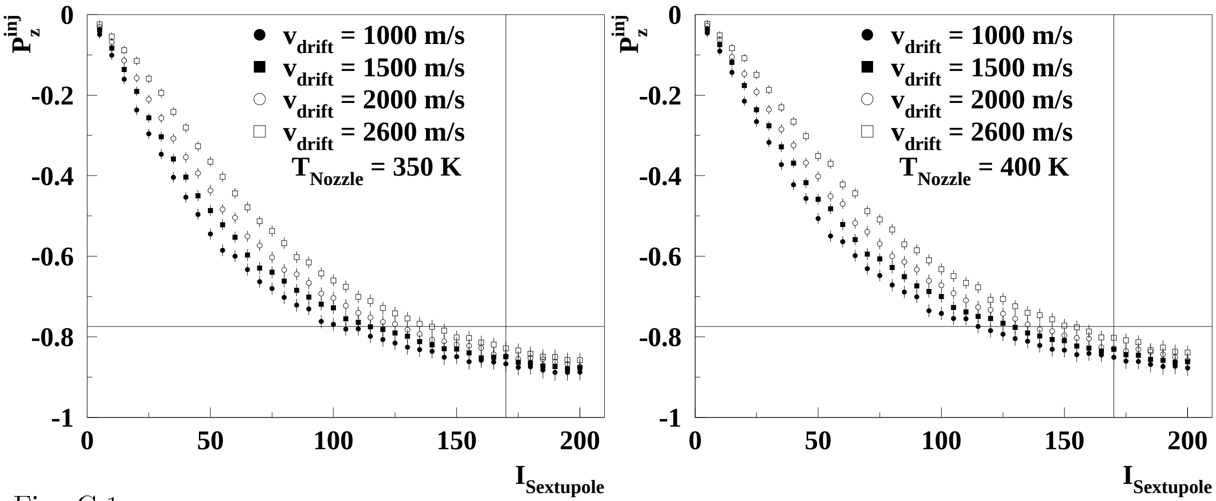

Fig. C.1:
Nuclear polarization of the atomic beam that is injected into the cell at the entry opening of the cell injection tube as a function of the source sextupole current at higher nozzle temperatures. For the calculation of the polarization from the hyperfine occupancies a field of 750 mT in the storage cell was assumed. The vertical line indicates the sextupole current, that was set during the polarization measurements, the horizontal one marks the initial polarization that must be expected according to the fit results in table C.1. For K_{mol} a value of 0.4 was assumed. The beam temperature was calculated from the drift velocity according to (6.19) using the approximation $v_{\text{rms}} \approx v_{\text{drift}}$. On the left side a nozzle temperature of 350 K, on the right side one of 400 K was assumed.

The fit of the initial occupancy contradicts the assumption that the efficiency of the WFT 1-3 is affected as a result of the high transmitted beam velocities in the sextupole magnet of the source (figure 9.9). If the efficiency of this transition is treated as a free parameter, a value of 100 % follows for all measurements, with a maximal deviation of 0.5 %. This agrees within the errors with the measured value in table 8.1. Therefore the efficiency of this high frequency transition was not listed in table C.1.

An effect on the efficiencies due to high beam velocities is more probable for the strong field transitions for deuterium than for WFT 1-3. This is supported by the results in table C.1. The fitted efficiencies differ significantly from the measured data in table 8.2.

During the deuterium measurements a beam block was installed in the sextupole magnet of the source. Therefore for the hyperfine occupancies in the atomic beam an ideal occupancy behind the sextupole magnet in the source of $n_1 = n_2 = n_3 = 1/3$ may be assumed. This assumption is supported by the fit, as can be seen in table C.1.

The results for the deuterium measurement indicate that in this case the measured polarization may at least in part be explained by a correction to the initial occupancy. However, it is still not clear in how far a molecular background in the beam is responsible for the polarization being smaller than expected.

D Initial Polarizations for Target Storage Cells

In this part of the appendix the hyperfine occupancies are calculated that are injected into the target storage cells by the respective atomic beam source of the FILTEX test experiment and the HERMES experiment. These are used in chapter 14 as realistic initial occupancies for the examination of the relaxation behaviour in the concerned storage cells. For the determination of the needed transmission probabilities the simulation program from chapter 6 is used. The transmission corrections for the storage cells (9.3) are in general only included as approximations. The atoms are only counted as transmitted, if they have passed one half of the injection tube without wall collisions.

D.1 Sextupole Systems in the Atomic Beam Source

The dimensions of the concerned sextupole systems for the FILTEX test experiment and the HERMES experiment are listed in table D.1. A simulation calculation for the two sextupole systems for the hydrogen state $|1\rangle$ can be seen in figure D.1.

Both systems consist of two parts in the sense that between third and forth sextupole magnet a high frequency transition is placed, which transfers the occupancy of one of the hyperfine states focused in the first part of the beam, so that it can be removed from the beam in the second part of the system. Only in the HERMES system for hydrogen no occupation transfers take place between the sextupole magnets.

Already W. Korsch reported a significant effect of the character of the flow between nozzle and collimator on the transmission properties of a sextupole system [45]. The more molecular the flow, the higher is also the average angular momentum of the trajectories in the sextupole magnets. As a result the focusing forces of the sextupole system are weakened and the transmissions of the focused states drop. The HERMES system reaches a transmission probability of 82.9 % for the hydrogen state $|1\rangle$ in laminar flow, while in molecular flow it is only 58.9 %.

Tab. D.1:
Sextupole system of the atomic beam source for the FILTEX test experiment at the TSR in Heidelberg and the HERMES experiment following [46]. The first sextupole magnet of the HERMES system has an outer radius of 30 mm, in all other cases it is 40 mm. Both systems contain tapered magnets with linearly varying pole tip radius. The variables are: r^i_{pt} and r^f_{pt} pole tip radius at the entry and exit opening, L the length and z_0 the distance between inlet and nozzle. The number of segments is given as well (figure 4.6).

	FILTEX					HERMES				
	r^i_{pt} [mm]	r^f_{pt} [mm]	L [mm]	z_0 [mm]	segm.	r^i_{pt} [mm]	r^f_{pt} [mm]	L [mm]	z_0 [mm]	segm.
Nozzle	1.00	—	—	0	—	1.00	—	—	0	—
Skimmer	2.50	—	—	15	—	2.50	—	—	15	—
Collimator	4.25	—	—	52	—	3.20	—	—	50	—
1. Sextupole	5.40	7.0	34	65	12	4.30	5.2	30	63	12
2. Sextupole	8.00	10.0	83	119	12	6.00	8.0	55	113	12
3. Sextupole	12.50	—	60	425	24	8.35	12.5	75	188	12
4. Sextupole	12.50	—	30	710	24	13.30	—	75	613	24
5. Sextupole	12.50	—	200	945	24	13.30	11.0	85	728	24
Cell	5.00	—	100	1185	—	5.00	—	100	1113	—

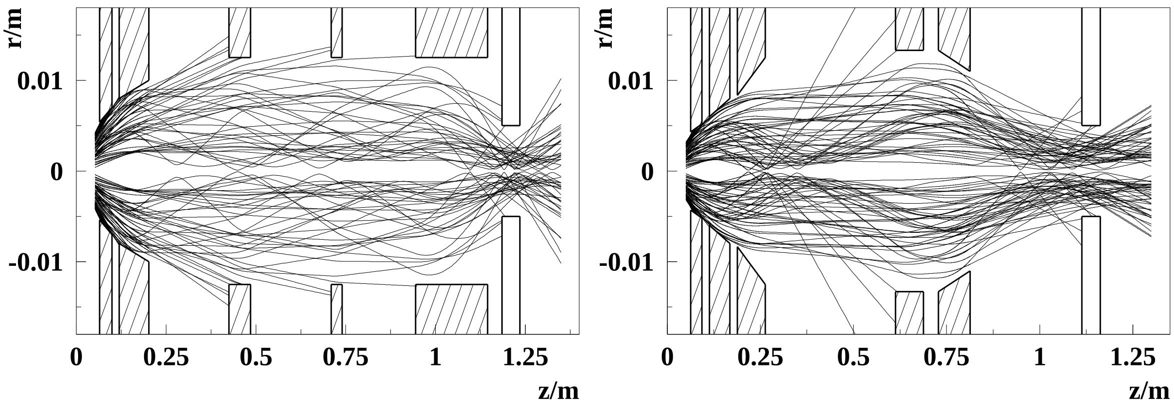

Fig. D.1:
Radial projections of the trajectories for hydrogen atoms in the state $|1\rangle$ in the sextupole systems for the FILTEX test experiment (left) and for the HERMES experiment (right). The nozzle temperature was assumed to be $80\,\mathrm{K}$ and $K_{\mathrm{mol}} = 1$. Drift velocity and beam temperature were calculated according to the parameterization by B. Lorentz (D.1). The sextupoles are shown as hashed beams. The white beams at the end of the system represent half of the cell injection tube, which has to be passed through by the atoms without a wall collision. 2×60 trajectories are shown for each setup.

Despite the significantly increased intensity of an atomic beam source for laminar flow this property is not desirable for the discussed sextupole systems, because the character of the flow also has an enormous effect on the maximal polarization of the atomic beam if an occupation transfer between a focused and a defocused state must happen between the sextupole magnets.

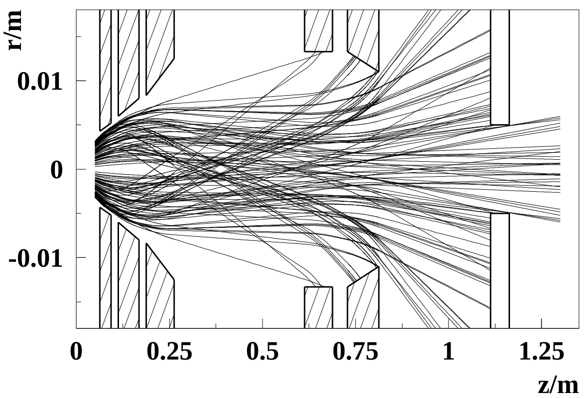

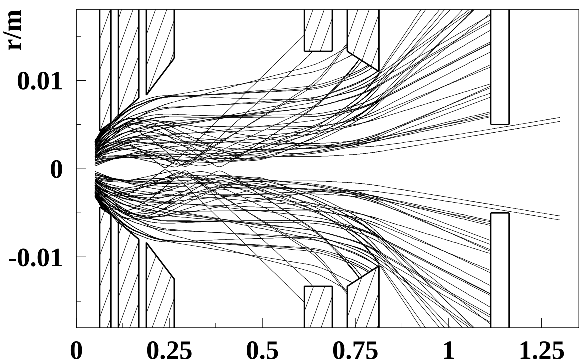

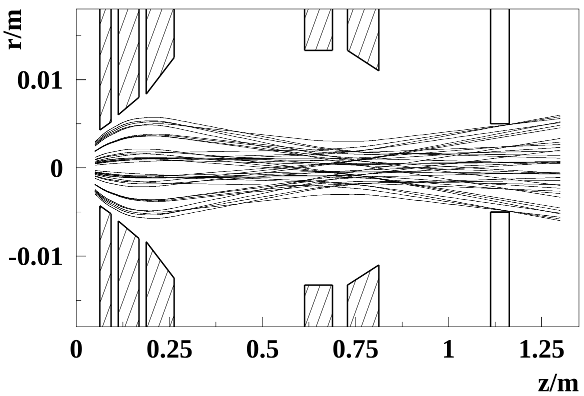

Fig. D.2: z/m
Trajectories for the transmission σ_{34} for deuterium in the sextupole system of the atomic beam source for the HERMES experiment. The sextupoles are shown as hashed beams. The white beams at the end of the system represent half of the cell injection tube, which must be passed through by the atoms without a wall collision. Above 2×60 arbitrary trajectories are shown, below 2×20 that were counted as transmitted. Left: Laminar flow, $K_{\mathrm{mol}} = 0$. Right: Molecular flow, $K_{\mathrm{mol}} = 1$.

This concerns the FILTEX system, in which a SFT 2-4 behind the third sextupole magnet affects an occupation transfer from the state $|\,2\,\rangle$ to $|\,4\,\rangle$, which is removed from the beam in the second part of the sextupole system, so that only the remaining state $|\,1\,\rangle$ is injected into the storage cell. It also concerns all operation states of the source of the HERMES experiment if a polarized deuterium beam is generated. For the polarization of the HERMES hydrogen beam the character of the flow is largely without importance, because hyperfine occupancies in the atomic beam are only transferred after the last sextupole magnet.

The problems that occur in the defocusing of a transferred state in the second part of the HERMES system for laminar flow are illustrated in figure D.2 for the example of the transmission σ_{34} for deuterium. This transmission contributes to all prepared hyperfine occupancies in the generated atomic beam (appendix D.4). Plotted are the radial projections of trajectories for this transmission, left for laminar and right for molecular flow. For laminar flow 24.3 % of the atoms reach the storage cell. It can be seen from the lower picture, which only shows trajectories for atoms that reach the cell, that those are atoms that due to the excellent focusing in the first three sextupoles enter the fourth sextupole with convergent trajectories close to the axis, where the fields, and thus the forces on the atoms, are weak. The two last magnets are able to make the beam divergent again, but the deflection is for a large part of the atoms not strong enough to direct them out of the acceptance of the storage cell.

Under these conditions a vector polarization of only $+0.72$ or -0.74 could be reached. The positive tensor polarization with $+0.98$ would even be particularly high, because an occupation of the state $|\,4\,\rangle$ in this case is not desirable, but nevertheless it contributes positively to the tensor polarization. However, the vector polarization in this case would have a value of $P_z = -0.1$ and not vanish. For negative sign the tensor polarization becomes only $P_{zz} = -1.55$. The situation cannot even be improved by using a beam block in the fourth sextupole magnet, because it would also reduce the intensity of two desired states, so that the quality of the source $(I \cdot P^2)$ would even be reduced.

As a result of the higher average angular momentum for molecular flow hardly any trajectories close to the axes in the sextupoles are seen anymore (see also figure 6.1). The atoms enter the fourth sextupole magnet with a larger distance from the axis and thus can be removed from the beam much more easily. The transmission σ_{34} now only reaches 5.2 %. As was shown by the offline analysis of the relaxation in the storage cell of the FILTEX experiment in chapter 14.1, the flow in the region of the nozzle must be especially molecular ($K_{\mathrm{mol}} > 0.85$). The beam formation using nozzle and skimmer is identical for both systems, so that also for the HERMES system a molecular flow and thus a high degree of polarization may be expected.

In the following the equations necessary for calculating the injected hyperfine occupancies are given. They were derived from the methods described in chapter 7. They represent the basis from which the injected hyperfine occupancy, flux, polarization and quality may be calculated for all modi of operation of both source configurations. The results are compiled into tables in chapter 14. The fluxes are determined from the sums of the contributing transmissions, that are labeled Σ in the tables. Σ is the sum of the non-normalized occupancy numbers in the occupation tuples that are listed in the following. The flux from the atomic beam source for the FILTEX experiment for the injection of two hyperfine states is known to be $\dot{n} = 8.1(2) \cdot 10^{16}\,\mathrm{s}^{-1}$ [46]. Therefore it is possible to relate the fluxes for the HERMES system to this value and calculate them from the values of the product $\Sigma \cdot \Omega$ where Ω is the spatial opening angle of the collimator with respect to the nozzle. In the case of deuterium a factor of 2/3 must also be included, because for hydrogen two out of four and for deuterium two out of six hyperfine states are injected into the storage cell.

For the determination of the needed transmission probabilities a completely laminar flow is assumed and K_{mol} is set to 1. Drift velocity and beam temperatures are calculated according to B. Lorentz from parameterizations of measurements for a gas throughput of $1\,\mathrm{mbar\,l\,s^{-1}}$ in the dissociator [108]. The nozzle temperature is assumed to be 80 K. This leads to the following values:

$$\begin{aligned} v^{\mathrm{H}}_{\mathrm{drift}} &= 1839\,\mathrm{m\,s^{-1}} & T^{\mathrm{H}}_{\mathrm{beam}} &= 23.2\,\mathrm{K} \\ v^{\mathrm{D}}_{\mathrm{drift}} &= 1346\,\mathrm{m\,s^{-1}} & T^{\mathrm{D}}_{\mathrm{beam}} &= 21.4\,\mathrm{K}. \end{aligned} \tag{D.1}$$

For the efficiencies of the used hyperfine states measured data quoted by [46] are used. For the deuterium transition MFT 1-4 normally the three efficiencies ε_{12}, ε_{23} and ε_{34} should be included. However, as these are not known individually, the same value was used for all three. The efficiency of the SFT 2-4 for the FILTEX configuration was determined through the analysis of the relaxation in the storage cell, as described in chapter 14.1. For each transmission 100, 000 trajectories were simulated in the concerned sextupole system. The tapering was approximated as a series of cylindrical magnets with a length of 200 μm.

D.2 Initial Polarization for the FILTEX Test Experiment

1. Nominal Values: $P_z = +0.5$, States $|\,1\,\rangle$ and $|\,2\,\rangle$

Scheme: Sextupole $\longrightarrow$ Sextupole:

$$\begin{pmatrix} \sigma_{11} \\ \sigma_{22} \\ \sigma_{33} \\ \sigma_{44} \end{pmatrix}. \tag{D.2}$$

2. Nominal Values: $P_z = +1$, State $|\,1\,\rangle$

Scheme: Sextupole $\longrightarrow$ SFT 2-4 $\longrightarrow$ Sextupole:

$$\begin{pmatrix} \sigma_{11} \\ (1-\varepsilon_{24})\,\sigma_{22} + \varepsilon_{24}\sigma_{42} \\ \sigma_{33} \\ (1-\varepsilon_{24})\,\sigma_{44} + \varepsilon_{24}\sigma_{24} \end{pmatrix}. \tag{D.3}$$

Transmission Probabilities

$$\begin{aligned} \sigma_{11} &= 4.189(16)\cdot 10^{-1} & \sigma_{33} &= 1.2(3)\cdot 10^{-4} \\ \sigma_{22} &= 4.217(16)\cdot 10^{-1} & \sigma_{42} &= 7.49(27)\cdot 10^{-3} \\ \sigma_{24} &= 4.081(63)\cdot 10^{-2} & \sigma_{44} &= 4.2(6)\cdot 10^{-4}. \end{aligned} \tag{D.4}$$

Efficiency of the High Frequency Transition

According to chapter 14.1:

$$\varepsilon_{24} = 99.5(10)\,\%. \tag{D.5}$$

D.3 Initial Polarization for Hydrogen in the HERMES Target

1. Nominal Values: $P_z = +1$, States $|\,1\,\rangle$ and $|\,4\,\rangle$

Scheme: Sextupole $\longrightarrow$ SFT 2-4:

$$\begin{pmatrix} \sigma_1 \\ (1-\varepsilon_{24})\,\sigma_2 + \varepsilon_{24}\sigma_4 \\ \sigma_3 \\ (1-\varepsilon_{24})\,\sigma_4 + \varepsilon_{24}\sigma_2 \end{pmatrix} . \tag{D.6}$$

2. Nominal Values: $P_z = -1$, States $|\,2\,\rangle$ and $|\,3\,\rangle$

Scheme: Sextupole $\longrightarrow$ WFT 1-3:

$$\begin{pmatrix} (1-\varepsilon_{13})\,\sigma_1 + \varepsilon_{13}\sigma_3 \\ \sigma_2 \\ (1-\varepsilon_{13})\,\sigma_3 + \varepsilon_{13}\sigma_1 \\ \sigma_4 \end{pmatrix} . \tag{D.7}$$

Transmission Probabilities

$$\begin{array}{lcl@{\qquad}lcr} \sigma_1 &=& 5.888(16)\cdot 10^{-1} & \sigma_3 &=& 3.5(6)\cdot 10^{-4} \\ \sigma_2 &=& 6.018(15)\cdot 10^{-1} & \sigma_4 &=& 1.31(11)\cdot 10^{-3}\,. \end{array} \tag{D.8}$$

Efficiencies of the High Frequency Transitions

According to [46]:

$$\begin{array}{lcl} \varepsilon_{24} &=& 98.2(10)\,\% \\ \varepsilon_{13} &=& 98.5(10)\,\%. \end{array} \tag{D.9}$$

D.4 Initial Polarization for Deuterium in the HERMES Target

1. Nominal Values: $P_z = +1$, $P_{zz} = +1$, States $|\,1\,\rangle$ and $|\,6\,\rangle$

Scheme: Sextupole $\longrightarrow$ MFT 3-4 $\longrightarrow$ Sextupole $\longrightarrow$ SFT 2-6:

$$\begin{pmatrix} \sigma_{11} \\ (1-\varepsilon_{26})\,\sigma_{22} + \varepsilon_{26}\sigma_{66} \\ (1-\varepsilon'_{34})\,\sigma_{33} + \varepsilon'_{34}\sigma_{43} \\ (1-\varepsilon'_{34})\,\sigma_{44} + \varepsilon'_{34}\sigma_{34} \\ \sigma_{55} \\ (1-\varepsilon_{26})\,\sigma_{66} + \varepsilon_{26}\sigma_{22} \end{pmatrix} . \tag{D.10}$$

2. Nominal Values: $P_z = -1$, $P_{zz} = +1$, States $|\,3\,\rangle$ and $|\,4\,\rangle$

Scheme: Sextupole $\longrightarrow$ MFT 3-4 $\longrightarrow$ Sextupole $\longrightarrow$ WFT 1-4/2-3:

$$\begin{pmatrix} (1-\varepsilon_{\mathrm{WFT}})\,\sigma_{11} + \varepsilon_{\mathrm{WFT}}\left[(1-\varepsilon'_{34})\,\sigma_{44} + \varepsilon'_{34}\sigma_{34}\right] \\ (1-\varepsilon_{\mathrm{WFT}})\,\sigma_{22} + \varepsilon_{\mathrm{WFT}}\left[(1-\varepsilon'_{34})\,\sigma_{33} + \varepsilon'_{34}\sigma_{43}\right] \\ (1-\varepsilon_{\mathrm{WFT}})\left[(1-\varepsilon'_{34})\,\sigma_{33} + \varepsilon'_{34}\sigma_{43}\right] + \varepsilon_{\mathrm{WFT}}\sigma_{22} \\ (1-\varepsilon_{\mathrm{WFT}})\left[(1-\varepsilon'_{34})\,\sigma_{44} + \varepsilon'_{34}\sigma_{34}\right] + \varepsilon_{\mathrm{WFT}}\sigma_{11} \\ \sigma_{55} \\ \sigma_{66} \end{pmatrix} . \tag{D.11}$$

3. Nominal Values: $P_z = 0$, $P_{zz} = +1$, States $|\,3\,\rangle$ and $|\,6\,\rangle$

Scheme: Sextupole $\longrightarrow$ MFT 1-4 $\longrightarrow$ Sextupole $\longrightarrow$ SFT 2-6:

$$\begin{pmatrix} (1-\varepsilon_{12})\,\sigma_{11} + \varepsilon_{12}\left\{(1-\varepsilon_{23})\,\sigma_{21} + \varepsilon_{23}\left[(1-\varepsilon_{34})\,\sigma_{31} + \varepsilon_{34}\sigma_{41}\right]\right\} \\ (1-\varepsilon_{26})\left\langle(1-\varepsilon_{12})\left\{(1-\varepsilon_{23})\,\sigma_{22} + \varepsilon_{23}\left[(1-\varepsilon_{34})\,\sigma_{32} + \varepsilon_{34}\sigma_{42}\right]\right\} + \varepsilon_{12}\sigma_{12}\right\rangle + \varepsilon_{26}\sigma_{66} \\ (1-\varepsilon_{23})\left[(1-\varepsilon_{34})\,\sigma_{33} + \varepsilon_{34}\sigma_{43}\right] + \varepsilon_{23}\sigma_{23} \\ (1-\varepsilon_{34})\,\sigma_{44} + \varepsilon_{34}\sigma_{34} \\ \sigma_{55} \\ (1-\varepsilon_{26})\,\sigma_{66} + \varepsilon_{26}\left\langle(1-\varepsilon_{12})\left\{(1-\varepsilon_{23})\,\sigma_{22} + \varepsilon_{23}\left[(1-\varepsilon_{34})\,\sigma_{32} + \varepsilon_{34}\sigma_{42}\right]\right\} + \varepsilon_{12}\sigma_{12}\right\rangle \end{pmatrix} . \tag{D.12}$$

4. Nominal Values: $P_z = 0$, $P_{zz} = -2$, States $|\,2\,\rangle$ and $|\,5\,\rangle$

Scheme: Sextupole $\longrightarrow$ MFT 1-4 $\longrightarrow$ Sextupole $\longrightarrow$ SFT 3-5:

$$\begin{pmatrix} (1-\varepsilon_{12})\,\sigma_{11} + \varepsilon_{12}\left\{(1-\varepsilon_{23})\,\sigma_{21} + \varepsilon_{23}\left[(1-\varepsilon_{34})\,\sigma_{31} + \varepsilon_{34}\sigma_{41}\right]\right\} \\ (1-\varepsilon_{12})\left\{(1-\varepsilon_{23})\,\sigma_{22} + \varepsilon_{23}\left[(1-\varepsilon_{34})\,\sigma_{32} + \varepsilon_{34}\sigma_{42}\right]\right\} + \varepsilon_{12}\sigma_{12} \\ (1-\varepsilon_{35})\left\{(1-\varepsilon_{23})\left[(1-\varepsilon_{34})\,\sigma_{33} + \varepsilon_{34}\sigma_{34}\right] + \varepsilon_{23}\sigma_{23}\right\} + \varepsilon_{35}\sigma_{55} \\ (1-\varepsilon_{34})\,\sigma_{44} + \varepsilon_{34}\sigma_{34} \\ (1-\varepsilon_{35})\,\sigma_{55} + \varepsilon_{35}\left\{(1-\varepsilon_{23})\left[(1-\varepsilon_{34})\,\sigma_{33} + \varepsilon_{34}\sigma_{43}\right] + \varepsilon_{23}\sigma_{23}\right\} \\ \sigma_{66} \end{pmatrix} . \tag{D.13}$$

Transmission Probabilities

$$\begin{aligned} \sigma_{11} &= 5.986(16)\cdot 10^{-1} & \sigma_{31} &= 6.005(15)\cdot 10^{-1} & \sigma_{42} &= 1.161(34)\cdot 10^{-2} \\ \sigma_{12} &= 6.003(15)\cdot 10^{-1} & \sigma_{32} &= 5.993(15)\cdot 10^{-1} & \sigma_{43} &= 1.128(33)\cdot 10^{-2} \\ \sigma_{21} &= 6.014(15)\cdot 10^{-1} & \sigma_{33} &= 6.035(15)\cdot 10^{-1} & \sigma_{44} &= 2.6(5)\cdot 10^{-4} \\ \sigma_{22} &= 5.985(16)\cdot 10^{-1} & \sigma_{34} &= 5.185(70)\cdot 10^{-2} & \sigma_{55} &= 6.7(8)\cdot 10^{-4} \\ \sigma_{23} &= 6.027(15)\cdot 10^{-1} & \sigma_{41} &= 1.161(34)\cdot 10^{-2} & \sigma_{66} &= 5.1(7)\cdot 10^{-4} . \end{aligned} \tag{D.14}$$

Efficiencies of the High Frequency Transitions

According to [46]:

$$\begin{aligned} \varepsilon_{26} &= 99.2(10)\,\% \\ \varepsilon_{35} &= 100.0(10)\,\% \\ \varepsilon_{\mathrm{WFT}} &= 100.0(10)\,\% \\ \varepsilon'_{34} &= 98.5(10)\,\% \\ \varepsilon_{12} = \varepsilon_{23} = \varepsilon_{34} &= 98.5(10)\,\% . \end{aligned} \tag{D.15}$$

E Coefficient Matrices for Polarization Measurements

In this part of the appendix the matrix elements of the coefficient matrices are listed for the linear equation systems (1.11) including the corrections introduced in chapter 7. The σ_i are the transmissions of the sextupole magnets defined by (7.1) and the ε_{ij} are the efficiencies of the high frequency transitions defined by (7.2), (7.3) and (7.4). Both for hydrogen and deuterium the first line of the matrices contains only ones; they represent the normalization (2.17). The other lines of the matrix each correspond to one of the used high frequency transitions. The order of these lines is arbitrary. In the following the matrix elements of such a line are ordered in blocks.

E.1 Coefficient Matrices for Polarization Measurements with Hydrogen

In the case of hydrogen there are four usable transitions out of which only three are needed for the determination of the occupation numbers. Therefore there are four possible analysis methods that each result from leaving out one of the high frequency transitions. Out of the four possible lines therefore three must be selected and entered in an arbitrary order into the matrix.

The structure of the lines is identical for the two medium field transitions MFT 1-3 and MFT 2-3, therefore only one line is listed for these high frequency transitions. For ε_{12} and ε_{23} the measured data from chapter 8.7 should be included for MFT 1-3 and MFT 2-3, while $y = 1$ for MFT 1-3 and $y = 2$ for MFT 2-3.

$$
\begin{array}{llcl}
\mathrm{SFT}\ 1-4: & M_{x1} & = & \sigma_1 (R_{14} - 1) + \varepsilon_{14} (\sigma_1 - \sigma_4) \\
 & M_{x2} & = & \sigma_2 (R_{14} - 1) \\
 & M_{x3} & = & \sigma_3 (R_{14} - 1) \\
 & M_{x4} & = & \sigma_4 (R_{14} - 1) - \varepsilon_{14} (\sigma_1 - \sigma_4) \\
 & & & \\
\mathrm{SFT}\ 2-4: & M_{x1} & = & \sigma_1 (R_{24} - 1) \\
 & M_{x2} & = & \sigma_2 (R_{24} - 1) + \varepsilon_{24} (\sigma_2 - \sigma_4) \\
 & M_{x3} & = & \sigma_3 (R_{24} - 1) \\
 & M_{x4} & = & \sigma_4 (R_{24} - 1) - \varepsilon_{24} (\sigma_2 - \sigma_4) \\
 & & & \\
\mathrm{MFT}\ \mathrm{y} - 3: & M_{x1} & = & \sigma_1 (R_{y3} - 1) + \varepsilon_{12} (\sigma_1 - \sigma_2) + \varepsilon_{12}\varepsilon_{23} (\sigma_2 - \sigma_3) \\
 & M_{x2} & = & \sigma_2 (R_{y3} - 1) - \varepsilon_{12} (\sigma_1 - \sigma_2) + \varepsilon_{23} (\sigma_2 - \sigma_3) - \varepsilon_{12}\varepsilon_{23} (\sigma_2 - \sigma_3) \\
 & M_{x3} & = & \sigma_3 (R_{y3} - 1) - \varepsilon_{23} (\sigma_2 - \sigma_3) \\
 & M_{x4} & = & \sigma_4 (R_{y3} - 1)
\end{array}
\tag{E.1}
$$

E.2 Coefficient Matrices for Polarization Measurements with Deuterium

There are seven practically usable high frequency transitions for deuterium, out of which only the three strong field transitions SFT 1-6, SFT 2-6 and SFT 3-5 and the two medium field transitions MFT 2-4 and MFT 3-4 are used for a polarization measurement. Nevertheless, in the following also the lines for the two other possible deuterium transitions SFT 2-5/3-6 and MFT 1-4 are listed. The efficiency of the transition 1-2 could not yet be measured for the medium field transitions, therefore for MFT 2-4 and MFT 3-4 it was assumed that $\varepsilon_{12} = 0$ for polarization measurements. If MFT 1-4 is used, this is not correct, however, this high frequency transition until now was not needed. For the future it is certainly desirable to include one of the high frequency transitions thus far not used in the analysis. As in the case of hydrogen, this would allow to check the functionality of the transitions during a polarization measurement by comparison of several analysis methods. The notation for the listing of the matrix elements is analogous to hydrogen.

$$
\begin{array}{llcl}
\text{SFT } 1-6: & M_{x1} & = & \sigma_1\,(R_{16}-1)+\varepsilon_{16}\,(\sigma_1-\sigma_6) \\
 & M_{x2} & = & \sigma_2\,(R_{16}-1) \\
 & M_{x3} & = & \sigma_3\,(R_{16}-1) \\
 & M_{x4} & = & \sigma_4\,(R_{16}-1) \\
 & M_{x5} & = & \sigma_5\,(R_{16}-1) \\
 & M_{x6} & = & \sigma_6\,(R_{16}-1)-\varepsilon_{16}\,(\sigma_1-\sigma_6) \\
 & & & \\
\text{SFT } 2-6: & M_{x1} & = & \sigma_1\,(R_{26}-1) \\
 & M_{x2} & = & \sigma_2\,(R_{26}-1)+\varepsilon_{26}\,(\sigma_2-\sigma_6) \\
 & M_{x3} & = & \sigma_3\,(R_{26}-1) \\
 & M_{x4} & = & \sigma_4\,(R_{26}-1) \\
 & M_{x5} & = & \sigma_5\,(R_{26}-1) \\
 & M_{x6} & = & \sigma_6\,(R_{26}-1)-\varepsilon_{26}\,(\sigma_2-\sigma_6) \\
 & & & \\
\text{SFT } 3-5: & M_{x1} & = & \sigma_1\,(R_{35}-1) \\
 & M_{x2} & = & \sigma_2\,(R_{35}-1) \\
 & M_{x3} & = & \sigma_3\,(R_{35}-1)+\varepsilon_{35}\,(\sigma_3-\sigma_5) \\
 & M_{x4} & = & \sigma_4\,(R_{35}-1) \\
 & M_{x5} & = & \sigma_5\,(R_{35}-1)-\varepsilon_{35}\,(\sigma_3-\sigma_5) \\
 & M_{x6} & = & \sigma_6\,(R_{35}-1) \\
 & & & \\
\text{SFT } 2-5/3-6: & M_{x1} & = & \sigma_1\,(R_{25/36}-1) \\
 & M_{x2} & = & \sigma_2\,(R_{25/36}-1)+\varepsilon_{25}\,(\sigma_2-\sigma_5) \\
 & M_{x3} & = & \sigma_3\,(R_{25/36}-1)+\varepsilon_{36}\,(\sigma_3-\sigma_6) \\
 & M_{x4} & = & \sigma_4\,(R_{25/36}-1) \\
 & M_{x5} & = & \sigma_5\,(R_{25/36}-1)-\varepsilon_{25}\,(\sigma_2-\sigma_5) \\
 & M_{x6} & = & \sigma_6\,(R_{25/36}-1)-\varepsilon_{36}\,(\sigma_3-\sigma_6) \\
 & & & \\
\text{MFT y}-4: & M_{x1} & = & \sigma_1\,(R_{y4}-1)+\varepsilon_{12}\,(\sigma_1-\sigma_2)+\varepsilon_{12}\varepsilon_{23}\,(\sigma_2-\sigma_3) \\
 & & & \qquad +\varepsilon_{12}\varepsilon_{23}\varepsilon_{34}\,(\sigma_3-\sigma_4) \\
 & M_{x2} & = & \sigma_2\,(R_{y4}-1)-\varepsilon_{12}\,(\sigma_1-\sigma_2)+\varepsilon_{23}\,(\sigma_2-\sigma_3)-\varepsilon_{12}\varepsilon_{23}\,(\sigma_2-\sigma_3) \\
 & & & \qquad +\varepsilon_{23}\varepsilon_{34}\,(\sigma_3-\sigma_4)-\varepsilon_{12}\varepsilon_{23}\varepsilon_{34}\,(\sigma_3-\sigma_4) \\
 & M_{x3} & = & \sigma_3\,(R_{y4}-1)-\varepsilon_{23}\,(\sigma_2-\sigma_3)+\varepsilon_{34}\,(\sigma_3-\sigma_4)-\varepsilon_{23}\varepsilon_{34}\,(\sigma_3-\sigma_4) \\
 & M_{x4} & = & \sigma_4\,(R_{y4}-1)-\varepsilon_{34}\,(\sigma_3-\sigma_4) \\
 & M_{x5} & = & \sigma_5\,(R_{y4}-1) \\
 & M_{x6} & = & \sigma_6\,(R_{y4}-1)
\end{array}
\tag{E.2}
$$

F Master Equations for the Spin Relaxation in Storage Cells

In this appendix the rate equations for the spin relaxation of hydrogen and deuterium due to spin exchange collisions, wall collisions and recombination are listed separately. The explanation for the notation used as well as the theoretical background for the calculation of the master equations can be found in chapter 2 and chapter 3. The rate equations for spin exchange collisions between hydrogen atoms were taken from [106]. The other equations for spin exchange and wall collisions were calculated by J. Stenger [150].

F.1 Relaxation trough Wall Collisions for Hydrogen

$$
\begin{aligned}
\frac{\mathrm{d}n_1}{\mathrm{d}t} &= \frac{C}{2}\left[j(\omega_{12})(n_2-n_1)\sin^2\theta + j(\omega_{14})(n_4-n_1)\cos^2\theta\right] \\
\frac{\mathrm{d}n_2}{\mathrm{d}t} &= \frac{C}{2}\left[j(\omega_{12})(n_1-n_2)\sin^2\theta + j(\omega_{23})(n_3-n_2)\cos^2\theta + j(\omega_{24})(n_4-n_2)\frac{\sin^2 2\theta}{2}\right] \\
\frac{\mathrm{d}n_3}{\mathrm{d}t} &= \frac{C}{2}\left[j(\omega_{34})(n_4-n_3)\sin^2\theta + j(\omega_{23})(n_2-n_3)\cos^2\theta\right] \\
\frac{\mathrm{d}n_4}{\mathrm{d}t} &= \frac{C}{2}\left[j(\omega_{34})(n_3-n_4)\sin^2\theta + j(\omega_{14})(n_1-n_4)\cos^2\theta + j(\omega_{24})(n_2-n_4)\frac{\sin^2 2\theta}{2}\right]
\end{aligned}
\tag{F.1}
$$

F.2 Relaxation through Wall Collisions for Deuterium

$$
\begin{aligned}
\frac{\mathrm{d}n_1}{\mathrm{d}t} &= \frac{C}{2}\left[j(\omega_{12})(n_2-n_1)\sin^2\theta_+ + j(\omega_{16})(n_6-n_1)\cos^2\theta_+\right] \\
\frac{\mathrm{d}n_2}{\mathrm{d}t} &= \frac{C}{2}\left[j(\omega_{12})(n_1-n_2)\sin^2\theta_+ + j(\omega_{23})(n_3-n_2)\cos^2\theta_+\sin^2\theta_-\right. \\
&\quad \left.+j(\omega_{25})(n_5-n_2)\cos^2\theta_+\cos^2\theta_- + 2j(\omega_{26})(n_6-n_2)\cos^2\theta_+\sin^2\theta_+\right] \\
\frac{\mathrm{d}n_3}{\mathrm{d}t} &= \frac{C}{2}\left[j(\omega_{34})(n_4-n_3)\cos^2\theta_- + j(\omega_{23})(n_2-n_3)\cos^2\theta_+\sin^2\theta_-\right. \\
&\quad \left.+j(\omega_{36})(n_6-n_3)\cos^2\theta_+\cos^2\theta_- + 2j(\omega_{35})(n_5-n_3)\cos^2\theta_-\sin^2\theta_-\right] \\
\frac{\mathrm{d}n_4}{\mathrm{d}t} &= \frac{C}{2}\left[j(\omega_{45})(n_5-n_4)\sin^2\theta_- + j(\omega_{34})(n_3-n_4)\cos^2\theta_-\right] \\
\frac{\mathrm{d}n_5}{\mathrm{d}t} &= \frac{C}{2}\left[j(\omega_{45})(n_4-n_5)\sin^2\theta_- + j(\omega_{25})(n_2-n_5)\cos^2\theta_+\cos^2\theta_-\right. \\
&\quad \left.+j(\omega_{56})(n_6-n_5)\cos^2\theta_-\sin^2\theta_+ + 2j(\omega_{35})(n_3-n_5)\cos^2\theta_-\sin^2\theta_-\right] \\
\frac{\mathrm{d}n_6}{\mathrm{d}t} &= \frac{C}{2}\left[j(\omega_{16})(n_1-n_6)\cos^2\theta_+ + j(\omega_{36})(n_3-n_6)\sin^2\theta_+\sin^2\theta_-\right. \\
&\quad \left.+j(\omega_{56})(n_5-n_6)\sin^2\theta_+\cos^2\theta_- + 2j(\omega_{26})(n_2-n_6)\cos^2\theta_+\sin^2\theta_+\right]
\end{aligned}
\tag{F.2}
$$

F.3 Relaxation through Spin Exchange Collisions for Hydrogen

$$\begin{aligned}
T_{HH}\frac{\mathrm{d}n_1}{\mathrm{d}t} &= n_2n_4 - n_1n_3 + \frac{\sin^2 2\theta}{4}\left(n_2 - n_4\right)^2 \\
T_{HH}\frac{\mathrm{d}n_2}{\mathrm{d}t} &= n_1n_3 - n_2n_4 + \frac{\sin^2 2\theta}{2}\left(n_1n_4 - n_1n_2 - n_2n_3 + n_3n_4 + n_2n_4 + \frac{1}{2}n_4^2 - \frac{3}{2}n_2^2\right) \\
T_{HH}\frac{\mathrm{d}n_3}{\mathrm{d}t} &= n_2n_4 - n_1n_3 + \frac{\sin^2 2\theta}{4}\left(n_2 - n_4\right)^2 \\
T_{HH}\frac{\mathrm{d}n_4}{\mathrm{d}t} &= n_1n_3 - n_2n_4 + \frac{\sin^2 2\theta}{2}\left(-n_1n_4 + n_1n_2 + n_2n_3 - n_3n_4 + n_2n_4 + \frac{1}{2}n_2^2 - \frac{3}{2}n_4^2\right)
\end{aligned} \tag{F.3}$$

F.4 Relaxation through Spin Exchange Collisions for Deuterium

$$
\begin{aligned}
T_{DD}\frac{\mathrm{d}n_1}{\mathrm{d}t} &= \frac{\sin^2 2\theta_+}{4}\left(n_2-n_6\right)^2 + n_2n_6 - n_1n_4 - n_1n_3\sin^2\theta_- - n_1n_5\cos^2\theta_- \\
&\quad + n_2n_5\sin^2\theta_+\sin^2\theta_- + n_3n_6\cos^2\theta_+\cos^2\theta_- \\
&\quad + n_2n_3\sin^2\theta_+\cos^2\theta_- + n_5n_6\cos^2\theta_+\sin^2\theta_- \\
T_{DD}\frac{\mathrm{d}n_2}{\mathrm{d}t} &= \frac{\sin^2 2\theta_-}{4}\left(n_3-n_5\right)^2\cos^2\theta_+ \\
&\quad + \frac{\sin^2 2\theta_+}{4}\Big[2n_1n_6 - 2n_1n_2 - 4n_2^2 - n_2n_4 + n_4n_6 + \left(n_2+n_6\right)^2 \\
&\qquad + \left(n_3n_6 - n_2n_3\right)\left(1+\sin^2\theta_-\right) + \left(n_5n_6 - n_2n_5\right)\left(1+\cos^2\theta_-\right)\Big] \\
&\quad + \left(n_1n_3 - n_2n_5\sin^2\theta_+\right)\sin^2\theta_- + \left(n_1n_4 - n_2n_3\cos^2\theta_-\right)\sin^2\theta_+ \\
&\quad - n_2n_6 + n_1n_5\cos^2\theta_- + \left(n_3n_5 - n_2n_4\right)\cos^2\theta_+ \\
T_{DD}\frac{\mathrm{d}n_3}{\mathrm{d}t} &= \frac{\sin^2 2\theta_+}{4}\left(n_2-n_6\right)^2\sin^2\theta_- \\
&\quad + \frac{\sin^2 2\theta_-}{4}\Big[2n_4n_5 - 2n_3n_4 - 4n_3^2 - n_1n_3 + n_1n_5 + \left(n_3+n_5\right)^2 \\
&\qquad + \left(n_5n_6 - n_3n_6\right)\left(1+\sin^2\theta_+\right) + \left(n_2n_5 - n_2n_3\right)\left(1+\cos^2\theta_+\right)\Big] \\
&\quad + \left(n_1n_4 - n_2n_3\sin^2\theta_+\right)\cos^2\theta_- + \left(n_2n_4 - n_3n_6\cos^2\theta_-\right)\cos^2\theta_+ \\
&\quad - n_3n_5 + n_4n_6\sin^2\theta_+ + \left(n_2n_6 - n_1n_3\right)\sin^2\theta_- \\
T_{DD}\frac{\mathrm{d}n_4}{\mathrm{d}t} &= \frac{\sin^2 2\theta_+}{4}\left(n_3-n_5\right)^2 + n_3n_5 - n_1n_4 - n_4n_6\sin^2\theta_+ - n_2n_4\cos^2\theta_+ \\
&\quad + n_2n_5\sin^2\theta_+\sin^2\theta_- + n_3n_6\cos^2\theta_+\cos^2\theta_- \\
&\quad + n_2n_3\sin^2\theta_+\cos^2\theta_- + n_5n_6\cos^2\theta_+\sin^2\theta_- \\
T_{DD}\frac{\mathrm{d}n_5}{\mathrm{d}t} &= \frac{\sin^2 2\theta_+}{4}\left(n_2-n_6\right)^2\cos^2\theta_- \\
&\quad + \frac{\sin^2 2\theta_-}{4}\Big[2n_3n_4 - 2n_4n_5 - 4n_5^2 - n_1n_5 + n_1n_3 + \left(n_3+n_5\right)^2 \\
&\qquad + \left(n_3n_6 - n_5n_6\right)\left(1+\sin^2\theta_+\right) + \left(n_2n_3 - n_2n_5\right)\left(1+\cos^2\theta_+\right)\Big] \\
&\quad + \left(n_1n_4 - n_5n_6\cos^2\theta_+\right)\sin^2\theta_- + \left(n_4n_6 - n_2n_5\sin^2\theta_-\right)\sin^2\theta_+ \\
&\quad - n_3n_5 + n_2n_4\cos^2\theta_+ + \left(n_2n_6 - n_1n_5\right)\cos^2\theta_- \\
T_{DD}\frac{\mathrm{d}n_6}{\mathrm{d}t} &= \frac{\sin^2 2\theta_-}{4}\left(n_3-n_5\right)^2\sin^2\theta_+ \\
&\quad + \frac{\sin^2 2\theta_+}{4}\Big[2n_1n_2 - 2n_1n_6 - 4n_6^2 - n_4n_6 + n_2n_4 + \left(n_2+n_6\right)^2 \\
&\qquad + \left(n_2n_3 - n_3n_6\right)\left(1+\sin^2\theta_-\right) + \left(n_2n_5 - n_5n_6\right)\left(1+\cos^2\theta_-\right)\Big] \\
&\quad + \left(n_1n_5 - n_5n_6\cos^2\theta_+\right)\cos^2\theta_- + \left(n_1n_4 - n_5n_6\sin^2\theta_-\right)\cos^2\theta_+ \\
&\quad - n_2n_6 + n_1n_3\sin^2\theta_- + \left(n_3n_5 - n_4n_6\right)\sin^2\theta_+
\end{aligned}
\tag{F.4}
$$

G Numerical Solution of Differential Equations

At several points in this thesis regular differential equations are solved numerically. On the one hand this concerns the solution of the master equation for the spin relaxation of hydrogen and deuterium, on the other hand the solution of the equation of motion for the mixed hyperfine states of a hydrogen or deuterium atom in a sextupole magnet (6.15, 6.16). In all cases it is an initial value problem that can be solved with a Rung-Kutta method following [151].

The master equations for the spin relaxation in storage cells are systems of regular first order differential equations of the general form

$$y' = f(x, y), \tag{G.1}$$

where both y' and $f(x, y)$ are defined as vectors:

$$y' := \begin{bmatrix} y'_1 \\ \vdots \\ y'_n \end{bmatrix}, \qquad f(x, y) := \begin{bmatrix} f_1(x, y_1, \ldots, y_n) \\ \vdots \\ f_n(x, y_1, \ldots, y_n) \end{bmatrix}. \tag{G.2}$$

The initial condition can also be given in vector form:

$$y(x_0) = y_0 = \begin{bmatrix} y_{10} \\ \vdots \\ y_{n0} \end{bmatrix}. \tag{G.3}$$

So-called one-step-methods for the solution of initial value problems are based on the calculation of approximate values η_i for the parameters $y_i := y(x_i)$ of the exact solution $y(x)$ by

$$\begin{aligned} \eta_0 &:= y_0 \\ \eta_{i+1} &:= \eta_i + h\Phi(x_i, \eta_i; h; f) \\ x_{i+1} &:= x_i + h. \end{aligned} \tag{G.4}$$

h is the step size of the method. The function $\Phi(x, y; h; f)$ defines the method. For the simplest one-step-method, the so-called Euler method, it is $\Phi(x, y; f) := f(x, y)$.

The order of a one-step-method is the power of h, with which the difference between approximate solution and exact solution converges to 0 for $h \longrightarrow 0$. The Euler method is a first order method and becomes rather imprecise after a few interactions (G.4).

The Runge-Kutta method used in this thesis is a fourth order method and is defined by the function Φ as follows:

$$\begin{aligned} \Phi(x, y; h) &:= \frac{1}{6}(k_1 + 2k_2 + 2k_3 + k_4) \\ k_1 &:= f(x, y) \\ k_2 &:= f\left(x + \frac{h}{2}, y + \frac{1}{2}hk_1\right) \\ k_3 &:= f\left(x + \frac{h}{2}, y + \frac{1}{2}hk_2\right) \\ k_4 &:= f(x + h, y + hk_3). \end{aligned} \tag{G.5}$$

The equation of motion for the mixed states in a sextupole magnet is a regular second order differential equation. However, it also may be transformed into an equivalent system of two first order differential equations. In general a m-th order differential equation of the form

$$y^{(m)}(x) = f\left(x, y(x), y^{(1)}(x), \ldots, y^{(m-1)}(x)\right) \tag{G.6}$$

can be transformed into an equivalent system of m first order differential equations by introducing dummy functions

$$\begin{array}{rcl} z_1(x) & := & y(x) \\ z_2(x) & := & y^{(1)}(x) \\ \vdots & & \vdots \\ z_m(x) & := & y^{(m-1)}(x) \end{array} \tag{G.7}$$

The resulting m first order differential equation may be written as

$$z' = \begin{bmatrix} z_1' \\ \vdots \\ z_{m-1}' \\ z_m' \end{bmatrix} = \begin{bmatrix} z_2 \\ \vdots \\ z_m \\ f(x, z_1, z_2, \ldots, z_m) \end{bmatrix}. \tag{G.8}$$

H Dimensions of the Apparatus

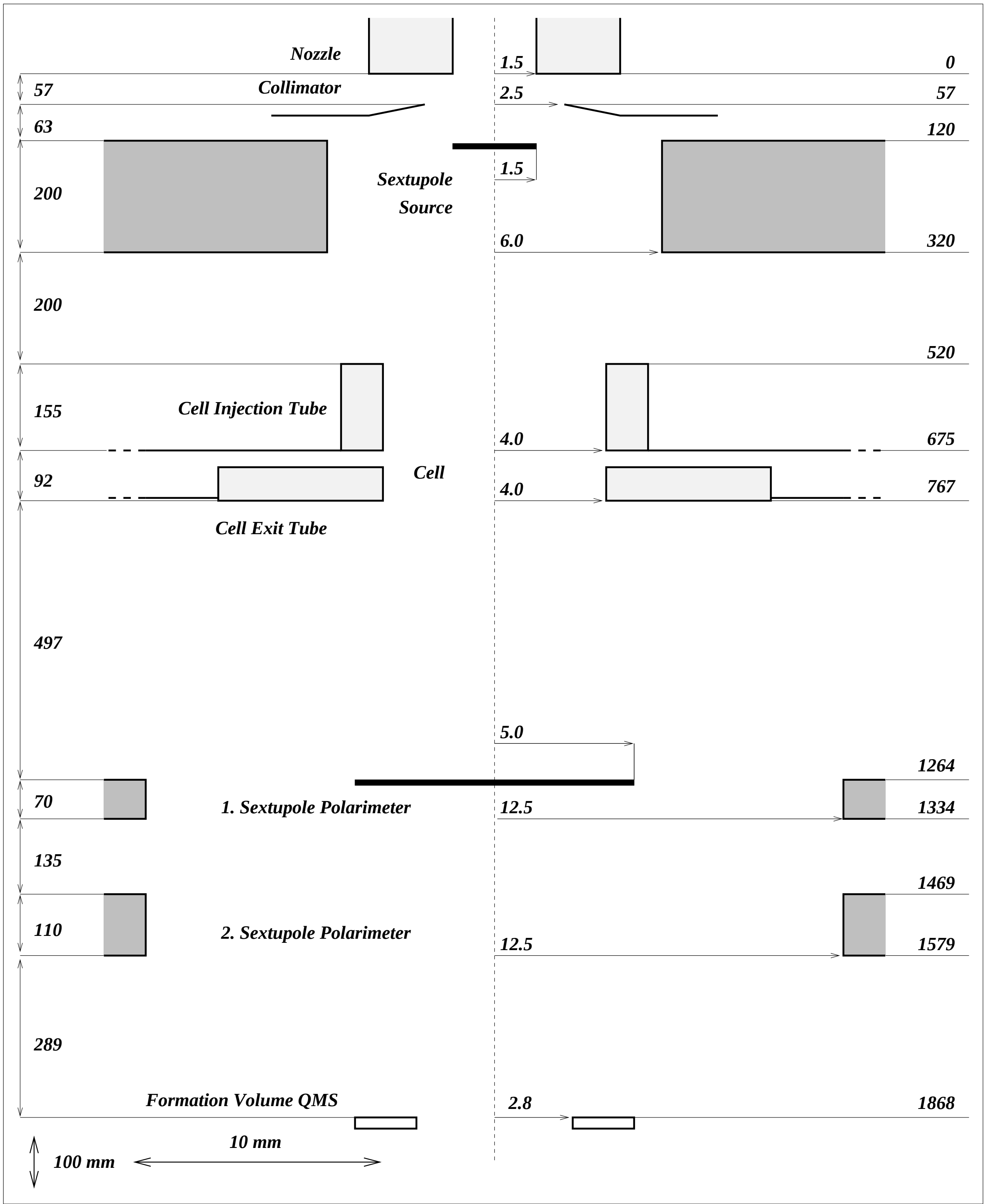

Fig. H.1:
Dimensions at the test stand. On the left side relative distances are shown, in the center radii relative to the atomic beam axis and on the right side absolute distances relative to the position of the nozzle. The skimmer is not shown, it is located at a distance of $7\,\mathrm{mm}$ from the nozzle and has a radius of $1.6\,\mathrm{mm}$. The beam blocks in the sextupole magnets are shown as black beams. Horizontal scale: $1 : 0.243$. Vertical scale:$1 : 10.87$.

Figures

Tables

Bibliography

[1] O. Nachtmann; *Elementarteilchenphysik* (1986) Vieweg, Braunschweig.

[2] B. Povh, K. Rith, Ch. Scholz und F. Zetsche; *Teilchen und Kerne* (1993); Springer-Verlag Berlin, Heidelberg, New York.

[3] J.D. Bjorken; *Phys. Rev.* **148** (1966) 1467.

[4] J.D. Bjorken; *Phys. Rev.* **D1** (1970) 1376.

[5] J. Ellis and R. Jaffe; *Phys. Rev.* **D9** (1974) 1444.

[6] SLAC E143-Collaboration; *Phys. Rev. Lett.* **74** (1995) 346.

[7] S.A. Larin; *Phys. Lett.* **B334** (1994) 192.

[8] SLAC E142-Collaboration; *Phys. Rev. Lett.* **71** (1993) 959.

[9] R.L. Jaffe and A. Manohar; *Nucl. Phys.* **B337** (1990) 509.

[10] SLAC E80-Collaboration; *Phys. Rev. Lett.* **37** (1976) 1261.

[11] SLAC E80-Collaboration; *Phys. Rev. Lett.* **41** (1978) 70.

[12] SLAC E130-Collaboration; *Phys. Rev. Lett.* **51** (1983) 1135.

[13] European Muon Collaboration; *Phys. Lett.* **B206** (1988) 364.

[14] European Muon Collaboration; *Nucl. Phys.* **B328** (1989) 1.

[15] Spin Muon Collaboration; *Phys. Lett.* **B329** (1994) 399-406.

[16] Spin Muon Collaboration; *Phys. Lett.* **B302** (1993) 533.

[17] Spin Muon Collaboration; *Phys. Lett.* **B320** (1994) 400.

[18] H. Burkhardt and W.N. Cottingham; *Ann. Phys.* **56** (1970) 453.

[19] Spin Muon Collaboration; *Phys. Lett.* **B336** (1994) 125-130.

[20] T.E. Chupp, M.E. Wagshul, K.P. Coulter, A.B. McDonald and W. Happer; *Phys. Rev.* **C36** (1987) 2244.

[21] T.E. Chupp, R.A. Loveman, A.K. Thompson, A.M. Bernstein and D.R. Tieger; *Phys. Rev.* **C45** (1992) 915.

[22] HERMES Collaboration; *A Proposal to measure the Spin-dependent Structure Functions of the Neutron and the Proton at HERA*; Proposal DESY **PRC-90/91** (1990).

[23] HERMES Collaboration; *Technical Design Report* (1993).

[24] C. Ekström; *Proc. 3rd adv. Accel. Phys. Course*, Uppsala University; S. Turner (eds.), Sweden (1989) 184.

[25] A.A. Sokolov and I.M. Ternov; *Sov. Phys. Dokl.* **8** (1964) 1203.

[26] J. Buon and K. Steffen; *Nucl. Instr. Meth.* **A245** (1986) 248.

[27] D.P. Barber et al.; *Nucl. Instr. Meth.* **A329** (1993) 79-111.

[28] M. Düren; *Proc. of Workshop on Polarized Beams and Targets, Les Houches* (1994).

[29] F.D. Colegrove, L.D. Schaerer and G.K. Walters; *Phys. Rev.* **132** (1963) 2561.

[30] P. Hoodbhoy, R.L. Jaffe and A. Manohar; *Nucl. Phys.* **B312** (1989) 571.

[31] R.L. Jaffe and A. Manohar; *Nucl. Phys.* **B321** (1989) 343.

[32] R.L. Jaffe and A. Manohar; *Phys. Lett.* **B223** (1989) 218.

[33] M. Veltri; *Dissertation*, University of Heidelberg, (1992).

[34] L.L. Frankfurt, M.I. Strikman, L. Mankiewicz, A. Schäfer, E. Rondio, A. Sandacz and V. Papavassiliou; *Phys. Lett.* **B230** (1989) 141.

[35] F.E. Close and R.G. Milner; *Phys. Rev.* **D44** (1991) 3691.

[36] R.L. Jaffe and X. Ji; *Phys. Rev. Lett.* **67** (1991) 552.

[37] E. Steffens; *private communication* (1995).

[38] J.S. Dunham, C.S. Galovich, H.F. Glavish, S.S. Hanna, D.G. Mavis and S.W. Wissink; *Nucl. Instr. Meth.* **219** (1984) 46.

[39] M.D. Barker, G. Cakey, C.A. Gosset, W. Haeberli, D.G. Mavis, P.A. Quin, S. Riedhauser, J. Sowinski and J. Ulbricht; *Proc. 5th Int. Symp. on Polarization Phenomena in Nuclear Physics*, Santa Fe 1980, G.G. Ohlsen, R.E. Brown, N. Jarmie, W.W. McNaughton and G.M. Hale (eds.); *AIP Conf. Proc.* **69** (1981) 931.

[40] K.P. Schüler; *Proc. in High Energy Physics with Polarized Beams and Polarized Targets*, Lausanne 1990; C. Joseph and J. Soffer (eds.) *Experimentia Suppl.* **38** (1991) 460.

[41] W. Haeberli; *Proc. Workshop on Nucl. Phys. with Stored, Cooled Beams*, Indiana 1984, P. Schwandt and H.O. Meyer (eds.); *AIP Conf. Proc.* **128** (1985) 251.

[42] G.E. Thomas, R.J. Holt, D. Boyer, M.C. Green, R.S. Kowalczyk and L. Young; *Nucl. Instr. Meth.* **A257** (1987) 32-34.

[43] D.R. Swenson and L.W. Anderson; *Nucl. Instr. Meth.* **B29** (1988) 627-642.

[44] W. Haeberli; *Ann. Rev. Nucl. Sci.*, **17** (1967) 373.

[45] W. Korsch; *Dissertation*, University of Marburg/Lahn (1990)

[46] F. Stock; *Dissertation*, University of Heidelberg (1994).

[47] F. Stock, K. Rith, H.G. Gaul, B. Lorentz, H. Mairon, B. Povh, E. Steffens, D. Toporkov, K. Zapfe, F. Rathmann, D. Fick, W. Korsch, G. Graw, K. Reinmüller, P. Schiemenz, W. Haeberli; *Nucl. Instr. Meth.* **A343** (1994) 334-342.

[48] E.D. Kinney; *HERMES-Report* **3/90** (1990).

[49] H.G. Gaul and E. Steffens; *Nucl. Instr. Meth.* **A316** (1992) 297.

[50] H.G. Gaul; *Dissertation*, University of Heidelberg, (1991).

[51] R. Gilman, R.J. Holt, E.R. Kinney, R.S. Kowalczyk, S.I. Mishnev, J. Napolitano, D.M. Nikolenko, S.G. Popov, D.H. Potterveld, I.A. Rachek, A.B. Temnykh, D.K. Toporkov, E.P. Tsentalovich, B.B. Wojtsekhowski and L. Young; *Phys. Rev. Lett.* **65** (1990) 1733.

[52] R. Gilman, R.J. Holt, E.R. Kinney, R.S. Kowalczyk, J. Napolitano, A.W. Nikitin, D.M. Nikolenko, S.G. Popov, D.H. Potterveld, I.A. Rachek, D.K. Toporkov, E.P. Tsentalovich, B.B. Wojtsekhowski and L. Young; *Nucl. Instr. Meth.* **A327** (1993) 277-286.

[53] J.F.J. van den Brand; *Proc. on Polarized Ion Sources and Polarized Gas Targets*, Madison 1993; L.W. Anderson and W. Haeberli (eds.); *AIP Conf. Proc., New York* **293** (1994) 54.

[54] H.O. Meyer, C. Horowitz, H. Nann, P.V. Pancella, S.F. Pate, R.E. Pollock, B. Von Przewoski, T. Rinckel, M.A. Ross and F. Sperisen; *Nucl. Phys.* **A539** (1992) 633-661.

[55] T. Wise, A.D. Roberts and W. Haeberli; *Nucl. Instr. Meth.* **A336** (1993) 410-422.

[56] M. Düren, Z. Moroz, M. Veltri, K. Zapfe, H. Mairon, M. Metzger, B. Povh, K. Rith, E. Steffens, F. Stock, D. Toporkov, F. Zetsche, T.A. Shibata, D. Fick, G. Graw, W. Haeberli and G.T. Garvey; *Nucl. Instr. Meth.* **A322** (1992) 13-19.

[57] K. Zapfe, B. Braun, H.G. Gaul, M. Grieser, B. Povh, M. Rall, E. Steffens, F. Stock, J. Tonhäuser, C. Montag, F. Rathmann, D. Fick and W. Haeberli; *Rev. Sci. Instr.* **66** (1995) 28.

[58] F. Rathmann, C. Montag, D. Fick, J. Tonhäuser, W. Brückner, H.G. Gaul, M. Grieser, B. Povh, M. Rall, E. Steffens, F. Stock, K. Zapfe, B. Braun, G. Graw and W. Haeberli; *Phys. Rev. Lett.* **71** (1993) 1379.

[59] F. Rathmann; *Dissertation*, University of Marburg/Lahn (1993)

[60] G. Fischer; *Lineare Algebra*, 8. Aufl., Vieweg (1984).

[61] A. Kastler; *J. Phys. Radium* **11** (1950) 255.

[62] H.G. Dehmelt; *Phys. Rev.* **105** (1950) 1487.

[63] W. Franzen; *Phys. Rev.* **115** (1959) 850.

[64] M.A. Bouchiat; *J. Phys. Radium* **24** (1963) 379.

[65] M.A. Bouchiat; *J. Phys. Radium* **24** (1963) 611.

[66] M.A. Bouchiat and J. Brossel; *Phys. Rev.* **147** (1966) 41.

[67] D.R. Swenson and L.W. Anderson; *Nucl. Instr. Meth.* **B12** (1985) 157-160.

[68] J.C. Camparo; *J. Chem. Phys.* **86** (1987) 1533.

[69] C.D.P. Levy, P.W. Schmor, W.M. Law; *J. Appl. Phys.* **63** (1988) 10.

[70] D. Fick; *Appl. Phys.* **A49** (1989) 343.

[71] W. Luck; *Dissertation*, University of Marburg/Lahn (1989).

[72] J. Stenger, E. Steffens and K. Zapfe; *Nucl. Instr. Meth.* **A330** (1993) 21.

[73] J. Stenger; *Diplomarbeit*, University of Heidelberg, (1992).

[74] J.S. Price and W. Haeberli; *Nucl. Instr. Meth.* **A326** (1993) 416.

[75] L. Buchmann; *Nucl. Instr. Meth.* **A301** (1991) 383.

[76] J. Arvieux, S.D. Baker, A. Boudard, J. Cameron, T. Hasegawa, D. Hutcheon, C. Kerboul, G. Gaillard and Nguyen Van Sen; *Nucl. Instr. Meth.* **A273** (1988) 48.

[77] K. Jeltsch, P. Huber, A. Janett and H.R. Streibel; *Helv. Phys. Acta* **43** (1970) 279.

[78] W. Grübler, V. König, P.A. Schmelzbach, B. Jenny and J. Vybrial; *Nucl. Phys.* **A369** (1981) 381.

[79] W. Haeberli, T. Wise and A. Converse; *Proc. 4th LEAR Workshop Villars*, 1987; C. Amsler, G. Backenstoss, R. Klapisch, C. Leluc, D. Simon and L. Tauscher (eds.); Harwood Academic Publishers, Chur (1988)

[80] J.S. Price; *Dissertation*, University of Wisconsin-Madison (1993); available from University Microfilms International, 300 Zeeb Road, P.O. Box 1346, Ann Arbor, MI 48106-1346, USA

[81] J.S. Price and W. Haeberli; *Nucl. Instr. Meth.* **A349** (1994) 321.

[82] J.S. Price; private communication (1994).

[83] J.E. Brolley, G.P. Lawrence and G.G. Ohlsen; *Proc. 3rd Int. Symp. on Polarization Phenomena in Nucl. Reactions*, Madison 1970; H.H. Barschall and W. Haeberli (eds.); Univ. of Wisconsin Press Madison (1971) 846.

[84] T.B. Clegg and S.K. Lemieux; *Triangle Univ. Nucl. Lab. Progress Report*, TUNL XXX, 1990-1991, Duke Station, Durham, North Carolina.

[85] A. Trützschler; *Diplomarbeit*, University of Köln (1994).

[86] W.E. Lamb and R.C. Retherford; *Phys. Rev.* **79** (1950) 549.

[87] J.L. McKibben; *Am. J. Phys.* **45** (1977) 1022.

[88] C. Cohen-Tanoudij, B. Diu, F. Laloë; *Quantum Mechanics*, Vol. 2, 2^{nd} ed., (1977).

[89] H. Hellwig, R.F.C. Vessot, M.W. Levine, P.W. Zitzewitz, D.W. Allen and D.J. Glaze; *IEEE Trans. Instr. Meas.* **IM-19**, (1970) 200.

[90] A. Dymanus; Beam-maser Spectroscopy; *Atomic and Molecular Beam Methods*, Vol. 2, G. Scoles, D. Laine, U. Valbusa (eds.); Oxford University Press (1992).

[91] K. Blum; *Density Matrix Theory and Applications*, New York (1981).

[92] C. Cohen-Tanoudij, B. Diu, F. Laloë; *Quantum Mechanics*, Vol. 1, 2^{nd} ed., (1977).

[93] K. Reinmüller; *Diplomarbeit*, University of München (1994).

[94] D.J. Larson, P.A. Valberg and N.F. Ramsey; *Phys. Rev. Let.* **23** (1969) 1369.

[95] D. Fick; *Einführung in die Kernphysik mit polarisierten Teilchen*, BI-Hochschulskripte Bd. **755a**, Mannheim (1971).

[96] N. Bloembergen, E.M. Purcell and P.V. Pound; *Phys. Rev.* **73** (1948) 679.

[97] E.M. Purcell and G.B. Field; *Astrophys. J.* **124** 542 (1956).

[98] A. Dalgarno and M.R.H. Rudge; *Proc. Roy. Soc.* **A286** (1965) 519-524.

[99] H.S.W. Massey and C.B.O. Mohr; *Proc. Roy. Soc.* **A144** (1934) 188.

[100] D.R. Swenson, D. Tupa and L.W. Anderson; *J. Phys. B: At. Mol. Phys.* **18** (1985) 4433-4444.

[101] M. Desaintfuscien and C. Audoin; *Phys. Rev.* **A13** (1976) 2070.

[102] A.C. Allison and A. Dalgarno; *Astrophys. J.* **158**, 423 (1969).

[103] A.C. Allison; *Phys. Rev.* **A5**, 2695 (1972).

[104] J.P. Wittke and R.H. Dicke; *Phys. Rev.* **103** (1956) 620.

[105] M.v. Ardenne; *Tabellen z. angew. Physik*, Band 2, 2. Auflage, VEB-Verlag Berlin (1964) 141.

[106] T. Walker and L.W. Anderson; *Nucl. Instr. Meth.* **A334** (1993) 313.

[107] K. Coulter, R. Holt, E. Kinney, R. Kowalczyk, D. Potterveld, L. Young, B. Zeidman, A. Zghiche and D. Toporkov; *Phys. Rev. Lett.* **68** (1992) 174.

[108] B. Lorentz; *Diplomarbeit*, University of Heidelberg (1993).

[109] G. Clausnitzer, R. Fleischmann und H. Schopper; *Z. Phys.* **144** (1956) 336.

[110] D. Kassen; *Dissertation*, University of Heidelberg, (1977).

[111] H. Meinke, G. Gundlach; *Taschenbuch der Hochfrequenztechnik*, 3. Auflage, Springer-Verlag (1968) 459-465

[112] I. Simiantonakis; *Diplomarbeit*, University of Heidelberg, (1994).

[113] W. Gerlach und O. Stern; *Z. Phys.* **8** (1921) 110.

[114] W. Gerlach und O. Stern; *Z. Phys.* **9** (1922) 349.

[115] P. Schiemenz, A. Ross and G. Graw; *Nucl. Instr. Meth.* **A305** (1991) 15.

[116] M.T. Lin; *Diplomarbeit*, University of Heidelberg (1993).

[117] P. Kusch, V.W. Hughes; *Handbuch der Physik* **37/1**, Springer-Verlag, Berlin (1959)

[118] I. Rabi, S. Millman, P. Kusch, J. Zacharias; *Phys. Rev.* **55** (1939) 526.

[119] A. Abragam and J.M. Winter; *Phys. Rev. Lett.* **1** (1958) 374.

[120] R.J. Philpott; *Nucl. Instr. Meth.* **A259** (1987) 317-323.

[121] H. Jänsch; *Diplomarbeit*, University of Marburg/Lahn (1982).

[122] A.D. Roberts, P. Elmer, M.A. Ross, T. Wise and W. Haeberli; *Nucl. Instr. Meth.* **A322** (1992) 6-12.

[123] S. Oh; *Nucl. Instr. Meth.* **82** (1970) 189-197.

[124] R. Beurtey; *Proc.* 2^{nd} *Int. Symp. on Polarization Phenomena of Nucleons*, Karlsruhe, P. Huber, H. Schopper, (eds.); American Institute of Physics, New York (1965) 33.

[125] K. Halbach; *Nucl. Instr. Meth.* **169** (1980) 1.

[126] A. Roth; *Vacuum Technology*, North-Holland publishing Company, Amsterdam (1982).

[127] G.A. Bird; *Molecular Gas Dynamics*, Clarendon Press, Oxford (1976).

[128] M. Schick; *Diplomarbeit*, University of Heidelberg (1990)

[129] D. Toporkov, *private communication* (1992).

[130] H. Kolster; *private communication* (1994).

[131] H. Mairon; *Diplomarbeit*, University of Heidelberg (1992).

[132] K. Meinhold; *Diplomarbeit*, University of München (1972).

[133] E.M. Gabriel; *Diplomarbeit*, University of Heidelberg, (1995).

[134] E. Wittmann; *Diplomarbeit*, University of Heidelberg, (1994).

[135] CERN Program Library Office, CERN-CN Division; *MINUIT - Function Minimization and Error Analysis, Reference Manual, Version 92.1*, (1992).

[136] B. Braun; *Diplomarbeit*, University of Heidelberg (1991).

[137] D. Kleppner; *Ann. Phys. Fr.* **10** (1985) 877.

[138] R. Sprik, J.T.M. Walraven and I.F.Silvera; *Phys. Rev.* **B32** (1985) 5668.

[139] U. Funk; *Diplomarbeit*, University of Heidelberg, (1995).

[140] F. Stock; Proc. Workshop on Pol. Ion Sources and Pol. Gas Targets, Madison, WI 1993; L.W. Anderson und W. Haeberli (eds.); *AIP Conf. Proc.*, New York **293** (1994) 22.

[141] A.C.L. Barnard, C.M. Jones and J.L. Weil; *Nucl. Phys.* **50** (1964) 604.

[142] P. Schwandt, T.B. Clegg and W. Haeberli; *Nucl. Phys.* **A163** (1971) 432.

[143] K. Zapfe-Düren; *private communication* (1995).

[144] A. Metz; *Diplomarbeit*, University of München, (1995).

[145] M. Knudsen; *Annalen der Physik* **48** (1915) 1113.

[146] G. Comsa and R. David; *Surface Science Report* **5** (1985) 145.

[147] J.A. Giordmaine and T.C. Wang; *J. Appl. Phys.* **31** (1960) 463.

[148] P. Zugenmaier; *Zeitschrift für angewandte Physik* **20** (1965) 184.

[149] Fa. Balzers; *Partialdruckmessung in der Vakuumtechnik.*

[150] J. Stenger und K. Rith; submitted for publication in *Nucl. Instr. Meth.* (Dez. 1994).

[151] J. Stoer und R. Bulirsch; *Numerische Mathematik*, Vol. 2, 3. Auflage, Springer-Verlag (1990) 117